

EPA/600/3-88/008  
February 1988

ROCKY MOUNTAIN ACID DEPOSITION MODEL ASSESSMENT  
Evaluation of Mesoscale Acid Deposition Models for  
Use in Complex Terrain

by

R. E. Morris  
R. C. Kessler  
S. G. Douglas  
K. R. Styles

SYSTEMS APPLICATIONS, INC.  
101 Lucas Valley Road  
San Rafael, California 94903

Contract No. 68-02-4187

Project Officer

Alan H. Huber  
Meteorology and Assessment Division  
Atmospheric Sciences Research Laboratory  
Research Triangle Park, North Carolina 27711

ATMOSPHERIC SCIENCES RESEARCH LABORATORY  
OFFICE OF RESEARCH AND DEVELOPMENT  
U.S. ENVIRONMENTAL PROTECTION AGENCY  
RESEARCH TRIANGLE PARK, NORTH CAROLINA 22771

**TECHNICAL REPORT DATA**  
(Please read Instructions on the reverse before completing)

1. REPORT NO. EPA/600/3-88/008		2.		3. RECIPIENT'S ACCESSION NO. <b>PB88 167481/AS</b>	
4. TITLE AND SUBTITLE ROCKY MOUNTAIN ACID DEPOSITION MODEL ASSESSMENT: Evaluation of Mesoscale Acid Deposition Models for Use in Complex Terrain				5. REPORT DATE February 1988	
				6. PERFORMING ORGANIZATION CODE	
7. AUTHOR(S) R. E. Morris, R. C. Kessler, S. G. Douglas, and K. R. Styles				8. PERFORMING ORGANIZATION REPORT NO.	
9. PERFORMING ORGANIZATION NAME AND ADDRESS Systems Applications, Inc. 101 Lucas Valley Road San Rafael, CA 94903				10. PROGRAM ELEMENT NO. N104/C/05/05-5145 (FY-89)	
				11. CONTRACT/GRANT NO.  68-02-4187	
12. SPONSORING AGENCY NAME AND ADDRESS Atmospheric Sciences Research Laboratory - RTP, NC Office of Research and Development U. S. Environmental Protection Agency Research Triangle Park, NC 27711				13. TYPE OF REPORT AND PERIOD COVERED	
				14. SPONSORING AGENCY CODE  EPA/600/03	
15. SUPPLEMENTARY NOTES					
16. ABSTRACT  This report includes an evaluation of candidate meteorological models and acid deposition models.  The hybrid acid deposition/air quality modeling system for the Rocky Mountains makes use of a mesoscale meteorological model, which includes a new diagnostic wind model, as a driver for a Lagrangian puff model that treats transport, dispersion, chemical transformation, and dry and wet deposition. Transport will be defined from the diagnostic wind model based on the wind at the puff center. The treatment of dispersion will be based on the parameterization in the PNL/MELSAR-POLUT, while re-training the MESOPUFF-II dispersion algorithms as an option. Based on the evaluation of the chemical mechanisms, the RIVAD chemistry appears to be the most scientifically sound, as well as consistent, with the Lagrangian puff model formulation. Dry deposition will use the CCADM dry deposition module with some minor adjustments. Wet deposition will be based on the scavenging coefficient approach as used in the ERT/MESOPUFF-II.					
17. KEY WORDS AND DOCUMENT ANALYSIS					
a. DESCRIPTORS		b. IDENTIFIERS/OPEN ENDED TERMS		c. COSATI Field/Group	
18. DISTRIBUTION STATEMENT  RELEASE TO PUBLIC		19. SECURITY CLASS (This Report)  UNCLASSIFIED		21. NO. OF PAGES 241	
		20. SECURITY CLASS (This page)  UNCLASSIFIED		22. PRICE	

N O T I C E

THIS DOCUMENT HAS BEEN REPRODUCED FROM THE  
BEST COPY FURNISHED US BY THE SPONSORING  
AGENCY. ALTHOUGH IT IS RECOGNIZED THAT CER  
TAIN PORTIONS ARE ILLEGIBLE, IT IS BEING RE  
LEASED IN THE INTEREST OF MAKING AVAILABLE  
AS MUCH INFORMATION AS POSSIBLE

## NOTICE

The information in this document has been funded by the United States Environmental Protection Agency under Contract No. 68-02-4187 to Systems Applications, Inc. It has been subjected to the agency's peer and administrative review, and it has been approved for publication as an EPA document. Mention of trade names or commercial products does not constitute endorsement or recommendation for use.

## ABSTRACT

The hybrid acid deposition/air quality modeling system for the Rocky Mountains makes use of a mesoscale meteorological model, which includes a new diagnostic wind model, as a driver for a Lagrangian puff model that treats transport, dispersion, chemical transformation, and dry and wet deposition. Transport will be defined from the diagnostic wind model based on the wind at the puff center. The treatment of dispersion will be based on the parameterization in the PNL/MELSAR-POLUT, while retaining the MESO-PUFF-II dispersion algorithms as an option. Based on the evaluation of the chemical mechanisms, the RIVAD chemistry appears to be the most scientifically sound as well as consistent with the Lagrangian puff model formulation. Dry deposition will use the CCADM dry deposition module with some minor adjustments. Wet deposition will be based on the scavenging coefficient approach, as used in the ERT/MESOPUFF-II.

This modeling approach was guided by the comments of members of the Western Acid Deposition Task Force (WADTF) in response to a questionnaire mailed in August 1986 and a meeting in May 1987 in Denver. The modeling approach recommended by members of the WADTF was use of a Lagrangian acid deposition model with a complex-terrain wind model to calculate long-term source-specific deposition of nitrogen and sulfur. This modeling approach must be cost effective, simple enough for use by the regulatory agencies, and similar to the existing regulatory models used for impact assessment. If possible, it was desirable that the model have the ability to calculate PSD increment consumption of  $\text{SO}_2$  and TSP sources. We feel that the hybrid modeling system described in this report meets these requirements in the most technically rigorous manner possible, subject to the cost and complexity constraints. The modeling approach is not as comprehensive as the Eulerian model development effort (RADM) currently being carried out by the National Center for Atmospheric Research and State University of New York at Albany. However, this approach is more technically rigorous than those currently used by regulatory agencies, and will generate more defensible estimates of incremental impacts of acid deposition and concentrations in regions of complex terrain in the Rocky Mountains.

In a previous report we reviewed existing meteorological and acid deposition models, and reported on the selection and preliminary evaluation of

four candidate mesoscale meteorological models (CIT/WINDMOD, LANL/ATMOS1, PNL/MELSAR-MET, AND SAI/CTWM) and four candidate acid deposition models (ERT/MESOPUFF-II, PNL/MELSAR-POLUT, SAI/CCADM, and SAI/RIVAD).<sup>\*</sup> This report is a continuation of that report and includes the following topics:

- (1) a more detailed evaluation of the candidate meteorological models over terrain within the Rocky Mountains;
- (2) the design of a new diagnostic wind (DWM) model that uses components of the candidate meteorological models;
- (3) an evaluation of the new DWM using the same criteria used to evaluate the candidate mesoscale meteorological models, then comparing its predictions with observations from the Rocky Mountains, and then evaluating the DWM for two geographic settings: a complex terrain/coastal environment and within a large valley;
- (4) a detailed evaluation of the candidate acid deposition models; and
- (5) the design of a new acid deposition/air quality based on components in the candidate acid deposition models.

---

<sup>\*</sup> R. E. Morris and R. C. Kessler, "Rocky Mountain Acid Deposition Model Assessment--Review of Existing Mesoscale Models for use in Complex Terrain" (Morris and Kessler, 1987).

## CONTENTS

	Abstract.....	iii
	Acknowledgments.....	xii
1	INTRODUCTION.....	1
	1.1 Background.....	1
	1.2 Purpose of This Report.....	2
	1.3 Overview of the New Hybrid Acid Deposition/ Air Quality Modeling System for the Rocky Mountains.....	3
	1.4 Report Organization.....	3
2	EVALUATION OF THE CANDIDATE METEOROLOGICAL MODELS.....	5
	2.1 Evaluation with an Idealized Terrain Obstacle.....	5
	2.1.1 CIT Wind Model.....	5
	2.1.2 MELSAR-MET.....	5
	2.1.3 ATMOS1.....	7
	2.1.4 Complex-Terrain Wind Model.....	7
	2.1.5 Conclusions.....	7
	2.2 Evaluation with Terrain from the Rocky Mountains.....	8
	2.2.1 CIT Wind Model.....	8
	2.2.2 MELSAR-MET.....	8
	2.2.3 ATMOS1.....	15
	2.2.4 Remarks.....	15
3	EVALUATION OF THE CANDIDATE ACID DEPOSITION MODELS.....	21
	3.1 Transport.....	21
	3.2 Dispersion.....	22
	3.2.1 Description of the Dispersion Algorithms.....	27
	3.2.2 Evaluation of the Dispersion Algorithms.....	29
	3.3 Chemical Transformation.....	40
	3.3.1 Review of the Chemistry of Acid Deposition.....	49
	3.3.2 Review of the Chemical Mechanisms in the Candidate Models.....	51
	3.3.3 Evaluation of the Chemical Mechanisms.....	53
	3.3.4 Remarks.....	63

3.4	Dry Deposition.....	69
3.4.1	MESOPUFF-II and CCADM Parameterizations.....	70
3.4.2	Comparison of MESOPUFF-II and CCADM Performance	77
3.5	Wet Deposition.....	86
3.5.1	Review of the Wet Deposition Algorithms in the Candidate Models.....	86
3.5.2	Evaluation of the Wet Deposition Algorithms....	88
3.5.3	Remarks.....	92
4	DESIGN OF THE METEOROLOGICAL MODEL.....	93
4.1	The Diagnostic Wind Model.....	94
4.1.1	Design Overview.....	94
4.1.2	Model Formulation.....	94
4.2	Evaluation of the Diagnostic Wind Model.....	102
4.2.1	Flow over Idealized Terrain.....	102
4.2.2	Flow over Rocky Mountain Terrain.....	103
4.2.3	Evaluation of the new DWM Using Observations from the Rocky Mountains.....	116
4.2.4	Evaluation of the DWM in a Complex Terrain/ Coastal Environment and Within a Large Valley	139
4.3	Specification of Other Meteorological Variables.....	144
4.3.1	Mixing Heights.....	148
4.3.2	Stability Classification.....	148
4.3.3	Friction Velocity.....	149
4.3.4	Convective Velocity.....	151
4.3.5	Monin-Obukhov Length.....	151
4.3.6	Temperature.....	151
4.3.7	Pressure.....	153
4.3.8	Relative Humidity.....	154
4.3.9	Precipitation Rate.....	154
5	DESIGN OF THE ACID DEPOSITION MODEL FOR THE ROCKY MOUNTAIN REGION	159
5.1	Transport.....	159
5.2	Dispersion.....	160
5.3	Chemical Transformation.....	160
5.4	Dry Deposition.....	161
5.5	Wet Deposition.....	161
5.6	Summary.....	161
6	SUMMARY AND RECOMMENDATIONS.....	163
	References.....	165
	Appendix: Dry Deposition Velocities Predicted by the MESOPUFF-II and CCADM.....	A-1



## FIGURES

<u>Number</u>	<u>Page</u>
2-1 Application scenario #1 mesoscale region containing the Clear Creek shale oil plant and two PSD class I areas-- Flat Tops and Maroon-Bells Snowmass Wilderness.....	6
2-2 CIT model-generated winds over Rocky Mountain domain at 50 m above ground.....	9
2-3 MELSAR model-generated winds over Rocky Mountain domain at 50 m above ground.....	12
2-4 ATMOS1 model-generated winds over Rocky Mountain domain at 50 m above ground.....	16
3-1 Comparison of trajectories starting at 1600 at plume heights of 10 m, 300 m, and 1000 m.....	23
3-2 Comparison of trajectories starting at 2200 at plume heights of 10 m, 300 m, and 1000 m.....	24
3-3 Comparison of trajectories starting at 0400 at plume heights of 10 m, 300 m, and 1000 m.....	25
3-4 Comparison of trajectories starting at 1000 at plume heights of 10 m, 300 m, and 1000 m.....	26
3-5 Comparison of horizontal plume dispersion rates for stability class A.....	30
3-6 Comparison of horizontal plume dispersion rates for stability class B.....	31
3-7 Comparison of horizontal plume dispersion rates for stability class C.....	32
3-8 Comparison of horizontal plume dispersion rates for stability class D.....	34

<u>Number</u>		<u>Page</u>
3-9	Sensitivity of the MELSAR MacCready horizontal dispersion rate to terrain roughness.....	35
3-10	Sensitivity of the MELSAR MacCready horizontal dispersion rate to height above terrain.....	36
3-11	Comparison of horizontal plume dispersion rates for stability class E.....	38
3-12	Comparison of horizontal plume dispersion rates for stability class F.....	39
3-13	Comparison of vertical plume dispersion rates for stability class A.....	41
3-14	Comparison of vertical plume dispersion rates for stability class B.....	42
3-15	Comparison of vertical plume dispersion rates for stability class C.....	43
3-16	Comparison of vertical plume dispersion rates for stability class D.....	44
3-17	Sensitivity of the MELSAR MacCready vertical dispersion rate to terrain roughness.....	45
3-18	Sensitivity of the MELSAR MacCready vertical dispersion rate to height above terrain.....	46
3-19	Comparison of vertical plume dispersion rates for stability class E.....	47
3-20	Comparison of vertical plume dispersion rates for stability class F.....	48
3-21	Sensitivity of the MESOPUFF-II and RIVAD chemical mechanisms to solar intensity.....	55
3-22	Sensitivity of the daytime MESOPUFF-II and RIVAD chemical mechanisms to temperature.....	56
3-23	Sensitivity of the nighttime MESOPUFF-II and RIVAD chemical mechanisms to temperature.....	57

<u>Number</u>		<u>Page</u>
3-24	Sensitivity of the daytime MESOPUFF-II and RIVAD chemical mechanisms to relative humidity.....	58
3-25	Sensitivity of the nighttime MESOPUFF-II and RIVAD chemical mechanisms to relative humidity.....	59
3-26	Sensitivity of the daytime MESOPUFF-II and RIVAD chemical mechanisms to ozone concentration.....	61
3-27	Sensitivity of the nighttime MESOPUFF-II and RIVAD chemical mechanisms to ozone concentration.....	62
3-28	Sensitivity of the daytime MESOPUFF-II and RIVAD chemical mechanisms to NO <sub>x</sub> concentration.....	64
3-29	Sensitivity of the nighttime MESOPUFF-II and RIVAD chemical mechanisms to NO <sub>x</sub> concentration.....	65
3-30	Sensitivity of the daytime MESOPUFF-II and RIVAD chemical mechanisms to SO <sub>2</sub> concentration.....	66
3-31	Sensitivity of the nighttime MESOPUFF-II and RIVAD chemical mechanisms to SO <sub>2</sub> concentration.....	67
3-32	Comparison of MESOPUFF-II and CCADM predicted SO <sub>2</sub> dry deposition velocities for three land use classes.....	79
3-33	Comparison of MESOPUFF-II and CCADM predicted sulfate dry deposition velocities for three land use classes.....	81
3-34	Comparison of MESOPUFF-II and CCADM predicted NO <sub>x</sub> dry deposition velocities for three land use classes.....	82
3-35	Comparison of MESOPUFF-II and CCADM predicted nitric acid dry deposition velocities for three land use classes.....	84
3-36	Comparison of MESOPUFF-II and CCADM predicted nitrates dry deposition velocities for three land use classes.....	85
3-37	Sensitivity of the MESOPUFF-II and RIVAD wet scavenging rates to precipitation rates for (a) SO <sub>2</sub> and (b) sulfate.....	90
3-38	Sensitivity of the MESOPUFF-II and RIVAD wet scavenging rates to precipitation rates for (a) NO <sub>x</sub> and (b) nitric acid.....	91

<u>Number</u>		<u>Page</u>
4-1	Winds generated by the Diagnostic Wind Model for simulation A1.....	104
4-2	Winds generated by the Diagnostic Wind Model for simulation A2.....	107
4-3	Winds generated by the Diagnostic Wind Model for simulation A3.....	110
4-4	Winds generated by the Diagnostic Wind Model for simulation B1.....	113
4-5	Winds generated by the Diagnostic Wind Model for simulation B2.....	117
4-6	Winds generated by the Diagnostic Wind Model for simulation B3.....	120
4-7	DWM-generated wind fields at 0500 on 18 September 1984.....	124
4-8	DWM-generated wind fields at 1400 on 18 September 1984.....	130
4-9	Scatterplot and statistics of predicted versus observed wind speeds at the three supplemental soundings.....	137
4-10	Histograms of deviations of predicted wind direction from observations at the three supplemental soundings.....	138
4-11	Locations of the SCCAB and Central Valley modeling regions.....	140
4-12	DWM generated and observed surface wind fields for the SCCAB region at 0400 PDT on 23 September 1987.....	142
4-13	DWM-generated and observed surface wind fields for the SCCAB region at 1200 PDT on 23 September 1987.....	143
4-14	Depiction of wind circulation air floww and boundary heights in the California Central Valley generated by the two-dimensional primitive equation.....	145
4-15	DWM-generated surface and upper-layer wind fields for the California Central Valley at 0400 on 7 August 1984.....	146
4-16	DWM-generated surface and upper-layer wind fields for the California Central Valley at 1200 on 7 August 1984.....	147

## TABLES

<u>Number</u>		<u>Page</u>
3-1	Summertime SO <sub>2</sub> canopy resistances used in the MESOPUFF-II as a function of land use type and stability class.....	74
3-2	SO <sub>2</sub> canopy resistance used in the CCADM.....	75
3-3	Canopy resistances used in the CCADM assumed for dry- deposited gases relative to SO <sub>2</sub> surface resistance.....	76
4-1	Slope and intercept of temperature lapse rate correction by Julian Day.....	152

## ACKNOWLEDGEMENTS

The evaluation and design of a new acid deposition model for the Rocky Mountains is the result of a team effort that involved personnel from the U.S. EPA and other federal and state agencies. Members of the Western Acid Deposition Task Force were an integral part of this effort. We would like to thank in particular Mr. Larry Svoboda of the U.S. EPA Region VIII and Mr. Al Ribieu of the Bureau of Land Management for their contributions. Finally, we would like to acknowledge Mr. Alan Huber, the EPA project officer, whose guidance helped focus the goals of this project.

# 1 INTRODUCTION

## 1.1 BACKGROUND

Acid deposition has recently become an increasing concern in the western United States (Roth et al., 1985). Although this problem may not be as acute in the western United States as it is in the eastern United States, it is currently a concern of the public and regulatory agencies because of the high sensitivity of western lakes at high altitudes and the rapid industrial growth expected to occur in certain areas of the West. An example of such an area is the region known as the Overthrust Belt in southwestern Wyoming. Several planned energy-related projects, including natural gas sweetening plants and coal-fired power plants, may considerably increase emissions of acid precursors in northeastern Utah and northwestern Colorado and significantly affect ecosystems in the sensitive Rocky Mountain areas.

Under the 1977 Clean Air Act, the U.S. Environmental Protection Agency (EPA), along with other federal and state agencies, is mandated to preserve and protect air quality throughout the country. As part of the Prevention of Significant Deterioration (PSD) permitting processes, federal and state agencies are required to evaluate potential impacts of new emission sources. In particular, Section 165 of the Clean Air Act stipulates that, except in specially regulated instances, PSD increments shall not be exceeded and air quality-related values (AQRV's) shall not be adversely affected. Air-quality-related concerns range from near-source plume blight to regional-scale acid deposition problems. By law, the Federal Land Manager of Class I areas has a responsibility to protect air-quality-related values within those areas. New source permits cannot be issued by the EPA or the states when the Federal Manager concludes that adverse impacts on air quality or air-quality-related values will occur. EPA Region VIII contains some 40 Class I areas in the West, including two Indian reservations. Similar designation is being considered for several of the remaining 26 Indian reservations in the region. State and federal agencies, industries, and environmental groups in the West need accurate data concerning western source-receptor relationships.

To address this problem, EPA Region VIII needs to designate an air quality model for application to mesoscale pollutant transport and deposition over

the complex terrain of the Rocky Mountain region for transport distances ranging from several km to several hundred km. The EPA recognizes the uncertainties and limitations of currently available air quality models and the need for continued research and development of air quality models applicable over regions of complex terrain. Therefore, the objective of the project reported here is to select and assemble the best air quality models available for application to the Rocky Mountain area on an interim basis.

Such modeling is needed to assess the relationship between source emissions and receptor impacts in the West. To address acid deposition problems in the East, the EPA has launched a major effort to develop a state-of-the-art regional acid deposition model--RADM (NCAR, 1985). According to the current plan, this model will undergo an intensive model evaluation during the period 1988-1989. Realistically, evaluation, adaptation, and application of this sophisticated model to the West will probably not occur until 1990 or beyond. Until that time, a practical modeling tool with which the federal and state agencies can assess air quality impacts in the West is needed.

Air quality modeling in this region is especially difficult because of the complex air flow patterns over the Rocky Mountains and the difficulty of predicting acid deposition levels. Available data bases are inadequate for thorough model evaluation studies. Major field studies and the establishment of a meteorological network throughout the Rocky Mountain area would be required to collect data necessary for any thorough model evaluation.

## 1.2 PURPOSE OF THIS REPORT

This report discusses the development and initial evaluation of a meso-scale acid deposition modeling system designed for the Rocky Mountain region for the Rocky Mountain Acid Deposition Modeling Assessment Project under the auspices of the U.S. EPA. The primary objective of the project is to assemble a mesoscale air quality model based primarily on models or modules currently available for use by federal and state agencies in the Rocky Mountain region. To develop criteria for model selection and evaluation, the EPA formed an atmospheric processes subgroup of the Western Atmospheric Deposition Task Force, referred to as WADTF/AP. This group comprises representatives from the National Park Service, U.S. Forest Service, EPA Region VIII, the National Oceanic and Atmospheric Administration, and other federal, state, and private organizations. On the basis of our review of the modeling needs identified by the WADTF/AP, the specific requirements of the model for this project are as follows:



Since the anticipated use of this model is to analyze permit applications and evaluate urban development plans, the model must be able to process various air pollutants from both point and area sources.

The modeling areas will typically cover spatial regions approximately 200 km to 300 km on the side to assist in permitting new sources within relatively short distances of Class I areas.

The temporal scales will emphasize longer time periods, such as seasonal and/or annual averages, to obtain cumulative impacts from both chronic and episodic events.

The model should be able to simulate transport, diffusion, transformation, and deposition of pollutants over complex terrain in the Rocky Mountain region using relatively sparse NWS upper-air soundings.

### 1.3 OVERVIEW OF THE NEW HYBRID ACID DEPOSITION/AIR QUALITY MODELING SYSTEM FOR THE ROCKY MOUNTAINS

The mathematical modeling system for the Rocky Mountain region described in this report consists of several components or modules. These components can be divided into two main categories: those that describe meteorological processes (a mesoscale meteorological model) and those that describe pollutant dispersion, chemical transformation, and deposition (an acid deposition/air quality simulation model).

The components of the Rocky Mountain modeling system were taken from existing mesoscale meteorological and acid deposition models that were selected previously (Morris and Kessler, 1987). The components of these candidate models were evaluated to determine which are the most scientifically sound yet internally consistent within the overall framework of a Rocky Mountain acid deposition modeling system. The most technically rigorous yet consistent components of the candidate models were integrated together to form the new modeling system. In the development of this modeling each of the components has been evaluated separately. When new components were designed that deviate significantly from the candidate models, such as the new diagnostic wind model (DWM), then a rigorous evaluation of these new components is made.

### 1.4 REPORT ORGANIZATION

The candidate mesoscale meteorological and acid deposition models are evaluated in Sections 2 and 3, respectively. Section 4 describes the

design and implementation of a mesoscale meteorological model for the Rocky Mountain region. The meteorological model contains a new diagnostic wind model (DWM), which was subjected to a rigorous performance evaluation using four different complex terrain regions; its predictions are compared with observations from the Rocky Mountains. Section 5 describes the design of the new Lagrangian acid deposition/air quality model. Finally, Section 6 summarizes the work to date on the development of the modeling system.

## 2 EVALUATION OF THE CANDIDATE METEOROLOGICAL MODELS

Four diagnostic wind models were considered for use in the Rocky Mountain modeling system--the CIT wind model, PNL's MELSAR-MET, SAI's Complex-Terrain Wind Model, and LANL's ATMOS1. In this section we expand on the preliminary evaluation of the four candidate models presented by Morris and Kessler in their review of the Rocky Mountain modeling system (1987). In that report the candidate models are compared and their performance is evaluated in application to an idealized terrain. Here we briefly summarize the results of applications of the candidate models to the terrain with 10 km resolution in the Rocky Mountain region depicted in Figure 2-1, and two new regions containing complex terrain.

### 2.1 EVALUATION WITH AN IDEALIZED TERRAIN OBSTACLE

As an initial test of the candidate models, the models were exercised using a three-dimensional bell-shaped mountain of a scale typically found in the Rocky Mountains using an initial uniform flow field. The results for each of the models can be summarized as follows.

#### 2.1.1 CIT Wind Model

The CIT model can treat the kinematic effects of terrain on the airflow; however, it lacks a provision for Froude number flow adjustment and thus cannot simulate blocking effects if they are not defined by the input wind data. If input data (wind observations) are plentiful and representative, the flexibility of the CIT interpolative scheme is desirable; however, when input data are sparse, the model cannot simulate blocking and deflection.

#### 2.1.2 MELSAR-MET

The MELSAR model is designed to simulate the blocking and deflection of air flows typically found in the Rocky Mountain region under weak synoptic conditions. However, due to the model's unique interpolation scheme used

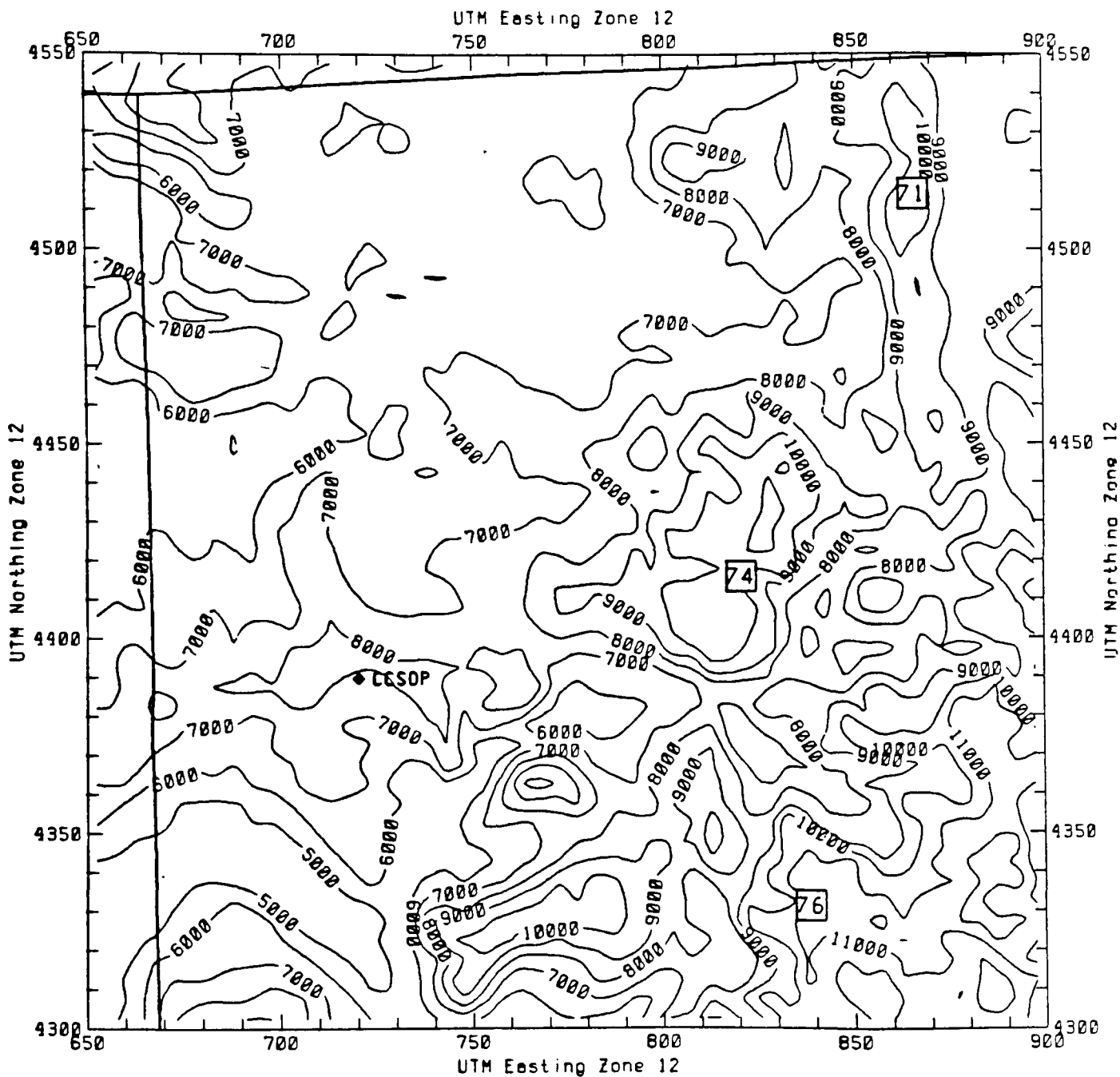


FIGURE 2-1. Application scenario #1 mesoscale region containing the Clear Creek shale oil plant (CCSOP) and two PSD class I areas--Flat Tops (74) and Maroon-Bells Snowmass Wilderness (76).

to define the gridded wind fields, spurious results are produced near the boundaries of the modeling domain. Since the MELSAR assumes its initial gridded wind field is mass consistent without additional constrained adjustments, it is the most inexpensive of the candidate models. If the details of the vertical velocity field are unimportant, MELSAR may be sufficient to represent blocking and deflection in the horizontal wind field.

### 2.1.3 ATMOS1

The ATMOS1 model lacks a Froude number adjustment term to treat blocking and deflection but can provide a gross simulation of blocking that is defined through a region-wide stability dependent parameter  $\alpha_{12}$  as user input. The ATMOS1 does adjust the wind fields to produce reasonable vertical velocities.

### 2.1.4 Complex-Terrain Wind Model

The CTWM alone of the candidate models is designed to generate wind fields using only a domain-mean wind input. It is also the only model that attempts to simulate thermally generated upslope and downslope flows in addition to deflection and blocking effects. However, the CTWM is also the only candidate model formulated in Cartesian coordinates. The use of a Cartesian coordinate system for simulating airflows in complex terrain is undesirable for the following reasons:

Airflows tend to follow the terrain.

The lower boundary condition is difficult to parameterize in Cartesian coordinates.

Increased vertical resolution near the surface is needed to resolve complex terrain airflows. In Cartesian coordinates this results in a prohibitive number of vertical layers.

Also the ability of the CTWM to utilize more than one wind observation within the model domain is unclear.

### 2.1.5 Conclusions

The comparative simulations of the mesoscale meteorological models using a hypothetical terrain obstacle cannot by themselves serve as a basis for recommending one model over another. Each of the models contain some desirable attributes that would be warranted in a meteorological model for the Rocky Mountain region. Although the CTWM contains several unique features, notably the lack of a requirement of extensive input data and the

treatment of upslope/downslope winds, the formulation of the model in a Cartesian coordinates is a serious drawback.

## 2.2 EVALUATION WITH TERRAIN FROM THE ROCKY MOUNTAINS

In order to evaluate model performance over typical Rocky Mountain terrain, the CIT wind model, MELSAR-MET, and ATMOS1 were exercised over the topographic domain depicted in Figure 2-1, which corresponds to the first proposed application scenario discussed in the review report (Morris and Kessler, 1987). The grid spacing used in these simulations was 10 km, which resulted in a 25 x 25 array of grid cells for this region. The CTWM was not included in this series of experiments because of the problems with the coordinate transformation demonstrated in the application to an idealized terrain obstacle.

In this series of experiments an initially uniform flow of 2 m/s from the southwest (225°) was specified. Winds were generated at heights of 50, 200, 500, 1000, and 2000 m above ground on a 26 x 26 horizontal grid with grid spacing of 10 km.

### 2.2.1 CIT Wind Model

As in the set of experiments using idealized terrain, the CIT divergence reduction procedure was exercised until maximum three-dimensional divergence was reduced to  $10^{-6} \text{ s}^{-1}$ . Figure 2-2 depicts CIT model wind fields at 50, 200, and 500 m above the ground for the Rocky Mountain domain. The initial wind field is minimally perturbed by the terrain. Note that the characteristic terrain slopes in the Rocky Mountain domain are substantially smaller than those of the idealized bell-shaped mountain; thus the perturbations in this experiment should have smaller magnitude than those in the previous experiment.

### 2.2.2 MELSAR-MET

As in the idealized terrain experiment, the atmosphere is assumed to be uniformly isothermal. As recommended by Allwine and Whiteman (1985) the spacing of the "Froude grid" is 50 km.

Figure 2-3 depicts the MELSAR wind fields at 50, 200, and 500 m above ground. The directional variability exhibited by these fields has a horizontal scale considerably larger than the characteristic terrain scales; the individual resolved terrain features do not seem to deflect the airflow. It is probable that the standard deviation of terrain height within the Froude grid cells provides relatively low estimates of "obstacle height" in this case. Also, several of the major terrain features are aligned along the assumed domain-mean wind direction, minimizing deflection.

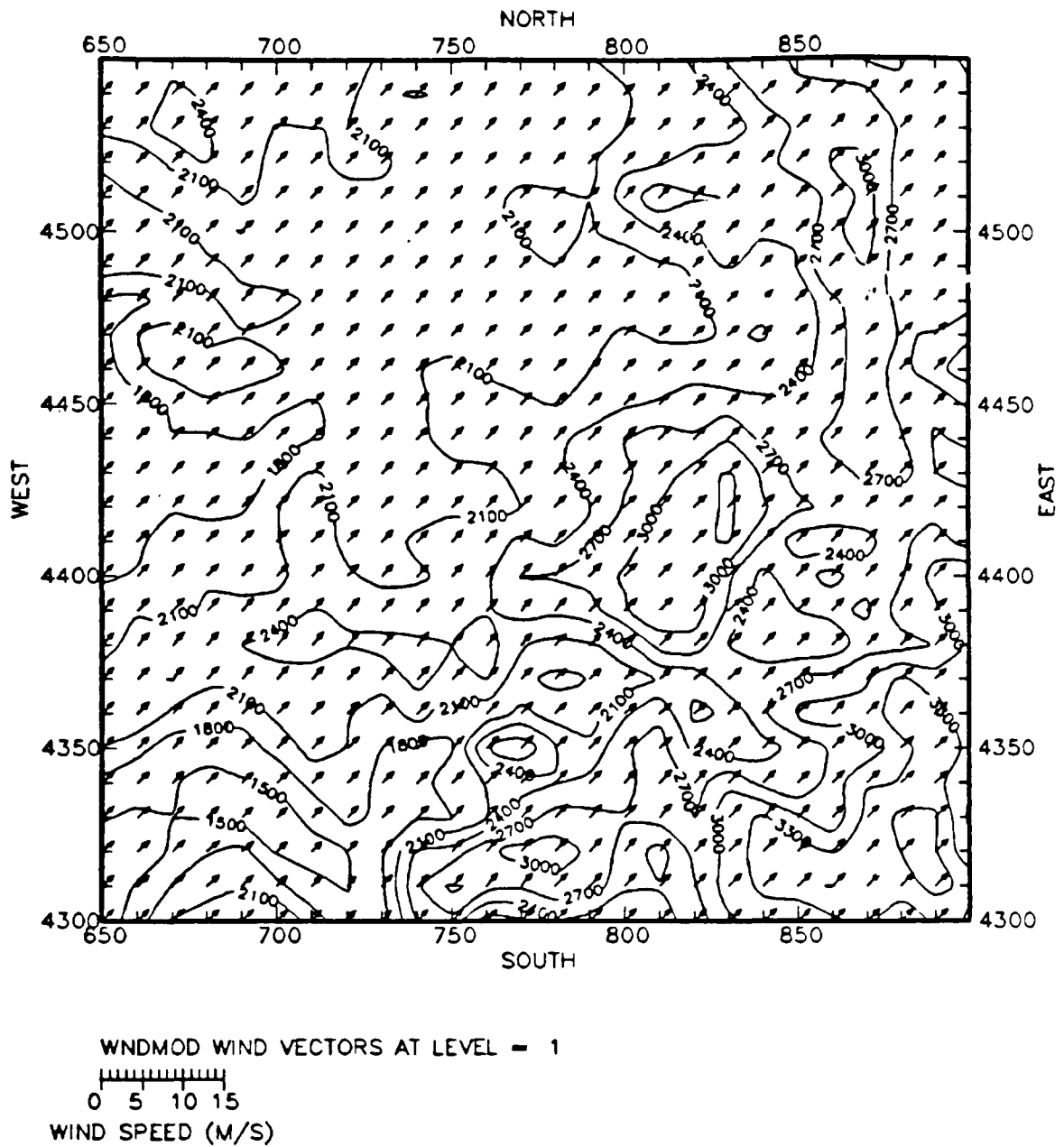


FIGURE 2-2a. CIT model-generated winds over Rocky Mountain domain at 50 m above ground. Scaling of plotted winds is given at lower left. Topography is contoured in meters. Horizontal grid spacing is 10 km.

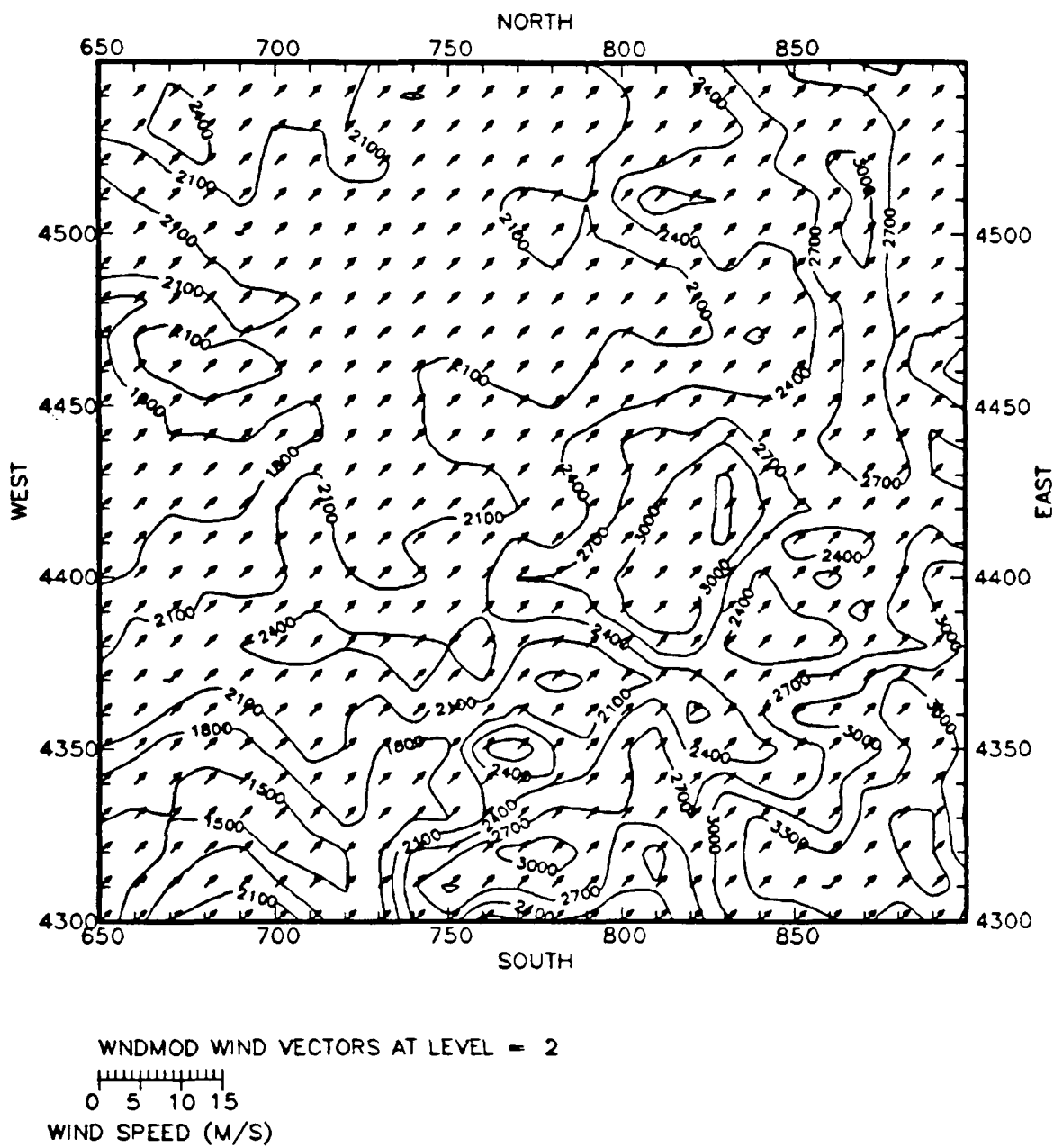
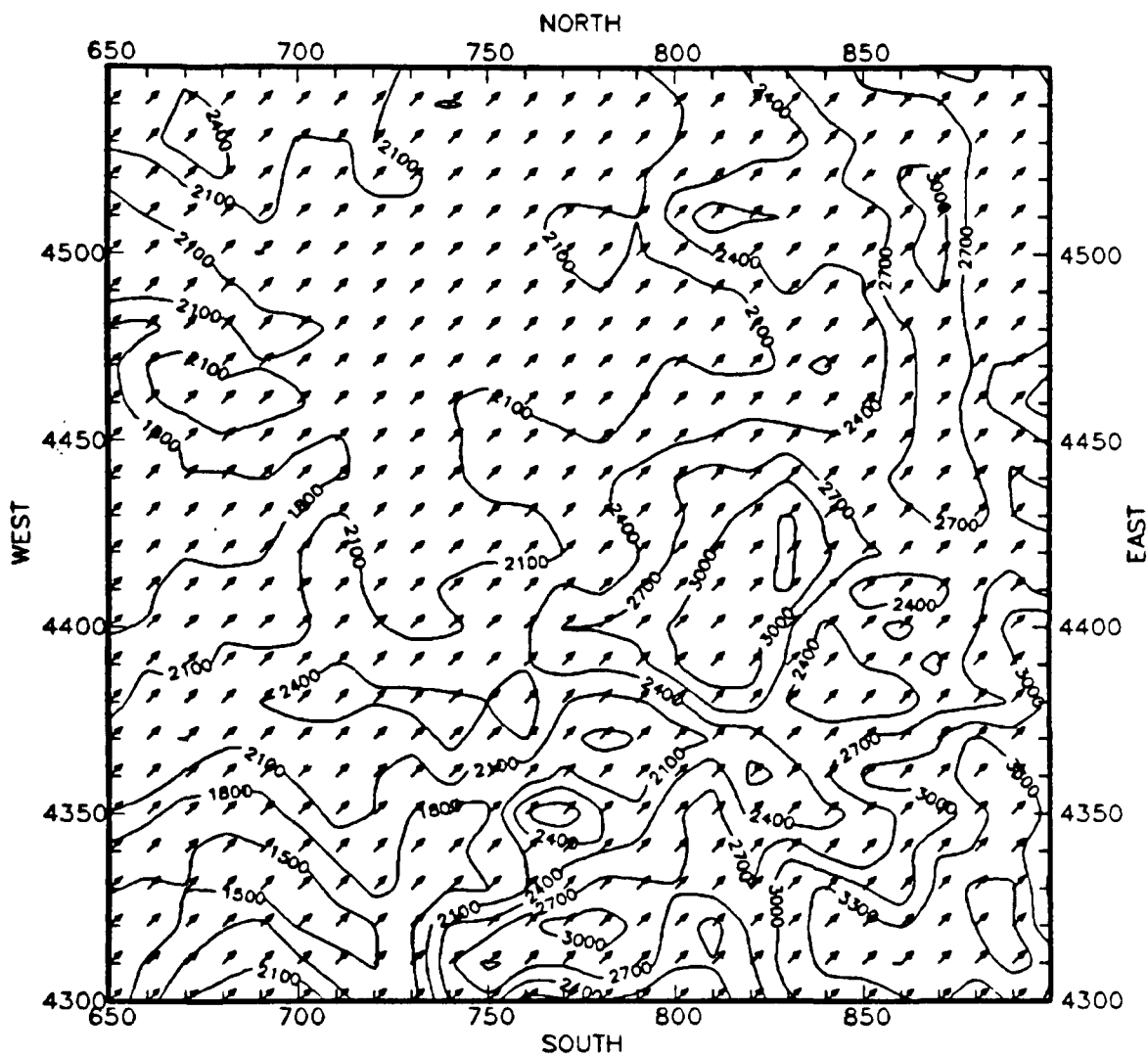


FIGURE 2-2b. At 200 m.





WNDMOD WIND VECTORS AT LEVEL = 3  
 0 5 10 15  
 WIND SPEED (M/S)

FIGURE 2-2c. At 500 m.

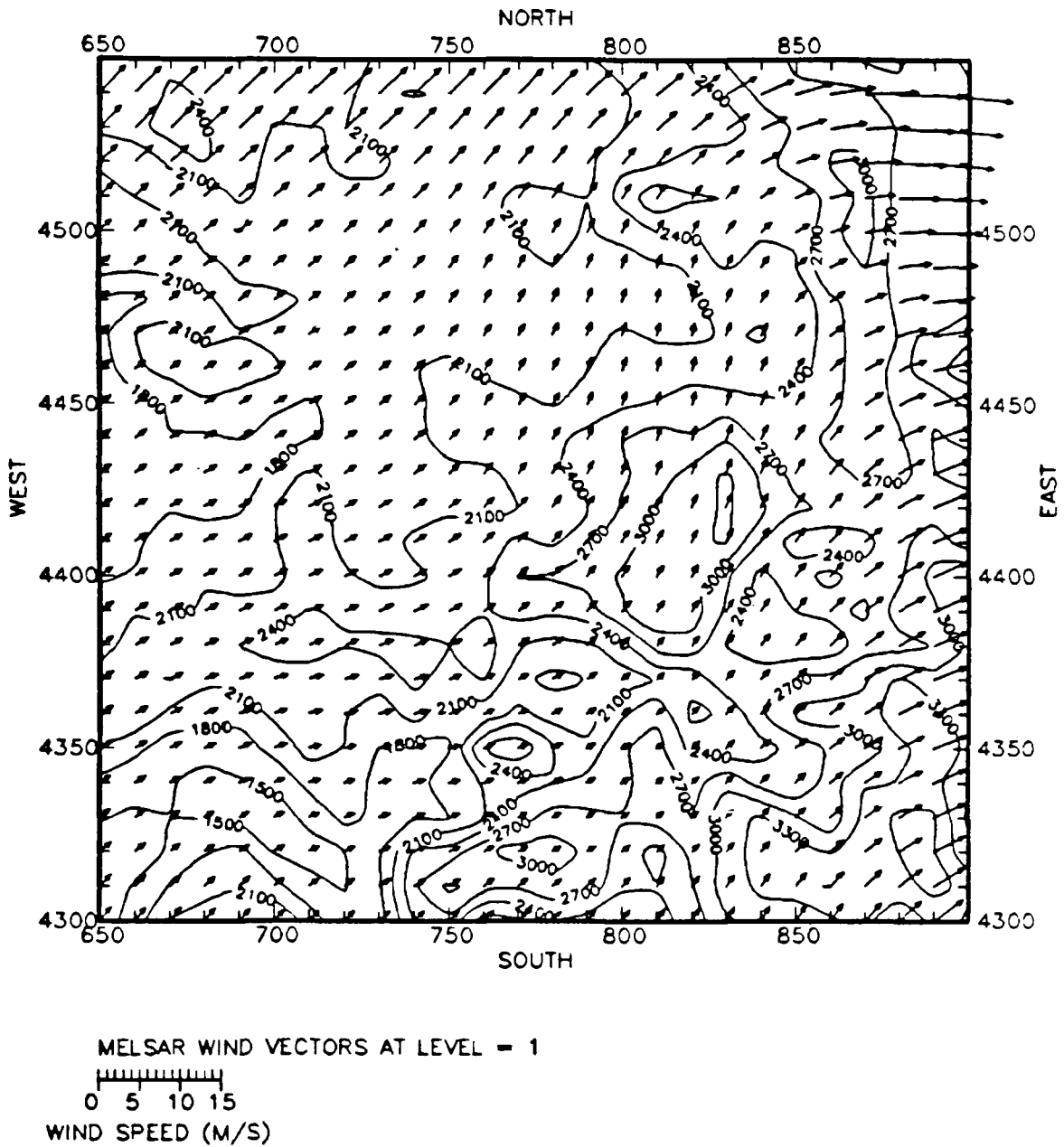
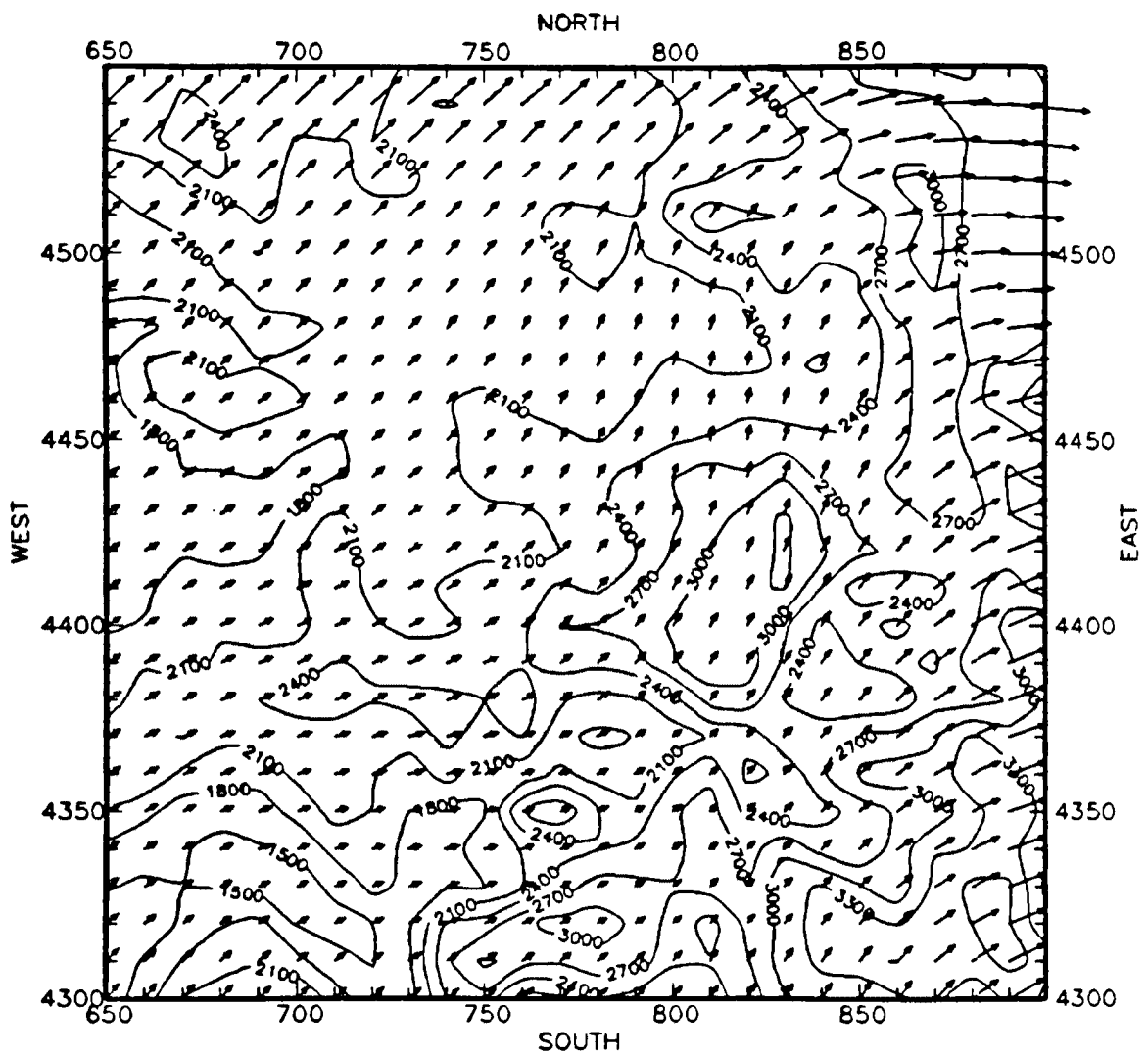


FIGURE 2-3a. MELSAR model-generated winds over Rocky Mountain domain at 50 m above ground. Scaling of plotted winds is given at lower left. Topography is contoured in meters. Horizontal grid spacing is 10 km.

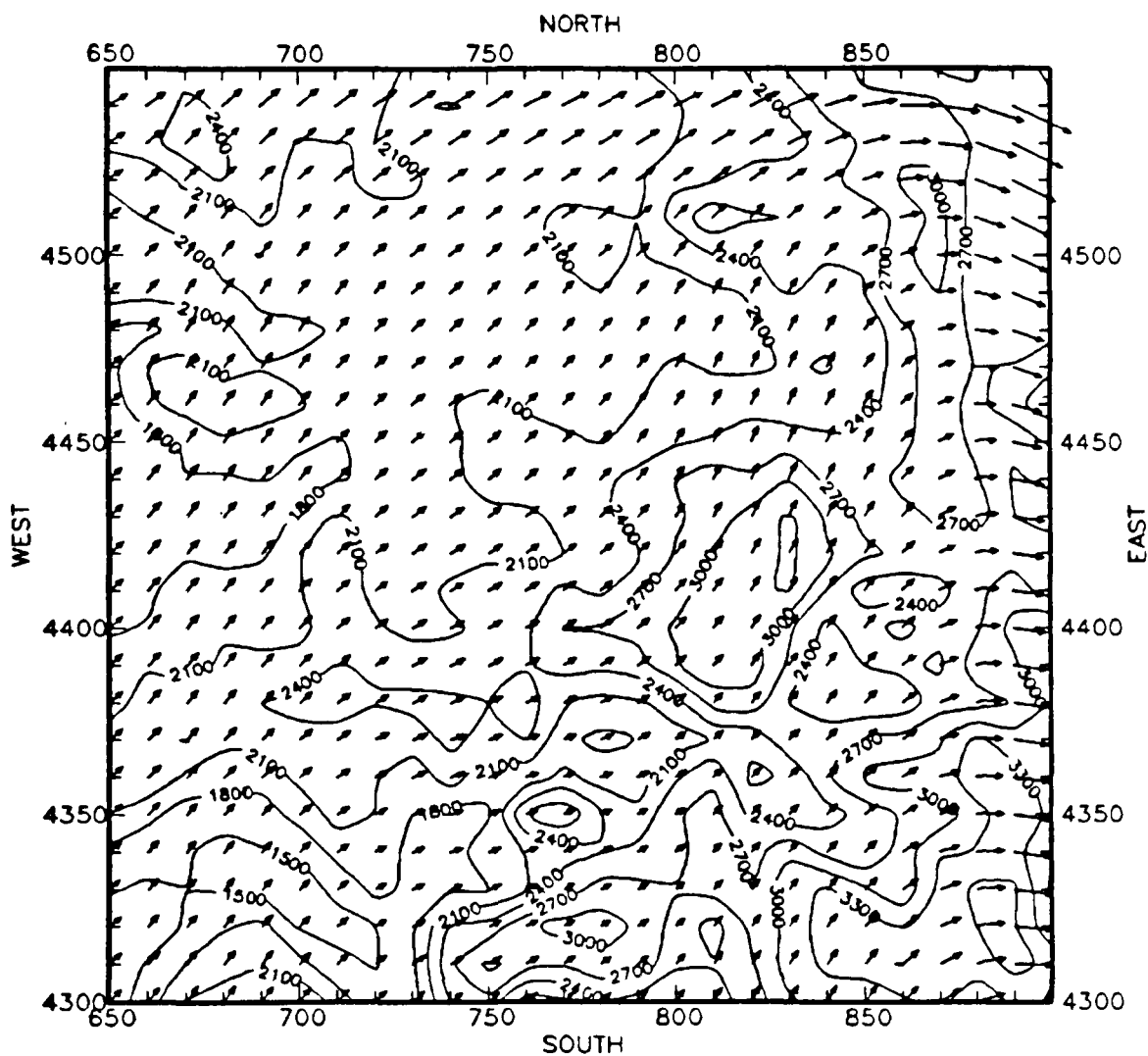


MELSAR WIND VECTORS AT LEVEL = 2

0 5 10 15

WIND SPEED (M/S)

FIGURE 2-3b. At 200 m.



MEL SAR WIND VECTORS AT LEVEL - 3

0 5 10 15

WIND SPEED (M/S)

FIGURE 2-3c. At 500 m.

Exaggerated flow appears along the northern and eastern boundaries of the domain. This behavior may indicate a problem with the the MELSAR polynomial interpolation scheme.

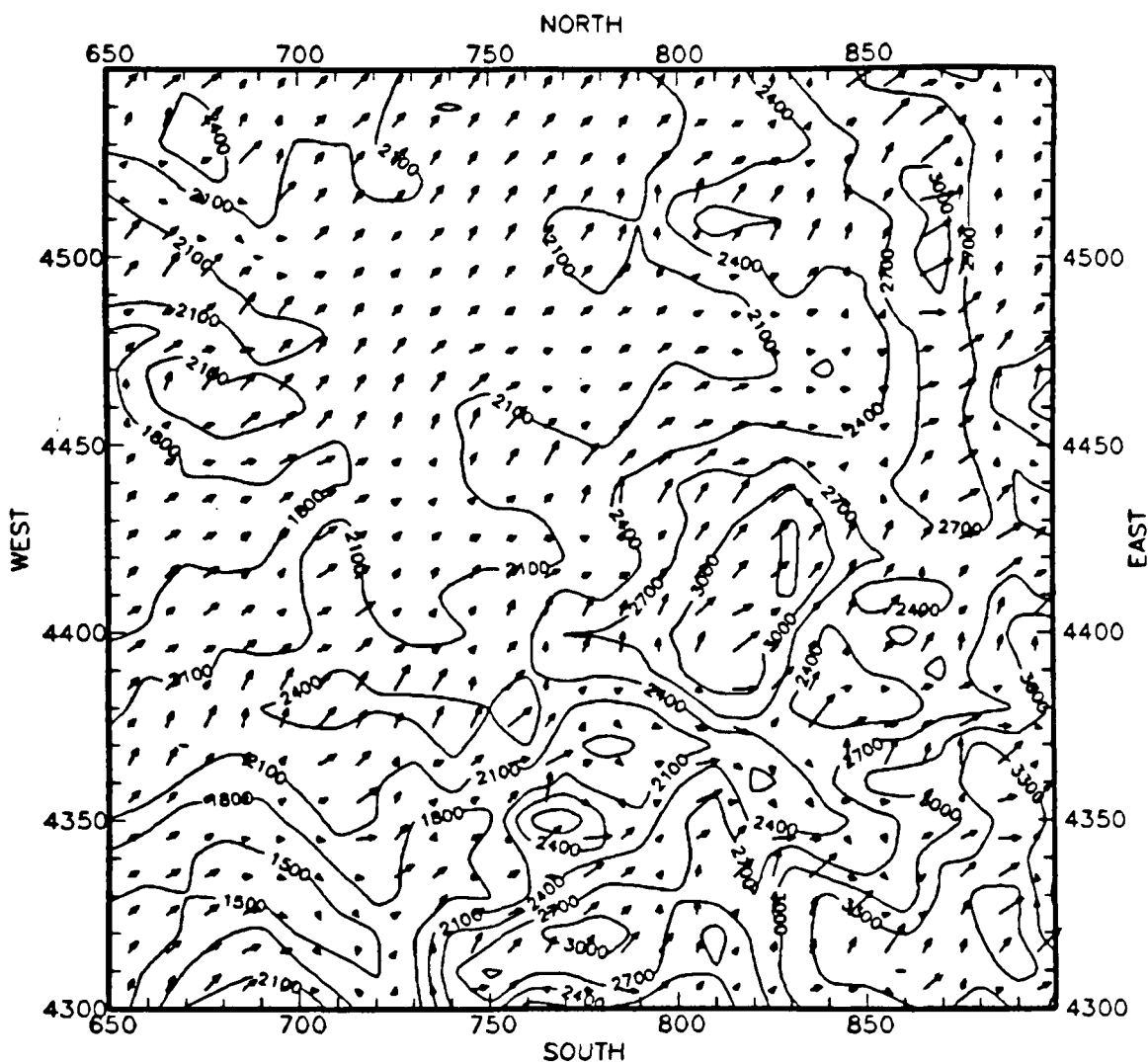
### 2.2.3 ATMOS1

ATMOS1 was exercised with the parameter  $\alpha_{12}$  set equal to 0.02, and the model run was halted after 20 iterations of the solution procedure. Figure 2-4 depicts the ATMOS1 wind fields at 50, 200, and 500 m above ground. Unlike the corresponding MELSAR-MET wind field, the ATMOS1 wind field at 50 m displays a great deal of variability at horizontal scales equal to or smaller than the characteristic terrain scales. Note that the mass-consistent adjustment in ATMOS1 does not contain a smoother; thus major differences between winds at adjacent grid points are preserved. In general, maximum ATMOS1 wind speeds occur above the tops of major terrain obstacles, consistent with potential flow theory.

### 2.2.4 Remarks

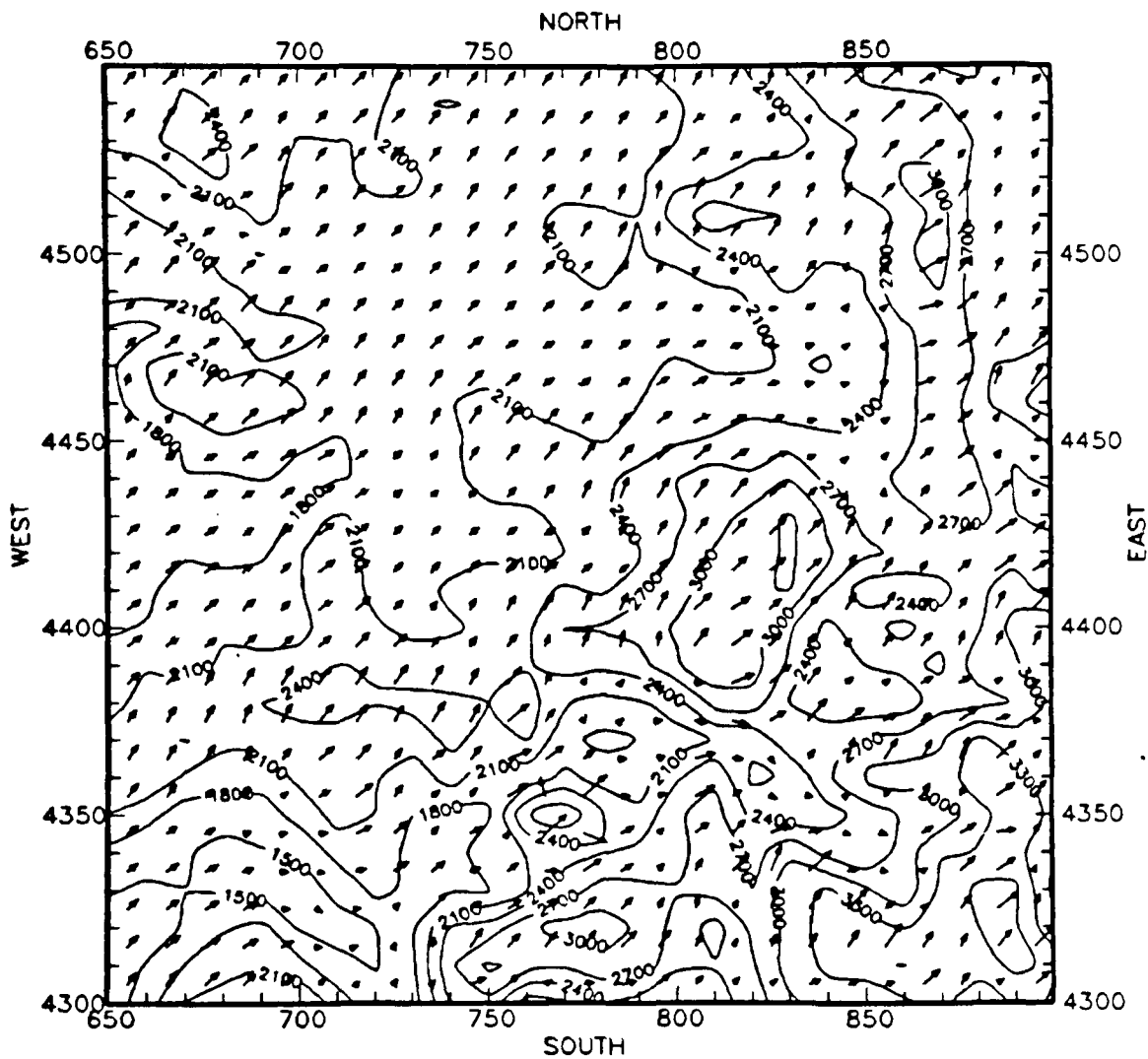
The comparative simulations discussed in this section indicate that no one of the candidate models is significantly better than another. A comprehensive model evaluation would involve tests of the ability of the models to simulate actual observations in complex terrain. Another approach to model evaluation is comparison of model results with analytic theory, as discussed by Pielke (1984). As noted previously, Ross and Smith (1986) demonstrate that ATMOS1 can reproduce analytic solutions for unstratified potential flow over idealized obstacles. However, based on the analyses of mountain-generated airflows by Smith (1979) and others, it is unclear to us that the potential-flow solutions are relevant on the terrain scales to be simulated in the Rocky Mountain region.

More relevant, perhaps, are two types of mountain wave disturbances: trapped lee waves and vertically propagating hydrostatic waves. Durran and Klemp (1982,1983) demonstrate the ability of a primitive-equation non-hydrostatic model to reproduce analytic solutions for each of these types of mountain waves. Additionally, Clark and Gall (1982) have utilized a nonhydrostatic primitive-equation model to simulate observed lee waves near Elk Mountain, Wyoming, a location which lies within the domain of current interest. We note here that none of the candidate models is capable of simulating either type of mountain wave disturbance unless the disturbance is fully accounted for by input wind data. There may be circumstances under which mountain waves play a significant role in horizontal and vertical transport of pollutants; primitive-equation numerical simulations would be necessary to delineate this role.



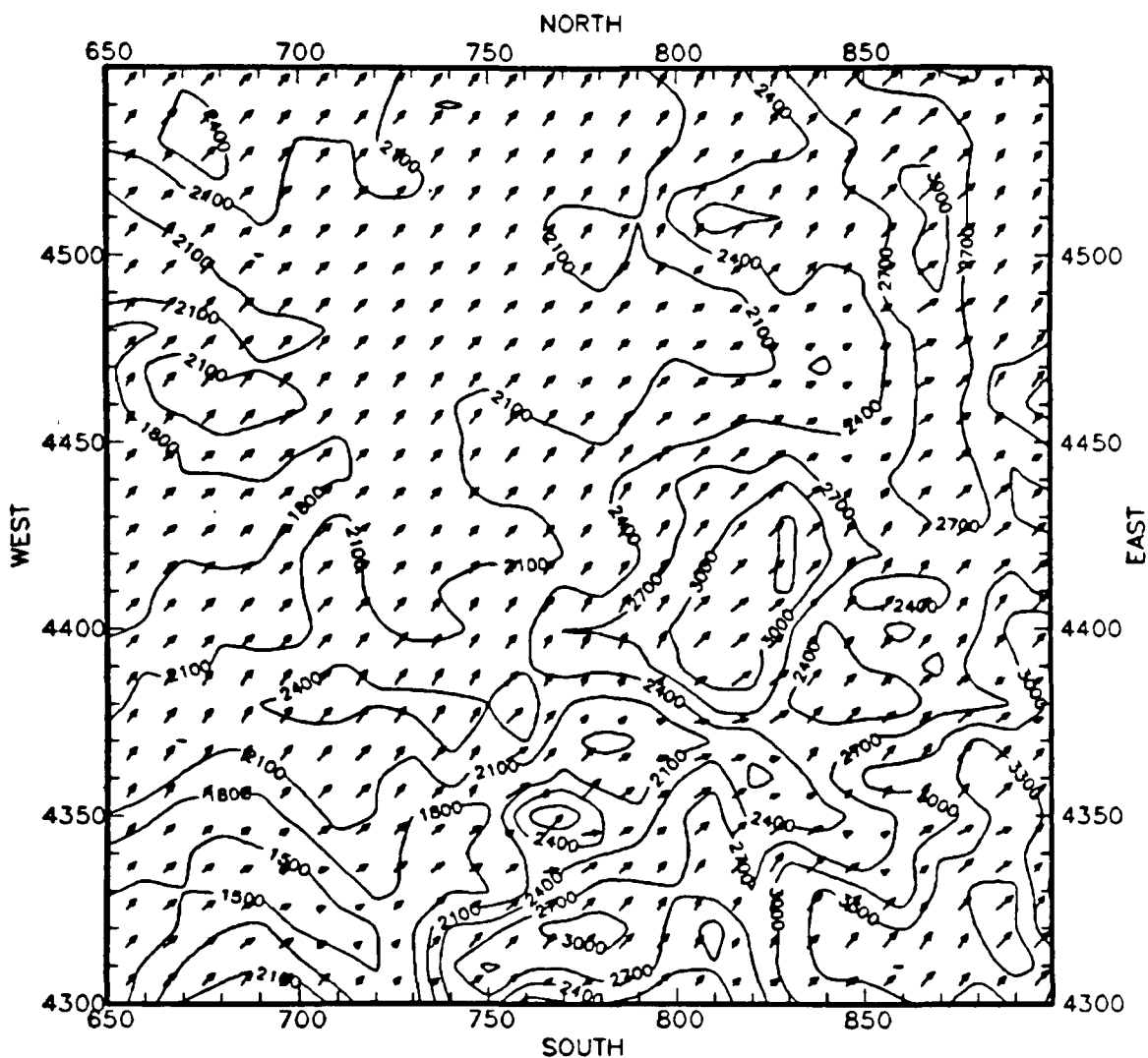
ATMOS1 WIND VECTORS AT LEVEL = 5  
 0 5 10 15  
 WIND SPEED (M/S)

FIGURE 2-4a. ATMOS1 model-generated winds over Rocky Mountain domain at 50 m above ground. Scaling of plotted winds is given at lower left. Topography is contoured in meters. Horizontal grid spacing is 10 km.



ATMOS1 WIND VECTORS AT LEVEL = 4  
 0 5 10 15  
 WIND SPEED (M/S)

FIGURE 2-4b. At 200 m.



ATMOS1 WIND VECTORS AT LEVEL = 3  
 0 5 10 15  
 WIND SPEED (M/S)

FIGURE 2-4c. At 500 m.



The blocking and deflection of airflow by terrain obstacles, especially important in the Rocky Mountain region under weak synoptic flow conditions, is simulated to varying extents by each candidate model. MELSAR, in particular, is designed to simulate this effect alone. The CIT model lacks a provision for Froude number flow adjustment and thus cannot simulate blocking effects if they are not defined by input wind data. ATMOS1 similarly lacks a Froude number term, but can provide a gross simulation of blocking depending on the magnitude of  $\alpha_{12}$ . Ross and Smith (1986) propose a scheme for calculation of a space-variable  $\alpha_{12}$  as a function of local Froude number; such a treatment might improve the ability of ATMOS1 to simulate blocking effects. The CTWM appears to be capable of treating kinematic deflection of airflow; while it attempts to parameterize blocking effects, the treatment produces somewhat questionable results.

The CPU time on a Prime 750 minicomputer required by each model for the idealized bell-shaped mountain simulations is as follows:

CIT wind model	86 s
MELSAR	23 s
ATMOS1 (20 iterations)	154 s
CTWM	140 s

MELSAR is inexpensive because its initial gridded wind fields are assumed to be mass-consistent without additional adjustments. If the details of the model's vertical velocity field are unimportant, MELSAR may be sufficient to represent blocking and deflection of the horizontal wind components by terrain, although the MELSAR obstacle height computation may be open to question.

If reasonable vertical velocities are desired, ATMOS1, which attempts adjustment of the vertical velocity based on gross stability considerations (i.e., the specification of  $\alpha_{12}$ ), may be a better choice. The CIT wind model is less desirable when input data are sparse because it lacks the ability to simulate blocking and deflection; however, if input wind data is plentiful and representative, the flexibility of the CIT model interpolation scheme may be of value.

The CTWM alone among the candidate models is designed to generate wind fields with only domain-scale input wind information. It is the only candidate model that explicitly attempts to treat thermally generated up-slope and downslope flows. The CTWM requires specification of several arbitrary coefficients with little guidance. Accurate specification of the coefficients would probably require a specific "tuning" of the

coefficients for the Rocky Mountain region, based on available observed wind data. Also, the CTWM does not have the ability to utilize randomly spaced observations.

The CTWM is formulated in Cartesian vertical coordinates. We believe that terrain-following vertical coordinates are strongly desirable for a wind model in complex terrain. The transformation of the CTWM from Cartesian to terrain-following coordinates is ambiguous when the slope flow treatment is included. Thus, as currently formulated in a Cartesian coordinate system, the CTWM would not be an appropriate wind model to simulate air flows over the complex terrain of the Rocky Mountains.

### 3 EVALUATION OF THE CANDIDATE ACID DEPOSITION MODELS

Four acid deposition/air quality models were chosen for possible incorporation into an acid deposition modeling system for application to the Rocky Mountain region. These four models are the SAI/CCADM, a Lagrangian box model; the ERT/MESOPUFF-II and PNL/MELSAR-POLUT, both Lagrangian puff models; and the SAI/RIVAD, a Lagrangian plume segment model. These four models contain different modeling approaches and parameterizations of the processes that lead to acid deposition and pollutant transport in complex terrain. These four models were not chosen with the idea that any one of the models would serve as the final acid deposition model, but that each of the models contains modules and parameterizations that can be incorporated into the final acid deposition model.

The review of the existing models (Morris and Kessler, 1987) presented a preliminary evaluation of the candidate acid deposition models' treatment of the processes of transport, dispersion, chemical transformation, and dry and wet deposition. Here we present a more detailed evaluation of the candidate acid models' treatment of these processes. Based on this evaluation, the most appropriate modules were chosen for incorporation into the new acid deposition model for the Rocky Mountains, which is described in Section 4.

#### 3.1 TRANSPORT

The transport winds for the acid deposition model will be defined from the multilayer terrain-following wind fields generated by the new diagnostic wind model described in Section 4. Three of the candidate acid deposition models--MELSAR-POLUT, MESOPUFF-II, and RIVAD--define the plume trajectory by using the wind at the plume centerline for advection. The fourth candidate model, the CCADM, requires user input of the Lagrangian box trajectory. As noted by Morris and Kessler (1987), use of the plume centerline wind vector to advect the entire puff, whose vertical extent may be over 1000 m, may not simulate the correct transport of the plume mass, especially under conditions of decoupled flow regimes as occurs in complex terrain. In this section we briefly examine the sensitivity of air parcel trajectories in complex terrain to the height of the air parcel above the ground.

Figures 3-1 through 3-4 depict air parcel trajectories at plume heights of 10, 300 and 1,000 m for release times at 0400, 1000, 1600, and 2200. Wind fields were generated by the diagnostic wind model for the September 17-18, 1984 simulations in the Rocky Mountains. These simulations used supplemental data collected for the ASCOT Brush Creek drainage flow experiments (see Section 4.1.2.3). The stagnant flow conditions present during these simulations should produce the maximum differences between trajectories at different heights above ground since the complex-terrain wind fields are not driven by synoptic forcing.

As seen in Figures 3-1 to 3-4, the surface trajectory (10 m) deviates greatly from the two elevated (300 and 1,000 m) trajectories. In fact, as can be seen by the symbols on the trajectories spaced six hours apart, the maximum wind speeds occur in the surface trajectories when the air parcel starts at the top of the 2400 m ridge during the two six-hour nighttime trajectory segments (2200-0400 and 0400-1000). Thus it appears that drainage winds dominate the surface trajectory paths on this day. This is confirmed by the upper-air trajectories, which tend to be disorganized due to the stagnant conditions.

This preliminary trajectory analysis illustrates the differences in transport of air parcels at different heights in complex terrain:

The difference in transport characteristics between surface and elevated releases confirms the need for multilevel wind fields in complex terrain. The use of a surface wind speed with the power law relationship with height cannot accurately characterize transport in complex terrain.

When an emission release becomes well mixed, the advection of the air parcel near the surface should ideally be handled differently than parcels aloft. Currently there are no Lagrangian models that treat the vertical splitting of puffs. The acid deposition model for the Rocky Mountains described in Section 4 has been formulated so that this vertical splitting can be easily incorporated at a future time.

### 3.2 DISPERSION

The plume segment model, RIVAD, and the two Gaussian puff models, MESO-PUFF-II and POLUT, all represent dispersion by expanding the plume segments or puffs in terms of the puff dispersion parameters  $\sigma_y$  and  $\sigma_z$ . In the CCADM there are two options for simulating diffusion. Either the horizontal and vertical diffusivities are specified at edges of the Lagrangian box, or the user specifies the size of the box as it moves downwind. Either method requires that the user specify the dispersion

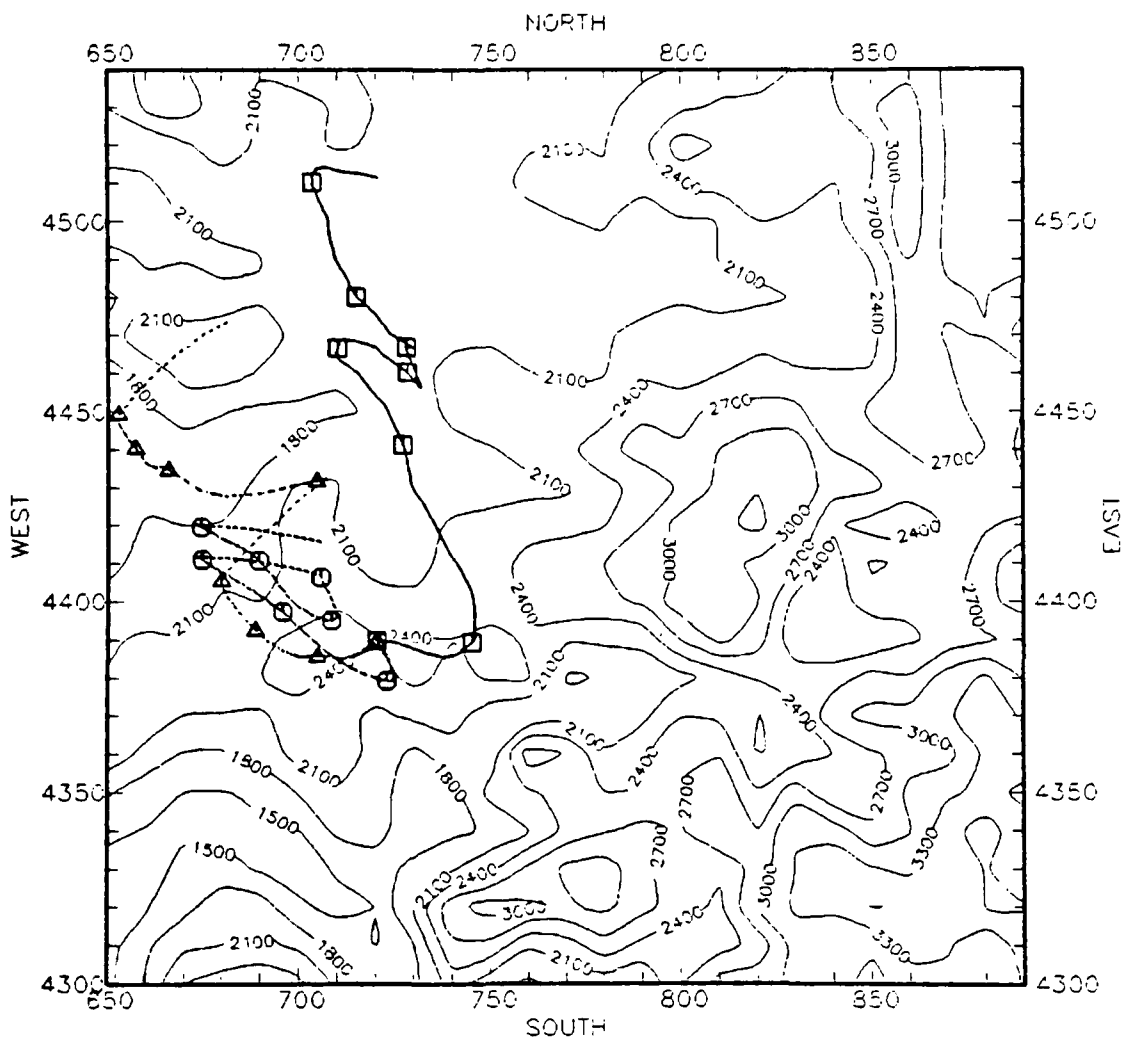


FIGURE 3-1. Comparison of trajectories starting at 1600 at plume heights of 10 m (□), 300 m (○), and 1000 m (△). Symbols on trajectories are spaced at six-hour intervals.

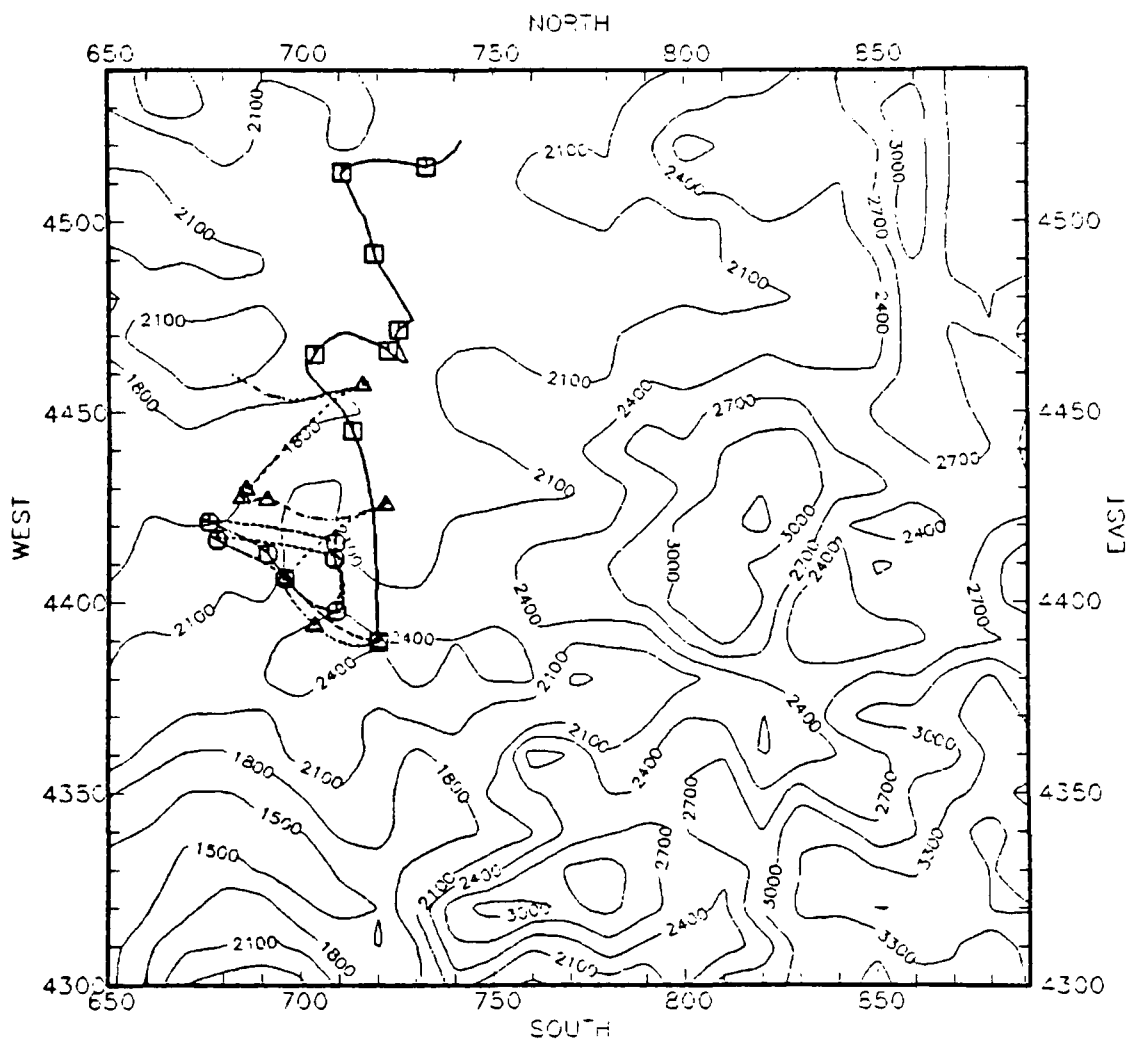


FIGURE 3-2. Comparison of trajectories starting at 2200 at plume heights of 10 m (□), 300 m (○), and 1000 m (△). Symbols on trajectories are spaced at six-hour intervals.

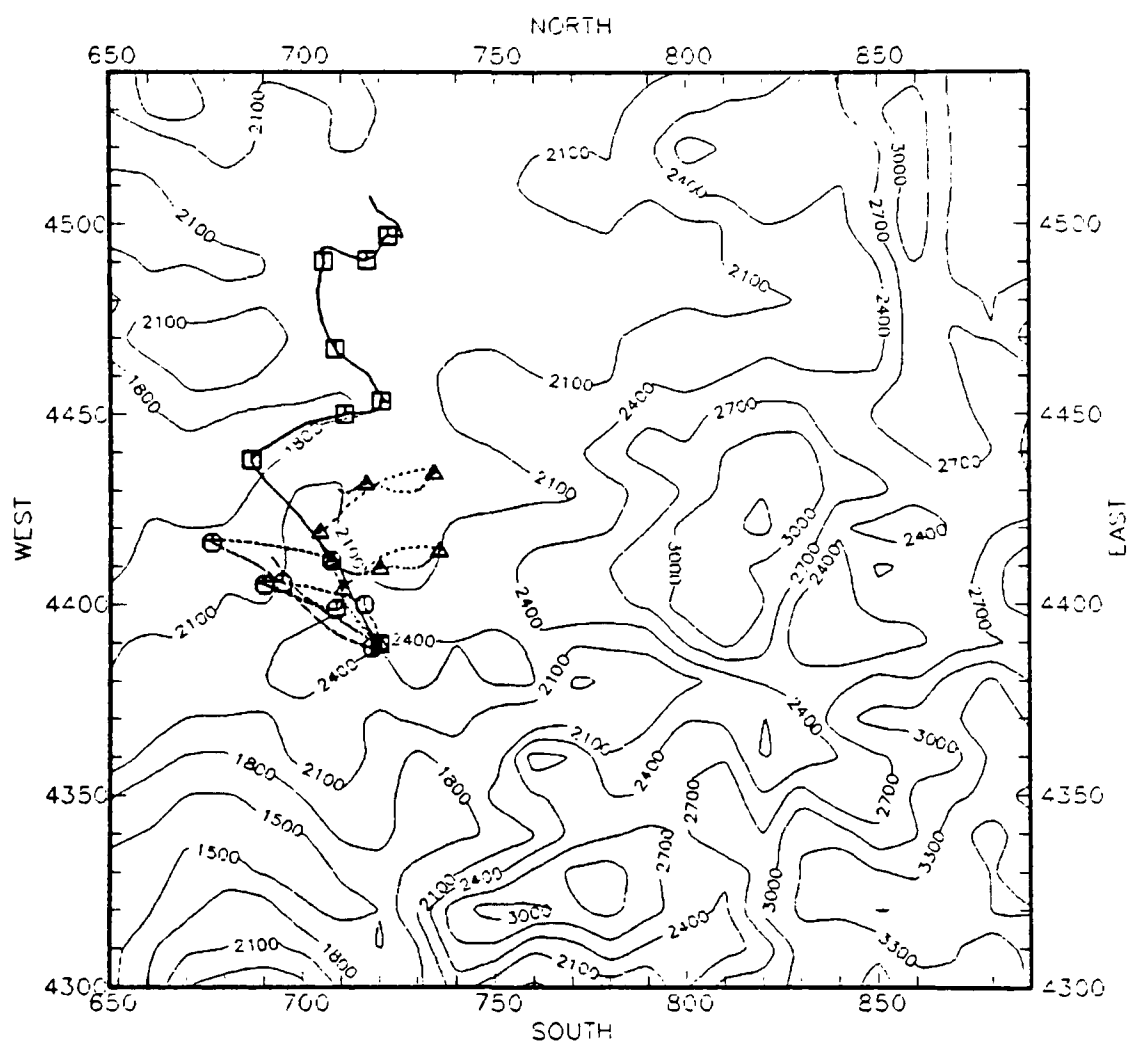


FIGURE 3-3. Comparison of trajectories starting at 0400 at plume heights of 10 m (□), 300 m (○), and 1000 m (△). Symbols on trajectories are spaced at six-hour intervals.

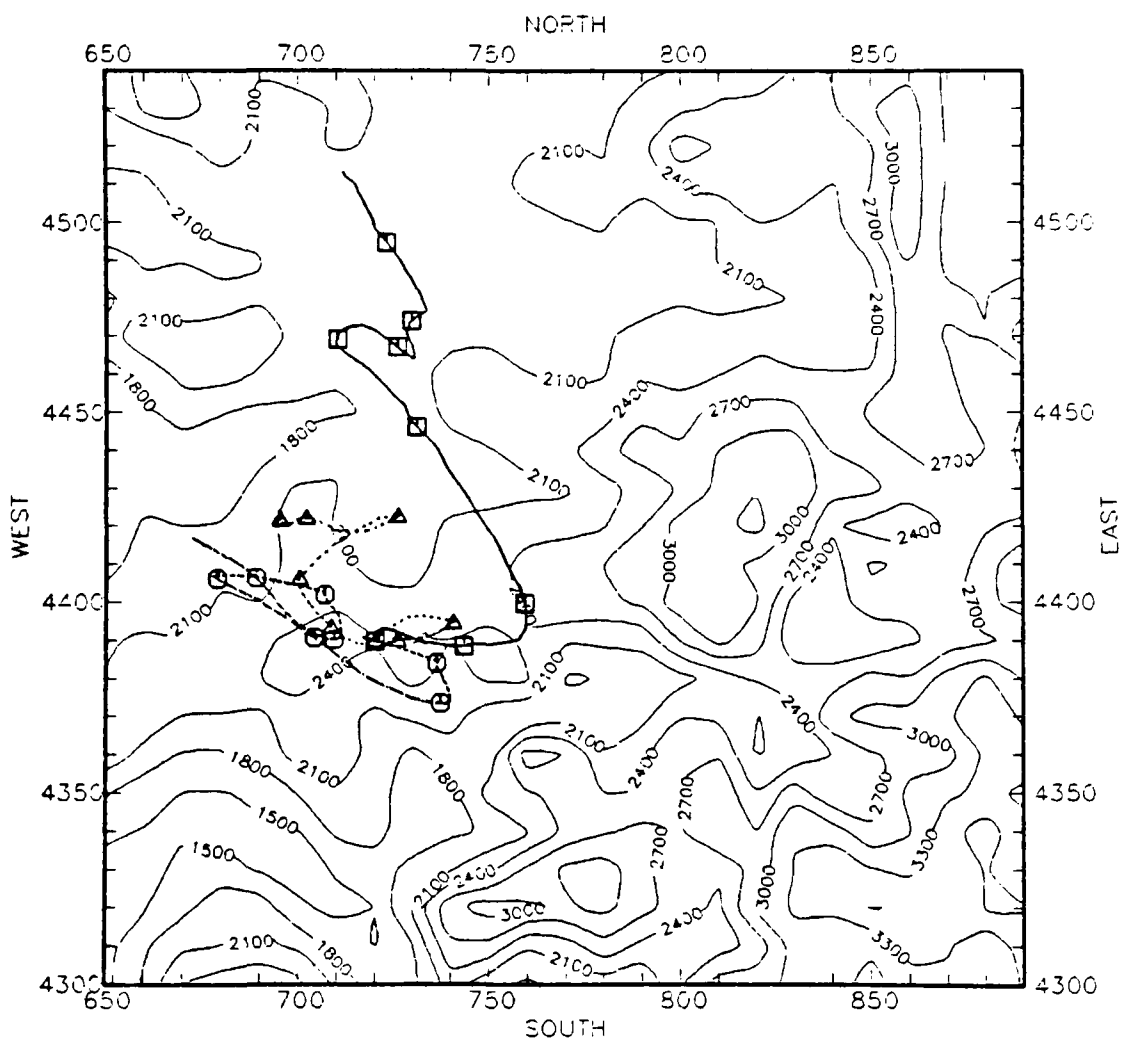


FIGURE 3-4. Comparison of trajectories starting at 1000 at plume heights of 10 m (□), 300 m (○), and 1000 m (△). Symbols on trajectories are spaced at six-hour intervals.



rate; thus the CCADM methods for dispersion involves excessive user interaction. In the following sections we briefly review how the horizontal and vertical dispersion parameters are calculated in the MESOPUFF-II, RIVAD, and POLUT models and then evaluate these dispersion algorithms by intercomparing the puff dispersion parameters predicted by the three algorithms and comparing these predictions with the dispersion curves estimates made by Pasquill, Gifford, and Turner (Turner, 1970).

### 3.2.1 Description of the Dispersion Algorithms

#### 3.2.1.1 MESOPUFF-II

The MESOPUFF-II calculates  $\sigma_y$  and  $\sigma_z$  for distances out to 100 km using formulas fitted to curves of Turner (1970). For distances greater than 100 km the plume growth rates given by Heffter (1965) are used. The implementation of the plume expansion at each time step is in the differential form:

$$\sigma_y(s + \Delta s) = \sigma_y(s) + \Delta s \left. \frac{d\sigma_y}{ds} \right|_s + \frac{\Delta s}{2} \quad (3-1)$$

so that the puffs always grow with time. The integral formulas for  $\sigma_y$  and  $\sigma_z$  for travel distances less than 100 km are as follows:

$$\begin{aligned} \sigma_y(s) &= a s^{0.9} \\ \sigma_z(s) &= c s^d \end{aligned} \quad (3-2)$$

where  $a$ ,  $c$ , and  $d$  are stability-dependent constants (Benkley and Bass, 1979b). For distances greater than 100 km, dispersion is based on time,  $t$  (seconds), instead of downwind distance, using the following formulas (Heffter, 1965):

$$\begin{aligned} \sigma_y(t + \Delta t) &= \sigma_y(t) + 0.5 \Delta t \\ \sigma_z(t + \Delta t) &= \sigma_z(t) + d \cdot \Delta t / \sqrt{t} \end{aligned} \quad (3-3)$$

where  $d$  is a stability-dependent parameter. The vertical extent of the plume defined by  $\sigma_z$  is limited to the mixing depth.

#### 3.2.1.2 RIVAD

Horizontal dispersion in the RIVAD accounts for the effect of vertical wind shear using an approach suggested by Randerson (1972). On the basis

of field measurements, Randerson found that diffusivities increase rapidly during a transition phase, which typically lasts about 10 hours. During this phase

$$\sigma_y = \sigma_y(0) \left( \frac{t}{t_0} \right)^{1.2} , \quad (3-4)$$

where  $\sigma_y(0)$  is  $\sigma_y$  at  $t = t_0$ , and  $t$  is the transport time.

This wind-shear-induced dispersion is several orders of magnitude greater than eddy diffusivity. Beyond about 10 hours, diffusivity becomes constant and we have the following limit on horizontal dispersion:

$$\sigma_y \leq (2 K_{H\infty} t)^{1/2} , \quad (3-5)$$

where  $K_{H\infty} = 7 \times 10^8 \text{ cm}^2/\text{s}$ .

Vertical dispersion in the RIVAD is handled in a somewhat similar way in that dispersion is keyed to transport time:

$$\sigma_z = \sigma_z(0) \left( \frac{t}{t_0} \right)^k , \quad (3-6)$$

where  $k$  is determined from Pasquill-Gifford curves to be 2.10, 1.09, 0.53, 0.36, and 0.30 for stabilities A, B, C, D, E, and F, respectively.

Vertical downward dispersion in RIVAD is ultimately limited by the ground, and vertical upward dispersion by the height of the mixed layer ( $H_m$ ).

### 3.2.1.3 MELSAR-POLUT

The horizontal dispersion in MELSAR-POLUT assumes that the square of the total horizontal diffusion,  $\sigma_y^2$ , is the sum of the squares of three components: an initial buoyancy-induced dispersion ( $A_y$ ), diffusion resulting from atmospheric turbulence ( $B_y$ ), and diffusion resulting from horizontal wind shear ( $C_y$ ):

$$\sigma_y = \left( A_y^2 + B_y^2 + C_y^2 \right)^{1/2} . \quad (3-7)$$

Similarly, the vertical diffusion coefficient is

$$\sigma_z = \left( A_z^2 + B_z^2 \right)^{1/2} \quad (3-8)$$

where  $A_z$  is the initial buoyancy-induced dispersion and  $B_z$  is the vertical diffusion due to atmospheric turbulence. The formulas used in calculating the diffusion coefficient in MELSAR-POLUT are complex and involve the use of downwind distance, travel time, standard deviation of the horizontal and vertical components of the wind, terrain roughness, Monin-Obukhov length, and friction velocity. These formulas are presented in Appendix A of the report by Morris and Kessler (1987).

The user has two options for the calculation of horizontal and vertical dispersion due to atmospheric turbulence under neutral and stable conditions in the POLUT model. The first option is a scheme proposed by Irwin (1979); the second option uses an empirical relationship developed by MacCready, Baboul, and Lissman (1974), which accounts for effects of terrain roughness on atmospheric turbulence. These parameterizations are described in detail by Morris and Kessler (1987) and by Allwine and Whiteman (1985).

### 3.2.2 Evaluation of the Dispersion Algorithms

The dispersion algorithms of the four candidate models are evaluated below by comparing the calculated horizontal and vertical dispersion values with each other and with the estimates of Pasquill, Gifford and Turner (PGT) at different downwind distances and stabilities.

#### 3.2.2.1 Horizontal Dispersion ( $\sigma_y$ )

##### Unstable Conditions

The growth of  $\sigma_y$  as a function of downwind distance as calculated by the four models and the Pasquill, Gifford, and Turner (PGT) estimates for the A, B, and C stability classes (unstable) are given in Figures 3-5, 3-6, and 3-7. Note that the two methods in the MELSAR-POLUT model, those of Irwin and MacCready, produce identical results for unstable conditions. The MELSAR-POLUT and MESOPUFF-II horizontal dispersion algorithm produce results very similar to the PGT dispersion estimates for downwind distance under 10 km. The MELSAR-POLUT algorithm for horizontal dispersion

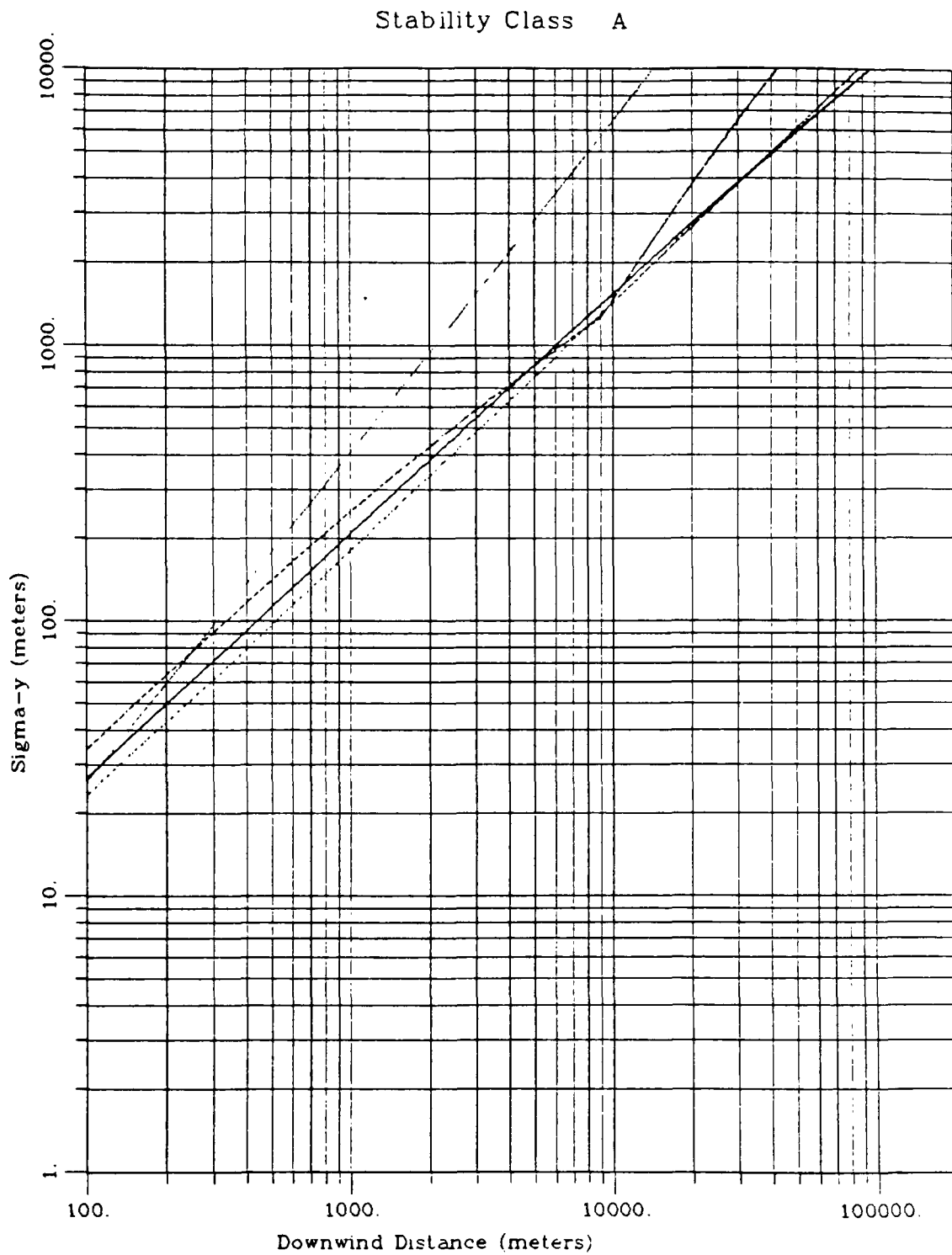


FIGURE 3-5. Comparison of horizontal plume dispersion rates for stability class A.

- PGT
- MELSAR using IRWIN scheme
- ..... MELSAR using MacCREADY scheme
- RIVAD
- . - . - MESOPUFF

# Stability Class B

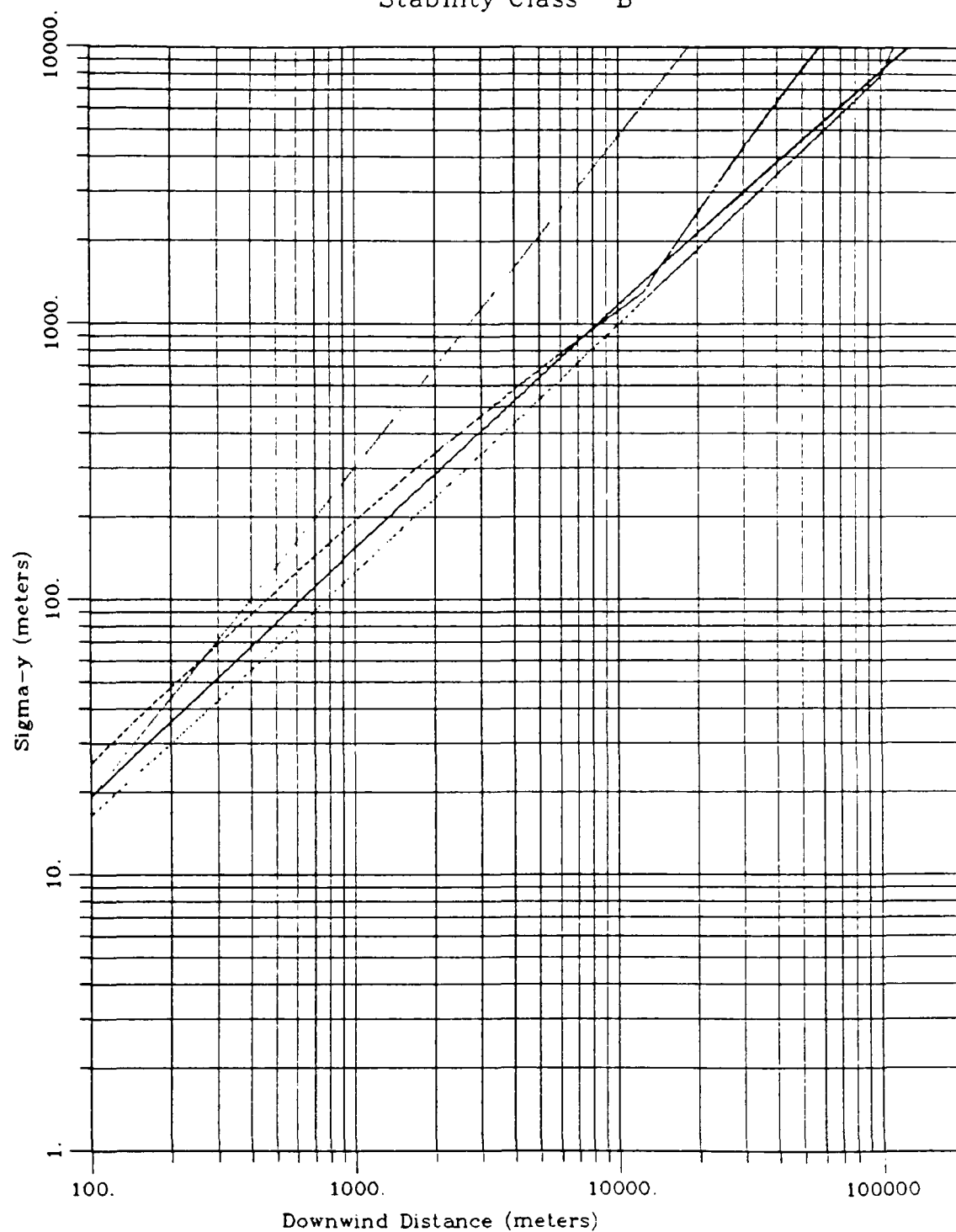


FIGURE 3-6. Comparison of horizontal plume dispersion rates for stability class B.

- PGT
- - - MELSAR using IRWIN scheme
- ..... MELSAR using MacCREADY scheme
- - - RIVAD
- . - MESOPUFF

# Stability Class C

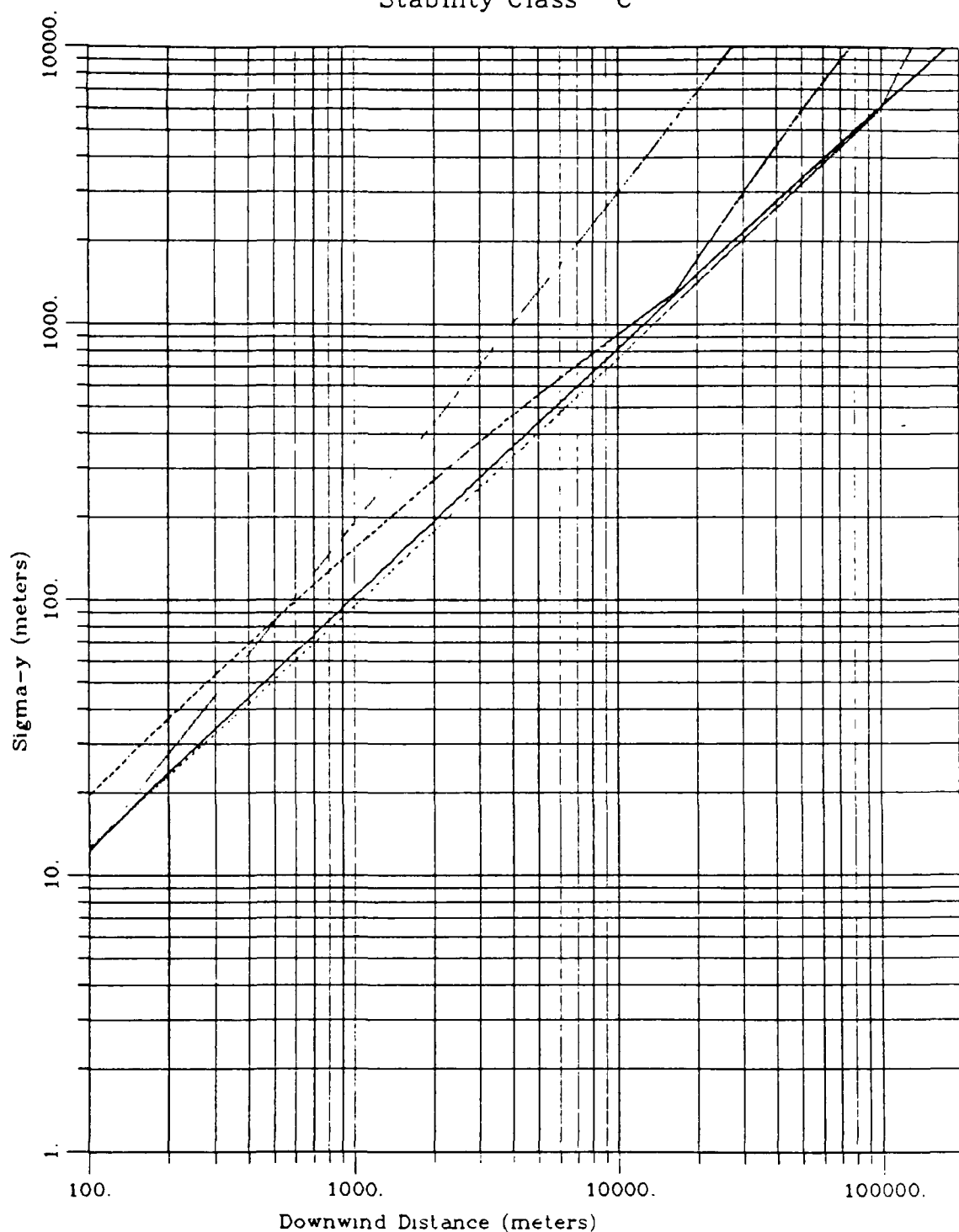


FIGURE 3-7. Comparison of horizontal plume dispersion rates for stability class C.

- PGT
- - - MELSAR using IRWIN scheme
- ..... MELSAR using MacCREADY scheme
- RIVAD
- . - MESOPUFF

due to atmospheric turbulence treats the near-field versus far-field dispersion effects by taking the maximum calculated dispersion rate of different formulas proposed by Draxler and Gifford. This produces a kink in the  $\sigma_y$  that appears at approximately 10 km downwind for the unstable cases. The MESOPUFF-II  $\sigma_y$  values match the PGT estimates better at greater downwind distances until the MESOPUFF-II switches to the far-field dispersion algorithms at 100 km, at which time the MESOPUFF-II  $\sigma_y$  curves deviate from the PGT estimates. Since the near-field MESOPUFF-II dispersion algorithms are designed to match the PGT curves, it is not surprising that they do. However, as noted by Gifford (1982), if typical short-range diffusion coefficients are extrapolated to large downwind distances, the results will fall short of both observed and theoretical values by amounts ranging up to nearly an order of magnitude.

The RIVAD model calculates the largest horizontal dispersion parameters for unstable conditions. At a distance of 10 km downwind the RIVAD horizontal plume extent is approximately four times that of the other models and the PGT estimate. This increased diffusion in the RIVAD is most probably due to its parameterization of diffusion at the regional-scale, which accounts for the effects of wind shear, while the MESOPUFF-II and MELSAR-POLUT contain separate near-field and far-field algorithms.

### Neutral Conditions

The horizontal dispersion parameters at different downwind distances under neutral stability for the different methods are given in Figure 3-8. The PGT, MESOPUFF-II, and MELSAR-POLUT, all of which use Irwin's scheme, produce similar dispersion curves for neutral conditions. The MELSAR-POLUT method, using MacCready's scheme, produces slightly higher horizontal diffusion, while the RIVAD model produces the highest horizontal dispersion parameters for neutral stability.

The MacCready algorithm in the MELSAR-POLUT model is the only algorithm in which variations in complex terrain are used. As such, it is sensitive to the terrain roughness and the height of the plume above ground. For the dispersion curves shown in Figure 3-8, a terrain roughness value of 300 m was specified, and the height above ground was 10 m. The terrain roughness value of 300 m was the average terrain roughness for the mesoscale region in the Rocky Mountain region depicted in Figure 2-1. The terrain roughness for that region varied from 40 to 1000 m.

The sensitivity of the MacCready scheme to the prescription of terrain roughness and height above ground for neutral conditions is shown in Figures 3-9 and 3-10. As can be seen in Figure 3-9, the MacCready scheme is very sensitive to the terrain roughness, where an increase by a factor

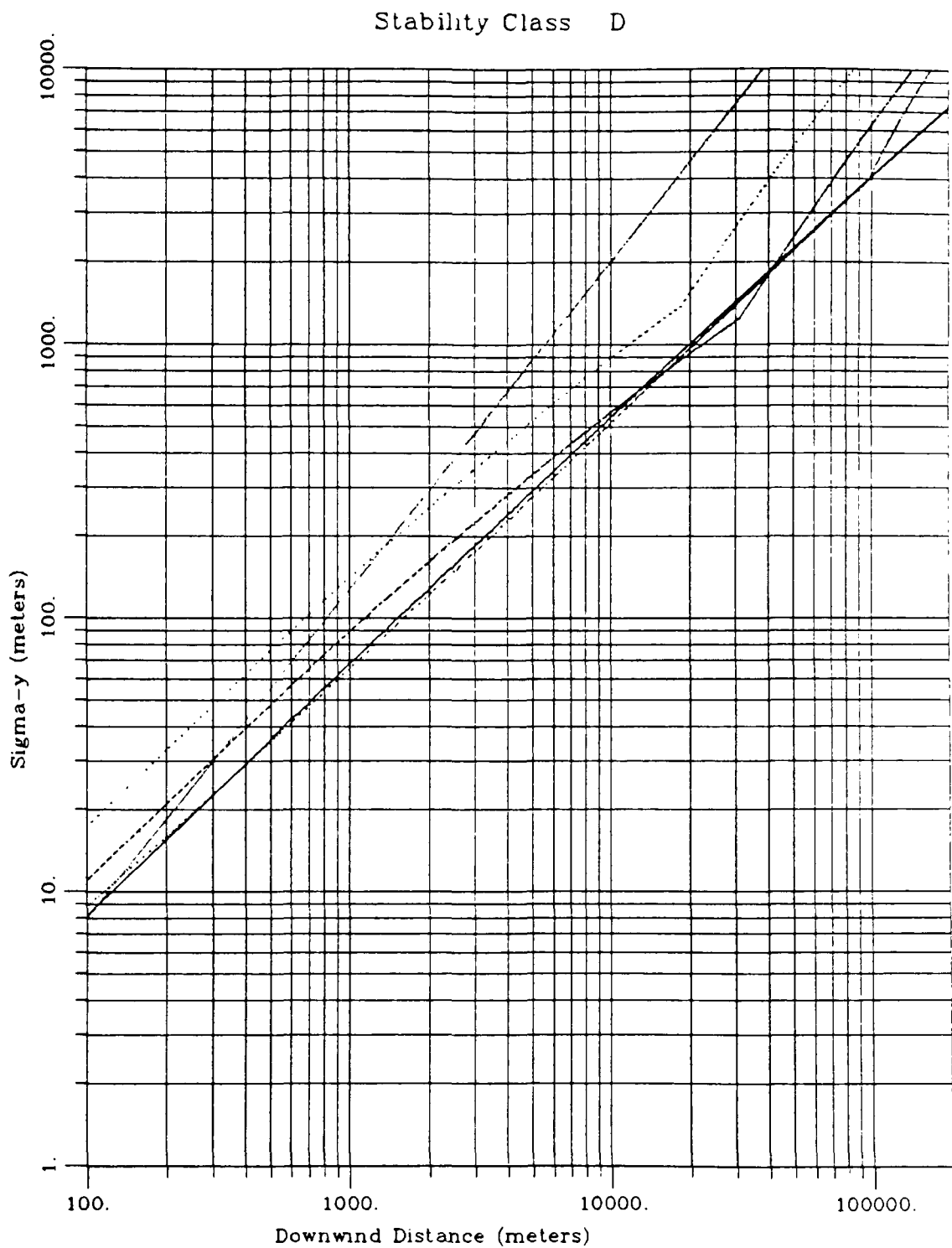


FIGURE 3-8. Comparison of horizontal plume dispersion rates for stability class D.

- PGT
- MELSAR using IRWIN scheme
- ..... MELSAR using MacCREADY scheme
- RIVAD
- MESOPUFF



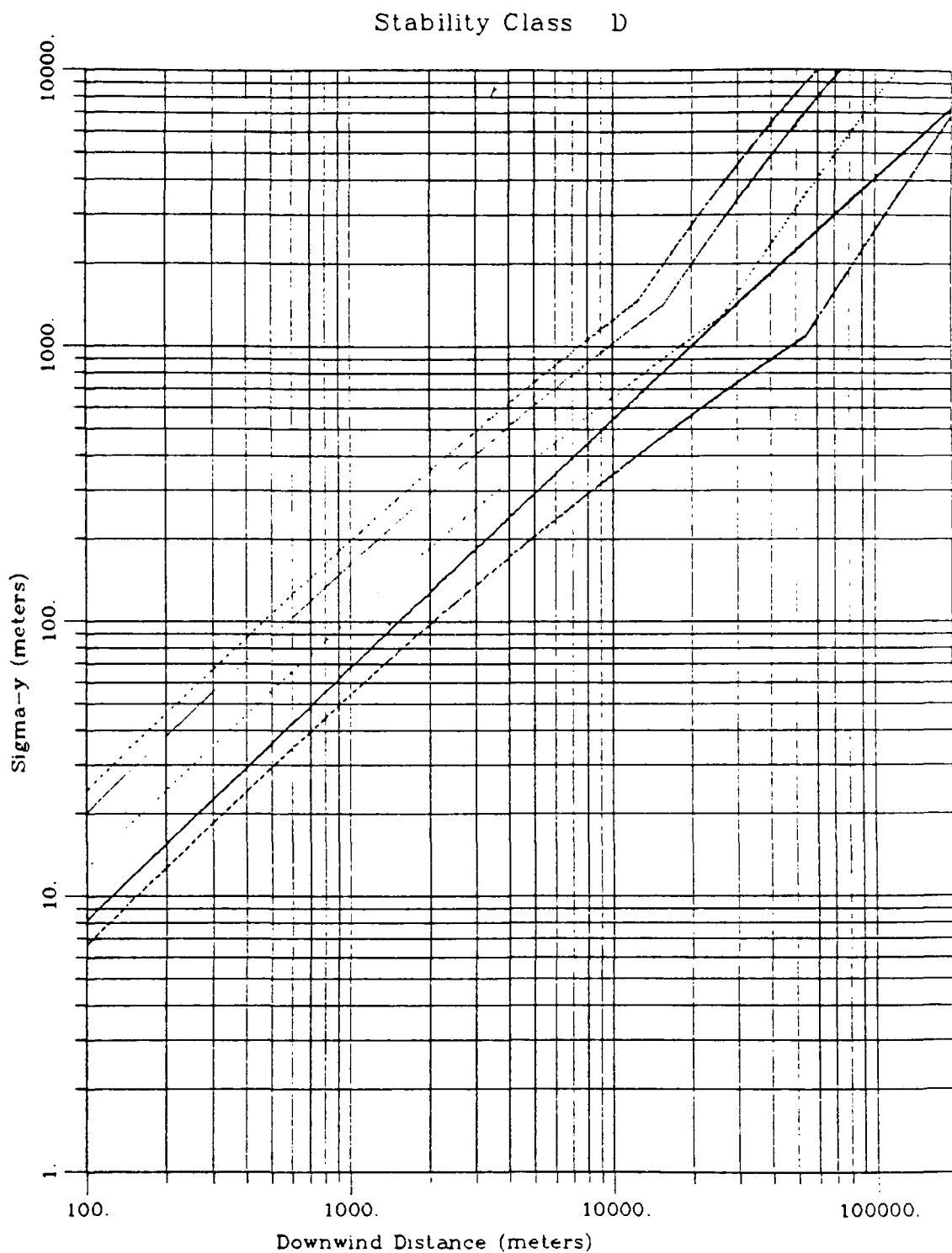


FIGURE 3-9. Sensitivity of the MELSAR MacCready horizontal dispersion rate to terrain roughness (R).

- PGT
- MacCREADY with R = 10 m
- ..... MacCREADY with R = 100 m
- MacCREADY with R = 500 m
- ..... MacCREADY with R = 1000 m

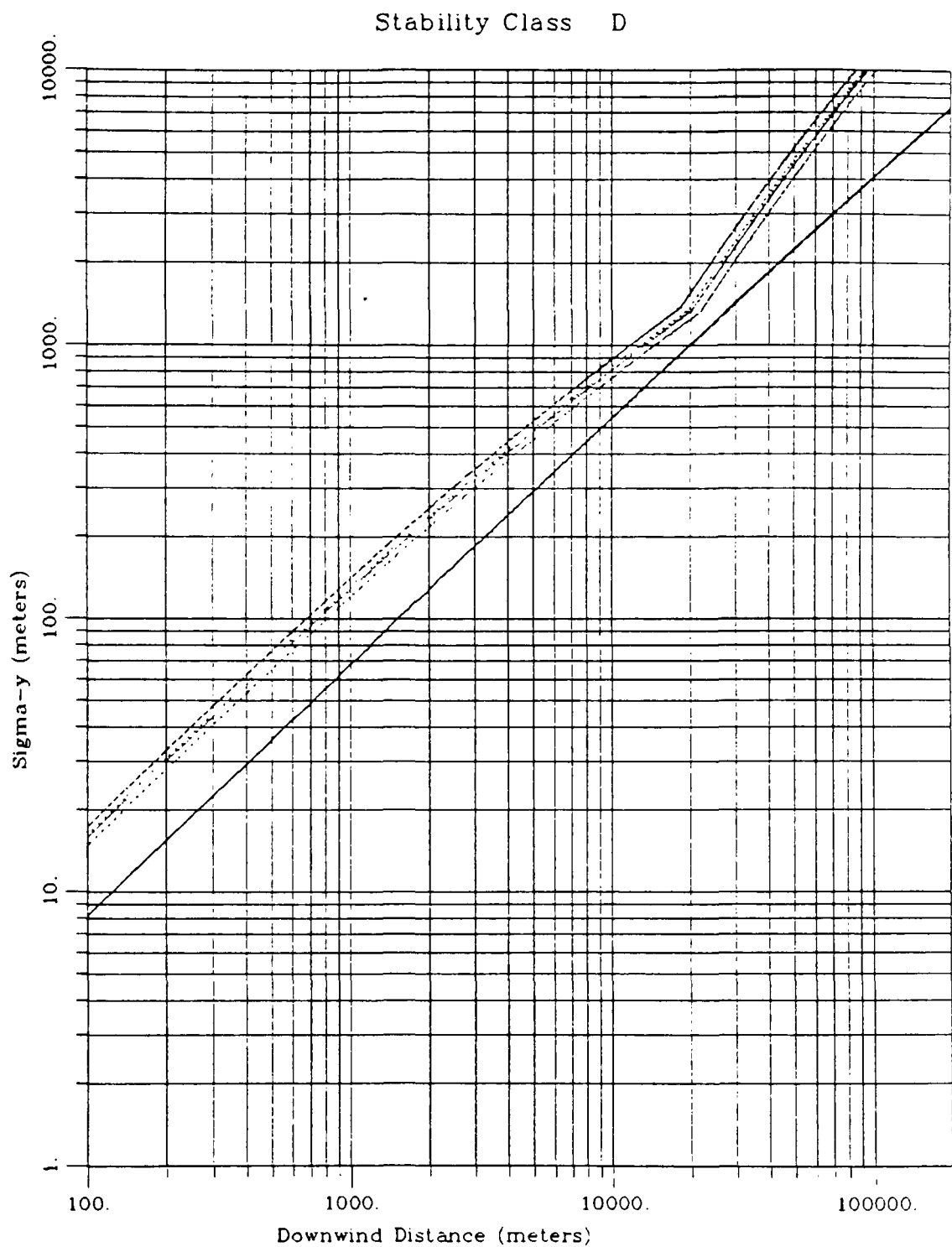


FIGURE 3-10. Sensitivity of the MELSAR MacCready horizontal dispersion rate to height above terrain (H).

- PGT
- MacCREADY with H = 10 m
- ..... MacCREADY with H = 50 m
- MacCREADY with H = 100 m
- ..... MacCREADY with H = 500 m

of 10 in the terrain roughness results in an increase by a factor of 2 in the horizontal plume extent. A terrain roughness value of between 10 and 100 m would give the best match with the PGT dispersion estimates; such values are consistent with the values used in the experiments that led to the development of the PGT curves. The MacCready scheme is less sensitive to the height above ground, as shown in Figure 3-10; a terrain roughness value of 300 m was used in the sensitivity tests. The behavior of the MacCready algorithm to variations in terrain roughness and plume height is as expected; the more complex terrain results in enhanced dispersion, and the influence of the terrain on the dispersion is less as the plume height above the terrain increases.

### Stable Conditions

The horizontal dispersion parameters for stable conditions (classes E and F) are given in Figures 3-11 and 3-12. These figures are similar to those produced for neutral conditions except that the MacCready scheme in MELSAR-POLUT produces the largest horizontal dispersion parameters. This is not surprising since complex terrain will enhance dispersion and the MacCready scheme is the only algorithm that takes into account this enhancement. The effect is increased in these figures because the terrain roughness chosen for these experiments, 300 m, was from a region of very complex terrain in the Rocky Mountains. Use of a lower value will produce dispersion results closer to those produced by the other algorithms (see Figure 3-9).

#### 3.2.3.2 Vertical Dispersion ( $\sigma_y$ )

All of the models assume that the vertical expansion of the plume segments or puffs is limited to the mixing height when the plume height lies below the mixing depth. Since over long distances the plume will eventually become uniformly mixed within the mixed layer, the characterization of vertical dispersion is not as important as that of horizontal dispersion. Rather, the correct calculation of the mixing depth and plume height is required. When the plume centerline is above the mixing height, the upward expansion of the plumes is at a rate for stable conditions regardless of the stability within the boundary layer.

### Unstable Conditions

The growth of the vertical dispersion parameter as a function of downwind distance for A, B, and C stabilities is shown in Figures 3-13, 3-14, and

# Stability Class E

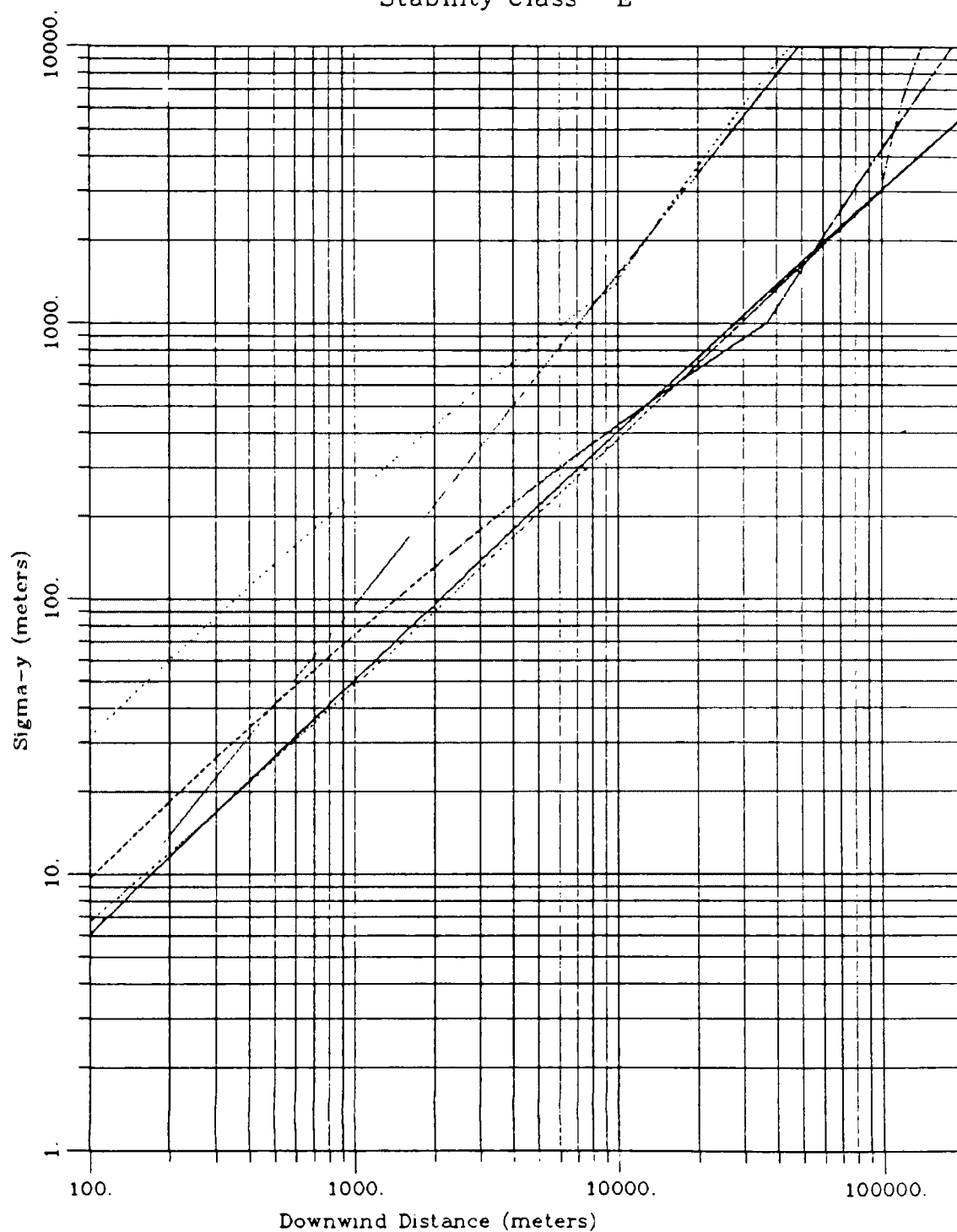


FIGURE 3-11. Comparison of horizontal plume dispersion rates for stability class E.

- PGT
- MELSAR using IRWIN scheme
- ..... MELSAR using MacCREADY scheme
- RIVAD
- · - · - MESOPUFF

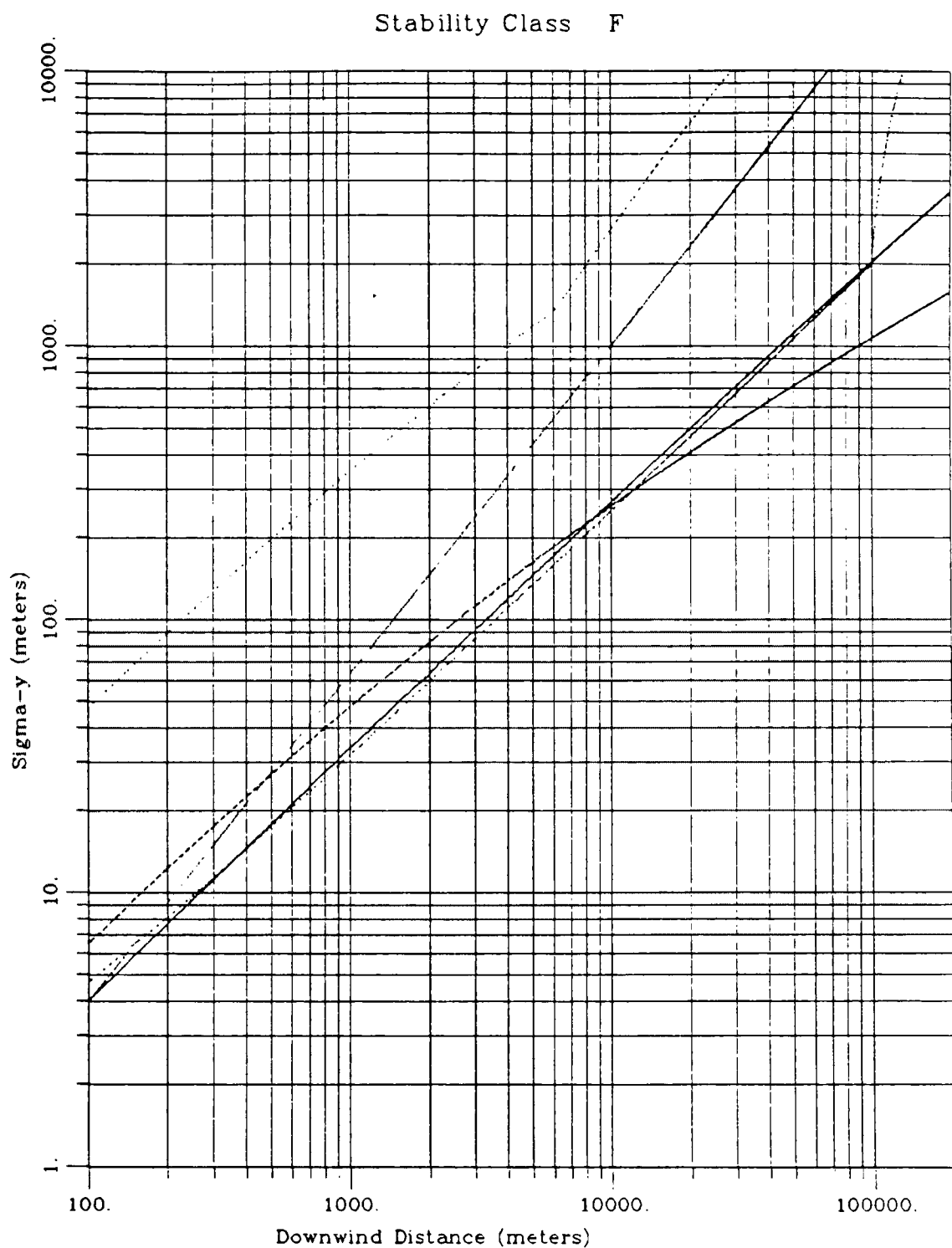


FIGURE 3-12. Comparison of horizontal plume dispersion rates for stability class F.

- PGT
- MELSAR using IRWIN scheme
- ..... MELSAR using MacCREADY scheme
- RIVAD
- ..... MESOPUFF

3-15. As for the horizontal dispersion parameters under unstable conditions, the RIVAD algorithms calculate the fastest vertical expansion, and the MESOPUFF-II matches the PGT dispersion estimates well. On the other hand, for class A stability, the MELSAR-POLUT algorithm (i.e., the Irwin method, since the MacCready method is used only for neutral and unstable conditions) produces the lowest vertical expansion rates. As the atmosphere becomes less unstable, the  $\sigma_y$  values produced by the MELSAR-POLUT algorithm tend toward those produced by the other parameterizations. As seen in Figure 3-15 for C stability, all of the algorithms show good agreement with each other and with the PGT estimates. As noted above, under unstable conditions the plume will eventually become well mixed in the mixed layer.

### Neutral Conditions

Under neutral conditions the MacCready scheme (in MELSAR-POLUT) produces the largest vertical dispersion rates, followed by the Irwin scheme (also in MELSAR-POLUT), the RIVAD, and the MESOPUFF-II. The MESOPUFF-II vertical dispersion curves again match the PGT dispersion estimates (Figure 3-16). As for the horizontal dispersion parameters calculated by the MacCready scheme, the vertical dispersion rates are very sensitive to the specification of the terrain roughness (Figure 3-17) and a little sensitive to the plume height above ground (Figure 3-18). Figure 3-17 shows that the large vertical diffusion rates produced by the MacCready scheme under neutral conditions (shown in Figure 3-16) are due to the terrain roughness value of 300 m used in these experiments.

### Stable Conditions

Due to the terrain roughness value used, the MacCready scheme in MELSAR-POLUT produces the largest vertical diffusion rate for stable conditions (Figure 3-19 and 3-20). The other methods all produce very low rates, with  $\sigma_z$  in the range of 100 to 200 m under F stability at a downwind distance of 100 km. Even under E stability, at a downwind distance of 100 km, the  $\sigma_z$  produced by all of the algorithms except the MacCready scheme are in the range of 200 to 400 m.

## 3.3 CHEMICAL TRANSFORMATION

Each of the four candidate acid deposition models contains different methods for treating the chemical transformation of  $\text{SO}_2$  to sulfates and  $\text{NO}_x$  to nitrates and nitric acid. The MELSAR-POLUT model does not treat chemical transformation; the MESOPUFF-II uses an empirical fit to chemical

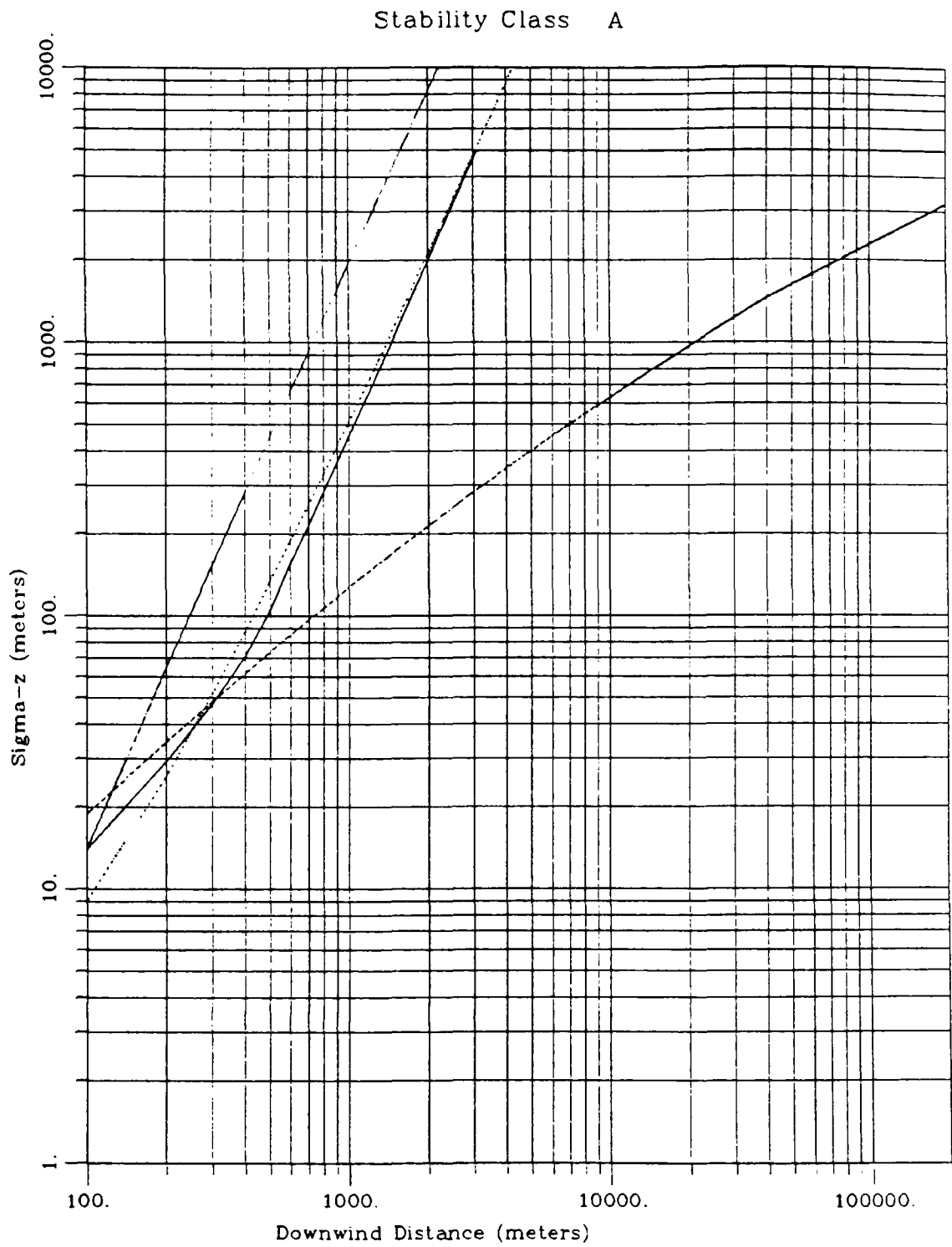


FIGURE 3-13. Comparison of vertical plume dispersion rates for stability class A.

- PGT
- - - MELSAR using IRWIN scheme
- ..... MELSAR using MacCREADY scheme
- RIVAD
- · - MESOPUFF

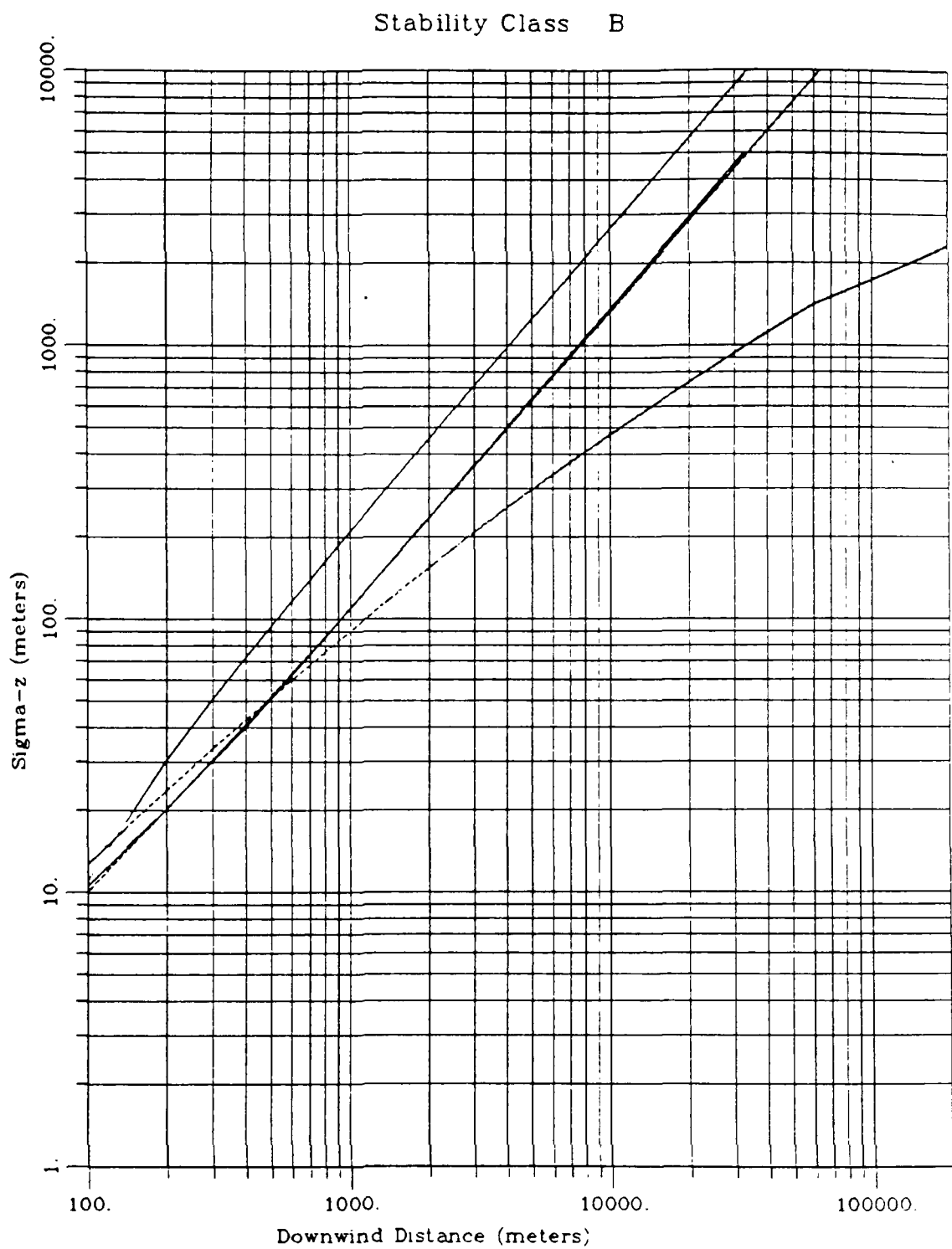


FIGURE 3-14. Comparison of vertical plume dispersion rates for stability class B.

- PGT
- MELSAR using IRWIN scheme
- ..... MELSAR using MacCREADY scheme
- RIVAD
- MESCPUFF



# Stability Class C

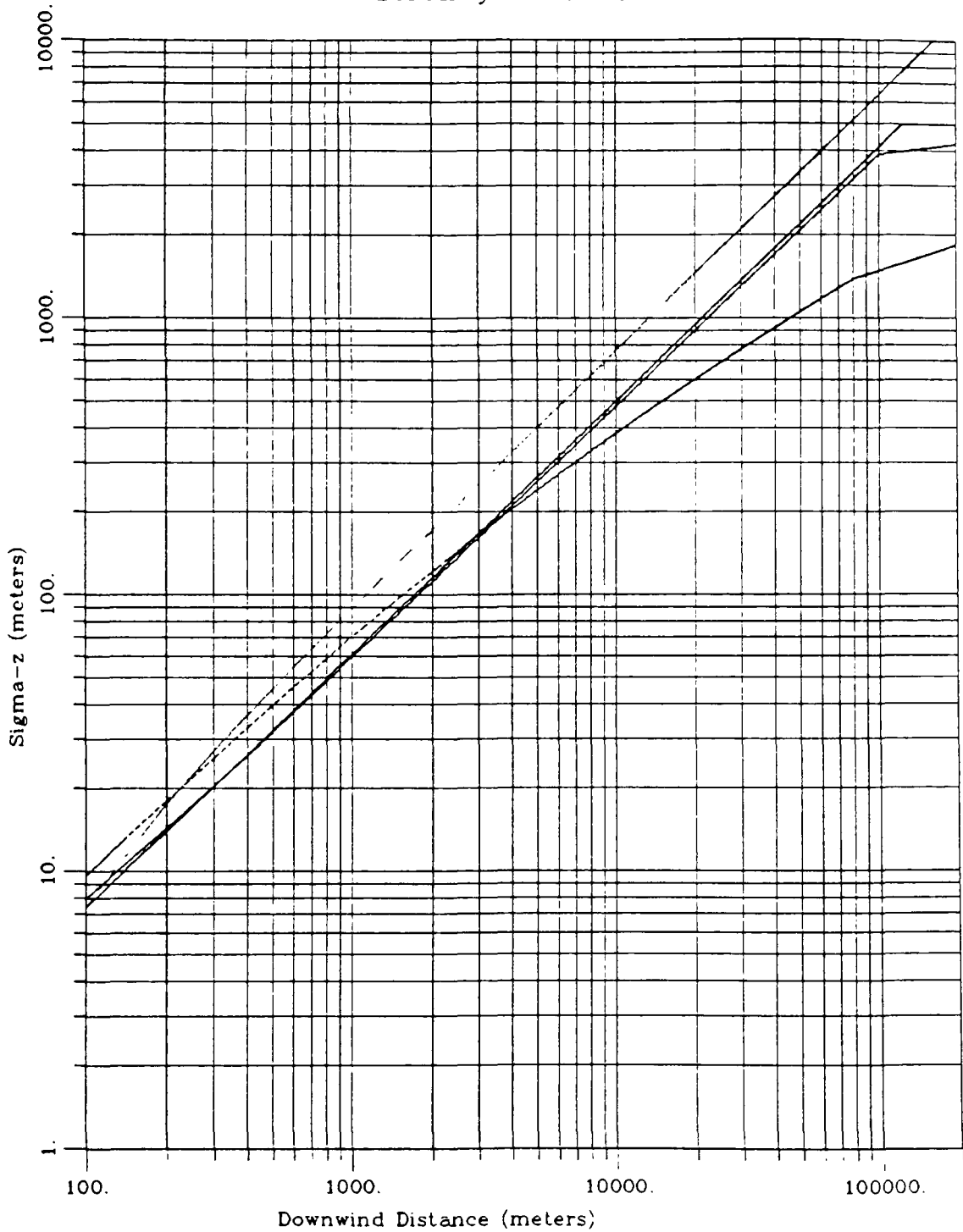


FIGURE 3-15. Comparison of vertical plume dispersion rates for stability class C.

- PGT
- MELSAR using IRWIN scheme
- ..... MELSAR using MacCREADY scheme
- RIVAD
- MESOPUFF

# Stability Class D

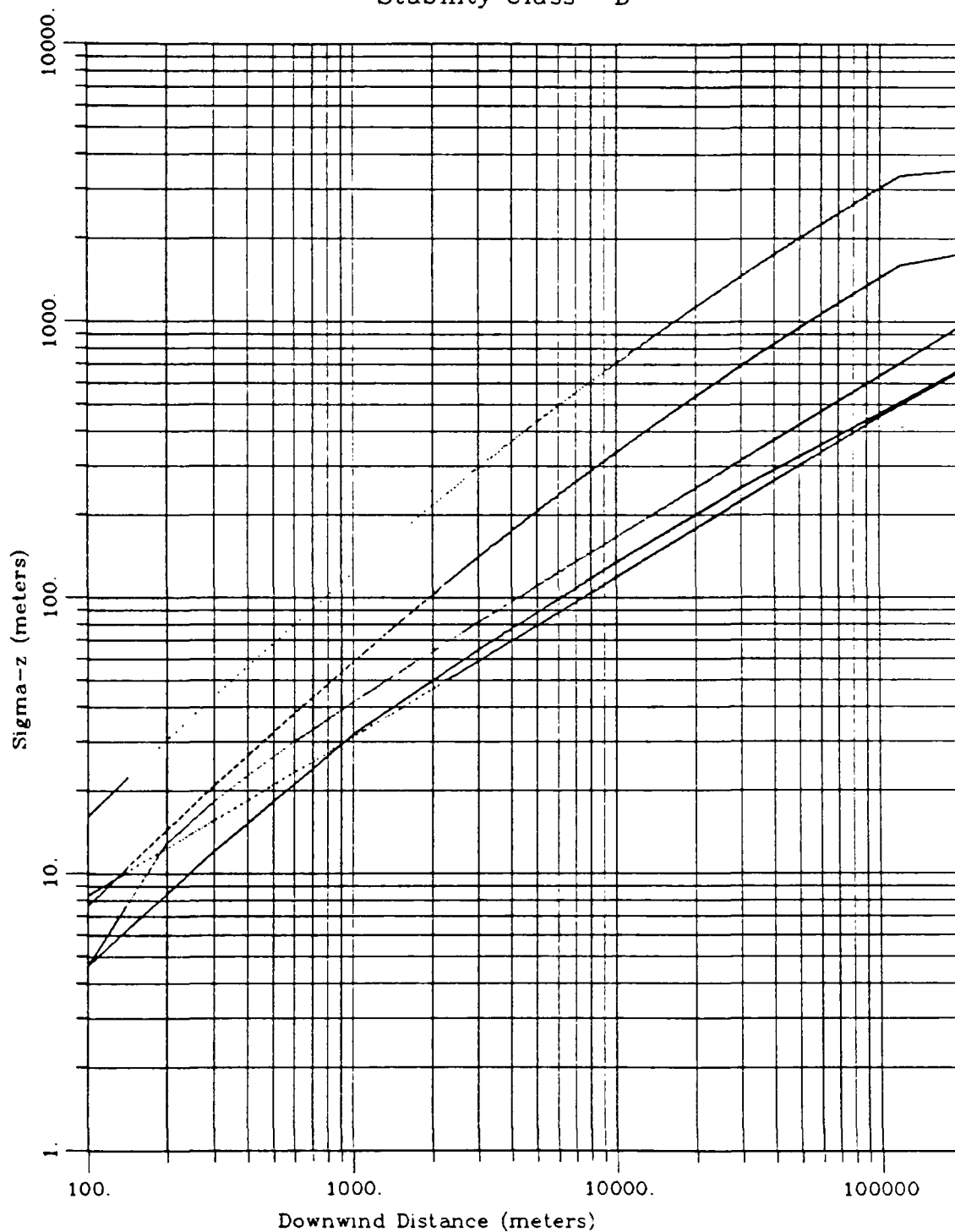


FIGURE 3-16. Comparison of vertical plume dispersion rates for stability class D.

- PGT
- - - MELSAR using IRWIN scheme
- ..... MELSAR using MacCREADY scheme
- RIVAD
- - - MESOPUFF

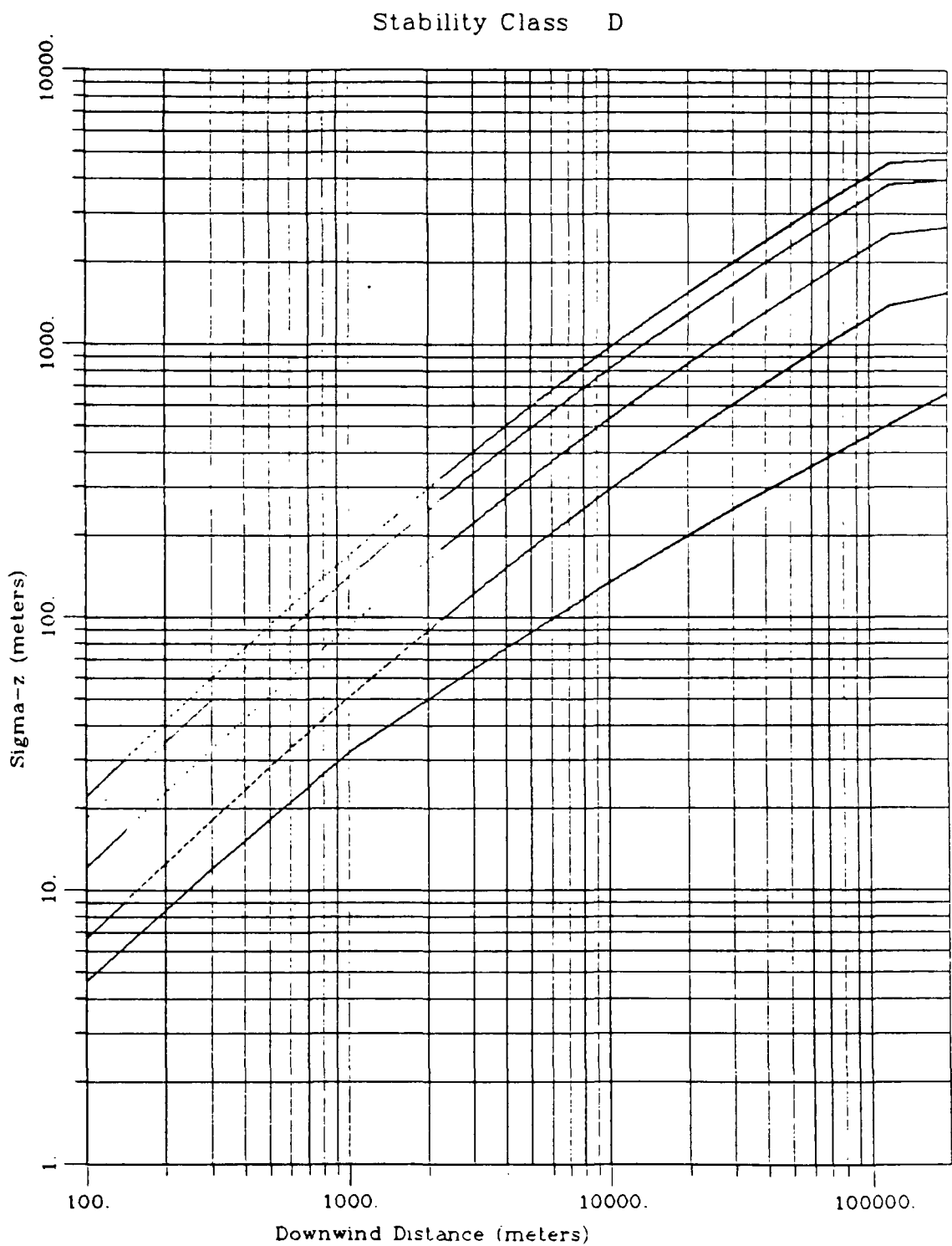


FIGURE 3-17. Sensitivity of the MELSAR MacCready vertical dispersion rate to terrain roughness (R).

- PGT
- MacCREADY with R = 10 m
- ..... MacCREADY with R = 100 m
- MacCREADY with R = 500 m
- . - . - MacCREADY with R = 1000 m

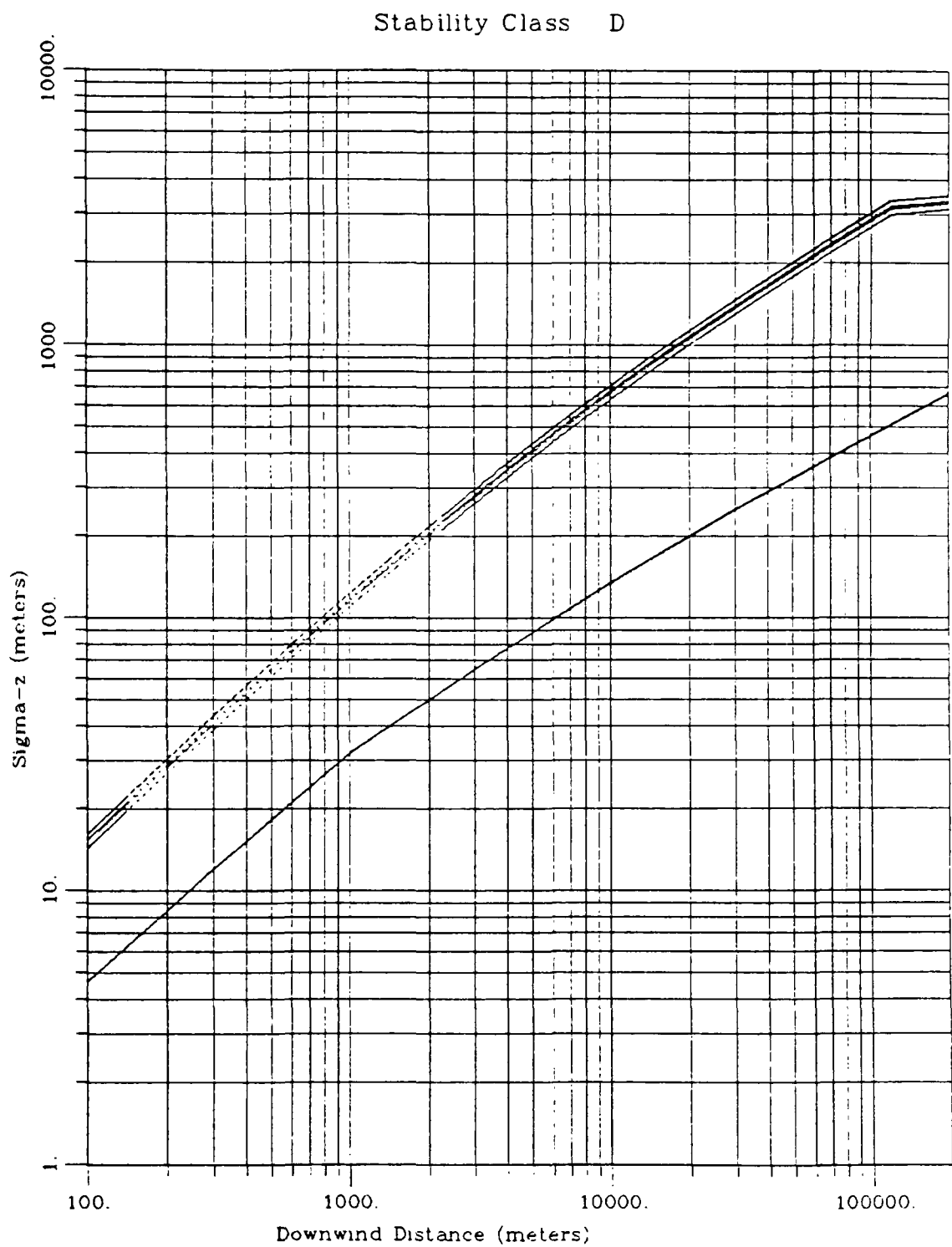


FIGURE 3-18. Sensitivity of the MELSAR MacCready vertical dispersion rate to height above terrain ( $H$ ).

- PGT
- - - MacCREADY with  $H = 10$  m
- ..... MacCREADY with  $H = 50$  m
- - - - MacCREADY with  $H = 100$  m
- · - · MacCREADY with  $H = 500$  m

# Stability Class E

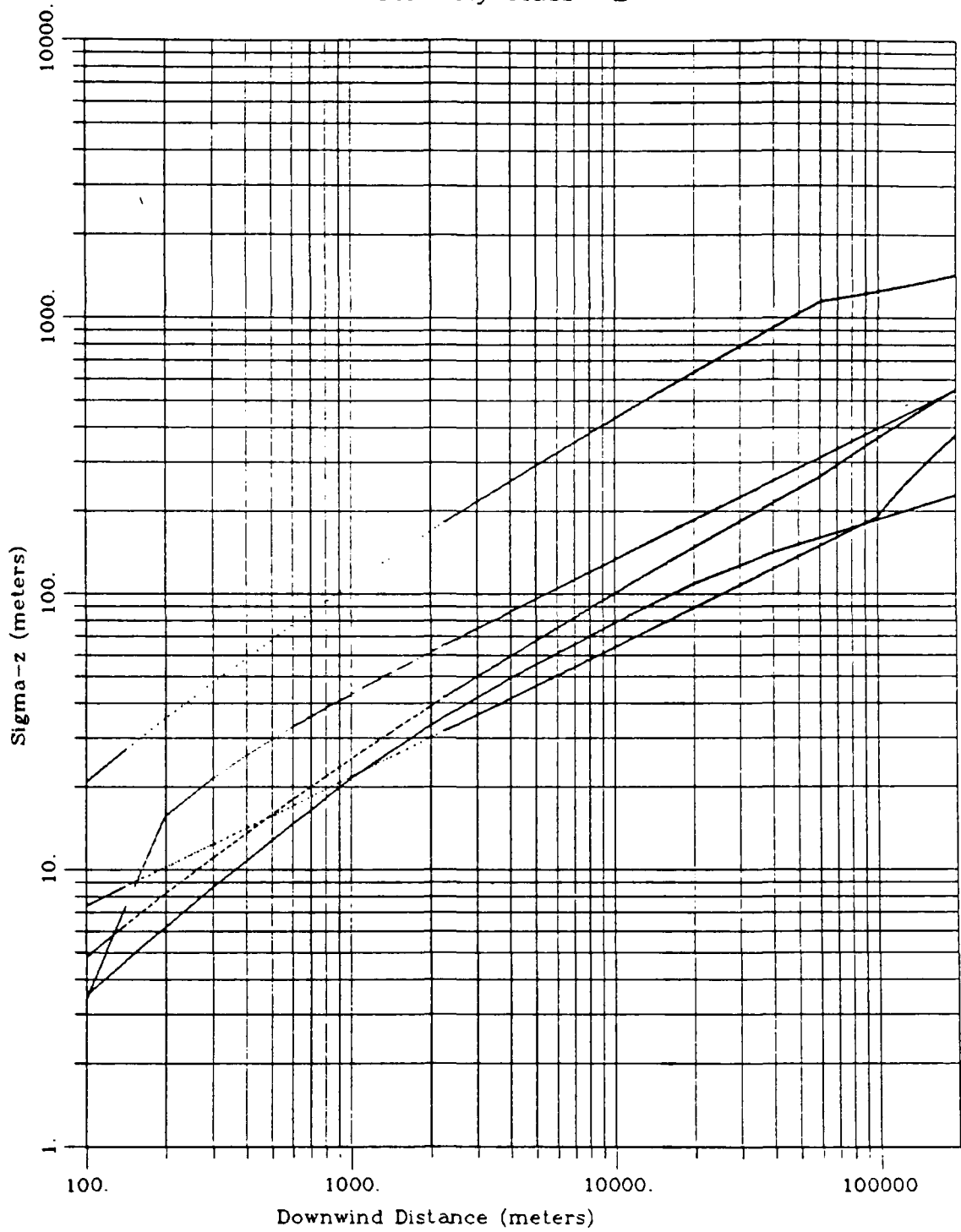


FIGURE 3-19. Comparison of vertical plume dispersion rates for stability class E.

- PGT
- MELSAR using IRWIN scheme
- ..... MELSAR using MacCREADY scheme
- RIVAD
- MESOPUFF

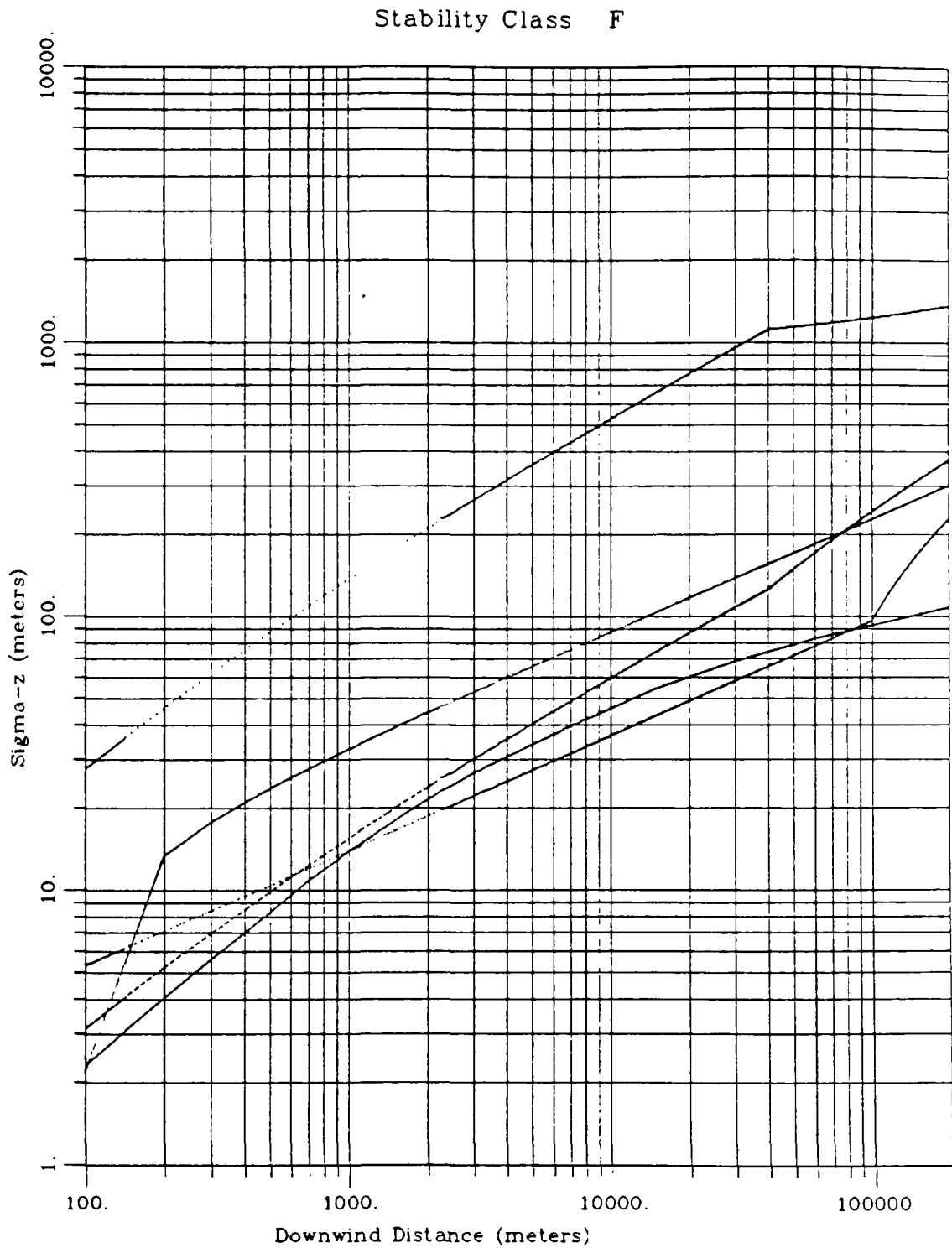


FIGURE 3-20. Comparison of vertical plume dispersion rates for stability class F.

- PGT
- - - MELSAR using IRWIN scheme
- ..... MELSAR using MacCREADY scheme
- RIVAD
- - - MESOPUFF

box model simulations; the RIVAD uses a highly condensed chemical mechanism that is an extension of the mechanism used in the PLUVUE-II model; and the CCADM uses comprehensive gas-phase and aqueous phase non-linear chemical kinetic mechanisms. The choice of one or more of these chemical modules for use in a Lagrangian model for the Rocky Mountain region is based on the following criteria:

At a minimum the mechanism must treat the oxidation of both SO<sub>2</sub> and NO<sub>x</sub>.

The chemical mechanism must be consistent with the formulation of a Lagrangian model. Any nonlinearities within the chemical mechanism must be based on conditions within the puff so that the puff superposition principle will not be violated.

The chemical mechanism must be appropriate for the Rocky Mountain region. A mechanism that is tuned for an urban atmosphere would greatly exaggerate the oxidation rates in the Rocky Mountain region.

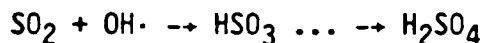
As with other components of the modeling system, the chemical mechanism must be computationally efficient so that long-term averages can be readily calculated.

The chemical reactions that lead to the formation of sulfates, nitrates, and nitric acid are briefly discussed below along with the chemical mechanisms used by the candidate models.

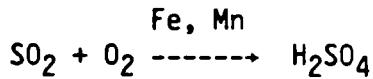
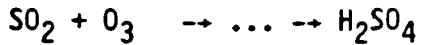
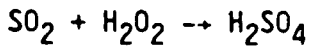
### 3.3.1 Review of the Chemistry of Acid Deposition

#### 3.3.1.1 Sulfate Chemistry

The oxidation of SO<sub>2</sub> to sulfate in the atmosphere involves both gas- and liquid-phase reactions (NRC, 1983). The most important gas-phase (homogeneous) reaction for the formation of sulfates is the oxidation of SO<sub>2</sub> by the hydroxyl radical (OH·), which is formed mainly through ozone photolysis:



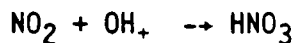
There are several pathways for the formation of sulfates in the liquid phase, including the direct oxidation of SO<sub>2</sub> by ozone and metal-catalyzed oxidation. The most important pathway for the oxidation of SO<sub>2</sub> in the aqueous phase is the reaction with hydrogen peroxide:



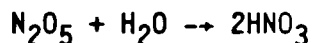
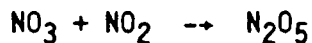
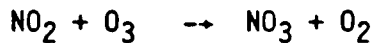
Although aqueous-phase oxidation of  $\text{SO}_2$  can be very rapid, near the source it is generally limited to the amount of  $\text{H}_2\text{O}_2$  available (oxidant limited). Further downwind the oxidation of  $\text{SO}_2$  by  $\text{H}_2\text{O}_2$  may be limited by the amount of  $\text{SO}_2$  available ( $\text{SO}_2$  limited).

### 3.3.1.2 Nitrate Chemistry

The formation of nitrate aerosol and nitric acid vapor from  $\text{NO}_2$  occurs mainly in the gas phase. During the day the reaction of  $\text{NO}_2$  with the hydroxyl radical forms nitric acid at a rate almost seven times faster than the reaction that forms sulfates:



Thus during the day the oxidation of  $\text{SO}_2$  and  $\text{NO}_2$  compete with each other for the available hydroxyl radical. At night, nitrates and nitric acid are formed with a direct reaction with ozone:



The relative concentrations of nitrates and nitric acid is dependent on the amount of ammonia present. For the typical nitrate and ammonia concentrations found in the Rocky Mountains, most of the nitrates are converted to nitric acid. Since both nitrates and nitric acid are scavenged efficiently by precipitation, the distinction between these species can be ignored for purposes of modeling nitrogen deposition. When calculating the pH of deposition or visibility impairment, however, it is important to distinguish between them. Information concerning the total nitrate and ammonia concentration is required in order to split the nitrate species between nitrates and nitric acid. Since the Lagrangian model being developed here only has information concerning concentrations from the source in question, it cannot distinguish between nitrates and nitric acid.

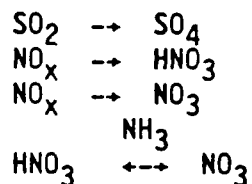


### 3.3.2 Review of the Chemical Mechanisms in the Candidate Models

#### 3.3.2.1 MESOPUFF-II

The MESOPUFF-II contains five methods for treating the oxidation of  $\text{SO}_2$  to sulfates and two methods for treating the oxidation of  $\text{NO}_x$  to nitrates and nitric acid. These methods are: user-specified rate constants, the ERT theoretical method, and three methods for treating  $\text{SO}_2$  oxidation based on an analysis of air quality data by Gillani (1981, St. Louis plume data), Henry and Hidy (1982, St. Louis urban data), and Henry and Hidy (1981, Los Angeles urban data). Clearly those  $\text{SO}_2$  oxidation methods based solely on the analysis of urban aerometric data would not be appropriate for the Rocky Mountains. Thus we restrict our discussion to the ERT method.

The ERT chemical transformation method produces rate constants for the following reactions:



The transformation rates for these reactions were developed by statistically analyzing hourly transformation rates produced by a box model using the Atkinson and Lloyd chemical kinetic mechanism (Atkinson, Lloyd, and Wines 1982). These transformation rates were obtained by simulating the dispersal of plume  $\text{SO}_x/\text{NO}_x$  into background air containing ozone and reactive hydrocarbons (RHC) over a wide range of environmental conditions representing different solar radiation intensities, temperatures, dispersion conditions, background ozone and RHC, and time of day. Stepwise linear regression on the logarithms of the resultant concentrations was performed to find the controlling variables. Linear regression techniques were then performed on these variables to determine the transformation rates for the above equations. Since the Atkinson and Lloyd mechanism treats only homogeneous oxidation of  $\text{SO}_2$ , an empirically determined heterogeneous  $\text{SO}_2$  conversion term based on relative humidity ( $3 \times 10^{-8}$  RHC) is added on to the homogeneous term with an imposed minimum value of 0.2 %/h.

The controlling variables for the homogeneous reactions for  $\text{SO}_2$  were solar radiation, atmospheric stability, and background ozone. For the oxidation of  $\text{NO}_x$  the controlling variables were atmospheric stability, background ozone, and plume  $\text{NO}_x$  concentrations. Although it is well known that

photochemical activity (and hence  $\text{SO}_2$  and  $\text{NO}_x$  oxidation rates) increases with increasing temperature, the MESOPUFF-II chemistry module does not account for the effects of temperature on oxidation rates. In addition, the oxidation rates produced by the ERT mechanism will be relevant for the background RHC levels used in the box model simulations. The dependence of the  $\text{NO}_x$  oxidation rate on the plume  $\text{NO}_x$  concentrations presents a different problem. As stated by the model developers, when puffs overlap it would be incorrect to calculate a  $\text{NO}_x$  oxidation rate for a puff based only on the puff's own  $\text{NO}_x$  concentration. Thus the MESOPUFF-II sums the  $\text{NO}_x$  concentrations from all overlapping puffs to obtain a single oxidation rate for the puff in question. However, what is not stated by the model developers is that a single puff from a  $\text{NO}_x$  source will have the  $\text{NO}_x$  concentrations in a Gaussian distribution around the plume centerline; thus the use of a single  $\text{NO}_x$  oxidation rate for the entire puff may nevertheless be incorrect.

#### 3.3.2.2 RIVAD

The RIVAD model uses a highly condensed, simplified chemical mechanism to calculate the chemical transformation rates for the formation of sulfates, nitrates, and nitric acid. The homogeneous oxidation of  $\text{SO}_2$  and  $\text{NO}_x$  comes from the reaction of  $\text{SO}_2$  with the hydroxyl radical ( $\text{OH}\cdot$ ). The RIVAD model estimates the concentration of the  $\text{OH}$  radical based on solar radiation intensity, ozone concentration, temperature, relative humidity, and  $\text{NO}_2$  and  $\text{SO}_2$  concentrations. A maximum possible calculated  $\text{OH}\cdot$  concentration is defined based on numerous smog chamber simulations that used a complete photochemical kinetic chemical mechanism. A constant  $\text{SO}_2$  oxidation rate of 0.2 %/h is added on to the homogeneous rate estimated from the  $\text{OH}\cdot$  concentration to take into account any heterogenous reactions.

At night, a reduction in the hydroxyl radical reduces the rate of  $\text{SO}_2$  oxidation in the RIVAD down to the heterogenous rate of 0.2 %h.

The RIVAD model uses the photo-steady relationship between  $\text{NO}$ ,  $\text{NO}_2$ , and  $\text{O}_3$  in order to determine the steady-state  $\text{NO}_2$  and  $\text{O}_3$  concentrations. The oxidation of  $\text{NO}_2$  to nitric acid in the RIVAD depends on the estimated hydroxyl radical concentration, as discussed above. At night, however, nitric acid is formed through a direct reaction with the  $\text{NO}_2$  and ozone concentrations. For a more complete explanation of the RIVAD nitrate chemistry mechanism, see Latimer, Gery, and Hogo (1986).

#### 3.3.2.3 CCADM

The CCADM contains complete gas-phase and aqueous-phase chemical kinetic mechanisms with associated mass transfer algorithms between phases (Gery

et al., 1987; Morris and Kessler, 1987). This mechanism contains up-to-date gas- and aqueous-phase reactions based on the literature as of November 1986. The mechanism is highly nonlinear and the reaction rates also depend on the background concentrations. As such, this mechanism would not be appropriate for use with a Lagrangian puff model treating a single source without complete information concerning the background concentrations. Since these background concentrations within the Rocky Mountain region are not available at this time, either through measurement programs or modeling of regional photochemistry or acid deposition, the explicit CCADM mechanism cannot be used in a Lagrangian puff model for this region.

However, the CCADM can be used to generate a table of oxidation rates, as has been done for the MESOPUFF-II and RTM-IINL models (Morris and Kessler, 1987). These oxidation rates would be obtained by repeated simulations of the CCADM using different ambient and chemical conditions in the Rocky Mountains. Although time constraints preclude development of this chemical mechanism for the initial version of the Rocky Mountain model, its development is currently underway and will be incorporated in later versions of the model.

### 3.3.3 Evaluation of the Chemical Mechanisms

The chemical mechanisms used in the MESOPUFF-II and RIVAD models were evaluated by calculating  $\text{SO}_2$  and  $\text{NO}_2$  oxidation rates for a variety of ambient and plume conditions. The evaluation procedure consisted of determining whether the mechanisms calculate reasonable oxidation rates and respond to changes in environmental conditions in a fashion expected by our knowledge of the chemistry of acid deposition. We started with the following baseline conditions:

Ozone concentration = 40 ppb

$\text{NO}_x$  concentration = 1 ppb

$\text{SO}_2$  Concentration = 1 ppb

Relative humidity = 50 %

Temperature = 298 K

Solar declination angle = 25° daytime, 90° nighttime

Each of the important environmental and plume parameters were then varied across a range of values to determine the responses of the two chemical mechanisms.

#### 3.3.3.1 Solar Radiation

Increases in solar radiation cause increases in ozone photolysis and hence increases in the hydroxyl radical and the oxidation of  $\text{SO}_2$  and  $\text{NO}_2$ .

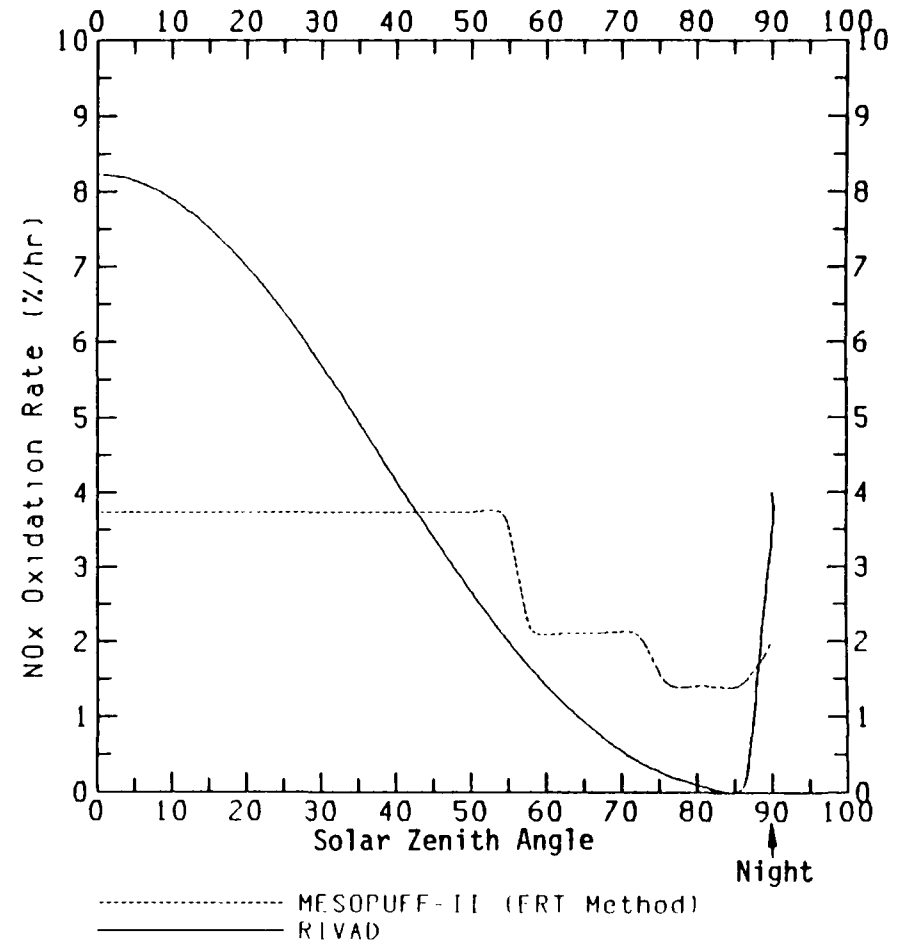
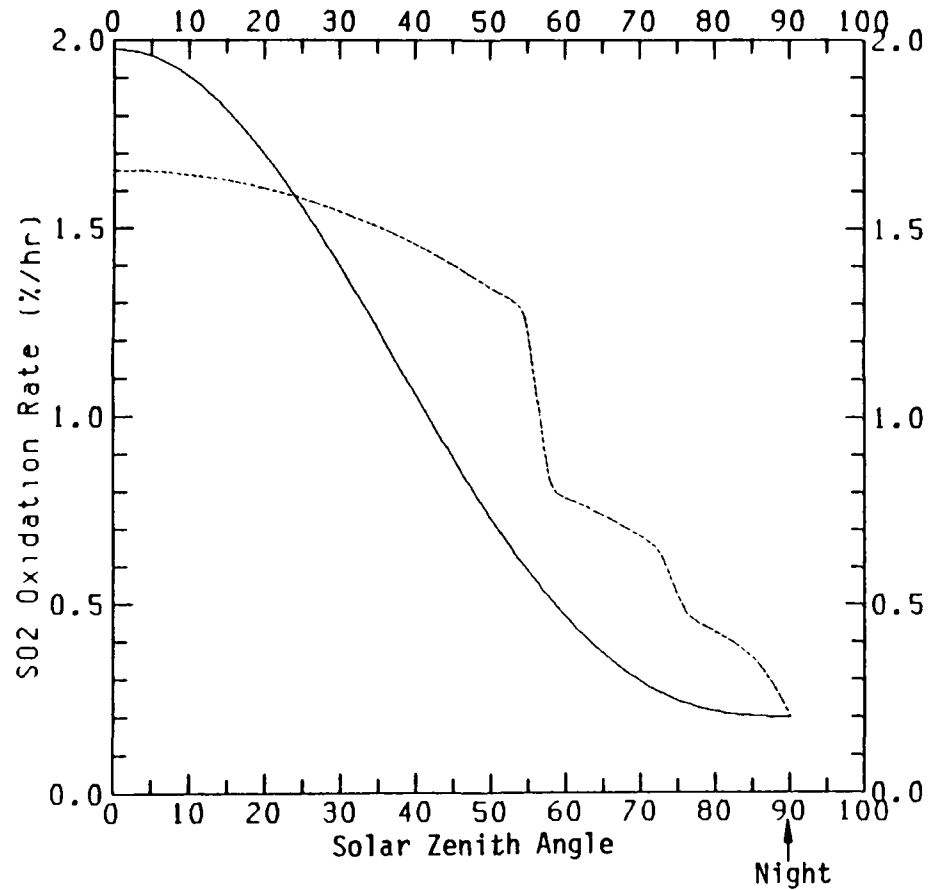
Figure 3-21 shows the oxidation rates produced by the MESOPUFF-II and RIVAD as a function of the solar zenith angle ( $90^\circ$  minus solar zenith angle) for the baseline environmental conditions. Both chemical mechanisms behave similarly in response to changes in solar intensity. The MESOPUFF-II oxidation rates illustrate a steplike response to changes in solar intensity that is a result of using the step function stability in its parameterization of oxidation rates rather a continuous function, such as the  $\text{NO}_2$  photolysis rate or solar elevation. The most important difference between the two mechanisms is that at maximum solar intensity the  $\text{NO}_x$  oxidation rate calculated by MESOPUFF-II peaks at 3.7 %/h whereas the rate calculated by RIVAD peaks at approximately 8.3 %/h. Since  $\text{NO}_x$  oxidation should be approximately seven times that of  $\text{SO}_2$  (which is approximately 1.6 to 2.0 %/h in Figure 3-2), we would expect  $\text{NO}_x$  oxidation rates from the models on the order of 10 %/h, which is about what the RIVAD calculates.

#### 3.3.3.2 Temperature

Figures 3-22 and 3-23 show the sensitivity of the chemical mechanisms to temperature variations for daytime and nighttime conditions respectively. The RIVAD chemical mechanism is highly sensitive to variations in temperature, while the MESOPUFF-II algorithm does not respond at all to temperature variations. At low temperatures the OH concentrations drop partly because several species, such as PAN, become strong sinks for OH under low temperatures. At night, under the ambient conditions shown in Figure 3-23, the  $\text{SO}_2$  oxidation rate for both the MESOPUFF-II and RIVAD mechanisms is at the minimum rate defined by the 0.2 %/h heterogeneous minimum value. The RIVAD  $\text{NO}_x$  oxidation rate at night is also sensitive to the ambient temperature; however, this is driven by the temperature-sensitive  $\text{NO}_2$ ,  $\text{N}_2\text{O}_5$ ,  $\text{NO}_3$ ,  $\text{HNO}_3$  equilibrium rather than the hydroxyl radical, which is zero at night. The temperature dependence of these oxidation rates could be an important advantage for an acid deposition model for the Rocky Mountains because the high terrain produces low temperatures even in the presence of sunlight.

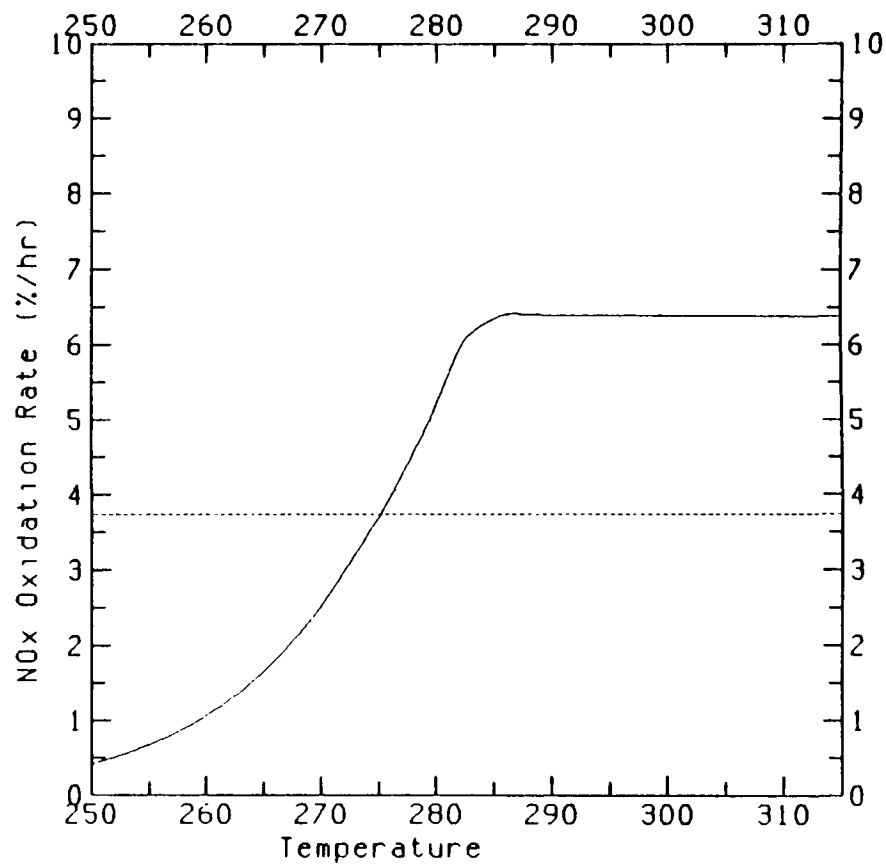
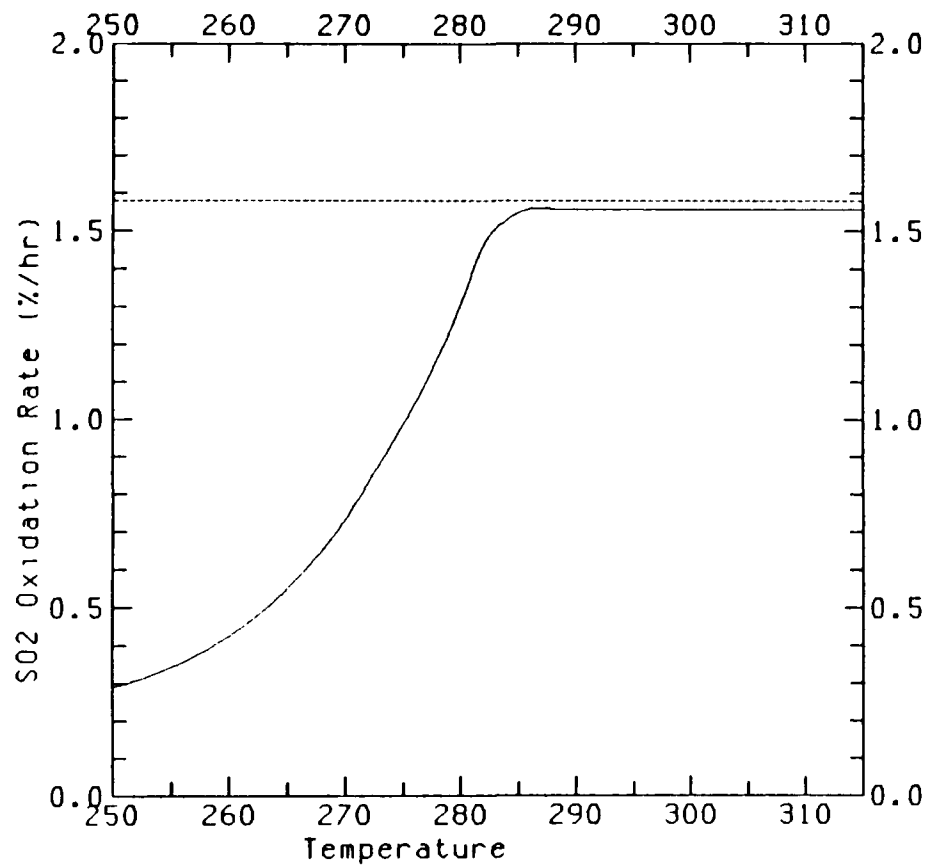
#### 3.3.3.3 Relative Humidity

The effect of relative humidity on the two chemical mechanisms for daytime and nighttime conditions are shown in Figures 3-24 and 3-25 respectively. It is interesting to note that although the MESOPUFF-II and RIVAD predict similar daytime  $\text{SO}_2$  oxidation rates for the range of relative humidity between 25 and 50 percent, they deviate from each other on the two extreme ranges of relative humidity. Under the daytime environmental conditions used in these tests, the RIVAD estimation of the  $\text{OH}_+$  concentration reaches the maximum allowable value at a relative humidity of about



Ozone = 39 (ppb)  
 NO<sub>x</sub> = 1 (ppb)  
 SO<sub>2</sub> = 1 (ppb)  
 Relative Humidity = 50 (%)  
 Temperature = 298 (K)

FIGURE 3-21. Sensitivity of the MESOPUFF-II and RIVAD chemical mechanisms to solar intensity.



----- MESOPUFF-II (ERT Method)  
 \_\_\_\_\_ RIVAD

Ozone = 39 (ppb)

NO<sub>x</sub> = 1 (ppb)

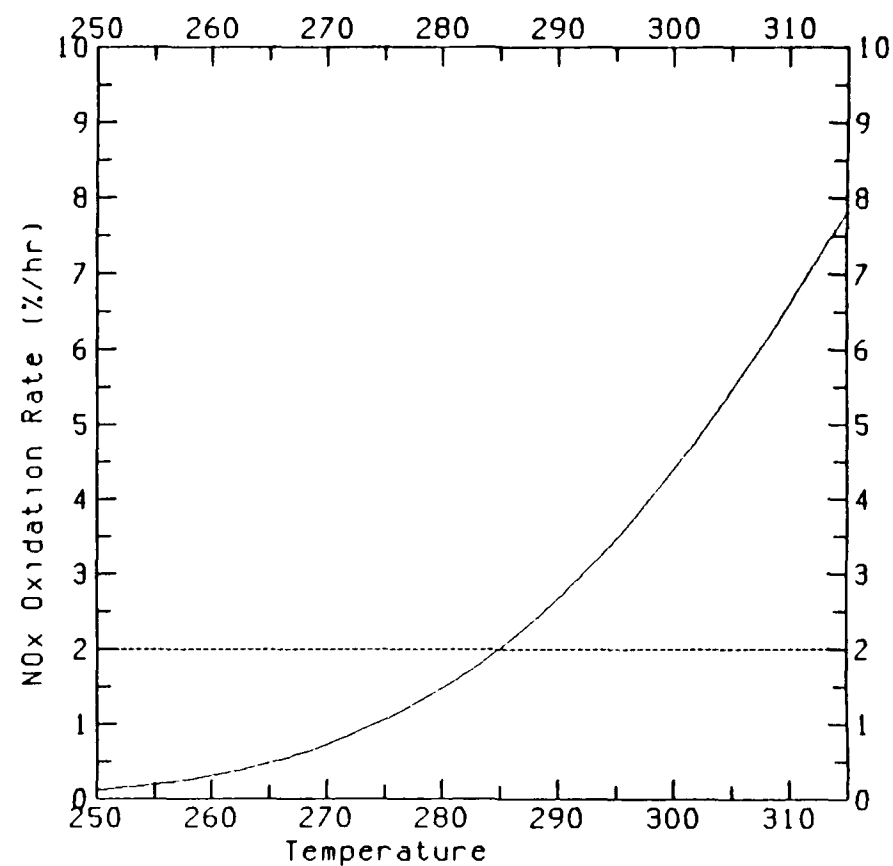
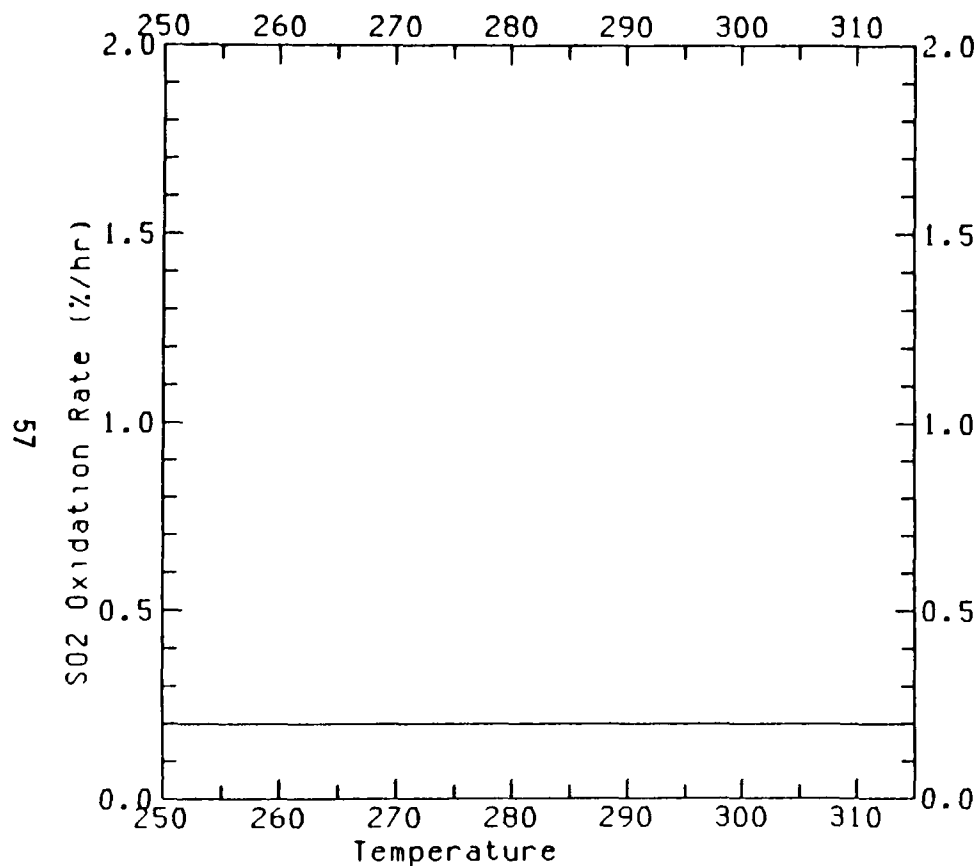
SO<sub>2</sub> = 1 (ppb)

Relative Humidity = 50 (%)

Solar Zenith Angle = 25 (deg.)

NO<sub>2</sub> Photolysis = 0.505

FIGURE 3-22. Sensitivity of the daytime MESOPUFF-II and RIVAD chemical mechanisms to temperature.



----- MESOPUFF-II (ERT Method)  
 ————— RIVAD

Ozone = 39 (ppb)

NO<sub>x</sub> = 1 (ppb)

SO<sub>2</sub> = 1 (ppb)

Relative Humidity = 50 (%)

Solar Zenith Angle = 90 (deg.)

Nuc. Photolysis = 0.028

FIGURE 3-23. Sensitivity of the nighttime MESOPUFF-II and RIVAD chemical mechanisms to temperature.

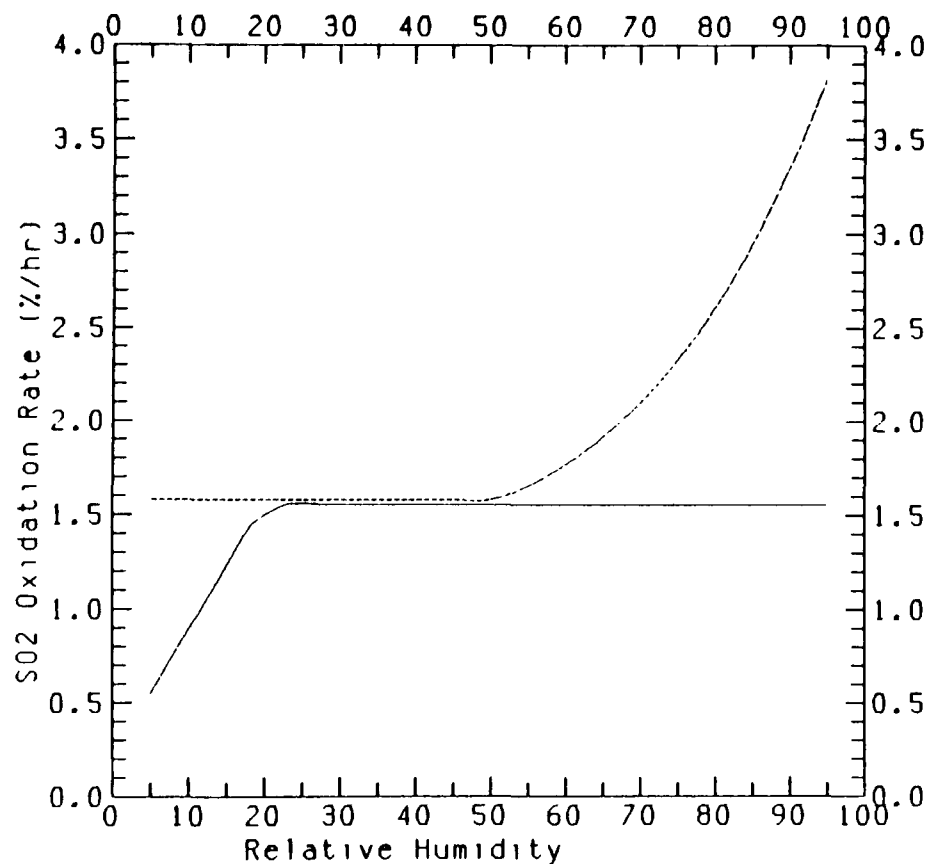
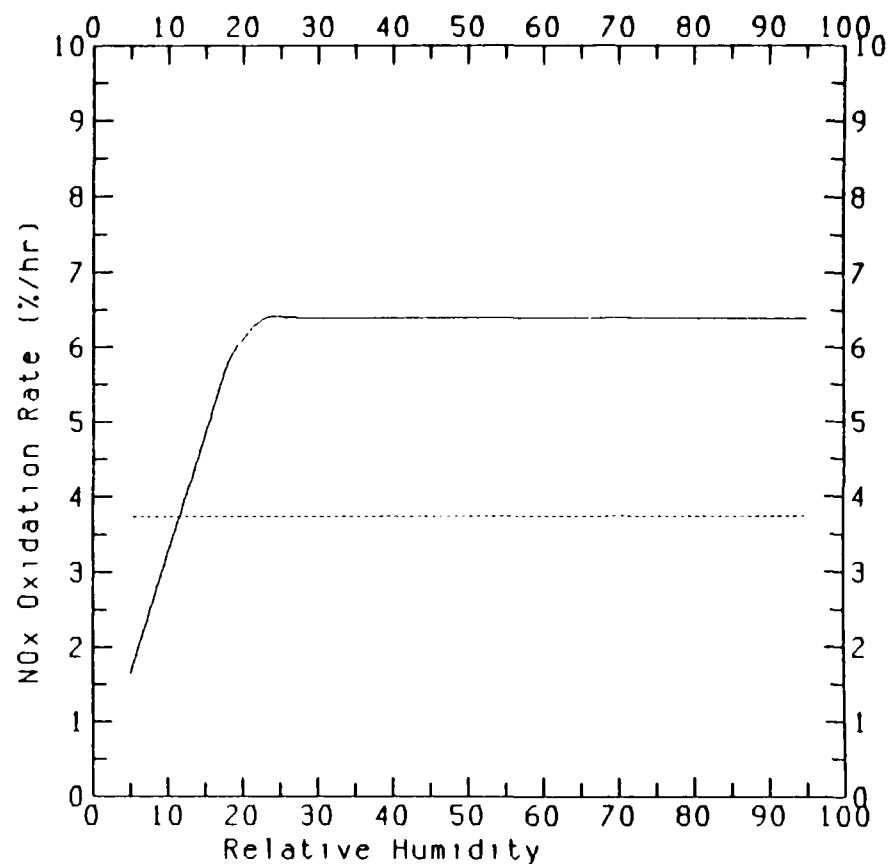


FIGURE 3-24. Sensitivity of the daytime MESOPUFF-II and RIVAD chemical mechanisms to relative humidity.



----- MESOPUFF-II (ERT Method)  
 \_\_\_\_\_ RIVAD

Ozone = 39 (ppb)  
 NOx = 1 (ppb)  
 SO2 = 1 (ppb)  
 Solar Zenith Angle = 25 (deg.)  
 NO2 Photolysis = 0.505  
 Temperature = 298 (K)



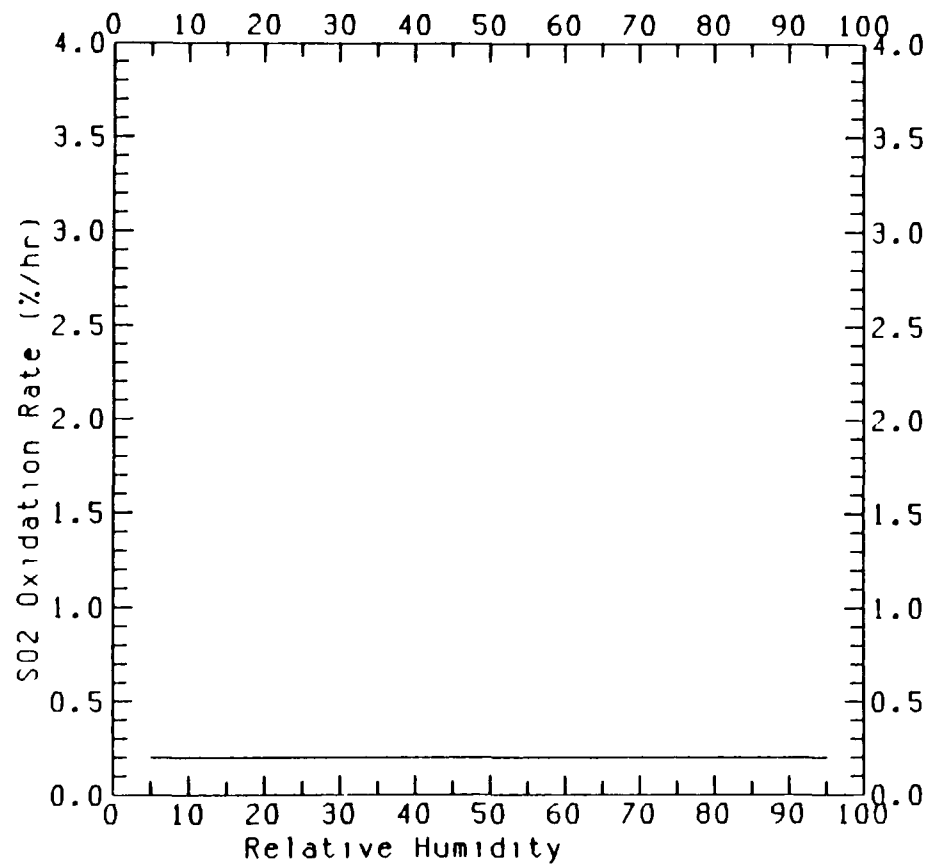
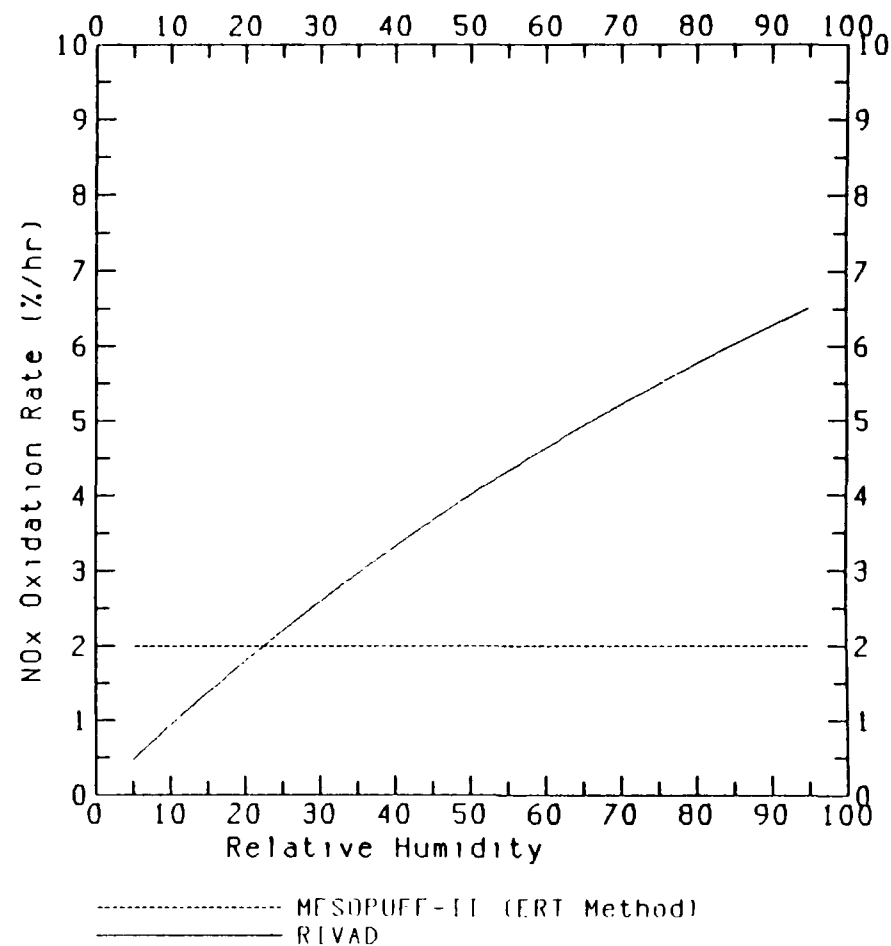


FIGURE 3-25. Sensitivity of the nighttime MESOPUFF-II and RIVAD chemical mechanisms to relative humidity.



Ozone = 39 (ppb)  
 NO<sub>x</sub> = 1 (ppb)  
 SO<sub>2</sub> = 1 (ppb)  
 Solar Zenith Angle = 90 (deg.)  
 NO<sub>2</sub> Photolysis = 0.000  
 Temperature = 298 (K)

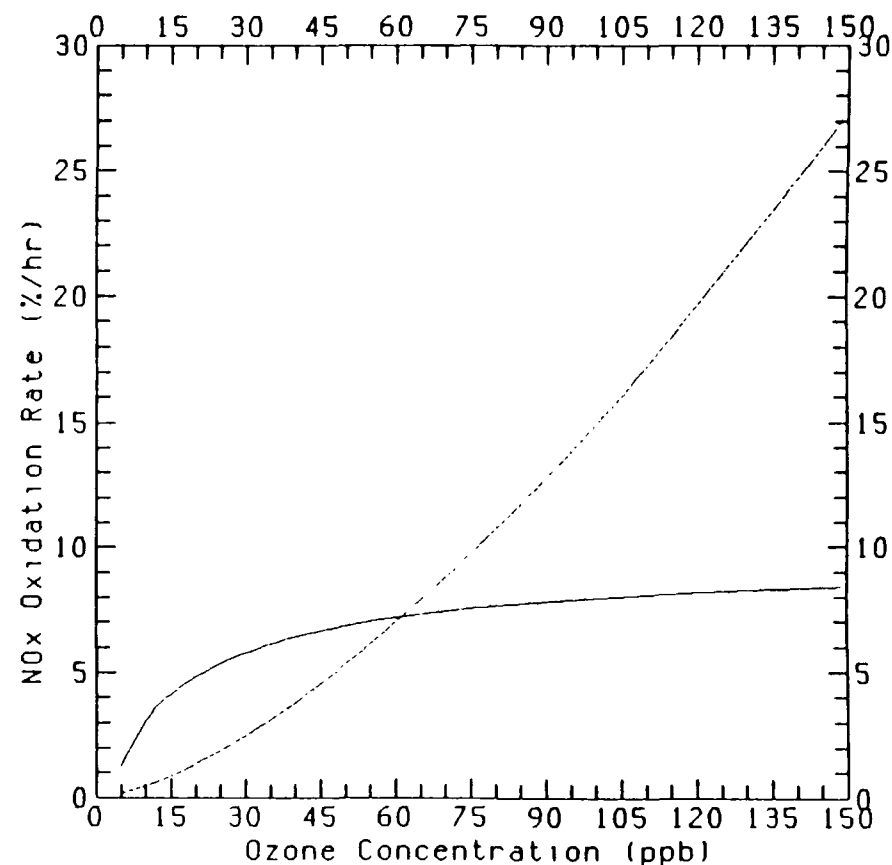
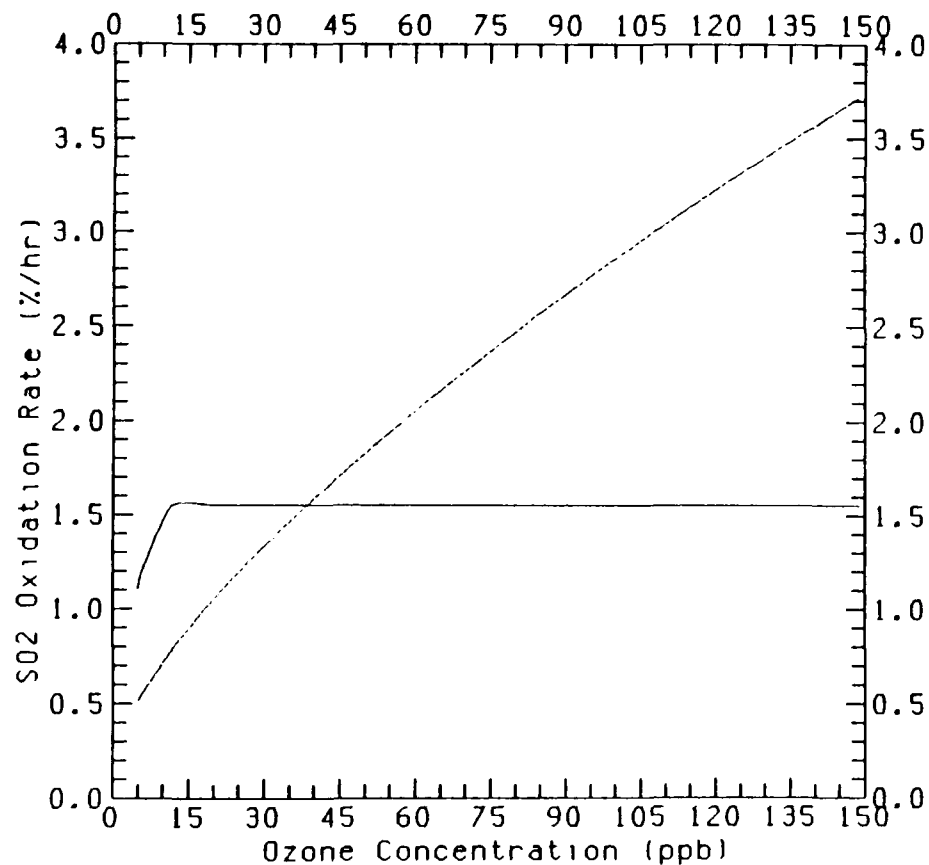
25 percent, which causes both the  $\text{SO}_2$  and  $\text{NO}_x$  oxidation rates to flatten out for relative humidities greater than 25 percent. On the other hand, the MESOPUFF-II  $\text{SO}_2$  oxidation rate starts increasing for relative humidities greater than about 50 percent. This is due to the parameterization of the heterogeneous oxidation of  $\text{SO}_2$  based on relative humidity,  $\text{RH}$  ( $3 \times 10^{-8} \text{ RH}$ ), which is a surrogate for the aqueous oxidation of  $\text{SO}_2$ . The reasoning behind this heterogeneous parameterization is unclear and no explanation is offered by the model developers in the documentation of the model (Scire et al., 1983). The aqueous-phase oxidation of  $\text{SO}_2$  should depend mainly on the liquid water content, hydrogen peroxide concentration, and solar intensity, not the water vapor concentration (relative humidity).

At night, for the environmental conditions used in these tests, both the MESOPUFF-II and RIVAD produce their minimal allowable  $\text{SO}_2$  oxidation rates of 0.2 %/h. For  $\text{NO}_x$  oxidation at night the MESOPUFF-II calculates its minimal allowable value of 2 %/h, while the RIVAD model shows some sensitivity to relative humidity because of the influence of water vapor in the  $\text{NO}_2$ ,  $\text{NO}_3$ ,  $\text{N}_2\text{O}_5$  equilibrium calculation.

#### 3.3.3.4 Ozone Concentrations

Both the MESOPUFF-II and RIVAD require estimates of the background ozone concentrations in order to estimate their oxidation rates. Figures 3-26 and 3-27 illustrate the sensitivity of the two mechanisms to ozone concentrations for day and night conditions. During the day the MESOPUFF-II  $\text{SO}_2$  and  $\text{NO}_x$  oxidation rates are very sensitive to the specification of the background ozone concentrations. For the environmental conditions used in these tests, the RIVAD calculated the maximum value for  $\text{OH}\cdot$  at a low ozone concentration; hence its  $\text{SO}_2$  oxidation rate is not very sensitive to background ozone. The RIVAD daytime  $\text{NO}_2$  oxidation rate shows a curiously weak dependency on the ozone concentration that cannot come from the reaction with  $\text{OH}\cdot$ , which has been set to the maximum allowable value for ozone greater than about 15 ppb. As it turns out, this increase in  $\text{NO}_x$  oxidation rate with increasing ozone concentration is a result of the photostationary state relationship of  $\text{NO}$ ,  $\text{NO}_2$ , and  $\text{O}_3$  used in the RIVAD. Since it is  $\text{NO}_2$  and not  $\text{NO}$  that converts to nitrates and nitric acid, the RIVAD model apportions the  $\text{NO}_x$  concentration to  $\text{NO}$  and  $\text{NO}_2$ , using the  $\text{NO}_2$  photolysis rate value and the background ozone concentration, and then calculates the amount of nitrate and nitric acid formed based on the  $\text{NO}_2$  concentration. Thus this weak dependency of the daytime  $\text{NO}_x$  oxidation rate on ozone in the RIVAD mechanism is actually the result of more of the  $\text{NO}_x$  being apportioned into  $\text{NO}_2$  as the ozone increases.

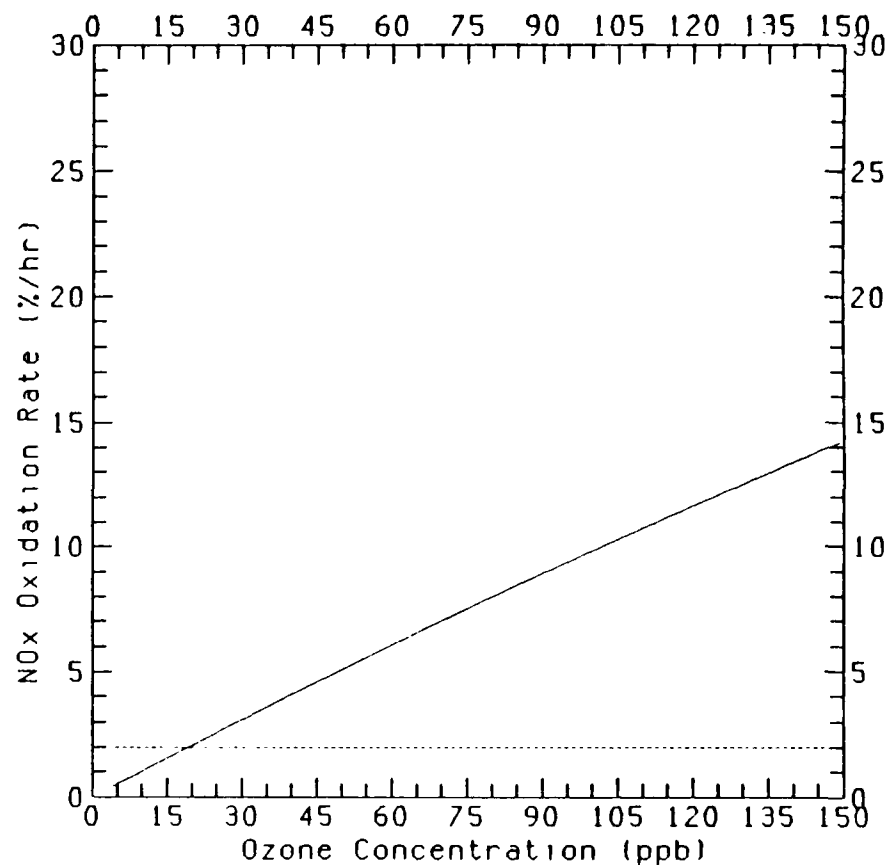
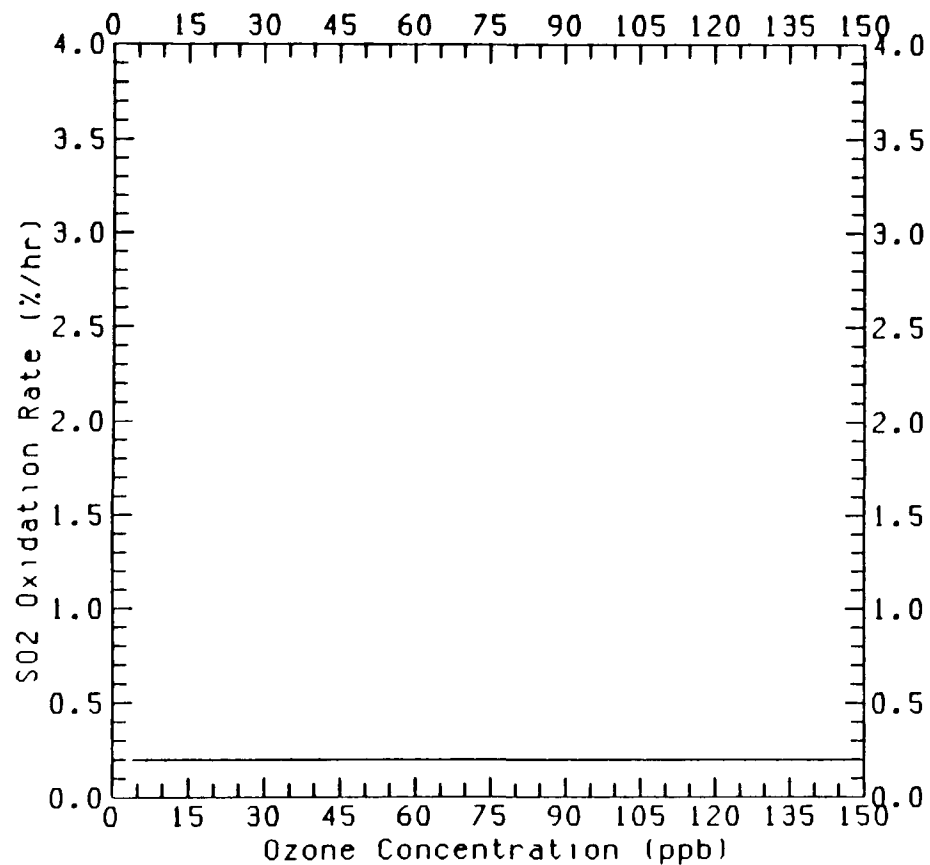
At night the MESOPUFF-II predicts its nighttime minimum  $\text{SO}_2$  and  $\text{NO}_x$  oxidation rates of 0.2 and 2.0 %/h. In the RIVAD the  $\text{SO}_2$  oxidation rate at



----- MESOPUFF-II (ERT Method)  
 \_\_\_\_\_ RIVAD

NOx = 1 (ppb)  
 SO2 = 1 (ppb)  
 Relative Humidity = 50 (%)  
 Solar Zenith Angle = 25 (deg.)  
 NO<sub>2</sub> Photolysis = 0.505  
 Temperature = 298 (K)

FIGURE 3-26. Sensitivity of the daytime MESOPUFF-II and RIVAD chemical mechanisms to ozone concentration.



----- MESOPUFF-II (ERT Method)  
 ————— RIVAD

NO<sub>x</sub> = 1 (ppb)  
 SO<sub>2</sub> = 1 (ppb)  
 Relative Humidity = 50 (%)  
 Solar Zenith Angle = 90 (deg.)  
 NO<sub>2</sub> Photolysis = 0.000  
 Temperature = 298 (K)

FIGURE 3-27. Sensitivity of the nighttime MESOPUFF-II and RIVAD chemical mechanisms to ozone concentration.

night is also 0.2 %/h regardless of the ozone concentration, while the  $\text{NO}_x$  oxidation rate increases with background ozone concentration because of the effect of ozone on the  $\text{NO}_2$ ,  $\text{NO}_3$ , and  $\text{N}_2\text{O}_5$  equilibrium calculation.

### 3.3.3.5 Nitrogen Oxide Concentration

The sensitivity of the oxidation rates to  $\text{NO}_x$  concentrations are shown in Figures 3-28 and 3-29 for daytime and nighttime conditions respectively. Daytime  $\text{NO}_x$  oxidation rates calculated by the MESOPUFF-II and RIVAD models exhibit similar responses to increases in  $\text{NO}_x$  concentration. However, the MESOPUFF-II daytime  $\text{SO}_2$  oxidation rate appears totally insensitive to changes in  $\text{NO}_x$  concentrations. Since the oxidation of  $\text{SO}_2$  and  $\text{NO}_x$  during the day revolves around competition for the hydroxyl radical, this lack of sensitivity is somewhat disturbing. Thus in a plume containing both  $\text{SO}_x$  and  $\text{NO}_x$ , as produced by a shale oil plant, the MESOPUFF-II will greatly overpredict the oxidation of  $\text{SO}_2$  because it does not account for the competition for the hydroxyl radical from the  $\text{NO}_2$  reaction.

In both MESOPUFF-II and RIVAD the  $\text{SO}_2$  oxidation rate at night is insensitive to changes in  $\text{NO}_x$  concentrations and is at its minimum value of 0.2 %/h. Similarly, the MESOPUFF-II produces its minimum 2 %/h  $\text{NO}_x$  oxidation rate during the night regardless of  $\text{NO}_x$  concentration. The RIVAD model, however, produces a peak nighttime  $\text{NO}_x$  oxidation rate at a  $\text{NO}_x$  concentration of 20 ppb, with the rate reducing to zero for a  $\text{NO}_x$  concentration of 40 ppb. This is because, for high  $\text{NO}_x$  concentrations, the RIVAD assumes all the  $\text{NO}_x$  is  $\text{NO}$ . Thus at night, when the  $\text{NO}_x$  concentration exceeds the ozone concentration, all of the ozone is titrated out, resulting in no more ozone to oxidize the  $\text{NO}_2$ .

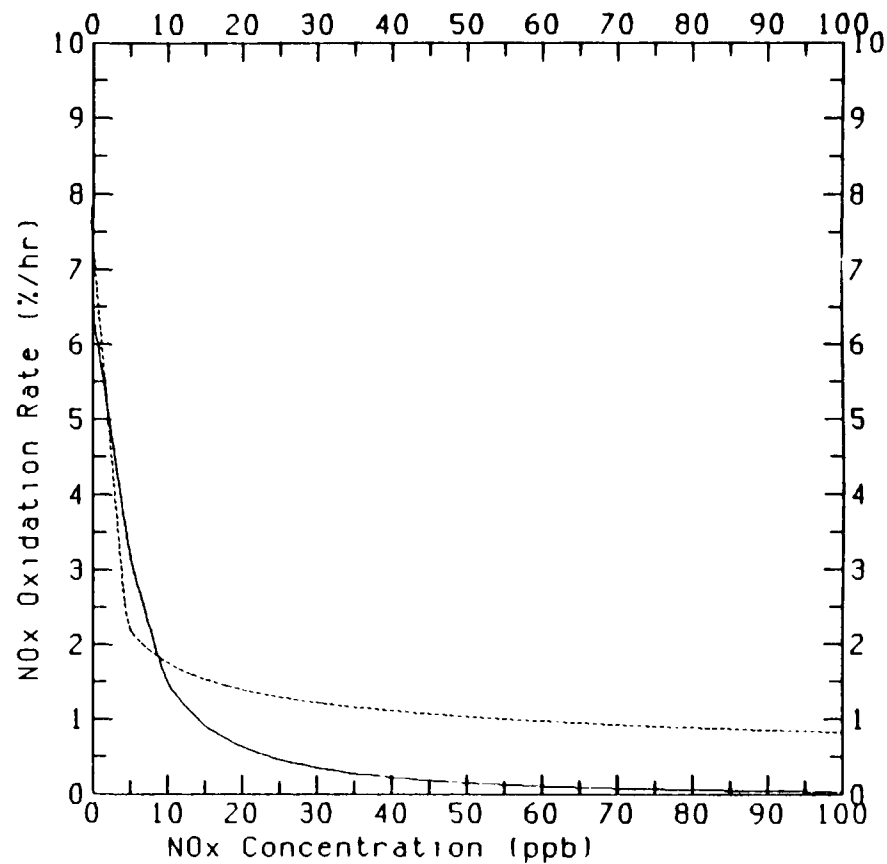
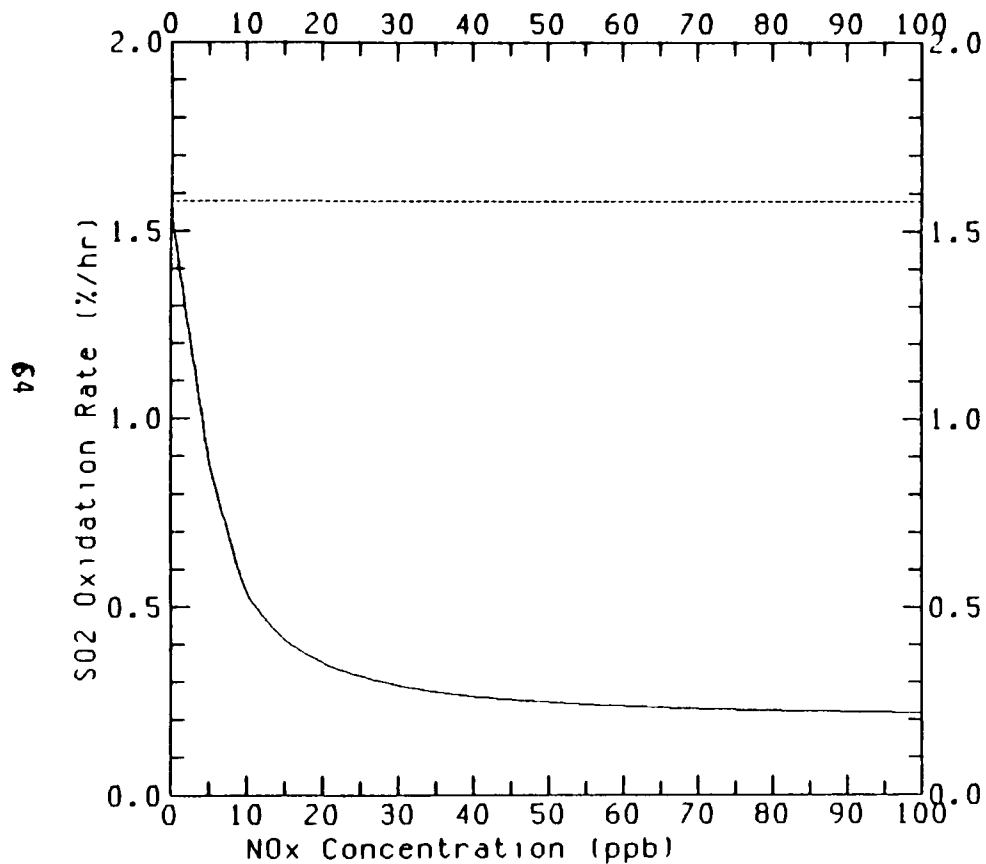
### 3.3.3.6 Sulfur Dioxide Concentration

The effects of changes in  $\text{SO}_2$  concentrations on the  $\text{SO}_2$  and  $\text{NO}_x$  oxidation rates calculated by MESOPUFF-II and RIVAD are given in Figures 3-30 and 3-31. The MESOPUFF-II chemistry is totally insensitive to changes in  $\text{SO}_2$  concentrations both during the day and night. The RIVAD mechanism is insensitive to changes in  $\text{SO}_2$  concentration at night; however, during the day both the  $\text{SO}_2$  and  $\text{NO}_x$  oxidation rates decrease as  $\text{SO}_2$  concentrations increase. This is because of the limited availability of the hydroxyl radical, which dominates the daytime oxidation of both  $\text{SO}_2$  and  $\text{NO}_x$ .

### 3.3.4 Remarks

#### 3.3.4.1 Daytime Chemistry

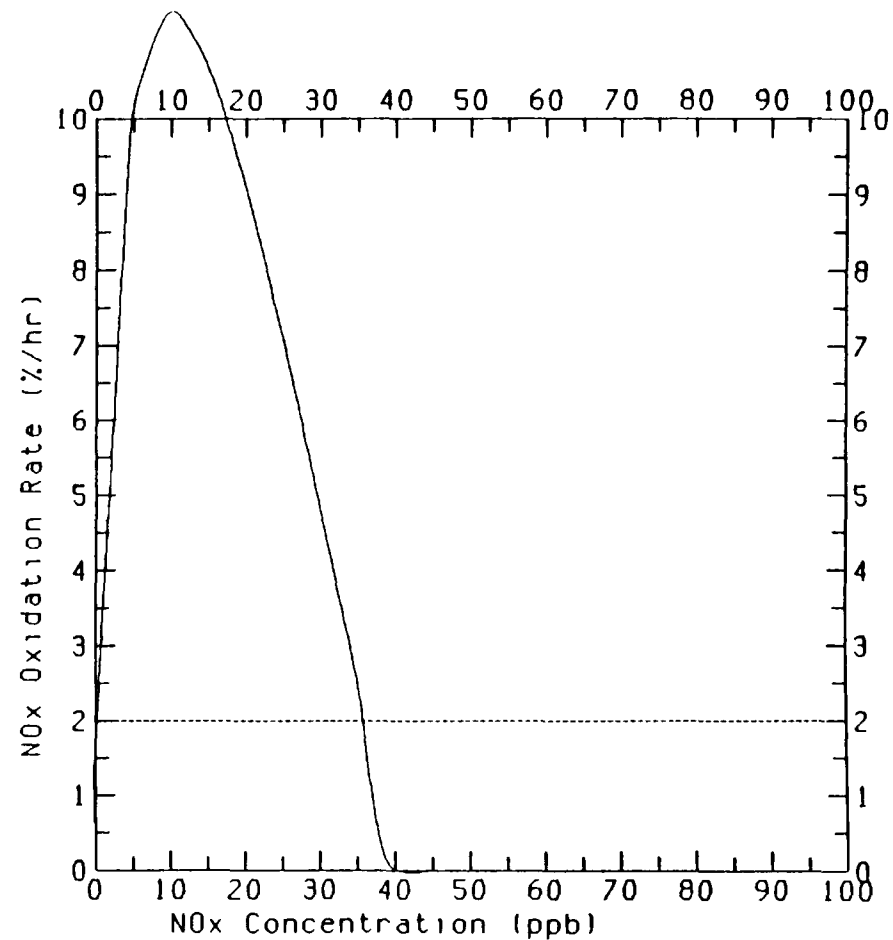
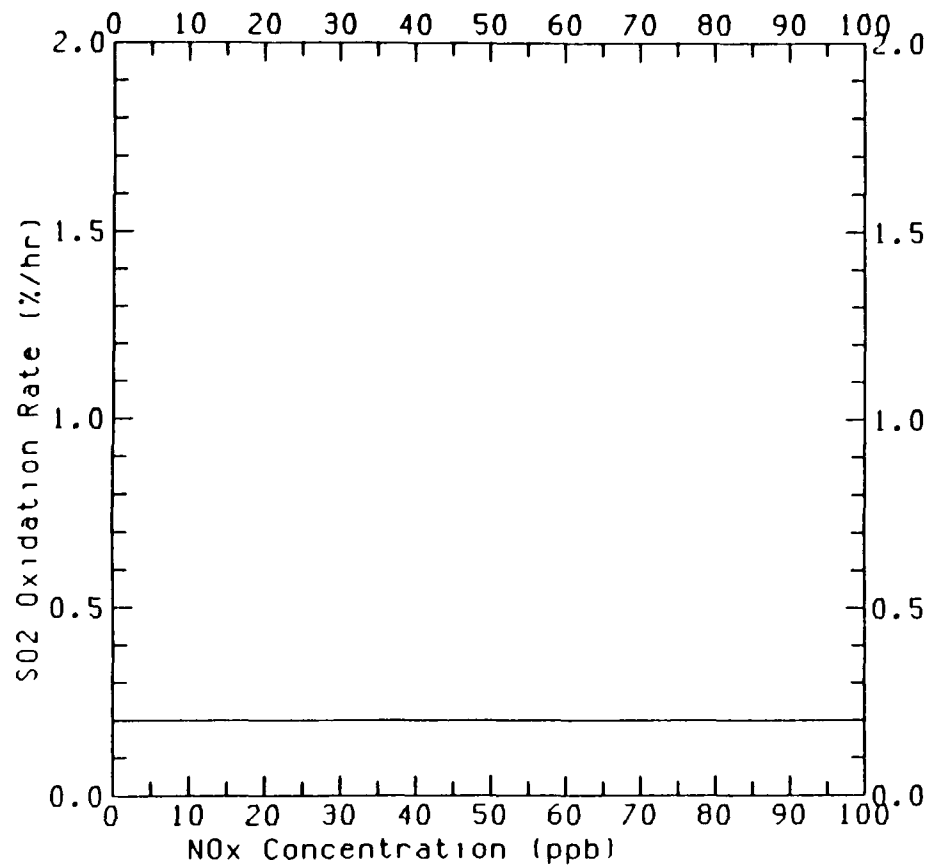
The MESOPUFF-II daytime oxidation rates appear to be most sensitive to changes in solar intensity and background ozone concentrations, while the



----- MESOPUFF-II (ERT Method)  
 ————— RIVAD

Ozone = 40 (ppb)  
 SO<sub>2</sub> = 1 (ppb)  
 Relative Humidity = 50 (%)  
 Solar Zenith Angle = 25 (deg.)  
 NO<sub>2</sub> Photolysis = 0.505  
 Temperature = 298 (K)

FIGURE 3-28. Sensitivity of the daytime MESOPUFF-II and RIVAD chemical mechanisms to NO<sub>x</sub> concentration.



----- MESOPUFF II (ERT Method)  
 ————— RIVAD

Ozone = 40 (ppb)  
 SO<sub>2</sub> = 1 (ppb)  
 Relative Humidity = 50 (%)  
 Solar Zenith Angle = 90 (deg.)  
 NO<sub>2</sub> Photolysis = 0.000  
 Temperature = 298 (K)

FIGURE 3-29. Sensitivity of the nighttime MESOPUFF-II and RIVAD chemical mechanisms to NO<sub>x</sub> concentration.

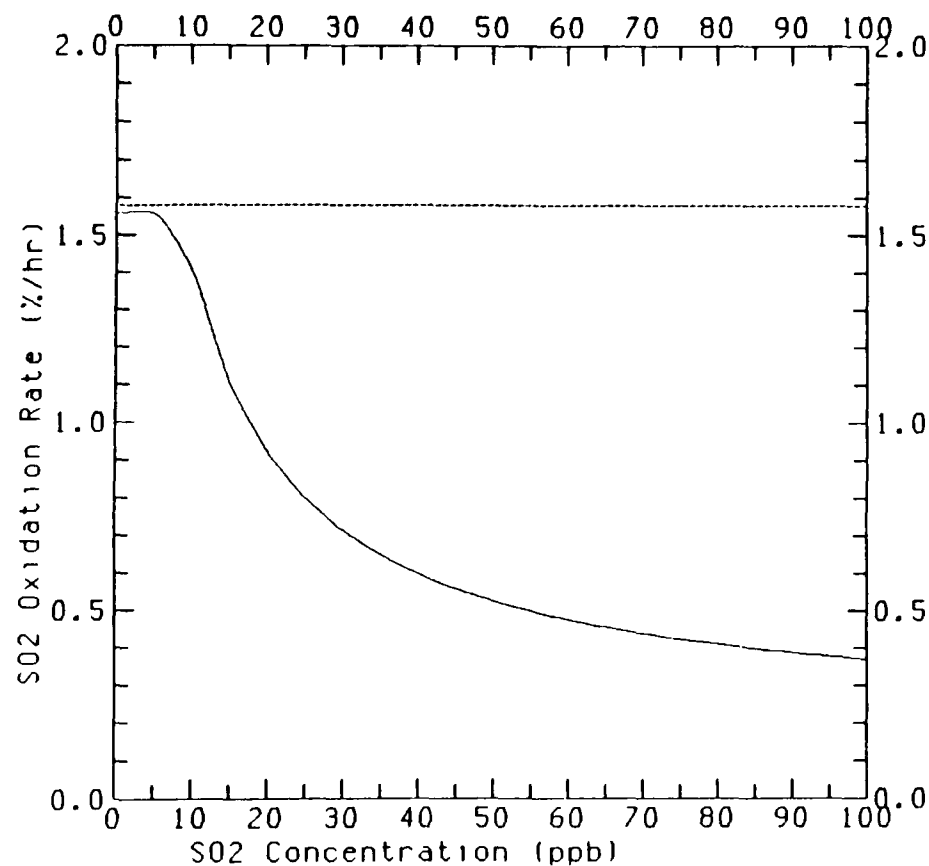
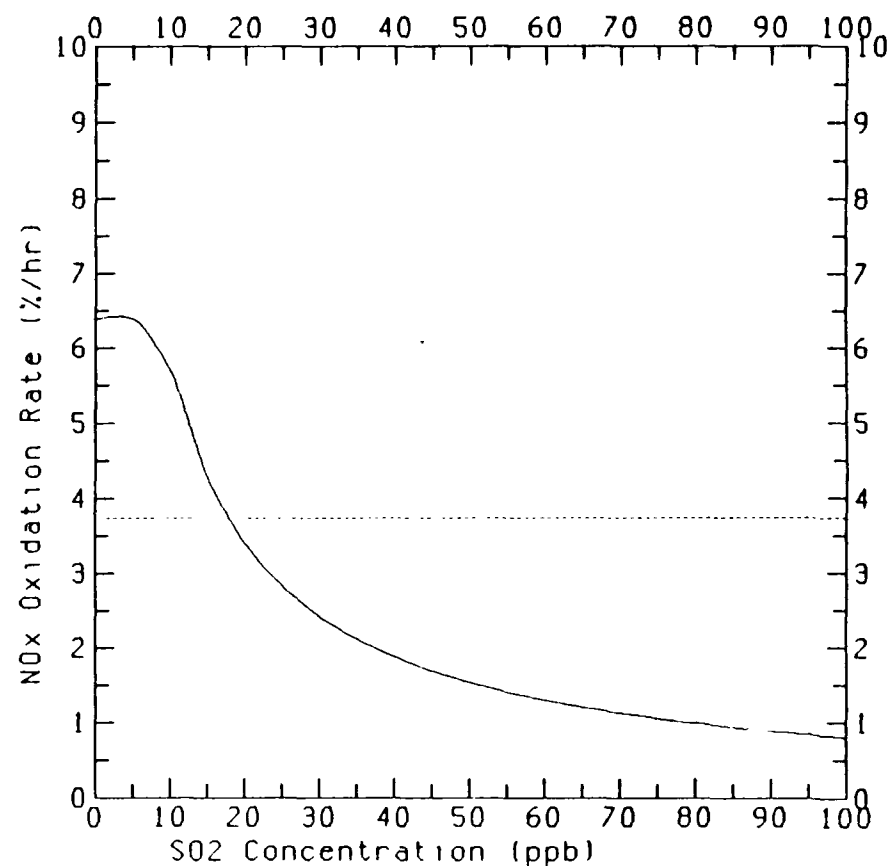


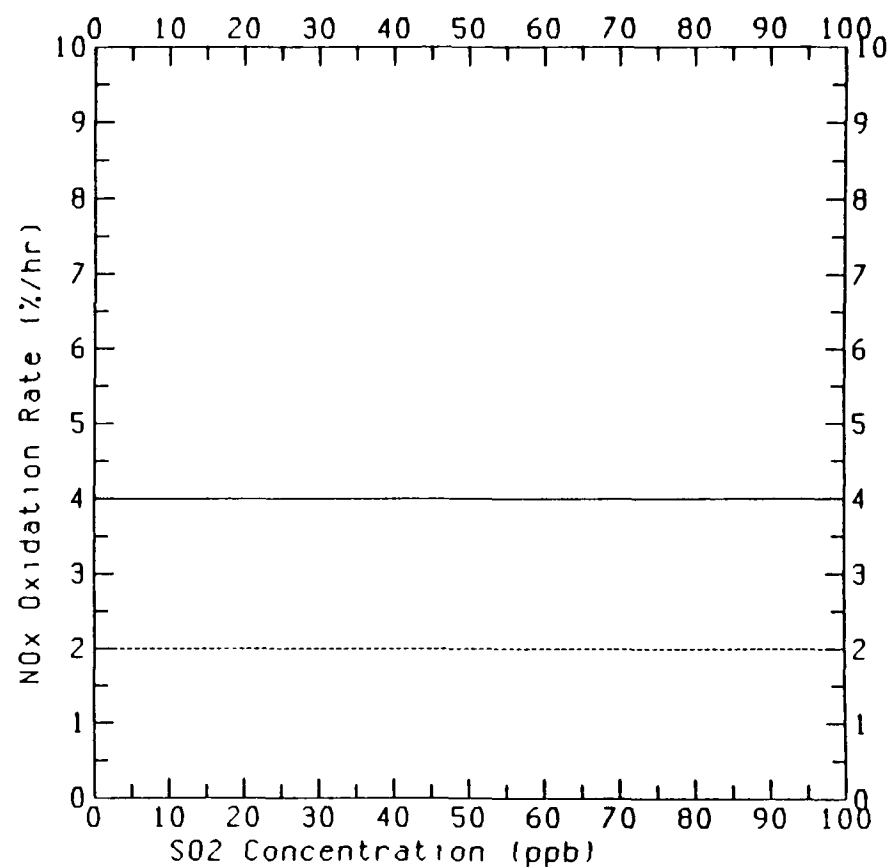
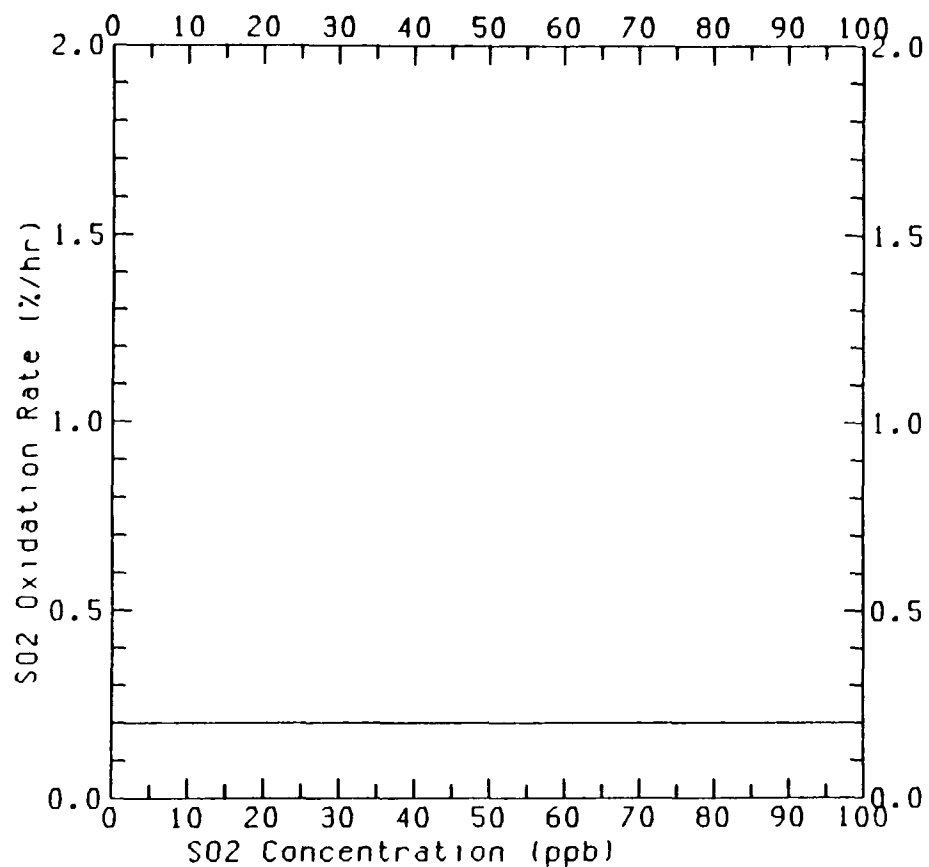
FIGURE 3-30. Sensitivity of the daytime MESOPUFF-II and RIVAD chemical mechanisms to SO<sub>2</sub> concentration.



----- MESOPUFF-II (ERT Method)  
 \_\_\_\_\_ RIVAD

Ozone = 39 (ppb)  
 NO<sub>x</sub> = 1 (ppb)  
 Relative Humidity = 50 (%)  
 Solar Zenith Angle = 25 (deg.)  
 NO<sub>2</sub> Photolysis = 0.505  
 Temperature = 298 (K)





----- MESOPUFF-II (ERT Method)  
 ——— RIVAD

FIGURE 3-31. Sensitivity of the nighttime MESOPUFF-II and RIVAD chemical mechanisms to SO<sub>2</sub> concentration.

Ozone = 39 (ppb)  
 NO<sub>x</sub> = 1 (ppb)  
 Relative Humidity = 50 (%)  
 Solar Zenith Angle = 90 (deg.)  
 NO<sub>2</sub> Photolysis = 0.028  
 Temperature = 298 (K)

RIVAD mechanism is less sensitive to changes in ozone concentrations during the day, at least for the environmental conditions used in these tests. However, the RIVAD chemistry is more sensitive to changes in temperature and  $\text{NO}_x$  and  $\text{SO}_2$  concentrations, and is also very sensitive to solar intensity. Of particular note is the ability of the RIVAD to correctly simulate the competition between  $\text{SO}_2$  and  $\text{NO}_x$  for the hydroxyl radical, which drives the daytime gas-phase oxidation of these species. Since the MESOPUFF-II shows no sensitivity to changes in  $\text{SO}_2$  concentrations, and no sensitivity in its  $\text{SO}_2$  oxidation rate to changes in  $\text{NO}_x$  concentrations, it will overpredict the oxidation rates of these species for plumes near the source.

#### 3.3.4.2 Nighttime Chemistry

The MESOPUFF-II produces constant  $\text{SO}_2$  and  $\text{NO}_x$  oxidation rates of 0.2 %/h and 2.0 %/h respectively. The RIVAD model also produces a constant 0.2 %/h  $\text{SO}_2$  oxidation rate at night regardless of the environmental conditions. However, the oxidation rate of  $\text{NO}_x$  is sensitive to changes in all environmental conditions examined except changes in  $\text{SO}_2$  concentrations. This is due to the influences of ozone, temperature, and water vapor on the  $\text{NO}_2$ ,  $\text{N}_2\text{O}_5$ ,  $\text{NO}_3$ , and  $\text{HNO}_3$  equilibrium.

#### 3.3.4.3 Aqueous Chemistry

Neither the MESOPUFF-II or the RIVAD chemical mechanisms contain explicit treatment of aqueous chemistry. Both contain surrogate heterogeneous  $\text{SO}_2$  oxidation rates with a minimum value of 0.2 %/h. The MESOPUFF-II ties this heterogeneous oxidation rate to relative humidity during daytime. However, as noted above, aqueous-phase chemistry should be tied to liquid water content, not water vapor concentrations; thus this parameterization of surrogate aqueous-phase chemistry appears to be unjustified by current knowledge.

#### 3.3.4.4 Conclusions

For the initial version of the Rocky Mountain acid deposition model (described in Section 5) both the MESOPUFF-II and RIVAD chemical mechanisms will be included as optional treatments of chemical transformation. Based on the evaluation of the two chemical mechanisms, the RIVAD parameterization is preferred over the MESOPUFF-II for the following reasons.

The RIVAD mechanism treats the competition between the  $\text{SO}_2$  and  $\text{NO}_x$  species for the hydroxyl radical during the day.

The oxidation rates produced by the RIVAD show sensitivity to changes in temperature, which can be important in the high terrain of the Rocky Mountain region.

The RIVAD model treats the sensitivity of  $\text{NO}_x$  oxidation to changes in conditions at night, whereas the MESOPUFF-II uses constant values regardless of the conditions.

The individual species of  $\text{NO}$  and  $\text{NO}_2$  are treated separately by the RIVAD model, while the MESOPUFF-II lumps  $\text{NO}$  and  $\text{NO}_2$  together as  $\text{NO}_x$ . Since  $\text{NO}_2$  is a criteria pollutant with an annual NAAQS, and several western states and counties have their own standards--e.g., New Mexico has a 24-hour  $\text{NO}_2$  standard, California has an hourly  $\text{NO}_2$  standard, and Santa Barbara County has an hourly incremental  $\text{NO}_2$  standard)--the distinction between  $\text{NO}$  and  $\text{NO}_2$  is important from a regulatory perspective.

### 3.4 DRY DEPOSITION

Two of the candidate models, the MESOPUFF-II and the CCADM, use the more technically rigorous resistance approach for the parameterization of dry deposition. The RIVAD uses the dry deposition velocity concept, while the POLUT does not consider pollutant loss from dry deposition.

The flux of pollutants to the ground due to dry deposition can be expressed as:

$$F_d = V_d c \quad (3-9)$$

where  $V_d$  is the deposition velocity, and  $c$  is concentration at some reference height. In the RIVAD the deposition velocity is a function of land-use type and is set to zero at night to account for the shielding effect of the stable nocturnal boundary layer. During the day, however, the deposition velocity is applied to the mixed-layer concentration, effectively enhancing the rate of vertical diffusion of pollutants because mass removed at the surface is immediately replaced with material from above.

In the resistance approach to dry deposition, the deposition velocity is expressed as the inverse sum of the atmosphere, surface, and canopy resistances:

$$V_d = (r_a + r_s + r_c) \quad (3-10)$$

In the MESOPUFF-II an option exists to treat vertically well-mixed puffs with a three-layer model. This parameterization essentially removes the enhanced rate of vertical diffusion by considering the loss of pollutants only out of the surface layer.

The CCADM uses the dry deposition algorithm in the NCAR/RADM for gaseous species (Walcek et al., 1986) and the algorithm in the ERT/ADOM for particulate species (Pleim, Venkatram, and Yamertino, 1984). It also uses a surface layer for calculating atmospheric resistance to minimize the exaggeration of depletion by instantaneous vertical mixing. The parameterizations of dry deposition used by the MESOPUFF-II and the CCADM are compared below.

### 3.4.1 MESOPUFF-II and CCADM Parameterizations

In the MESOPUFF-II the atmospheric (aerodynamic) resistance,  $r_a$ , is given by the following formula proposed by Wesley and Hicks (1977):

$$r_a = (ku_\star)^{-1} [\ln(z_r/z_0) - \psi_H] \quad (3-11)$$

The stability-dependent function  $\psi_H$  is given by:

$$\begin{aligned} \psi_H &= -5 z_r/L, & 0 < z_r/L < 1 \text{ (stable)} \\ &= \exp\{0.509 + 0.39 \ln(-z_s/L) - 0.090[\ln(-z_r/L)]^2\} & -1 < z_r/L < 0 \text{ (unstable)} \\ &= 0 & z_r/L = 0 \text{ (neutral)} \end{aligned} \quad (3-12)$$

where:

- $z_r$  = the reference height (10 m)
- $z_0$  = the surface roughness (m)
- $u_\star$  = the friction velocity (m/s)
- $K$  = the von Karman constant
- $L$  = the Monin-Obukhov length (m)

In the CCADM the surface resistance is given by the following equations (Businger, 1973):

$$\begin{aligned}
r_a &= \frac{1}{ku_*} \left\{ \ln \left[ \frac{1 - \phi_h(z_h/L)}{1 + \phi_h(z_h/L)} \right] - \ln \left[ \frac{1 - \phi_h(z_0/L)}{1 + \phi_h(z_0/L)} \right] \right. \\
&\quad \left. + 2 \left[ \tan^{-1} \left( \frac{1}{\phi_h(z_h/L)} \right) - \tan^{-1} \left( \frac{1}{\phi_h(z_0/L)} \right) \right] \right\} \quad \text{for } \zeta < 0 \text{ (unstable)} \\
r_a &= \frac{1}{ku_*} \ln \left[ (z_h/L) + 4.7 \frac{(z_h - z_0)}{L} \right] \quad \text{for } \zeta > 0 \text{ (stable)} \\
r_a &= \frac{1}{ku_*} \ln(z_h/z_0) \quad \text{for } \zeta = 0 \text{ (neutral)}
\end{aligned} \tag{3-13}$$

$$\begin{aligned}
\phi_h(\zeta) &= 0.74 \cdot (1 - 9\zeta)^{-1/2} \quad \text{for } \zeta < 0 \text{ (unstable)} \\
&= 0.74 + 4.7\zeta \quad \text{for } \zeta = 0 \text{ (neutral)} \\
&= 0.74 \quad \text{for } \zeta > 0 \text{ (stable)}
\end{aligned} \tag{3-14}$$

where  $\zeta = z/L$ . These two representations of the atmospheric resistance are similar; both are proportional to the inverse friction velocity. Thus as the wind speed increases, the atmospheric resistance decreases.

For gaseous species the surface resistance (also known as the quasilaminar sublayer resistance),  $r_s$ , can be expressed as follows (Wesley and Hicks, 1977):

$$r_s = (k u_*) kB^{-1} \tag{3-15}$$

where  $B^{-1}$  is the surface transfer coefficient. As suggested by Wesley and Hicks (1977), a value of 2.6 is used for  $kB^{-1}$  for  $SO_2$  and the other gases ( $NO_x$  and  $HNO_3$ ) in the MESOPUFF-II. For the aerosol species in MESOPUFF-II (sulfate and nitrate) the surface resistance is assumed to be 10 s/cm.

In the CCADM the surface resistance is obtained using a species-dependent formula taken from the ADOM/TADAP model:

$$r_s = \frac{a \cdot Sc^{2/3}}{u_*} \quad (3-16)$$

where  $Sc$  is the Schmidt number, defined as the ratio of the molecular diffusivity of air (0.149) to the molecular diffusivity of the gaseous species in question. As currently implemented in the CCADM, all gaseous species are assumed to have the same molecular diffusivity as  $SO_2$  (0.126). The value of  $a$  in Equation 3-16 is set to 5 as recommended by Hicks (1983).

For aerosol species in the CCADM the gravitational settling resistance  $1/V_g$  acts in parallel to the other resistances:

$$V_d = V_g + \frac{1}{r_a + r_s + r_a r_b V_g} \quad (3-17)$$

The gravitational settling velocity in the CCADM is given by Stokes law:

$$V_g = \frac{\rho d^2 g C}{18\eta} \quad (3-18)$$

where

$\rho$  = particle density =  $1.0 \text{ g m}^{-3}$

$d$  = particle diameter =  $10^{-6} \text{ m}$

$g$  = gravitational acceleration =  $9.8 \text{ m/s}^2$

$\eta$  = dynamic viscosity coefficient for air =  $1.83 \cdot 10^{-4} \text{ Pa}\cdot\text{s}$

and the value  $C$  is a correction factor for small particles, given by

$$C = 1 + \frac{2\lambda}{d} \cdot 1.257 + 0.4 \exp[-0.55 \cdot d/\lambda] \quad (3-19)$$

where  $\lambda$  is the mean free path of air molecules. Although the mean free path is known to be dependent upon pressure, both the ADOM model (Pleim, Venkatram, and Yamartino, 1984) and the CCADM model (Gery et al., 1987) assume a constant value of  $6.53 \times 10^{-6} \text{ cm}$  for  $\lambda$ .

The quasilaminar sublayer resistance (surface resistance) for particles is obtained from the friction velocity and collection efficiency as follows (Pleim, Venkatram, and Yamartino, 1984):

$$r_s = \frac{a}{u_* E} \quad (3-20)$$

where  $E$  is the collection efficiency given by

$$E = Sc^{-2/3} + 10^{-3}/St \quad (3-21)$$

and  $St$  is the Stokes number defined as  $St = \tau u_*^2 / \eta$ , where  $\tau$  is the stopping time specified as  $1.31 \times 10^{-5}$  m for a particle with a radius of  $1 \mu\text{m}$  and  $\eta$  is the dynamic viscosity of air.

In Equation 3-20 the value of  $a$  is 1.7, as recommended by Moller and Schumann (1970), because it gives the best fit to measured deposition velocities for particles.

The values for canopy resistance,  $r_c$ , to  $\text{SO}_2$  used in the MESOPUFF-II are from Sheih and co-workers (1979), who estimate summertime canopy resistance for  $\text{SO}_2$  as a function of land use and stability class for summertime conditions (Table 3-1). The canopy resistance to  $\text{HNO}_3$  and the aerosol species ( $\text{SO}_4^-$  and  $\text{NO}_3^-$ ) are assumed to be 0. For  $\text{NO}_x$  the canopy resistances (in s/cm) are defined as follows:

$$\begin{aligned} r_c(\text{NO}_x) &= 1.3, \text{ unstable} \\ &= 5, \text{ neutral} \\ &= 15, \text{ stable} \end{aligned}$$

In the CCADM the canopy resistance to  $\text{SO}_2$  varies diurnally and seasonally and also varies if the surface is wet, as shown in Table 3-2 (Walcek et al., 1986). The canopy resistances to other gaseous species are related to the canopy resistance to  $\text{SO}_2$  according to the multiplicative factors given in Table 3-3.

For aerosol species in the CCADM the canopy resistance is 0. However, in the equation for particulate deposition velocity there is a third resistance,  $r_a r_b V_g$ , referred to as a virtual resistance in view of the fact

TABLE 3-1. Summertime SO<sub>2</sub> canopy resistances used in the Mesopuff-II as a function of land use type and stability class. (From: Sheih, Wesely, and Hicks, 1979).

<u>Category</u>	<u>Land Use Type</u>	<u>z<sub>0</sub></u> <u>(m)</u>	<u>Stability Class</u>			
			<u>A,B,C</u>	<u>D</u>	<u>E</u>	<u>F</u>
1	cropland and pasture	0.20	100.	300.	1000.	0.
2	cropland, woodland and grazing land	0.30	100.	300.	1000.	0.
3	irrigated crops	0.05	100.	300.	1000.	0.
4	grazed forest and woodland	0.90	100.	300.	1000.	0.
5	ungrazed forest and woodland	1.00	100.	300.	1000.	0.
6	subhumid grassland and semiarid grazing land	0.10	100.	300.	1000.	0.
7	open woodland grazed	0.20	100.	300.	1000.	0.
8	desert shrubland	0.30	200.	500.	1000.	1000.
9	swamp	0.20	50.	75.	100.	0.
10	marshland	0.50	75.	300.	1000.	0.
11	metropolitan city	1.00	1000.	1000.	1000.	0.
12	lake or ocean	10 <sup>-4</sup>	0.	0.	0.	0.



TABLE 3-2.  $\text{SO}_2$  canopy resistance,  $R_{\text{SO}_2}$  ( $\text{s m}^{-1}$ ), used in the CCADM. (Source: Walcek et al., 1985.)

LAND USE	SEASON	INSOLATION ( $\text{Watts m}^{-2}$ )			NIGHT	WETTED
		>400	200-400	0-200		
Urban	spring	1000	1000	1000	1000	1000
	summer	1000	1000	1000	1000	0
	early fall	1000	1000	1000	1000	1000
	late fall	1000	1000	1000	1000	1000
	winter	200	200	200	200	200
Agriculture	spring	50	60	75	100	0
	summer	70	120	200	500	0
	early fall	500	500	500	500	100
	late fall	50	50	50	50	50
	winter	100	100	100	100	100
Range	spring	100	140	200	400	0
	summer	100	140	200	500	0
	early fall	500	500	500	500	100
	late fall	500	500	500	500	100
	winter	100	100	100	100	100
Deciduous forest	spring	100	200	400	1000	0
	summer	60	130	300	1000	0
	early fall	1000	1000	1000	1000	500
	late fall	1000	1000	1000	1000	500
	winter	1000	1000	1000	1000	1000
Coniferous forest	spring	150	240	400	1000	0
	summer	150	240	400	1000	0
	early fall	800	800	800	800	100
	late fall	800	800	1000	1000	100
	winter	500	500	500	500	500
Forested swamp	spring	100	200	400	1000	0
	summer	70	140	300	1000	0
	early fall	800	800	800	800	300
	late fall	800	800	1000	1000	300
	winter	800	800	800	800	800
Water	spring	0	0	0	0	0
	summer	0	0	0	0	0
	early fall	0	0	0	0	0
	late fall	0	0	0	0	0
	winter	0	0	0	0	0
Swamp	spring	50	60	75	100	0
	summer	50	60	75	100	0
	early fall	100	100	100	100	75
	late fall	100	100	100	100	75
	winter	100	100	100	100	100
Agriculture-range mixture	spring	75	100	150	250	0
	summer	100	140	200	500	0
	early fall	500	500	500	500	100
	late fall	200	200	200	200	100
	winter	100	100	100	100	100

TABLE 3-3. Canopy resistances used in the CCADM assumed for dry-deposited gases relative to  $\text{SO}_2$  surface resistance. (Source: Chang et al., 1986).

Pollutant	Surface Resistance ( $\text{s m}^{-1}$ )*	
	Over Land Surfaces	Over wetted surfaces
NO	$R_{\text{SO}_2}$	500
$\text{NO}_2$	$R_{\text{SO}_2}$	500
$\text{O}_3$	$0.6R_{\text{SO}_2}$	2000
$\text{HNO}_3$	0.0	0.0
$\text{H}_2\text{O}_2$	$0.1R_{\text{SO}_2}$	$0.1R_{\text{SO}_2}$
Aldehyde	$2.0R_{\text{SO}_2}$	$2.0R_{\text{SO}_2}$
HCHO	$0.5R_{\text{SO}_2}$	$0.5R_{\text{SO}_2}$
Methyl-hydrogen peroxide	$0.3R_{\text{SO}_2}$	$0.3R_{\text{SO}_2}$
Peroxyacetic acid	$0.3R_{\text{SO}_2}$	$0.3R_{\text{SO}_2}$
HCOOH	$R_{\text{SO}_2}$	$R_{\text{SO}_2}$
$\text{NH}_3$	$0.2R_{\text{SO}_2}$	$0.2R_{\text{SO}_2}$

\* Values for  $R_{\text{SO}_2}$  given in Table 3-2.

that it is a mathematical artifact of the equation manipulation rather than a physical resistance (see Pleim, Venkatram, and Yamertino, 1984; and Gery et al., 1987).

The canopy resistance for the MESOPUFF-II is chosen from Table 3-1 based on one of the 12 land-use classifications specified in the grid cell containing the puff centroid. Clearly, when the puff is large and covers an area that includes several different land uses, this simplification may introduce some errors.

In the CCADM the fraction of coverage of each of the nine land-use classifications (in Table 3-2) is specified for each grid cell. The CCADM then calculates the fraction coverage across the base of the Lagrangian box through weighted averaging of the grid cells covered by the box. Then an average deposition velocity for the area covered is calculated using the method proposed by Walcek and others (1986).

#### 3.4.2 Comparison of MESOPUFF-II and CCADM Performance

The deposition velocities produced by the dry deposition algorithms in MESOPUFF-II and CCADM are compared here using a variety of environmental conditions and several land use classifications. Since the two algorithms do not use the same land use classification scheme, the land use categories for the CCADM (Table 3-2) are adjusted to match the MESOPUFF-II land use classes as closely as possible. The environmental conditions that vary are the surface wind speed and the exposure class, which is a measure of insolation as follows:

$C_e$	= 3,	strong	
	= 2,	moderate	Daytime insolation
	= 1,	slight	
	= 0,	heavy overcast	Day or night
	= -1,	$\geq \frac{4}{8}$ cloud cover	
			Nighttime cloudiness
	= -2,	$\leq \frac{3}{8}$ cloud cover	

The stability class can be estimated from the exposure class and wind speed using the method of Turner (1970). Although the CCADM predicts deposition velocities for many species, we compare only the deposition

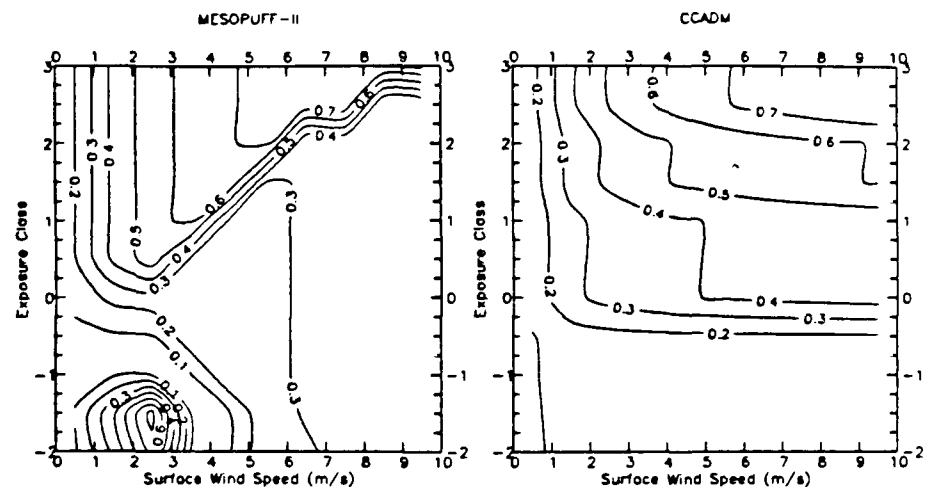
velocities for the five species in the MESOPUFF-II:  $\text{SO}_2$ , sulfate,  $\text{NO}_x$ , nitrate, and nitric acid. Since there are very few measurements of dry deposition, we cannot directly evaluate the two dry deposition algorithms. Instead, the two methods will be compared against each other and against the ranges of measured deposition velocities reported in the literature.

#### 3.4.2.1 Sulfur Dioxide Dry Deposition

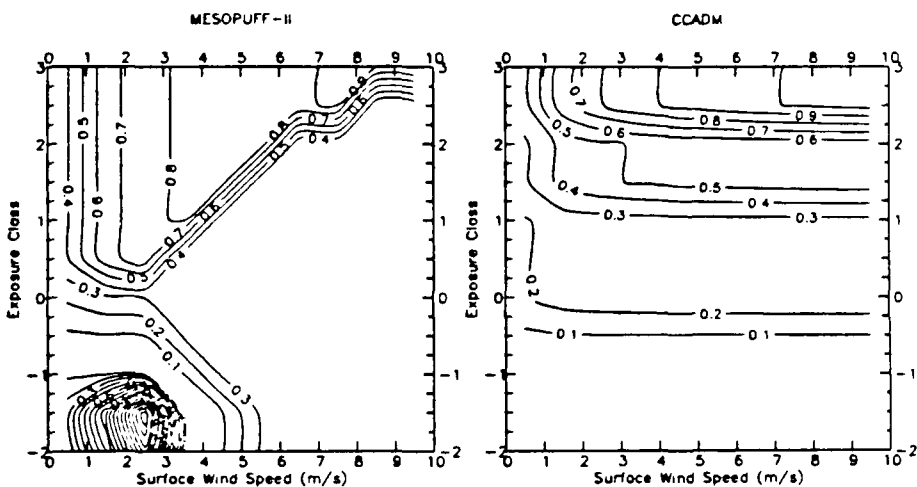
The  $\text{SO}_2$  deposition velocities predicted by the MESOPUFF-II and the CCADM for three different land use classes are given in Figure 3-32. (A complete set of predicted  $\text{SO}_2$  deposition velocities for all land use classifications is given in the Appendix.) The results for MESOPUFF-II and CCADM are similar for all three of the land use classes depicted in Figure 3-32. For cropland and pasture, the MESOPUFF-II predicts deposition velocities that range from 0.1 to 1.0 cm/s, while the CCADM values range from 0.1 to 0.7 cm/s. For the forest land use class, both models predict slightly higher deposition velocities, ranging from 0.1 to 1.0 cm/s. The deposition velocities for these two land use classes produced by the two models also have similar characteristics as a function of exposure class and surface wind speed.

The differences between the MESOPUFF-II and the CCADM for the positive exposure class (daytime) can be attributed to differences in the methods of representing stability in the two algorithms. The CCADM uses the exposure class directly, whereas the MESOPUFF-II uses the Pasquill-Gifford stability classification scheme in which stability (A-F) is a function of exposure class and wind speed. At night the MESOPUFF-II appears to produce an anomalous  $\text{SO}_2$  dry deposition velocity peak for clear skies and wind speed around 2.5 m/s. These environmental conditions result in a stability F classification, by which the MESOPUFF-II will assume a zero canopy resistance to  $\text{SO}_2$  (see Table 3-1). In general, under night conditions the atmospheric resistance should be the dominant resistance, thus the sensitivity to the canopy resistance under these conditions is questionable. Both the MESOPUFF-II and CCADM predict  $\text{SO}_2$  dry deposition velocities that are well within the range 0.04 to 2.8 cm/s for several surface types cited in the literature (McMahon and Dennison, 1979).

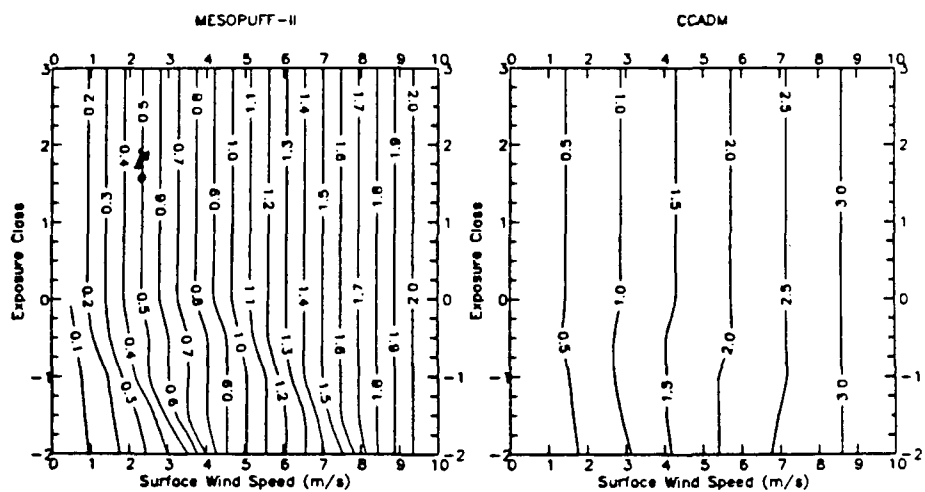
For dry deposition over water, the MESOPUFF-II and the CCADM predict remarkably similar patterns of  $\text{SO}_2$  deposition velocities. The CCADM predicts values ranging from 0.5 to 3.0 cm/s, while the MESOPUFF-II values from 0.1 to 2.0 cm/s. The reported measured values for  $\text{SO}_2$  dry deposition over water are 0.2 and 1.4 cm/s (Spedding, 1969), 0.9 and 0.5 cm/s (Owers and Powell 1974), 2.2 cm/s (Whelpdale and Shaw, 1974), 2 cm/s (Prahm, Tarp, and Stern, 1976), 0.41 cm/s (Garland, 1977), 0.5 cm/s (Smith and



SO<sub>2</sub> Deposition Velocities (cm/s) for CROPLAND AND PASTURE Land Use Type



SO<sub>2</sub> Deposition Velocities (cm/s) for UNGRAZED FOREST/WOODLAND Land Use Type.



SO<sub>2</sub> Deposition Velocities (cm/s) for LAKE OR OCEAN Land Use Type

FIGURE 3-32. Comparison of MESOPUFF-II and CCADM predicted SO<sub>2</sub> dry deposition velocities for three land use classes.

Hunt, 1978), and 0.4 to 4.0 cm/s (Sehemel, 1980). Sheih, Wesley, and Hicks (1979) estimated SO<sub>2</sub> deposition velocities over the Atlantic Ocean that ranged from 0.1 to 0.7 cm/s.

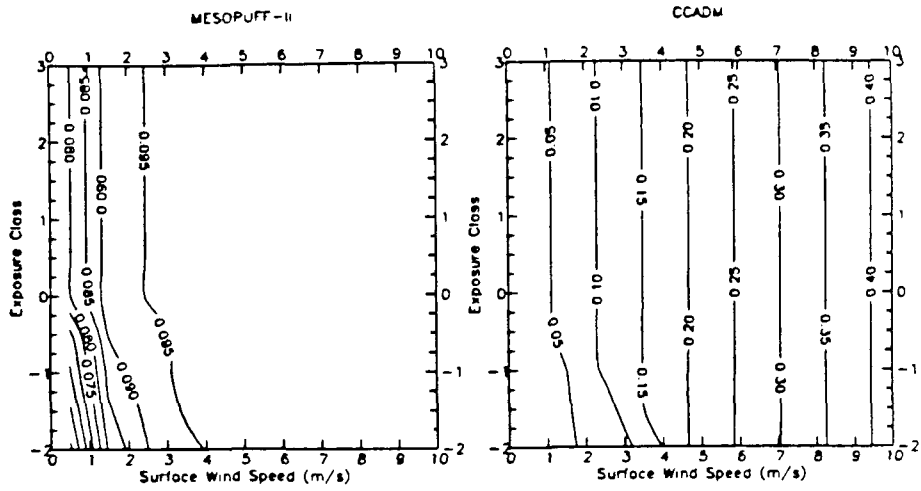
#### 3.4.2.2 Sulfate Deposition

Predicted sulfate deposition velocities for three land use types--cropland/pasture, forest/woodland, and water--are shown in Figure 3-33 (sulfate deposition velocities for all land use classes are displayed in the appendix). Although the MESOPUFF-II and the CCADM predict similar patterns for sulfate deposition, the MESOPUFF-II predicts much smaller values. This result is directly related to the assumption in the MESOPUFF-II of a constant surface (quasilaminar sublayer) resistance of 10 s/cm for aerosols. Thus the maximum possible sulfate deposition velocity in the MESOPUFF-II is 0.1 cm/s. Measured values of sulfate deposition velocities range from 0.03 to 1.0 cm/s (McMahon and Dennison, 1979); thus the upper limit of 0.1 cm/s imposed by the MESOPUFF-II appears a little low. This can be easily rectified by changing the assumed constant surface resistance in the MESOPUFF-II. The CCADM predicts sulfate deposition velocities from 0.05 to 0.8 cm/s for the three land use classes in Figure 3-32; the highest values occur for the forest land use class. For all land use classes, the MESOPUFF-II predicts sulfate dry deposition values with little variation at wind speeds above 1 m/s (0.070 to 0.1 cm/s).

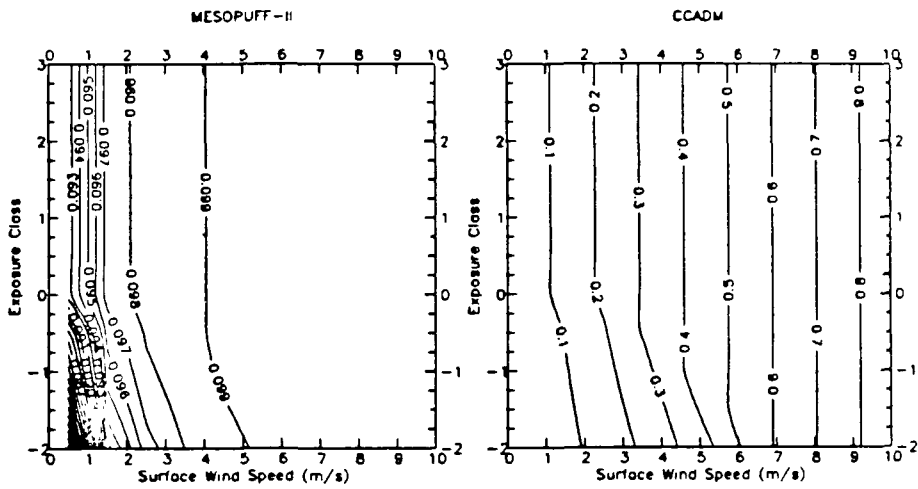
#### 3.4.2.3 Nitrogen Oxide Deposition

The CCADM predicts deposition velocities for NO and NO<sub>2</sub> separately, whereas the MESOPUFF-II gives values for NO<sub>x</sub>. However, the NO and NO<sub>2</sub> deposition velocities predicted by the CCADM are identical to each other since the same canopy resistances are used for these two species (see Table 3-3). Figure 3-34 compares the NO<sub>x</sub> deposition velocities predicted by the MESOPUFF-II and CCADM for three land use classes. The CCADM predicts the same dry deposition velocities for NO<sub>x</sub> as it does for SO<sub>2</sub>. The MESOPUFF-II deposition velocities for NO<sub>x</sub> resemble those calculated by MESOPUFF-II for SO<sub>2</sub> without the anomalous peak for F stability. This is because the MESOPUFF-II uses constant NO<sub>x</sub> resistances for the stable case.

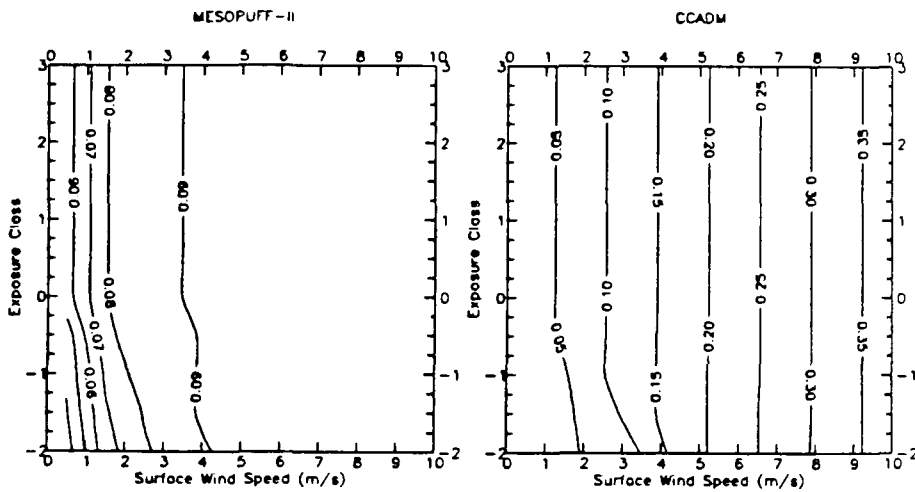
For the cropland/pasture and forest/woodland land use classes the range of NO<sub>x</sub> dry deposition velocities for the MESOPUFF-II is 0.1 to 0.7 cm/s and for the CCADM 0.1 to 1.0 cm/s. The two models predict different deposition behavior over water; the CCADM-predicted dry deposition velocity for NO<sub>x</sub> is as high as 3.0 cm/s. Since NO and NO<sub>2</sub> are not as soluble as SO<sub>2</sub>, the use of the same canopy resistance for these species over water seems questionable. It should be noted that over wet surfaces, regardless of



SO<sub>4</sub> Deposition Velocities (cm/s) for CROPLAND AND PASTURE Land Use Type

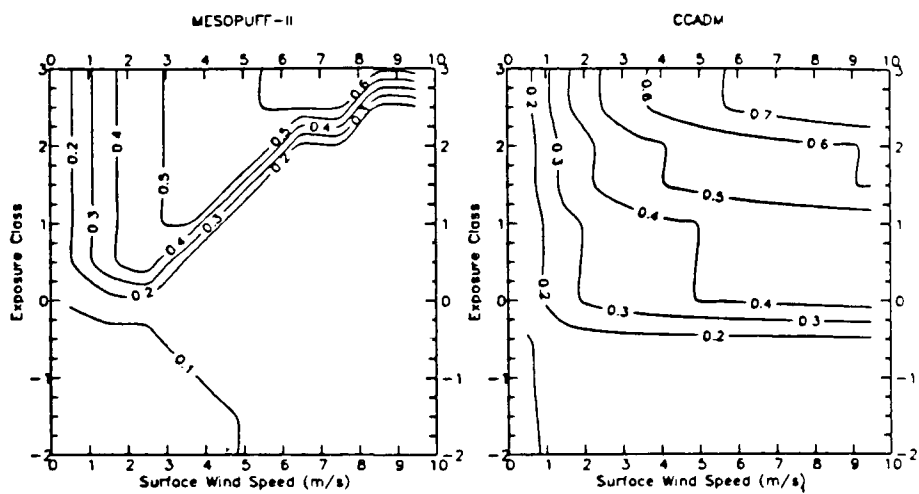


SO<sub>4</sub> Deposition Velocities (cm/s) for UNGRAZED FOREST/WOODLAND Land Use Type

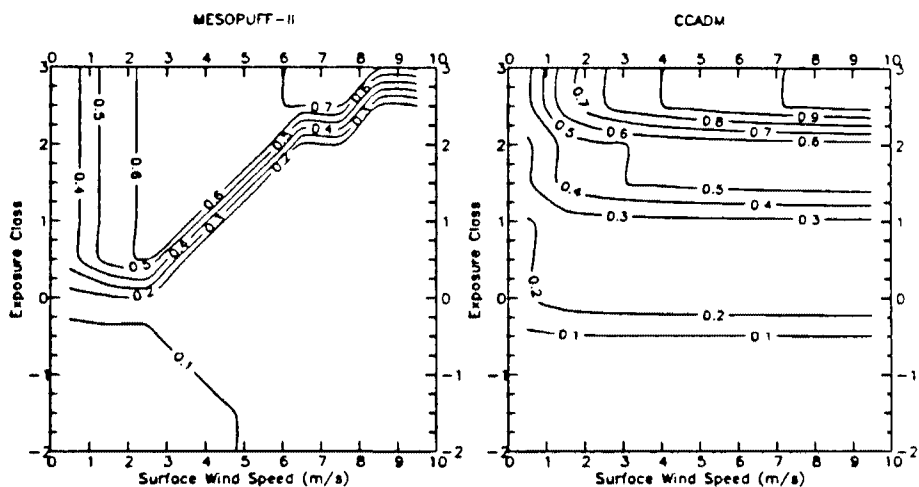


SO<sub>4</sub> Deposition Velocities (cm/s) for LAKE OR OCEAN Land Use Type

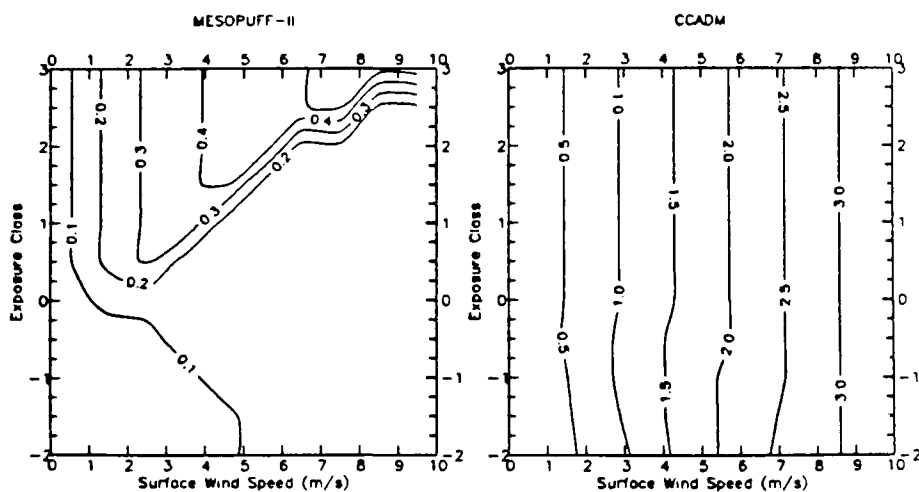
FIGURE 3-33. Comparison of MESOPUFF-II and CCADM predicted sulfate dry deposition velocities for three land use classes



NO<sub>2</sub> Deposition Velocities (cm/s) for CROPLAND AND PASTURE Land Use Type



NO<sub>2</sub> Deposition Velocities (cm/s) for UNGRAZED FOREST/WOODLAND Land Use Type



NO<sub>2</sub> Deposition Velocities (cm/s) for LAKE OR OCEAN Land Use Type

FIGURE 3-34. Comparison of MESOPUFF-II and CCADM predicted NO<sub>x</sub> dry deposition velocities for three land use classes.



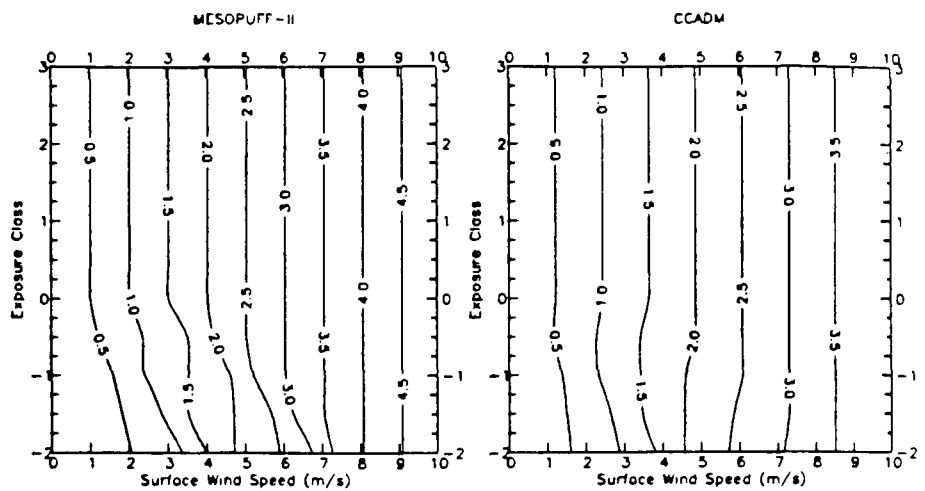
land use class, the CCADM predicts  $\text{NO}_x$  dry deposition velocities that range from 0.1 to 0.2 cm/s, i.e., over a factor of 10 lower than for water. Measurement of  $\text{NO}_x$  deposition velocities is extremely difficult because of the fast  $\text{NO}-\text{O}_3$  reaction and because the release of nitrogen compounds from the soil may result in a net negative deposition rate. Hill and Chamberlain (1976) reported an  $\text{NO}_2$  dry deposition velocity of 1.9 cm/s and a deposition velocity for  $\text{NO}$  of 0.1 cm/s. In a review of dry deposition velocities from three studies, Sehmel (1980) reported a range of  $\text{NO}_x$  deposition velocities from negative values to 0.5 cm/s. Studying dry deposition in the Netherlands, van Aalst and co-workers (1983) measured values of the dry deposition velocities of  $\text{NO}_x$  that ranged from -2.6 to 1.5 cm/s. Except for the  $\text{NO}_x$  dry deposition velocity over water calculated by CCADM, both models predict numbers that are within the range of the measurements. Since there are no reported measurements of deposition of  $\text{NO}_x$  over water at this time, one cannot discount the CCADM-predicted  $\text{NO}_x$  deposition velocity; however, since  $\text{NO}$  and  $\text{NO}_2$  are not as soluble as  $\text{SO}_2$ , it is expected that over water the deposition velocity for  $\text{NO}$  and  $\text{NO}_2$  would be lower than for  $\text{SO}_2$ . Thus the CCADM-predicted deposition velocities for  $\text{NO}$  and  $\text{NO}_2$  over water are questionable.

#### 3.4.2.4 Nitric Acid Deposition

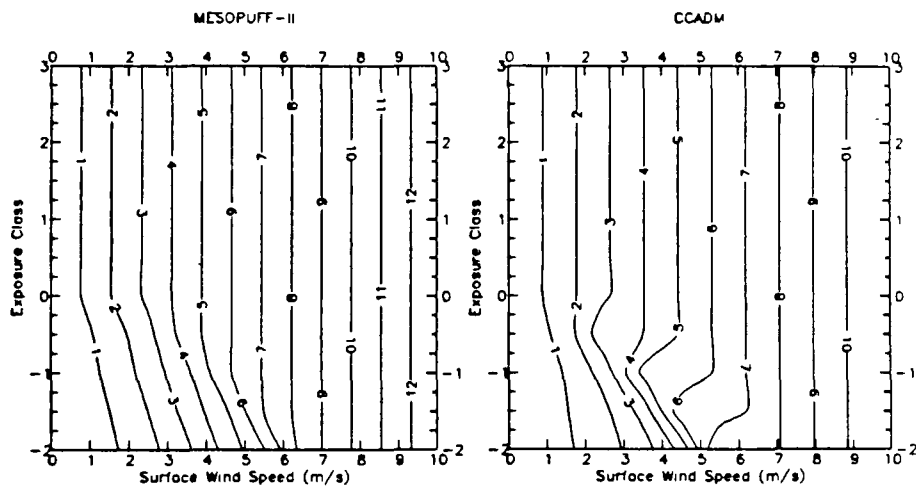
Nitric acid has a very high deposition rate compared with the other gases studied because of its high reactivity. Both the MESOPUFF-II and the CCADM assume a zero canopy resistance to nitric acid for all land use categories. As shown in Figure 3-35 and the appendix, the two models also predict remarkably similar dry deposition velocities of nitric acid for different environmental conditions and land use characteristics. The ranges of nitric acid dry deposition velocities for the two models are approximately 0.5 to 4.0 cm/s for cropland, 1 to 11 cm/s for forest, and 0.1 to 2.5 cm/s for water. There are very few measurements of the dry deposition velocity of nitric acid; van Aalst (1983) reports a value of 0.6 cm/s. However, the fact that the two models agree on the dry deposition velocities for nitric acid gives us some confidence that the predictions are reasonable.

#### 3.4.2.5 Nitrate Deposition

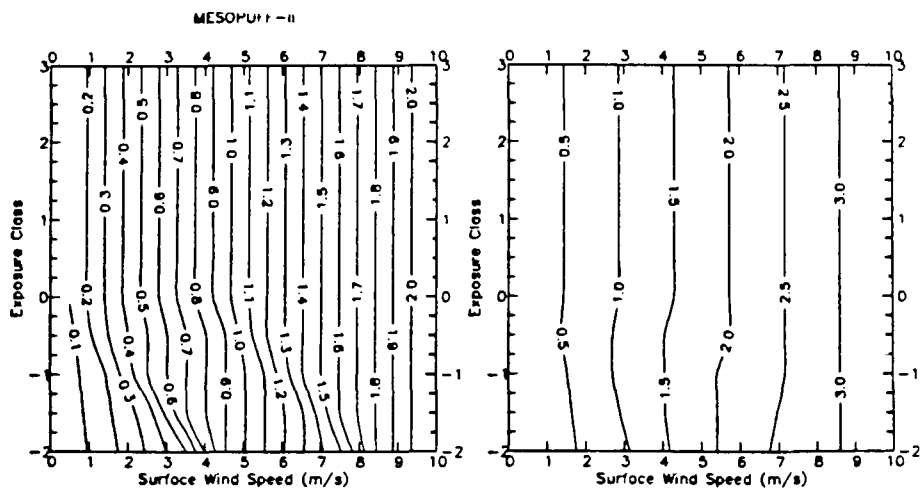
Both the MESOPUFF-II and the CCADM predict similar dry deposition velocities for nitrate (Figure 3-36) as for sulfate (Figure 3-33). Thus the discussion of sulfate dry deposition applies to nitrate. In particular, the very low nitrate deposition velocities predicted by the MESOPUFF-II (less than 0.1 cm/s) may be questionable.



HNO<sub>3</sub> Deposition Velocities (cm/s) for CROPLAND AND PASTURE Land Use Type



HNO<sub>3</sub> Deposition Velocities (cm/s) for UNGRAZED FOREST/WOODLAND Land Use Type



HNO<sub>3</sub> Deposition Velocities (cm/s) for LAKE OR OCEAN Land Use Type.

FIGURE 3-35. Comparison of MESOPUFF-II and CCADM predicted nitric acid dry deposition velocities for three land classes



### 3.5 WET DEPOSITION

The wet removal of pollutants consists of both in-cloud scavenging (rain-out) and below-cloud scavenging (washout). Many factors contribute to the scavenging rate of pollutants, including pollutant type, cloud type and history, and the precipitation rate. It is generally believed that the scavenging of particulates, such as sulfate and nitrate aerosols, is irreversible and the scavenging of gaseous species is reversible (NRC, 1983). Reversible scavenging refers to the release of contaminants from a rain droplet back into the atmosphere before the rain drop impacts the ground. We now briefly discuss the wet deposition parameterizations within the three candidate models that treat wet scavenging. For a more complete description of these algorithms and a review of the processes that lead to wet deposition see Morris and Kessler (1987).

#### 3.5.1 Review of the Wet Deposition Algorithms in the Candidate Models

##### 3.5.1.1 CCADM

Of the candidate models, the CCADM is the only model with a wet deposition algorithm to treat both reversible and irreversible scavenging. The calculation of rainout for the gaseous species in the CCADM relies on the gaseous-liquid equilibrium component of the aqueous-phase chemistry module (Gery et al., 1987). Particulate species are assumed to be totally in the liquid state (i.e. complete nucleation for aerosols) within the cloud. Washout of particulates is parameterized using the algorithms of Scott (1978). Gaseous species are washed out assuming that the species concentrations within the raindrop are in gaseous-liquid equilibrium with the ambient air as the raindrop falls. Thus it is possible for some of the gaseous species inside the raindrop to be released back into the atmosphere. The calculation of the gaseous-liquid equilibrium is dependent on the species concentrations, the temperature, and the pH of the cloud water. Since this algorithm requires knowledge of the total concentration of all species that contribute to the cloud pH, and all species for which scavenging rates are being calculated, use of this algorithm in a Lagrangian puff model is not appropriate.

##### 3.5.1.2 MESOPUFF-II

The MESOPUFF-II and the RIVAD both contain simplified wet deposition algorithms that are consistent with a Lagrangian puff model. The MESOPUFF-II uses the scavenging coefficient approach to calculate the wet

deposition of  $\text{SO}_2$ ,  $\text{SO}_4$ ,  $\text{NO}_x$ ,  $\text{HNO}_3$  and  $\text{NO}_3$ . This approach assumes that the loss of pollutant mass over one time step,  $\Delta t$  (s), due to a precipitation rate,  $R$  (mm/h), is expressed as follows:

$$Q(t + \Delta t) = Q(t) \exp(-\Lambda \Delta t)$$

where  $Q(t)$  and  $Q(t + \Delta t)$  represent the mass of the pollutant at the beginning and end of the time step, and  $\Lambda$  ( $\text{s}^{-1}$ ) is the scavenging ratio expressed as:  $\Lambda = \lambda(R/R_1)$ .

Here  $R_1$  is a reference rainfall rate (1 mm/h) and  $\lambda$  is the scavenging coefficient ( $\text{s}^{-1}$ ) whose value depends on the species and whether the precipitation is liquid or frozen. The MESOPUFF-II uses the rainfall rate and type from the nearest observation site.

### 3.5.1.3 RIVAD

The parameterization of wet deposition of gases in the RIVAD follows the method suggested by Hales and Sutter (1973). The wet deposition rate constant,  $W$  (1/h), for a gaseous species is defined as follows:

$$W = \frac{24.026 R}{h(0.00667 R/V + \text{SOL})}$$

where  $R$  = precipitation rate (m/h)

$h$  = plume parcel depth (m)

$V$  = raindrop velocity (m/s)

$\text{SOL}$  = species-dependent solubility parameter based on Henry's law constant and the cloud pH (assumed to be 4.5 in the RIVAD)

The parameterization of wet deposition of particulates and sulfate aerosol uses a method proposed by Scott (1978). The irreversible scavenging algorithm is based on the assumptions that sulfate is scavenged within clouds primarily by cloud droplet nucleation and beneath clouds the largest aerosols are washed out by impaction. Scott's algorithm, which is used in RIVAD, can be expressed as

$$x = \frac{14 M_s}{R^{0.88}} + \frac{0.75 S_0 (1 - 4.41 \times 10^{-2} R^{-0.88})}{(1.56 + 0.44 \ln R)} + 0.3 c_1 m_a \Delta t_b \quad (3-22)$$

where

$x$  = ratio of sulfate mass to precipitation mass (gram sulfate/gram  $H_2O$ ),

$R$  = rainfall rate (mm/h),

$m_a$  = Concentration of subcloud sulfate aerosols greater than  $1\ \mu m$  in diameter, assumed equal to  $0.1\ S_0$ ,

$S_0$  = Subcloud sulfate hydrometeor concentration,

$\Delta t_b$  = time required for hydrometeor to fall from cloud base to ground,

$c_1 = 5.2 \times 10^{-3}$  for liquid hydrometeor  
 $= 3.7 \times 10^{-3}$  for frozen hydrometeor

$$M_s = 0.75\ S_0\ \exp\ \frac{(4.41 \times 10^{-2} - R^{0.88})(435\ R^{-0.71} + 1200)}{(8450 - 2383\ \ln R)}$$

For convective clouds or clouds whose tops are warmer than  $0^\circ\ C$

$= 0.1\ S_0$  For layer clouds not dependent on Bergeron process for rain initiation

$= 0$  For layer clouds dependent on Bergeron process for rain initiation.

The RIVAD is currently configured for layer clouds dependent on Bergeron process for rain initiation.

### 3.5.2 Evaluation of the Wet Deposition Algorithms

Of the three candidate models that treat wet deposition, both the MESO-PUFF-II and the RIVAD wet deposition formulation are consistent with the Lagrangian puff model framework. Although the two methods used--scavenging coefficient and solubility approach--are basically different, they have some similarities. First, sulfate and nitrate aerosols are both scavenged at the same rate by the MESOPUFF-II and the RIVAD. Second, neither model treats gaseous scavenging as irreversible. Third, both

parameterizations combine in-cloud scavenging (rainout) and below-cloud scavenging (washout) into one scavenging rate. Finally, these parameterizations are linear and the scavenging rate depends only on the precipitation rate and species type and for MESOPUFF-II, whether the precipitation is liquid or frozen, not on the species concentrations.

#### 3.5.2.1 Sulfur Dioxide

The  $\text{SO}_2$  wet scavenging rates produced by the MESOPUFF-II and RIVAD models as a function of precipitation rate are shown in Figure 3-37a. The MESOPUFF-II assumes that  $\text{SO}_2$  is not scavenged by a frozen hydrometer. Despite the differences in their formulations, the shapes of the curves for the two models are very similar. However, the MESOPUFF-II produced wet scavenging rates that are approximately twice those of the RIVAD model. Due to the lack of quantitative measurements, it cannot be determined whether one algorithm is predicting a more accurate scavenging rate than the other.

#### 3.5.2.2 Sulfate

In both the MESOPUFF-II and the RIVAD the scavenging of particulates is calculated based on the scavenging rate calculated for sulfate. Thus the evaluation of the scavenging rates for sulfates also applies to nitrates and particulate matter species. The wet sulfate scavenging rates for the two models as a function of precipitation rate are given in Figure 3-37b. Given the differences in their formulations, the similarity of the sulfate scavenging rates produced by the two models for liquid precipitation is quite encouraging. For precipitation rates below 0.1 in/h, the RIVAD produces a rate that is about 10 %/h higher than the rate given by the MESOPUFF-II. The MESOPUFF-II wet scavenging rate for the frozen case is much lower than that for the liquid case, reflecting the fact that it is difficult for the particles to become embedded in ice crystals except through the process of rimming.

#### 3.5.2.3 Nitrogen Oxides

The MESOPUFF-II assumes that  $\text{NO}_x$  is not scavenged through the process of precipitation. This is verified by the RIVAD model, which produces very low  $\text{NO}_x$  scavenging rates (Figure 3-38a). This is because  $\text{NO}_2$  and, even more so,  $\text{NO}$  are both not very soluble and have a very low Henry's Law constant.

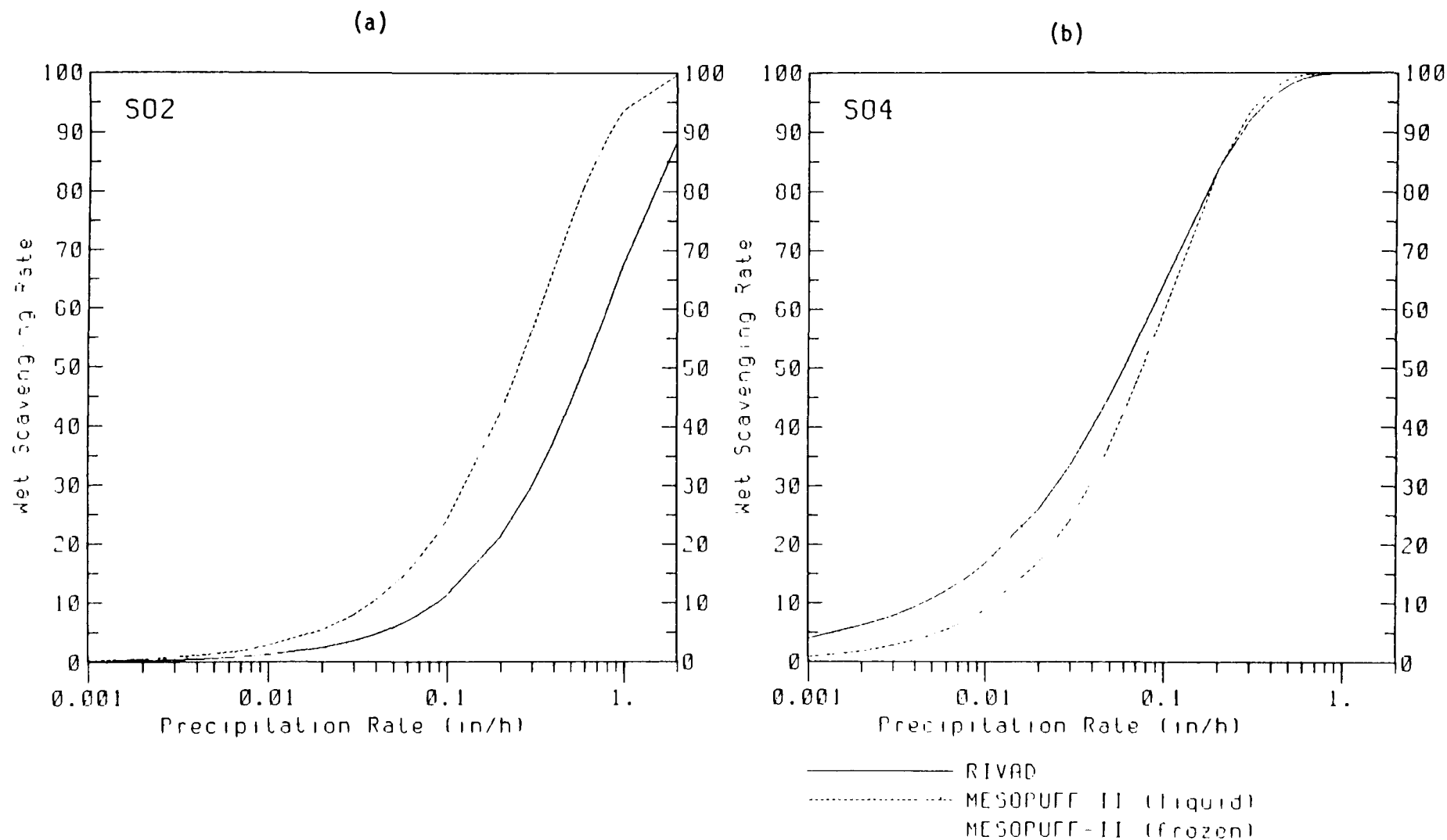


FIGURE 3-37. Sensitivity of the MESOPUFF-II and RIVAD wet scavenging rates to precipitation rates for (a) SO<sub>2</sub> and (b) sulfate.



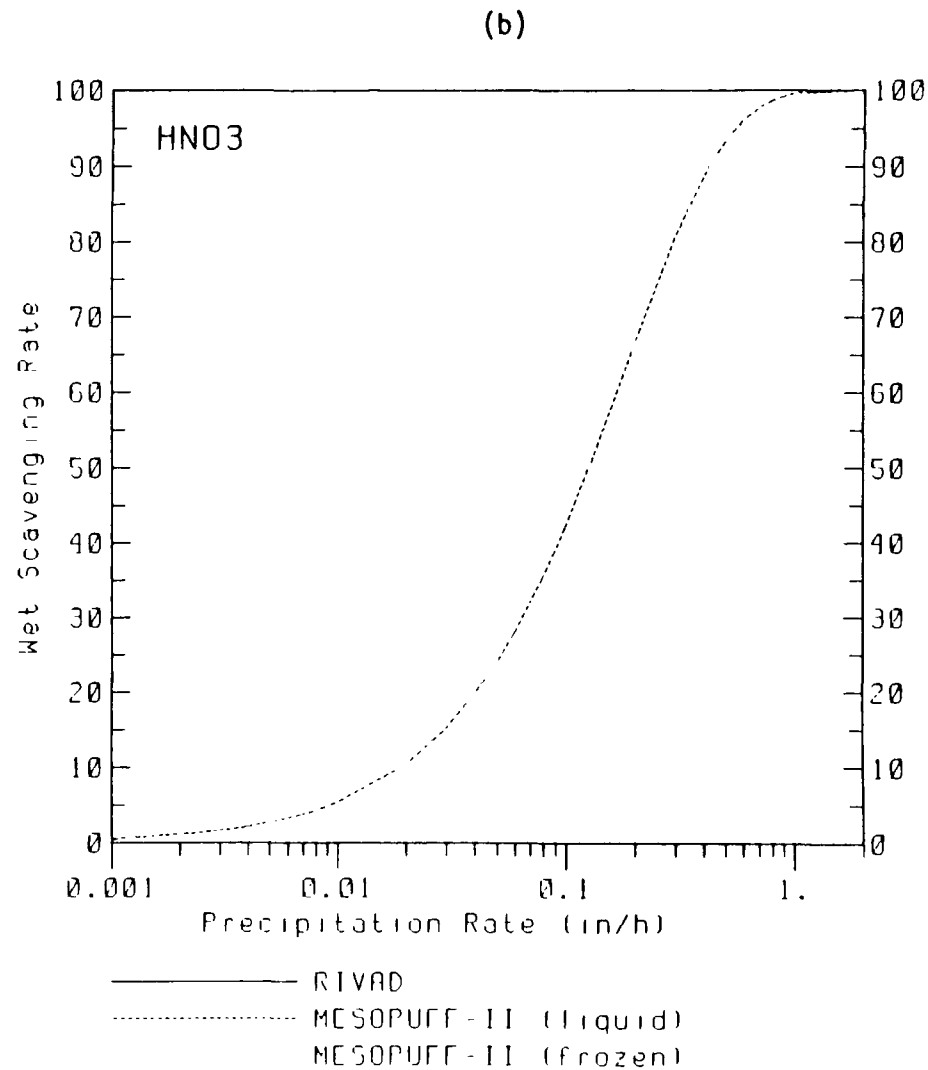
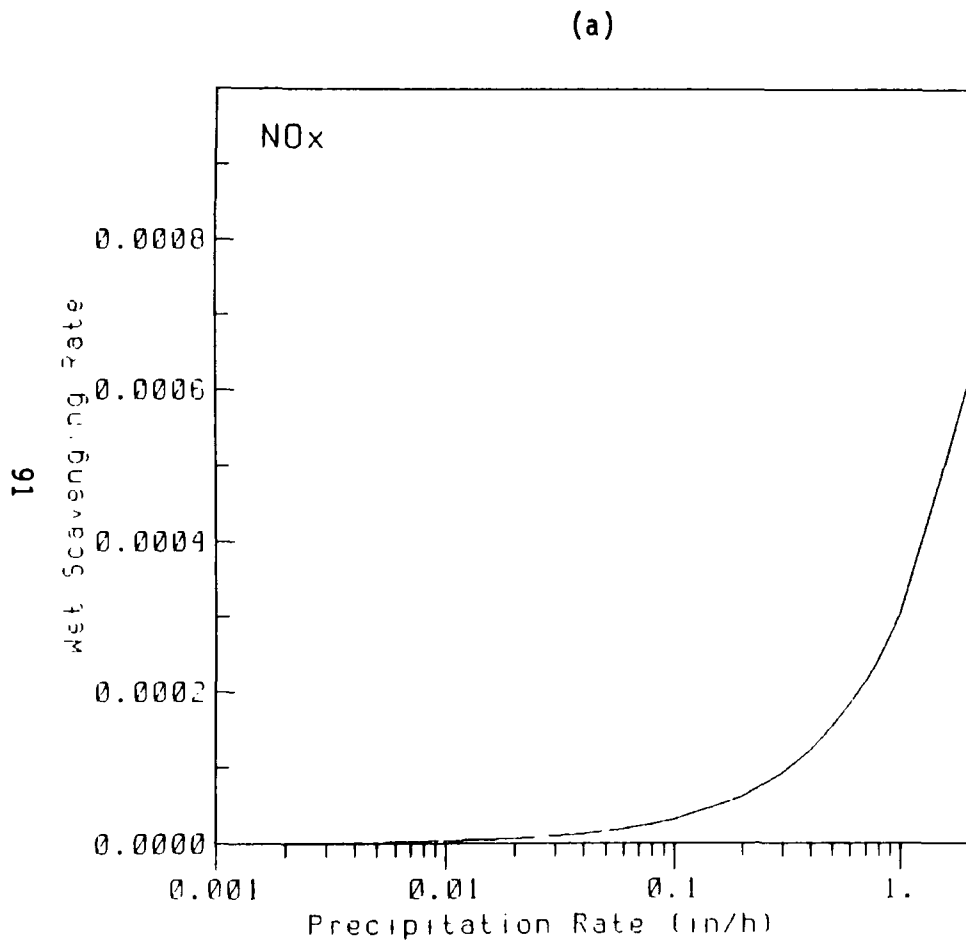


FIGURE 3-38. Sensitivity of the MESOPUFF-II and RIVAD wet scavenging rates to precipitation rates for (a) NO<sub>x</sub> and (b) nitric acid.

#### 3.5.2.4 Nitric Acid

Nitric acid is very soluble. The solubility parameter used for nitric acid in the RIVAD is approximately 14 magnitudes greater than for  $\text{NO}_x$  and 8 magnitudes greater than for  $\text{SO}_2$ . Thus the RIVAD model calculates a wet scavenging rate for nitric acid of 100 %/h for precipitation rates as low as 0.0001 in/h. The MESOPUFF-II produces scavenging rates that are comparable to those produced for sulfate (Figure 3-38b). The calculation of a wet scavenging rate of 100 %/h regardless of the precipitation rate is a little suspicious; however, because of the high solubility and reactivity of nitric acid it cannot be discounted.

#### 3.5.3 Remarks

This discussion on wet deposition has deliberately been restricted to the calculation of scavenging rates for given precipitation rates. The process of wet deposition of pollutants involves the complex interaction of cloud physics, including entrainment, venting, vertical transport within the cloud, and cloud microphysics (phase changes of  $\text{H}_2\text{O}$  between gas, ice, cloud water, and rain water), aqueous- and gas-phase chemistry, as well as wet scavenging. In addition, there are several other issues relating to the modeling of wet deposition, including the representation of the patchiness of clouds and cloud ensembles. Current research, by groups such as the Regional Acid Deposition Model (RADM) team, is underway to develop modeling techniques for dealing with these issues. However, for the purposes of developing an acid deposition model capable of estimating annual acid deposition increments from specified sources in a cost-effective manner, rigorous treatment of all these processes is impossible.

#### 4 DESIGN OF THE METEOROLOGICAL MODEL

The heart of the new mesoscale meteorological model is the wind field generation algorithm. Of the diagnostic wind models reviewed, no one model appears to be clearly superior to the other models. If there were a total lack of observational data, the CTWM would be the best choice for a wind field generator; however, it cannot take full advantage of any existing meteorological data. The MELSAR-MET wind model is attractive because of its ability to represent blocking and deflection in a cost-effective manner. However, the MELSAR, ATMOS1, and CIT wind models all require meteorological measurements to infer any dynamic properties in the wind field.

In addition to wind fields, an acid deposition model requires other meteorological inputs, including boundary layer heights, temperatures, temperature lapse rates, relative humidities, stability, and such micro-meteorological variables as friction velocity and Monin-Obukhov length. The only candidate model that also generates fields of such meteorological variables is the MELSAR-MET. The MELSAR-MET is coded in a highly modular fashion, which allows for ease of addition, replacement, or modification of any existing module. Thus the mesoscale meteorological model for the Rocky Mountains will make use of the MELSAR-MET code as a basis for generating wind fields and other meteorological variables needed for acid deposition modeling in complex terrain.

Rather than adopt an existing wind model, we have elected to design a new model that combines features from several existing diagnostic wind models. This wind model would utilize all existing wind observations, while simulating the effects of complex terrain in data-sparse sub-regions. The design and formulation of the wind model is discussed in detail in Section 4.1. A preliminary evaluation of the model is reported in Section 4.2. The model is first evaluated using the same tests as for the candidate models; then the model predictions are compared against wind observations from the Rocky Mountains; finally, the model is applied to entirely different terrain settings--a large valley and a complex terrain/coastal environment.

## 4.1 THE DIAGNOSTIC WIND MODEL

### 4.1.1 Design Overview

The diagnostic model is used to generate gridded fields of the horizontal wind components,  $u$  and  $v$ , at several user-specified vertical levels and at a specified time. This model will use local surface and upper-air wind observations, where available, while providing some information on terrain-generated air flows in regions where local observations are insufficient to account for terrain effects.

The diagnostic model requires gridded terrain heights, a mean wind value for the modeling region, and region-average stability information ( $dT/dz$ , or Pasquill stability class). The model will also accept surface and upper-air wind observations.

The generation of the wind field involves two major steps. Step 1 is based on the approach taken in the SAI Complex Terrain Wind Model, as described by Liu and Yocke (1980). A mean wind value for the modeling region is adjusted for the kinematic effects of terrain, thermodynamically generated slope flows, and blocking effects based on a set of gross parameterizations of these effects. Step 1 produces a spatially varying gridded field of  $u$  and  $v$  at each vertical level.

Step 2 involves the addition of observational information to the step 1 ( $u,v$ ) field. An objective analysis scheme is used to produce a new gridded ( $u,v$ ) field. The scheme is designed so that the observations are weighted relatively heavily in subregions where they are deemed representative of the mesoscale air flow, whereas in subregions where observations are deemed unrepresentative the ( $u,v$ )-values from step 1 are weighted heavily. Once the new gridded ( $u,v$ ) field is generated, it can be adjusted to mass consistency by the divergence-reduction procedure described by Goodin and co-workers (1980).

### 4.1.2 Model Formulation

#### 4.1.2.1 Vertical Coordinates

The diagnostic model is formulated in terrain-parallel vertical coordinates. This allows computation of winds at constant heights above ground, as well as variable vertical resolution. The horizontal position variables ( $x,y$ ) and velocity variables ( $u,v$ ) are invariant upon transformation from Cartesian to terrain-parallel coordinates. If  $h$  denotes terrain height,  $z$  denotes the Cartesian vertical position variable, and  $Z$  denotes the terrain-parallel position variable, then

$$Z = z - h(x,y) \quad . \quad (4-1)$$

If  $w$  denotes Cartesian vertical velocity, and  $W$  denotes terrain-parallel vertical velocity, then

$$W = w - u \, dh/dx - v \, dh/dy \quad . \quad (4-2)$$

In terrain-parallel coordinates the incompressible conservation-of-mass equation becomes

$$du/dx + dv/dy + dW/dZ = 0 \quad (4-3)$$

#### 4.1.2.2 Divergence Minimization Procedure

The divergence minimization procedure is utilized in both steps 1 and 2 and thus is described here. This procedure is nearly identical to the procedure described by Goodin and co-workers (1980). The inputs to the procedure are a "first-guess" three-dimensional  $(u,v)$  field and a three-dimensional  $W$  field defined at points horizontally and vertically staggered with the  $(u,v)$  levels. Assuming the  $W$  field is invariant, the procedure performs an iterative adjustment of the  $(u,v)$  field until the centered-difference approximation of the inequality,

$$du/dx + dv/dy + dW/dZ < \epsilon \quad (4-4)$$

is satisfied at all grid points.  $\epsilon$  is the maximum allowable three-dimensional divergence specified by the user.

The iterative adjustment is carried out as follows. At each grid point  $(i,j,k)$  the three-dimensional divergence  $D(i,j,k)$  is computed,

$$D_{ijk} = \frac{W_{i,j,k+1/2} - W_{i,j,k-1/2}}{\Delta z} + \frac{u_{i+1,j,k} - u_{i-1,j,k}}{2\Delta x} + \frac{v_{i,j+1,k} - v_{i,j-1,k}}{2\Delta y} \quad , \quad (4-5)$$

where  $\Delta x$  and  $\Delta y$  are the horizontal grid spacing in the  $x$  and  $y$  direction (assumed constant) and  $\Delta z$  is the vertical layer thickness between  $k - 1/2$  and  $k + 1/2$ . Note that  $W$  is defined at vertically staggered grid levels.

Velocity components at the surrounding grid points are adjusted so that  $D(i,j,k)$  is zero. The adjustment at a given grid point adds divergence at surrounding grid points; thus the entire grid must be scanned iteratively until the divergence minimization criterion is met at all points. The adjustments take the form

$$u(i+1,j,k) = u(i+1,j,k) + u_T \quad (4-6)$$

$$u(i-1,j,k) = u(i-1,j,k) - u_T$$

$$v(i,j+1,k) = v(i,j+1,k) + v_T$$

$$v(i,j-1,k) = v(i,j-1,k) - v_T$$

In making this adjustment, it is arbitrarily assumed that  $u_T = v_T$ ; given constant horizontal grid spacing, one can then show from Equation 4-5 that

$$u_T = - D \Delta x / 2 \quad (4-7)$$

#### 4.1.2.3 Step 1 of Wind Field Generation

Kinematic Effects of Terrain. The treatment of the kinematic effects of terrain follows the procedure described by Liu and Yocke (1980). Given a mean wind,  $V$ , for the modeling region, and terrain height,  $h(x,y)$ , a terrain-forced Cartesian vertical velocity of the following form is assumed:

$$w = (V \cdot \text{grad } h) \exp^{-kz} \quad (4-8)$$

where  $k$  is a coefficient of exponential decay that increases with atmospheric stability. Liu and Yocke assume that

$$k = N/|V| \quad (4-9)$$

where  $N$  is the Brunt-Vaisala frequency,  $(g/\theta) (d\theta/dz)$ ;  $Q$  is the potential temperature; and  $|V|$  is the magnitude of the mean wind.

In the current model the Cartesian  $w$  of Equation 4-8 is transformed to a terrain-parallel  $W$ , as in Equation 4-2, using the mean wind for the modeling region. Thus  $dW/dZ = dw/dz$ . Assuming the mean wind as a first-guess gridded  $(u,v)$  field, the divergence minimization scheme is exercised to produce a gridded wind field,  $(u,v)_k$ , adjusted for the kinematic effects of terrain.

Slope Flows. At each grid point in regions of complex terrain, the diagnostic model computes a slope flow vector  $(u,v)_s$ . This vector is added to the gridded wind field  $(u,v)_k$  to obtain a new field  $(u,v)_{ks}$ .

Let  $h_x$  and  $h_y$  denote  $\partial h/\partial x$  and  $\partial h/\partial y$ , respectively. We define the slope angle,  $\alpha$ ,

$$\alpha = \tan^{-1}[h_x^2 + h_y^2]^{1/2} . \quad (4-10)$$

The drainage direction,  $\beta_d$ , is computed as shown by Allwine and Whiteman (1985). An angle,  $\beta'$ , is defined as

$$\beta' = \tan^{-1}(h_y/h_x) . \quad (4-11)$$

A second angle,  $\beta''$ , is defined from the following table:

Condition	$h_x = 0$	$h_x < 0$	$h_x > 0$
$h_y = 0$	*	$\beta' + 180$	$\beta' + 360$
$h_y < 0$	270	$\beta' + 180$	$\beta + 360$
$h_y > 0$	90	$\beta' + 180$	$\beta'$

\* Terrain is flat, no drainage direction.

The final definition of  $\beta_d$  (in degrees) is

$$\begin{aligned} \beta_d &= 90 - \beta'', \quad 0 < \beta'' < 90 \\ \beta_d &= 450 - \beta'', \quad 90 < \beta'' < 360 \end{aligned} \quad (4-12)$$

The slope flow vector is oriented in the drainage direction. The speed of the slope flow component is determined by the details of the parameterization; in our discussion a positive speed denotes upslope flow.

Analytic solutions for downslope flows under highly idealized conditions have been obtained by Prandtl (1942) and, more recently, by Mahrt (1982) and Fitzjarrald (1984). However, analysis of upslope flow has received much less attention, perhaps because the presence of turbulent mixing over

a heated slope complicates the analysis. Although analytic solutions provide useful insight into the physics of slope flow, their direct application to complex-terrain situations is doubtful. Given the crudity of other parameterizations in the diagnostic model, and given that local air flow is frequently influenced by terrain features of horizontal scales significantly smaller than model grid scales, we feel justified in formulating a relatively arbitrary parameterization of slope flow effects.

The speed,  $S$ , of the parameterized slope flow is defined as follows:

$$S = S_0 \times f_1(t) \times f_2(Z,t) \times f_3(\alpha) \quad . \quad (4-13)$$

$S_0$  is an arbitrarily specified slope flow "amplitude"; this is a region-average parameter that is an estimate of the maximum speed of the slope flow. The function  $f_1$  is a specified function of time of day that, in general, will be assigned a value of -1 for fully developed downslope flow and +1 for fully developed upslope flow. It may be allowed to vary during periods of transition. The function  $f_2$  is a vertical profile function. Loosely guided by the Prandtl analytic solution for slope flow (as presented by Rao and Snodgrass, 1981), the following expression is proposed for  $f_2$ :

$$f_2(Z/l_s) = A \sin(Z/l_s) \exp(-Z/l_s) \quad (4-14)$$

Here  $l_s$  is a vertical scale length for the slope flow, and

$$A = 0.707 \exp(-\pi/4) \quad (4-15)$$

normalizes  $f_2$  so that its maximum value is 1. Note that we have substituted the terrain-parallel vertical coordinate  $Z$  for Prandtl's slope-normal coordinate  $n$ . Note also that the expression for  $f_2$  allows for an overlying layer of reverse flow considerably weaker than the ground-based slope flow. The depth of the ground-based slope flow layer is  $\pi \times l_s$ ; the maximum slope flow speed occurs at  $Z/l_s = \pi/4$ .

Although an expression for  $l_s$  is derived as part of Prandtl's solution, for the purposes of this model  $l_s$  will be specified arbitrarily as a function of time. For daytime upslope flow,  $l_s$  should probably be set equal to the estimated mixing height; for nighttime downslope flow,  $l_s$  should probably be set at 50-100 m based on the analyses and numerical experiments of Rao and Snodgrass (1981), Arritt and Pielke (1986), and others. If the vertical resolution of the model is coarse compared to the estimate of  $l_s$ ,  $f_2$  can be arbitrarily specified, independent of Equation 4-14, for each model level as a function of time.



The function  $f_3$  describes the variability of the slope flow speed with slope angle. The numerical simulations of Arritt and Pielke (1986) indicate that the slope flow intensity is relatively insensitive to slope angle when the angle is between 5 and 20 degrees, and that slope flow is virtually absent for slope angles of 1 degree. On the basis of these results, we propose for  $f_3$  the form

$$\begin{aligned} f_3 &= \alpha/\alpha_0, & \alpha < \alpha_0 \\ f_3 &= 1, & \alpha \geq \alpha_0 \end{aligned} \quad (4-16)$$

where  $\alpha_0$  is an arbitrarily specified angle somewhere between 1 and 5 degrees. This slope flow parameterization does not at this time account for nonlinear interaction of slope flow with ambient flow. Again we justify this omission on the basis of the one-dimensional downslope flow simulations reported by Arritt and Pielke (1986); the range of results obtained by Arritt for a variety of ambient flows seems well within the uncertainty of this crude parameterization technique in complex terrain.

Terrain Blocking Effects. The treatment of the blocking effects of terrain in the diagnostic model follows the procedure described by Allwine and Whiteman (1985). From the gridded wind field,  $(u,v)$ , the available atmospheric stability information, and the gridded terrain heights, a local Froude number,

$$Fr = S / N \Delta h \quad (4-17)$$

is computed at each grid point. Here  $S$  is the grid-point wind speed,  $N$  is the Brunt-Vaisala frequency as defined in Equation 4-9, and  $\Delta h$  is the "effective obstacle height" at the given grid point. If  $Fr$  is less than a critical Froude number,  $Fr_c$  (usually equal to 1), and  $(u,v)_{ks}$  at the given grid point has an uphill component,  $(u,v)_{ks}$  is adjusted so that the flow is in a terrain-tangent direction, with no change in speed. If  $Fr > Fr_c$ , the flow is not adjusted. Thus a new gridded wind field  $(u,v)_1$  is obtained that reflects both terrain kinematic effects and thermodynamic blocking effects.

We assume that

$$\Delta h(x,y,Z) = h_{\max}(x,y) - z(x,y,Z) \quad (4-18)$$

where  $h_{\max}$  is the elevation (MSL or above some reference height) of the "obstacle top" and  $z$  is the elevation of the grid point. The assignment of a value to  $h_{\max}$  in regions of complex terrain can be somewhat arbitrary. One option is to assume that  $h_{\max}(x,y)$  is the largest value of the

terrain height,  $h$ , within a specified radius of the given grid point; this radius should be determined by the dominant horizontal scale of the terrain. A second option is simply to subjectively assign a value of  $h_{\max}$  to each grid point. Both options will be available in this model.

#### 4.1.2.4 Step 2 of Wind Field Generation

Step 2 of the diagnostic model combines the gridded wind field  $(u,v)_1$  generated in step 1 with available observed data to produce a "final" gridded wind field  $(u,v)_2$ . This involves four substeps: (1) objective analysis; (2) smoothing of the analyzed field; (3) computation of a vertical velocity field; and (4) minimization of three-dimensional divergence.

Objective Analysis. The objective analysis procedure is a modified inverse-distance weighting scheme based on procedures utilized by Goodin and others (1980), Godden and Lurmann (1983), and Ross and Smith (1986). It is carried out separately for each model level. It is assumed that all surface wind observations will be incorporated at the lowest model level. A preprocessor program will interpolate upper-air observations vertically and temporally so that "soundings" of  $u$  and  $v$  are defined at all model levels at a given horizontal location.

For the purpose of discussion,  $(u_0, v_0)_k$  denotes an observed wind at station  $k$ , and  $r_k$  denotes the horizontal distance from station  $k$  to a given grid point. At each grid point, the wind vector is thus updated:

$$(u,v)' = \left[ \sum_k [r_k^{-n} (u_0, v_0)_k] + R_1^{-n} (u,v)_1 \right] / \left[ \sum_k r_k^{-n} + R_1^{-n} \right] \quad (4-19)$$

This procedure weights the step 1 wind field,  $(u,v)_1$ , heavily in regions far removed from observations; the degree of influence exerted by  $(u,v)_1$  is inversely related to the value of the parameter  $R_1$ . The exponent,  $n$ , controls the relative influence of observations distant from a given grid point. Goodin and co-workers suggest that  $n$  should be 2 for a relatively dense set of surface observations, and 1 for a relatively sparse set of upper-air observations.

Several constraints can be placed on the evaluation of Equation 4-19 at the option of the user. A maximum radius of influence,  $R_{\max}$ , may be specified; if  $r_k > R_{\max}$ , the observation at station  $k$  is excluded from Equation 4-19. If observations are densely spaced and representative of the spatial variability of the air flow,  $R_{\max}$  should be relatively small; otherwise, evaluation of Equation 5-18 may result in unwanted smoothing effects.

Alternatively, a parameter  $K_{\max}$  may be specified that allows inclusion in Equation 4-19 of only the  $K_{\max}$  closest stations. With this parameter the effective maximum radius of influence can increase or decrease depending on local observation density.

Finally, the user may construct barriers by specifying end points of line segments in (x,y) space; if a specified barrier lies between a station and a given grid point, that station is not considered when evaluating Equation 4-19. This technique can be used to reduce or eliminate deleterious effects on the analysis of stations heavily influenced by local terrain features (e.g., a canyon).

The parameters  $n$ ,  $R_1$ ,  $R_{\max}$ , and  $K_{\max}$  as just defined are specified separately for surface and upper-air observations. Each barrier specification will include a specification of the maximum model vertical grid level at which the barrier will be applied.

Smoothing of the Analyzed Wind Field. Goodin and co-workers (1980) indicate the desirability of smoothing the gridded wind field resulting from Equation 4-19. Thus, a simple five-point smoothing of the form

$$A_{sm}(i,j) = 0.2[A(i,j) + A(i+1,j) + A(i-1,j) + A(i,j-1) + A(i,j+1)] \quad (4-20)$$

may be applied to  $(u,v)'$ . Although Goodin and co-workers indicate that the amount of smoothing should be an increasing function of atmospheric stability, we prefer to simply specify the number of smoothing passes (usually no more than three) at each model vertical level. Smoothing of the gridded wind field speeds up the divergence minimization procedure. However, it should also be noted that overuse of such smoothing can obliterate important air flow features (e.g., a well-defined sea-breeze convergence zone).

Computation of Vertical Velocity. An initial field of vertical velocities in terrain-parallel coordinates,  $W'$ , is computed from  $(u,v)'$  by integrating the equation for incompressible conservation-of-mass (Equation 4-3). The resulting three-dimensional velocity field is thus mass-consistent. However, Godden and Lurmann (1983) note that vertical velocities obtained from objectively analyzed  $(u,v)$  fields may be unrealistically large near the top of the model domain. Godden and Lurmann utilize a procedure suggested by O'Brien (1970) to modify  $W'$ :

$$W_2(Z) = W'(Z) - (Z/Z_{top}) W'_{top} \quad (4-21)$$

Note that  $W_2$  is zero at the model top and is not mass-consistent with  $(u,v)'$ . We believe that there may be situations in which utilization of

the O'Brien procedure may not be desirable; for example, the model top may pass through a well-resolved sea-breeze convergence zone within which a large  $W$  value is legitimate (not an issue in the Rocky Mountains). Thus, in this model, imposition of Equation 4-21 is an option. If Equation 4-21 is not invoked, the final product of the model,  $(u,v)_2$ , is equal to  $(u,v)'$ .

Minimization of Three-Dimensional Divergence. If Equation 4-21 is invoked, it is necessary to adjust the objective analysis product,  $(u,v)'$ , so that it is mass consistent with  $W_2$ . The divergence minimization procedure described at the beginning of Section 4.1.2.2 is exercised with  $(u,v)'$  as a first-guess horizontal wind field and with  $W_2$  held constant. The adjusted horizontal wind field,  $(u,v)_2$ , is the final product of the diagnostic model.

## 4.2 EVALUATION OF THE DIAGNOSTIC WIND MODEL

We carried out a preliminary evaluation of the new diagnostic wind model (DWM) in the same manner as our evaluation of the candidate wind models (see Section 2). The DWM was exercised on both the hypothetical bell-shaped mountain described in the review report (Section 5.1.2; Morris and Kessler, 1987) and the Rocky Mountain terrain (see Section 2 here). For these tests the model was run without input of mesoscale observational data, with an initially uniform flow.

The new DWM is also evaluated using observations from the Rocky Mountain region. These simulations illustrate the ability of the new DWM to assimilate observational data into its mesoscale wind field. Simulations are carried out with all wind observations, and then without some of the observations so that the model predictions can be compared with observations not used in its wind field generation procedure.

As an illustration of the applicability of the new DWM, the DWM was exercised for two completely new and different terrain configurations. The first is a coastal/complex terrain environment with a dense network of wind observations; the second is within a large valley where the wind pattern is dominated by complicated slope flows. In the latter simulation the flexibility and adaptability of the new DWM is further illustrated by the use of output from two-dimensional simulations of a primitive equation mesoscale meteorological model used as input to the DWM.

### 4.2.1 Flow Over Idealized Terrain

Three simulations of flow over a bell-shaped mountain were carried out. In simulation A1 an isothermal atmosphere is assumed and slope flow

effects are excluded. Simulation A2 is identical to simulation A1 except that slope flow effects are added, with the slope flow parameterization tuned to produce maximum downslope flow of approximately  $2 \text{ m s}^{-1}$  at the 50 m level only. Simulation A3 is similar to simulation A2 except that the atmosphere is assumed to be neutrally stratified and the slope flow parameterization is tuned to produce maximum upslope flow of approximately  $2 \text{ m s}^{-1}$  at the 50 m level.

As in the previous tests, an initially uniform flow of  $2 \text{ m s}^{-1}$  from the West ( $270^\circ$ ) was specified. The model grid specifications are identical to those reported in the review report (Morris and Kessler, 1987).

Figure 4-1 shows the wind fields predicted by DWM under simulation A1 at 50, 200, and 500 m above ground. The parameterization of blocking effects produces marked deflection of flow upwind of the mountain top at each of these levels, while the mountain top acceleration due to terrain kinematic effects is most apparent at the 50 m level. Although the blocking parameterization in DWM is essentially that of MELSAR, the results in Figure 4-1 differ substantially from those of the MELSAR simulation (depicted in Figure 5-2 of the review report) for two reasons: (1) the methods of computing obstacle heights in the two models are different; and (2) the MELSAR polynomial representation of the wind field tends to act as a smoother.

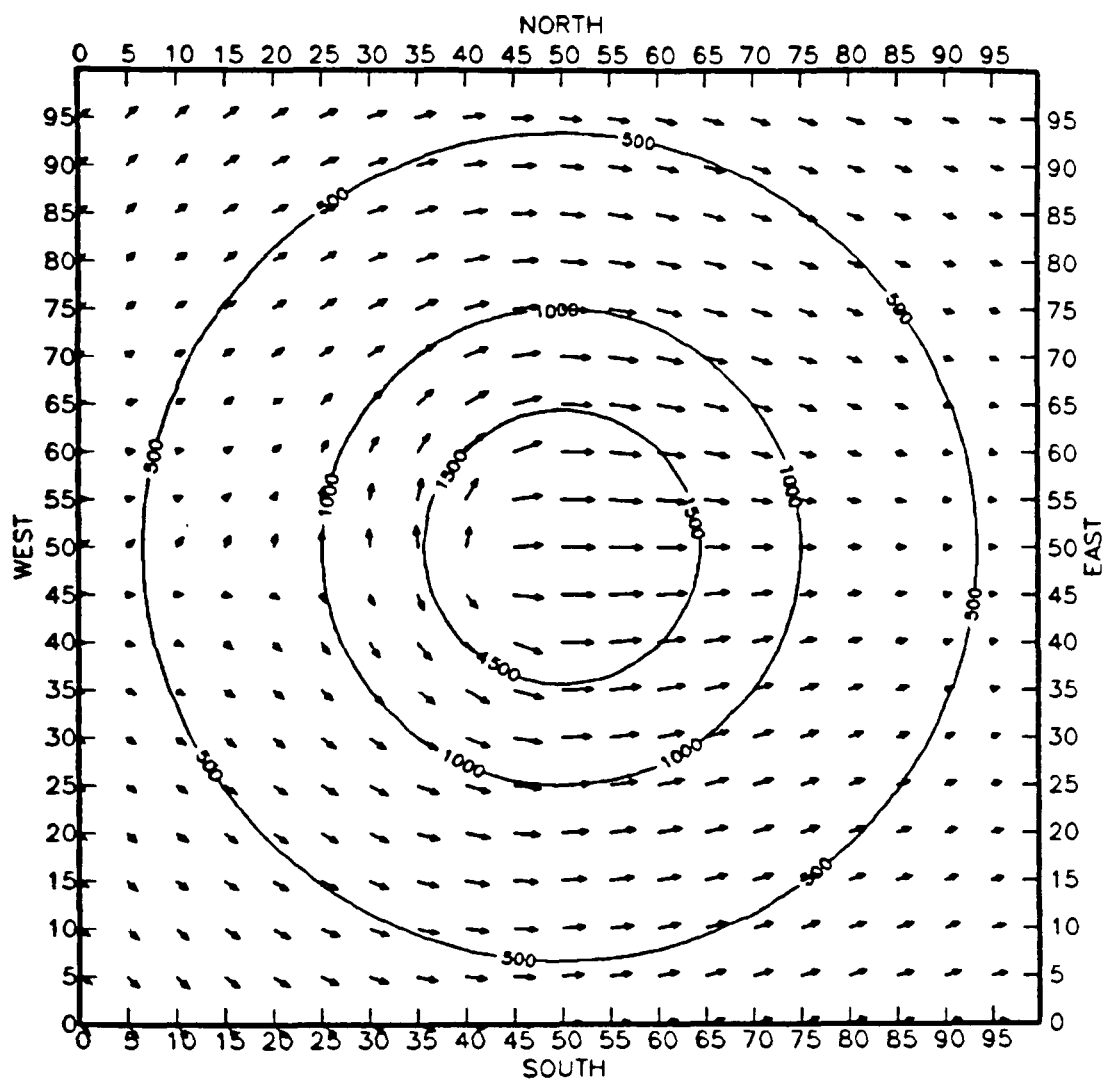
Figure 4-2 shows the results of simulation A2. At the 50 m level results are qualitatively similar to those obtained with the CTWM for downslope flow (Figure 5-6 of the review report) although the slope flow magnitude is weaker. However, at the 200 m and 500 m levels the results of simulation A2 are nearly identical to those of simulation A1; the spurious "return" flow produced by the transformed CTWM does not appear in the corresponding DWM simulation.

Model results for simulation A3 at the 50 m level reflect the combination of the kinematic effects of terrain and the imposed upslope flow (Figure 4-3). The levels above are minimally effected; blocking effects are absent given the assumed neutral stratification.

#### 4.2.2 Flow Over Rocky Mountain Terrain

We carried out three DWM simulations of flow over the Rocky Mountain domain depicted in Figure 2-1. Simulations B1, B2, and B3 are identical respectively to simulations A1, A2, and A3 in idealized terrain except that the Rocky Mountain terrain depicted in Figure 2-1 is substituted for the bell-shaped mountain. Grid specifications and initial conditions are as described in Section 2.2.

Results of simulation B1 are depicted in Figure 4-4. Simulation B1 is most directly comparable to the MELSAR and ATMOS1 simulations depicted in

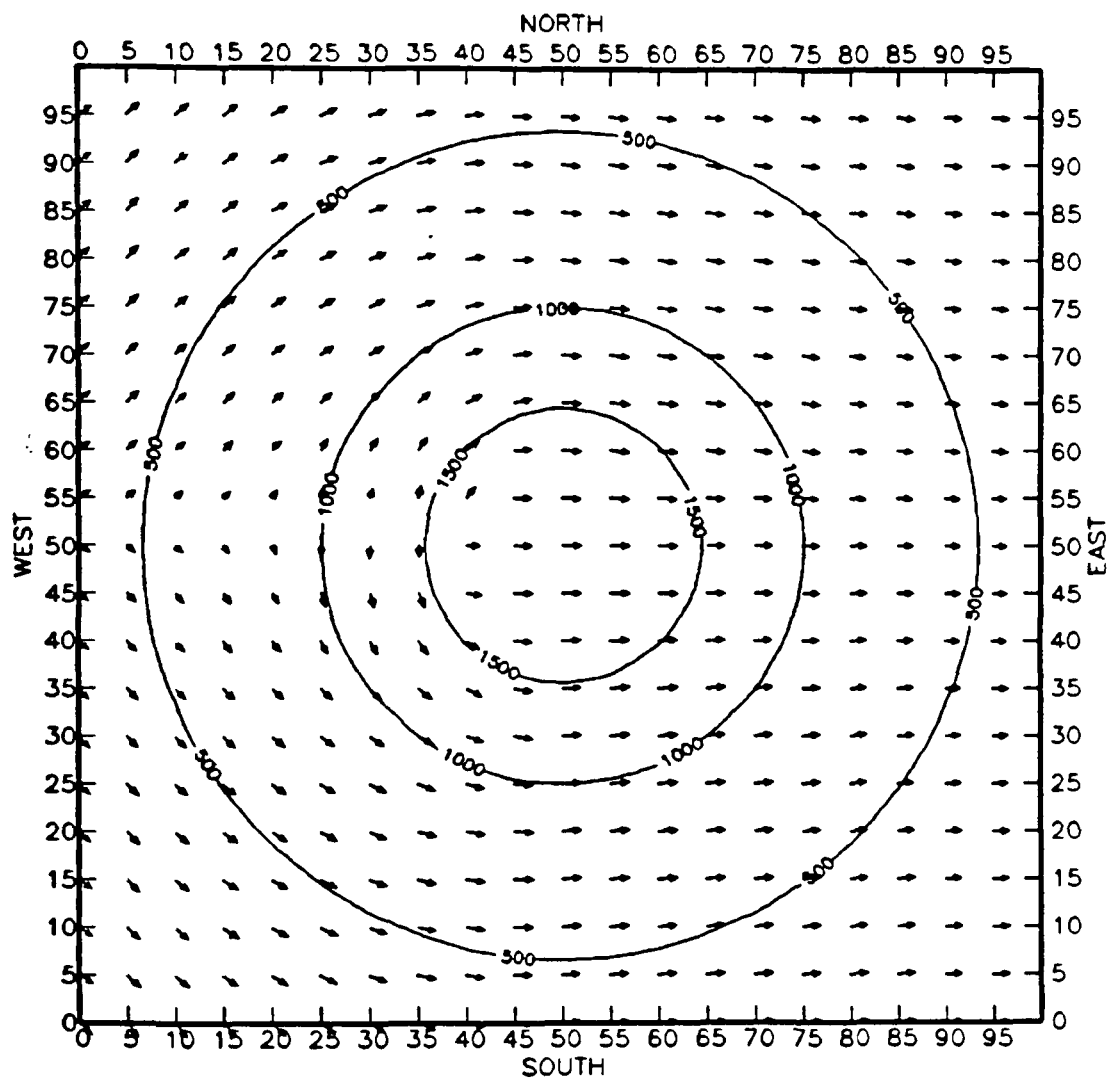


DWM WIND VECTORS AT LEVEL = 1

0 5 10 15

WIND SPEED (M/S)

FIGURE 4-1a. Winds generated by the Diagnostic Wind Model for simulation A1 at 50 m above ground. Scaling of plotted winds is given at lower left. Topography is contoured in meters. Horizontal grid spacing is 5 km.

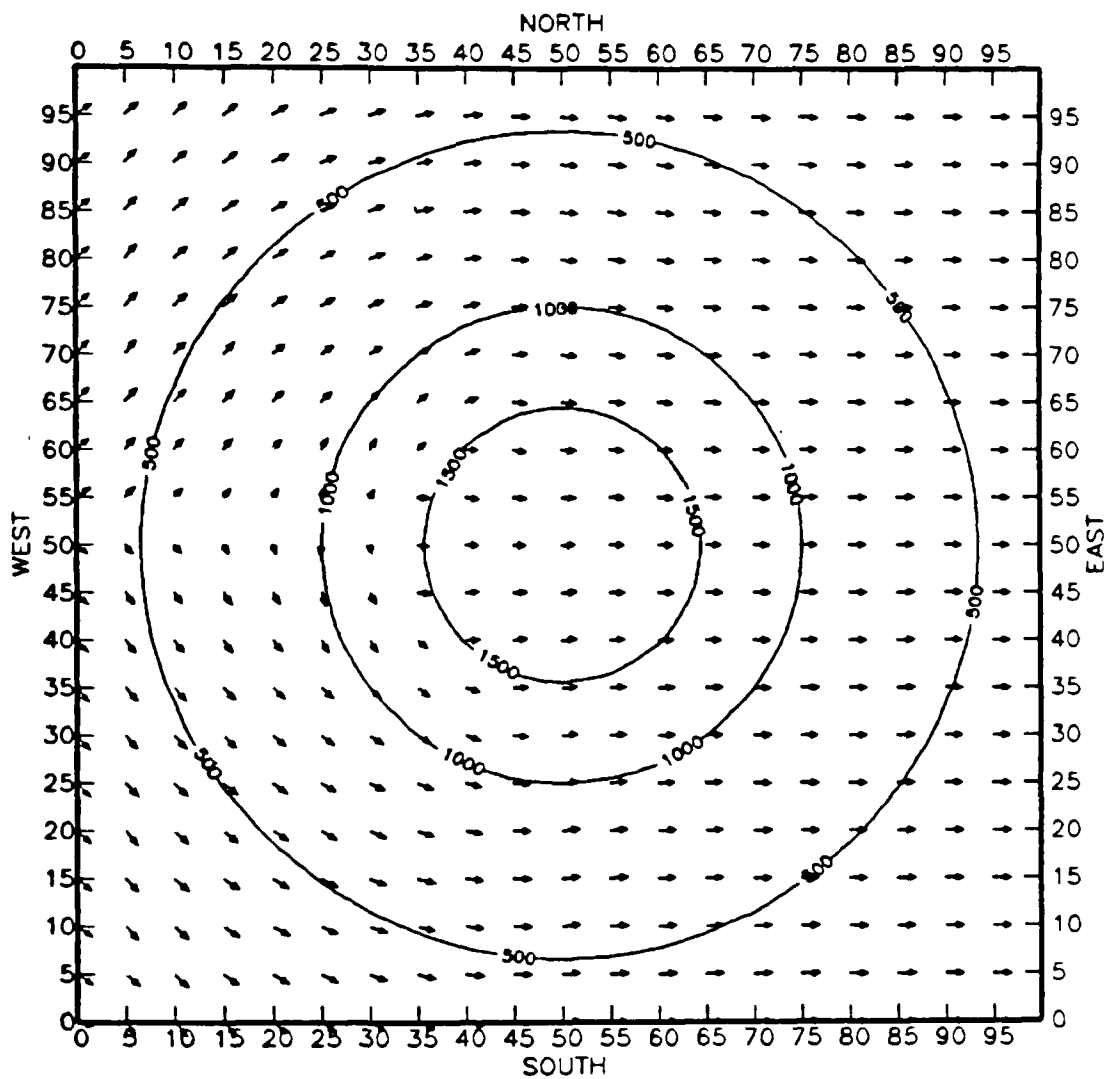


DWM WIND VECTORS AT LEVEL = 2

0 5 10 15

WIND SPEED (M/S)

FIGURE 4-1b. At 200 m.



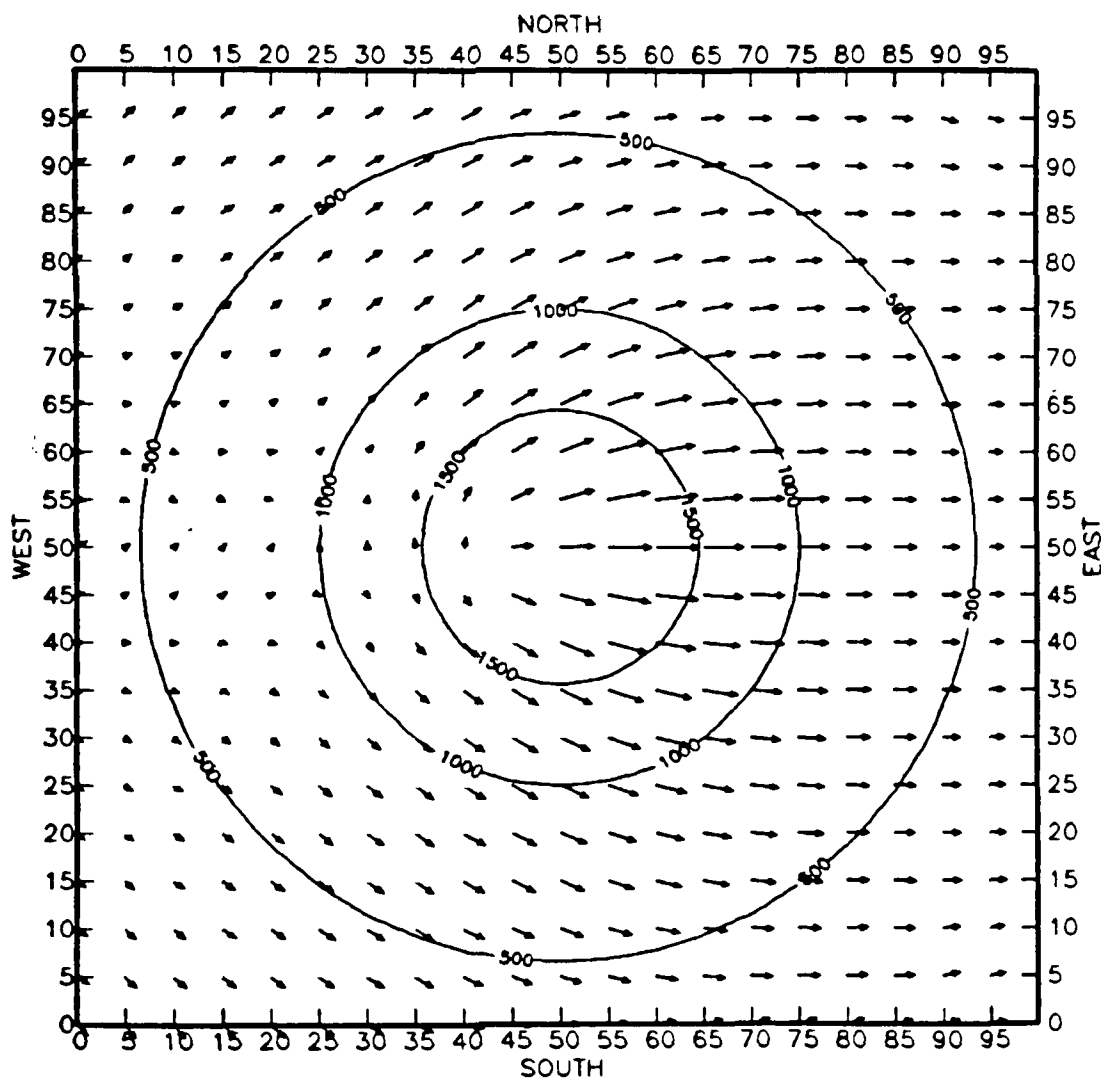
DWM WIND VECTORS AT LEVEL = 3

0 5 10 15

WIND SPEED (M/S)

FIGURE 4-1c. At 500 m.





DWM WIND VECTORS AT LEVEL = 1  
 0 5 10 15  
 WIND SPEED (M/S)

FIGURE 4-2a. Winds generated by the Diagnostic Wind Model for simulation A2 at 50 m above ground. Scaling of plotted winds is given at lower left. Topography is contoured in meters. Horizontal grid spacing is 5 km.

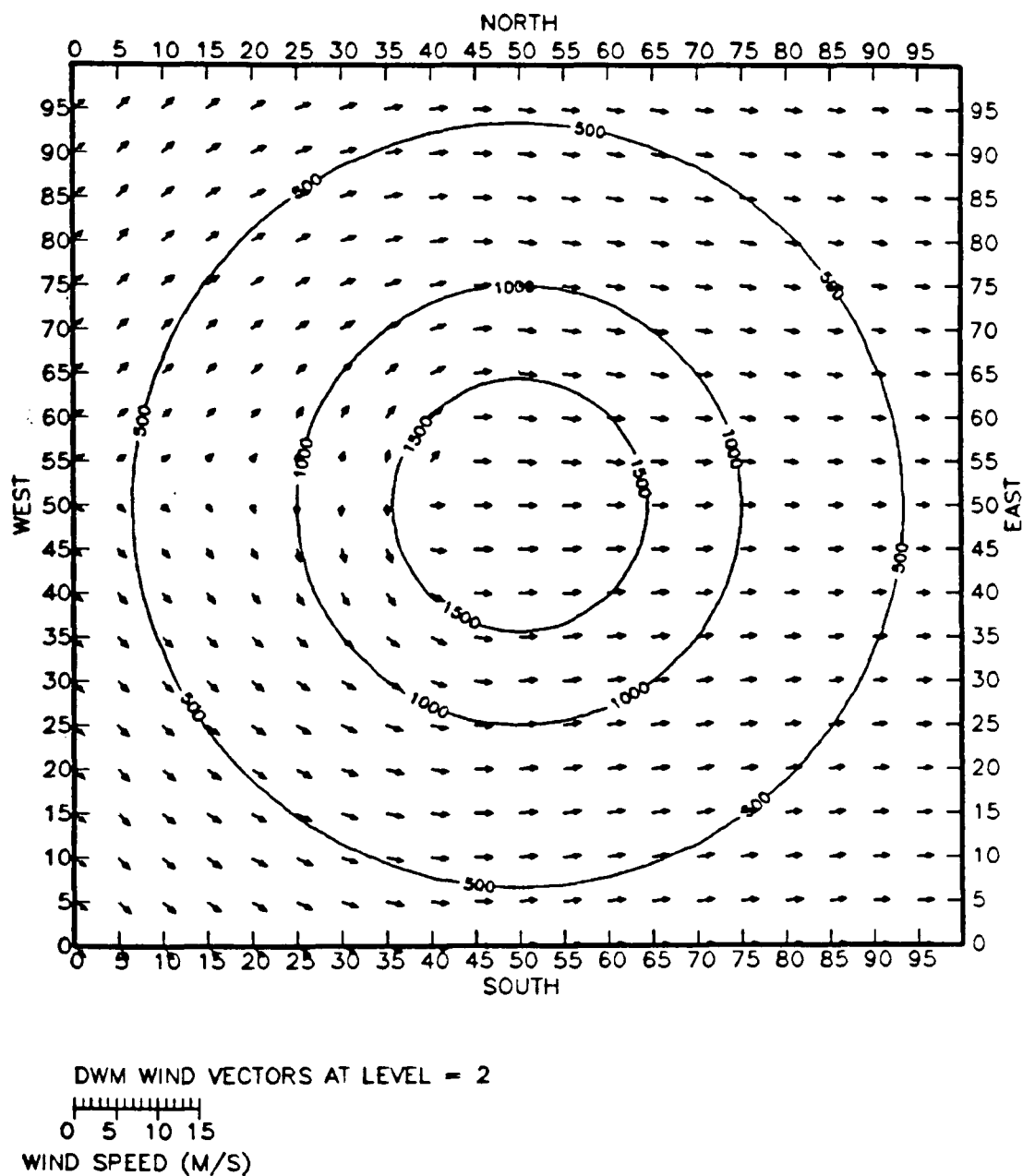


FIGURE 4-2b. At 200 m.

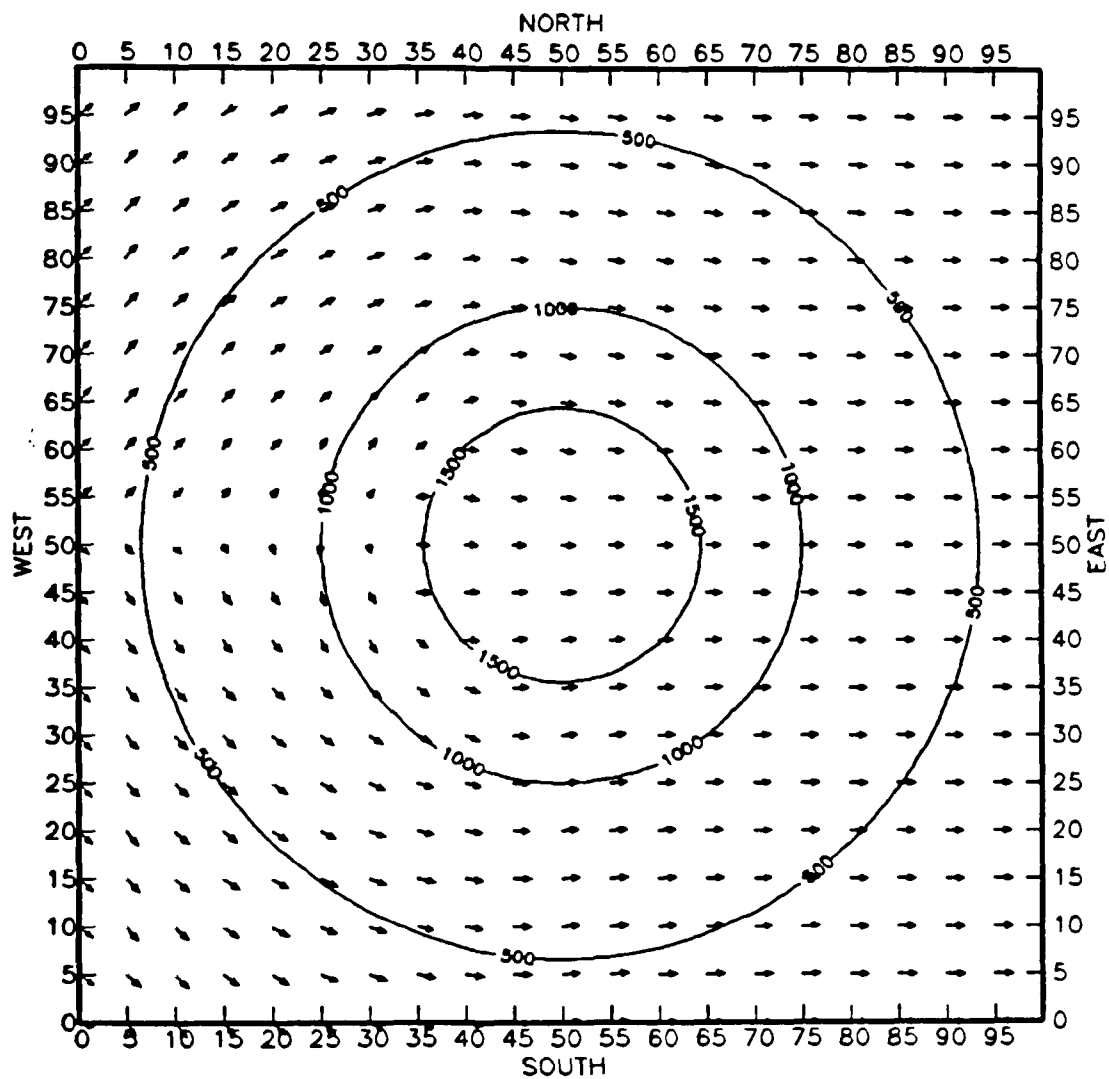


FIGURE 4-2c. At 500 m.

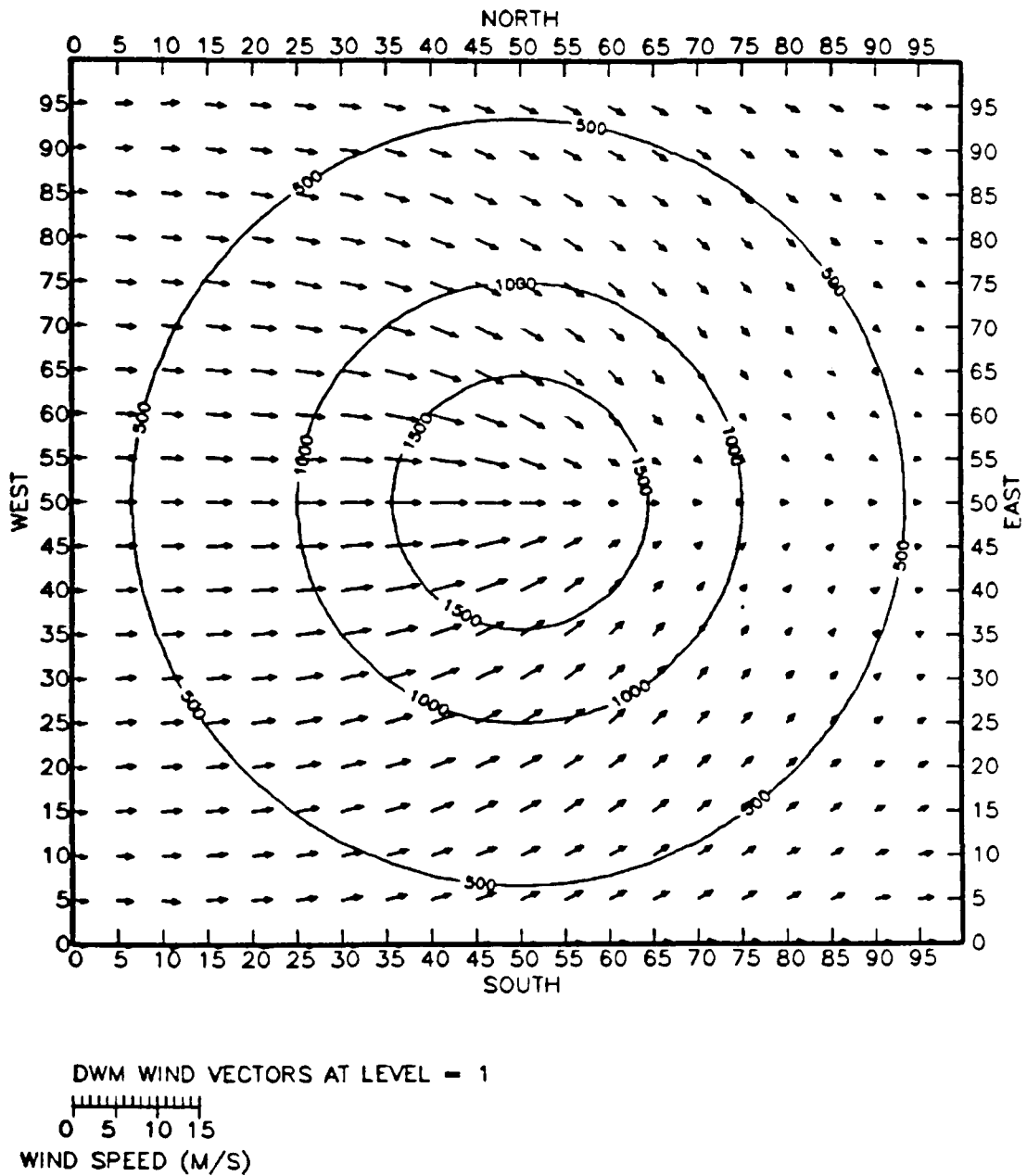
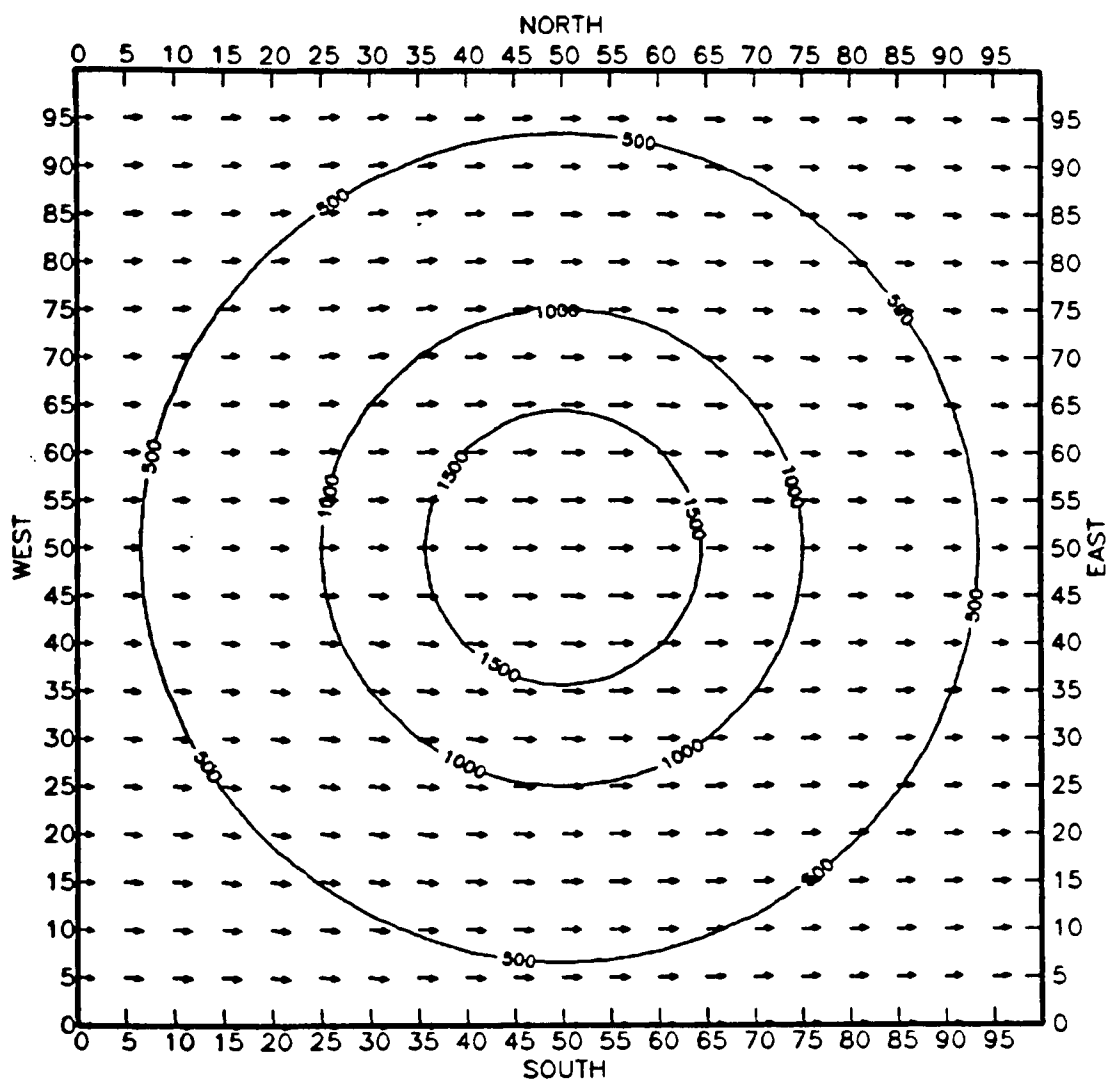


FIGURE 4-3a. Winds generated by the Diagnostic Wind Model for simulation A3 at 50 m above ground. Scaling of plotted winds is given at lower left. Topography is contoured in meters. Horizontal grid spacing is 5 km.

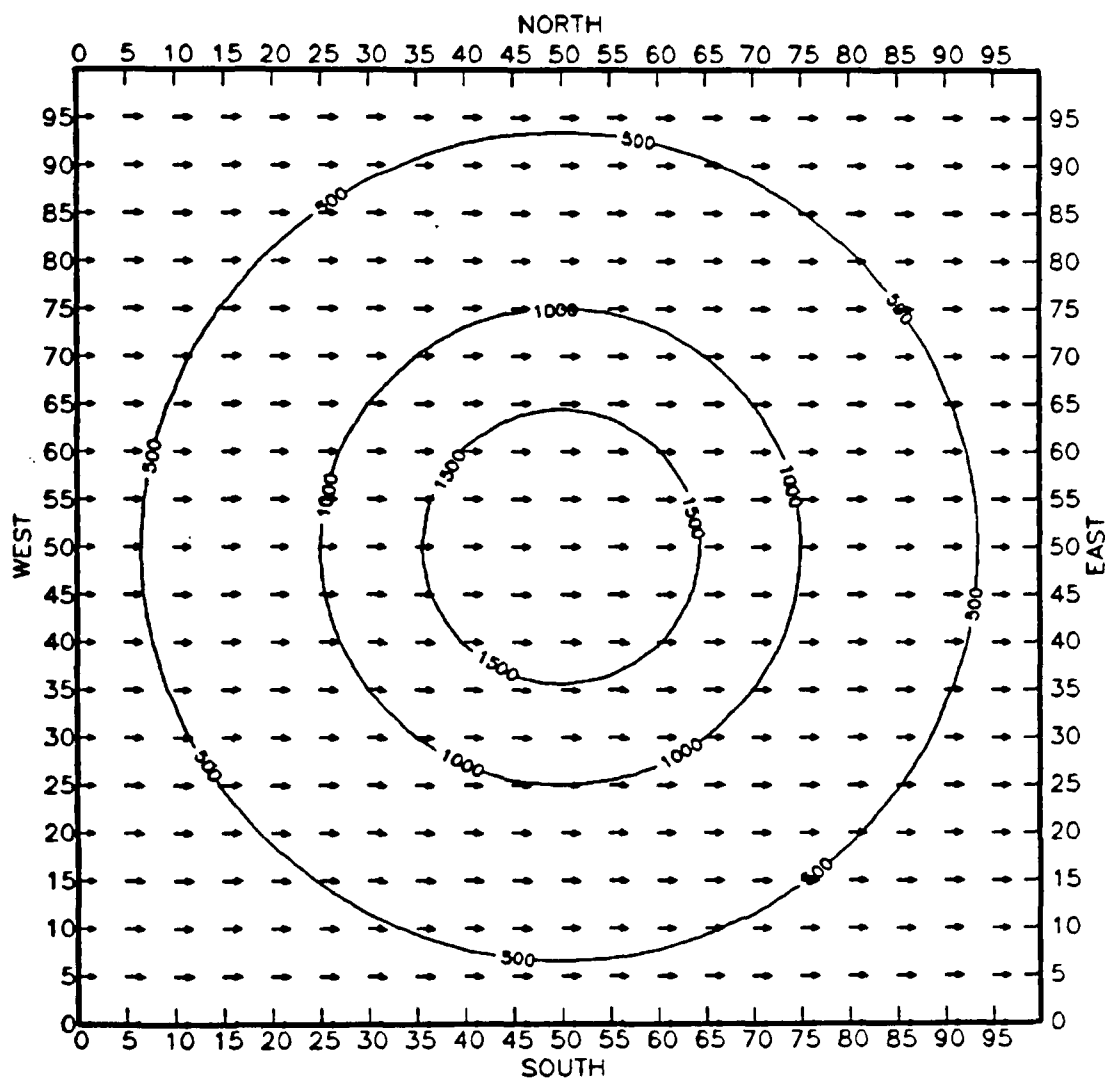


DWM WIND VECTORS AT LEVEL = 2

0 5 10 15

WIND SPEED (M/S)

FIGURE 4-3b. At 200 m.



DWM WIND VECTORS AT LEVEL = 3

0 5 10 15

WIND SPEED (M/S)

FIGURE 4-3c. At 500 m.

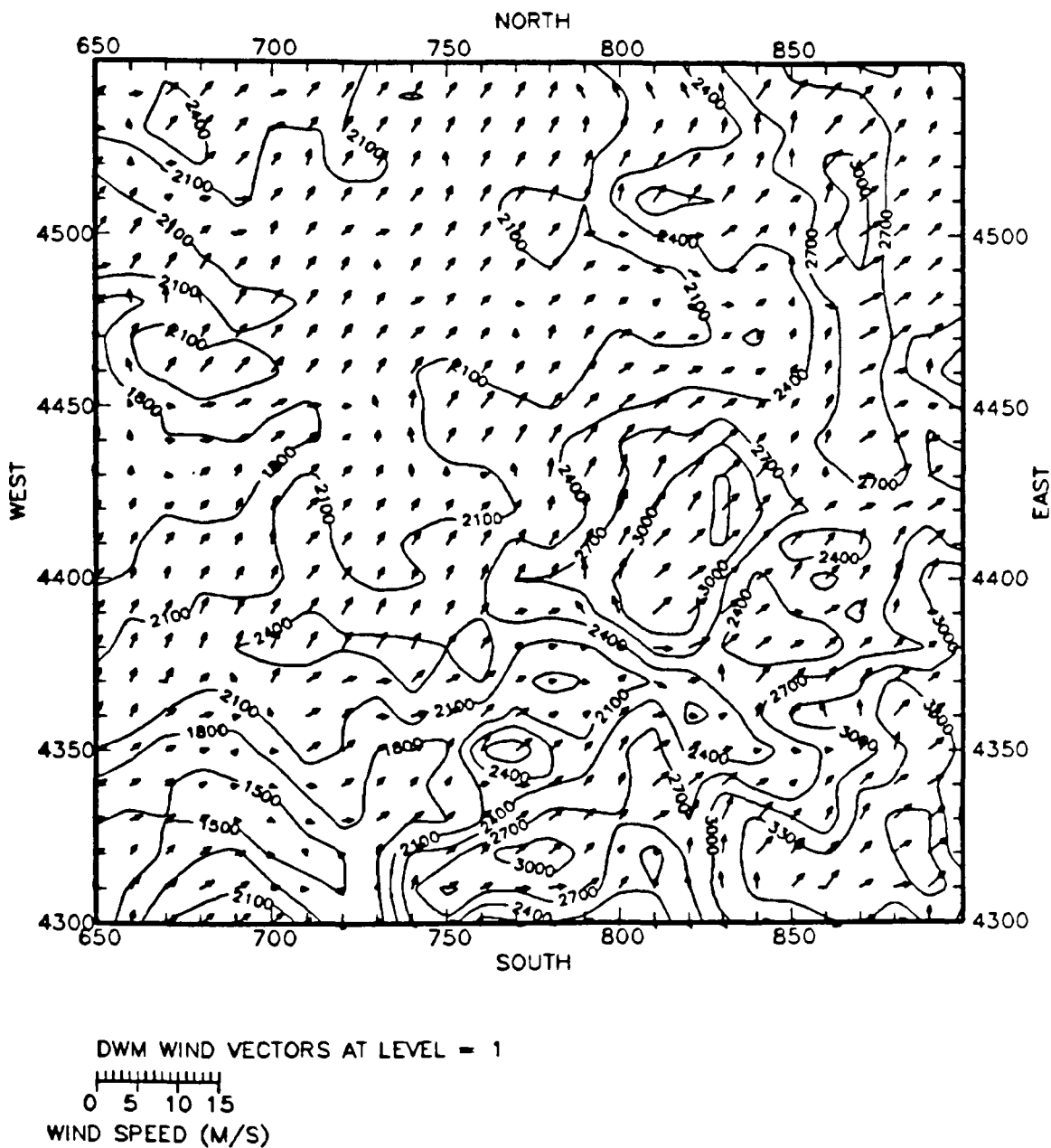


FIGURE 4-4a. Winds generated by the Diagnostic Wind Model for simulation B1 at 50 m above ground. Scaling of plotted winds is given at lower left. Topography is contoured in meters. Horizontal grid spacing is 10 km.

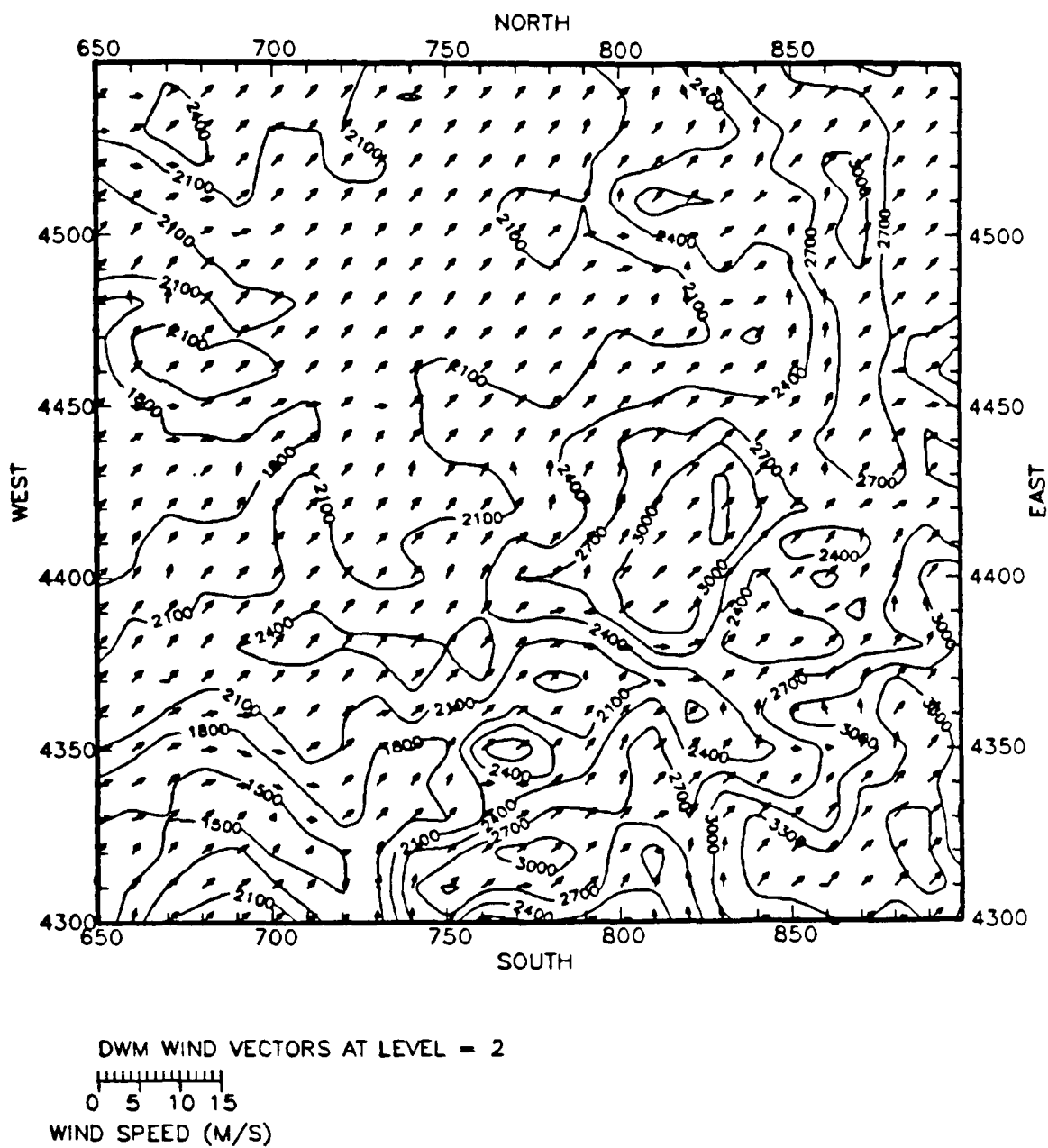
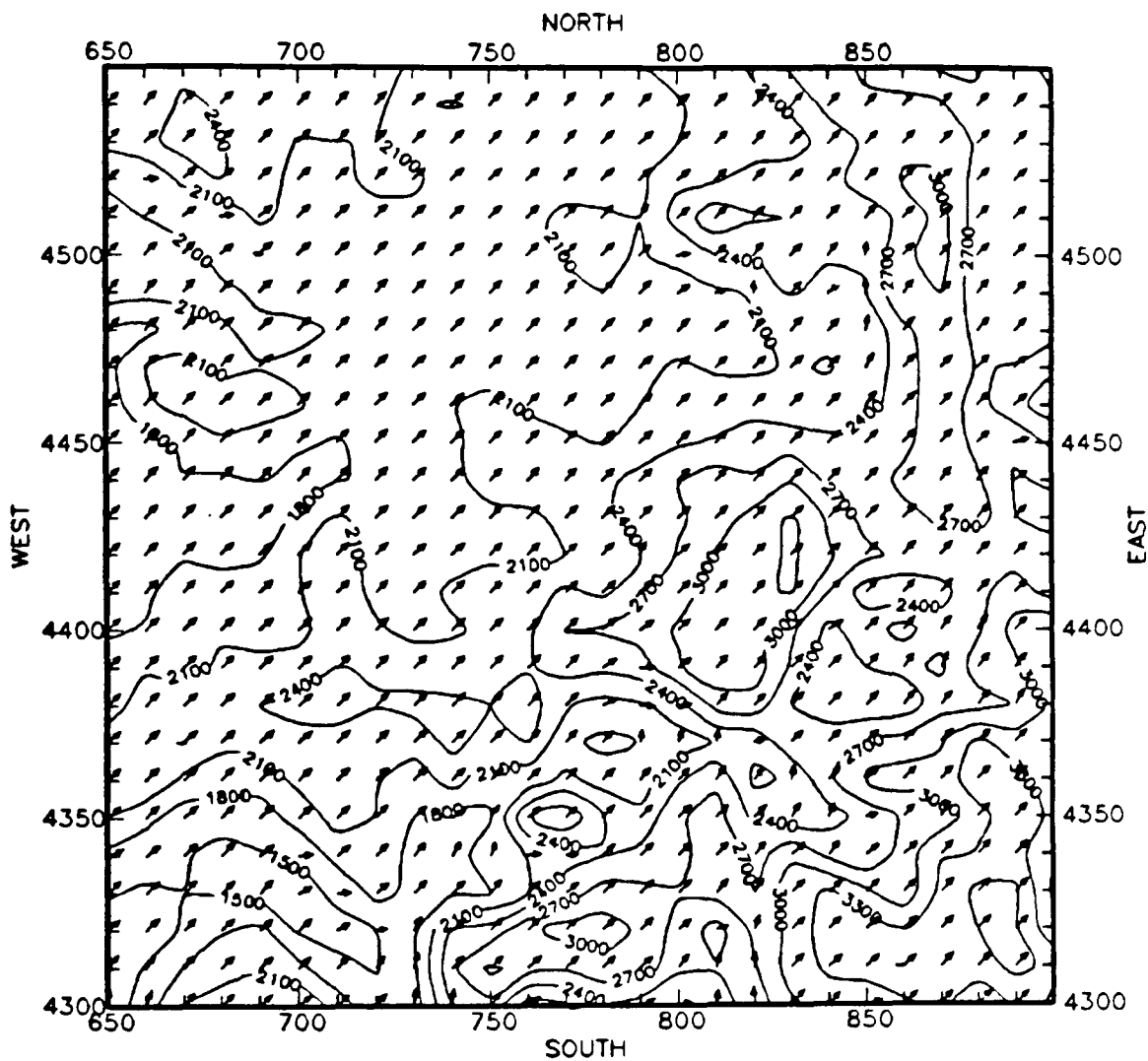


FIGURE 4-4b. At 200 m.





DWM WIND VECTORS AT LEVEL = 3

0 5 10 15

WIND SPEED (M/S)

FIGURE 4-4c. At 500 m.

Figures 2-3 and 2-4, respectively. Like ATMOS1, and unlike MELSAR, the DWM appears to respond on the characteristic horizontal terrain scales. The differences in the ATMOS1 and DWM solutions are most apparent to the lee of terrain obstacles, for two reasons: (1) the DWM includes a direct parameterization of blocking that operates upstream but not downstream of an obstacle; and (2) the DWM includes a smoothing operation, while ATMOS1 does not.

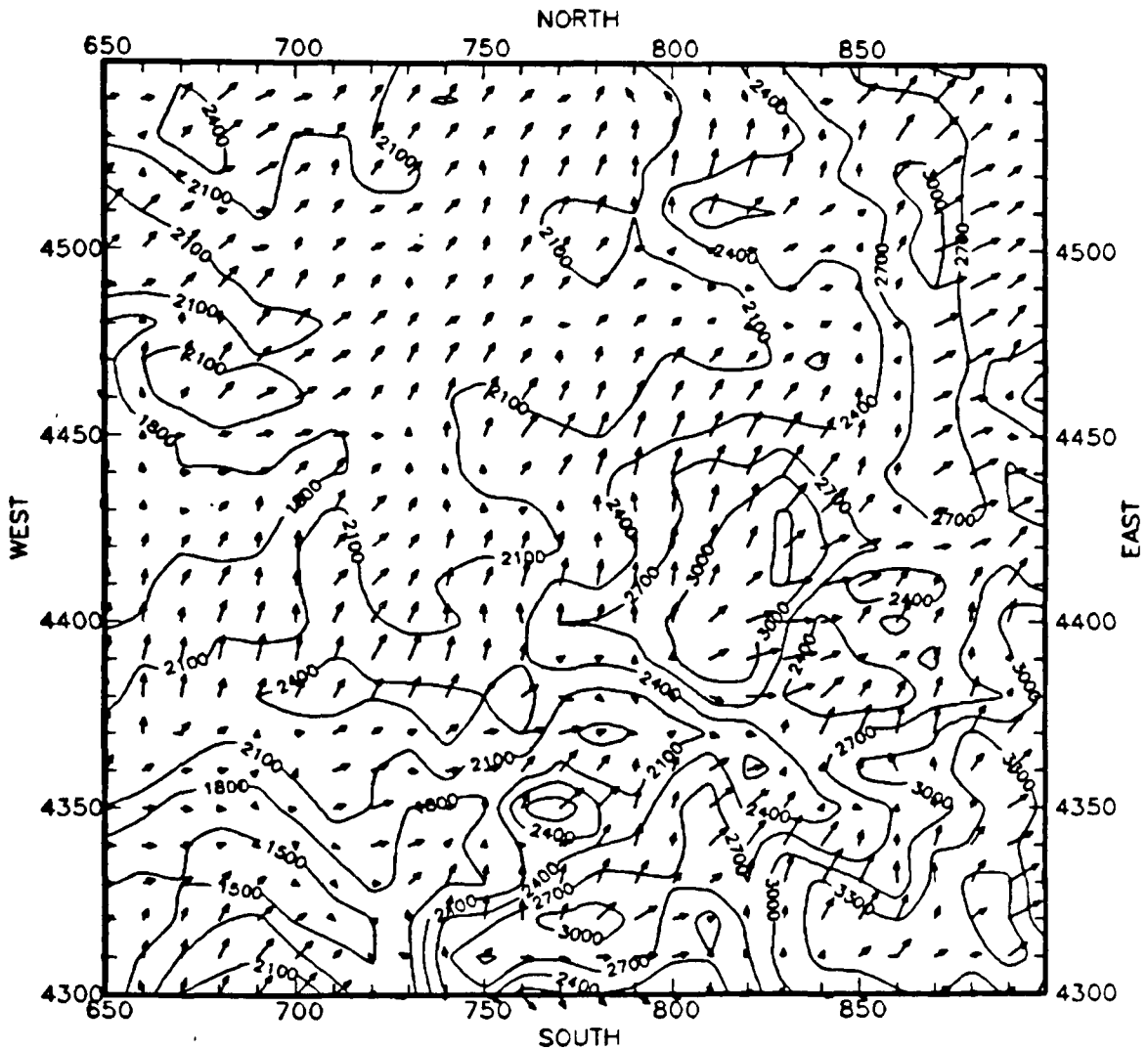
Results of simulations B2 and B3 are depicted in Figures 4-5 and 4-6 respectively. In simulation B2 downslope flow vectors are added at the 50 m level to the corresponding field obtained in simulation B1; at upper levels the wind fields from simulations B1 and B2 are nearly identical. In simulation B3 the lowest level reflects the addition of upslope flow vectors. Upper levels are essentially undisturbed; the parameterizations of terrain kinematic effects and blocking effects are essentially inoperative in the assumed neutral atmosphere.

#### 4.2.3 Evaluation of the New DWM Using Observations from the Rocky Mountains

Using the same mesoscale domain in the Rocky Mountains that was used in the previous tests, we exercised the new DWM with surface and upper-air measurements. The DWM was exercised from 1600 on 17 September 1984 to 1500 on 18 September 1984 to produce hourly gridded wind fields in six vertical layers. This period was selected because of the availability of supplementary radiosonde observations at three sites within the mesoscale modeling domain. These three supplemental observations (Meeker, Rangely, and Rifle, CO) were collected as part of the Atmospheric Studies in Complex Terrain (ASCOT) Brush Creek experiments. Although many more meteorological measurements were available within Brush Creek Canyon itself, this canyon is very narrow and measurements made within it are only applicable to the canyon.

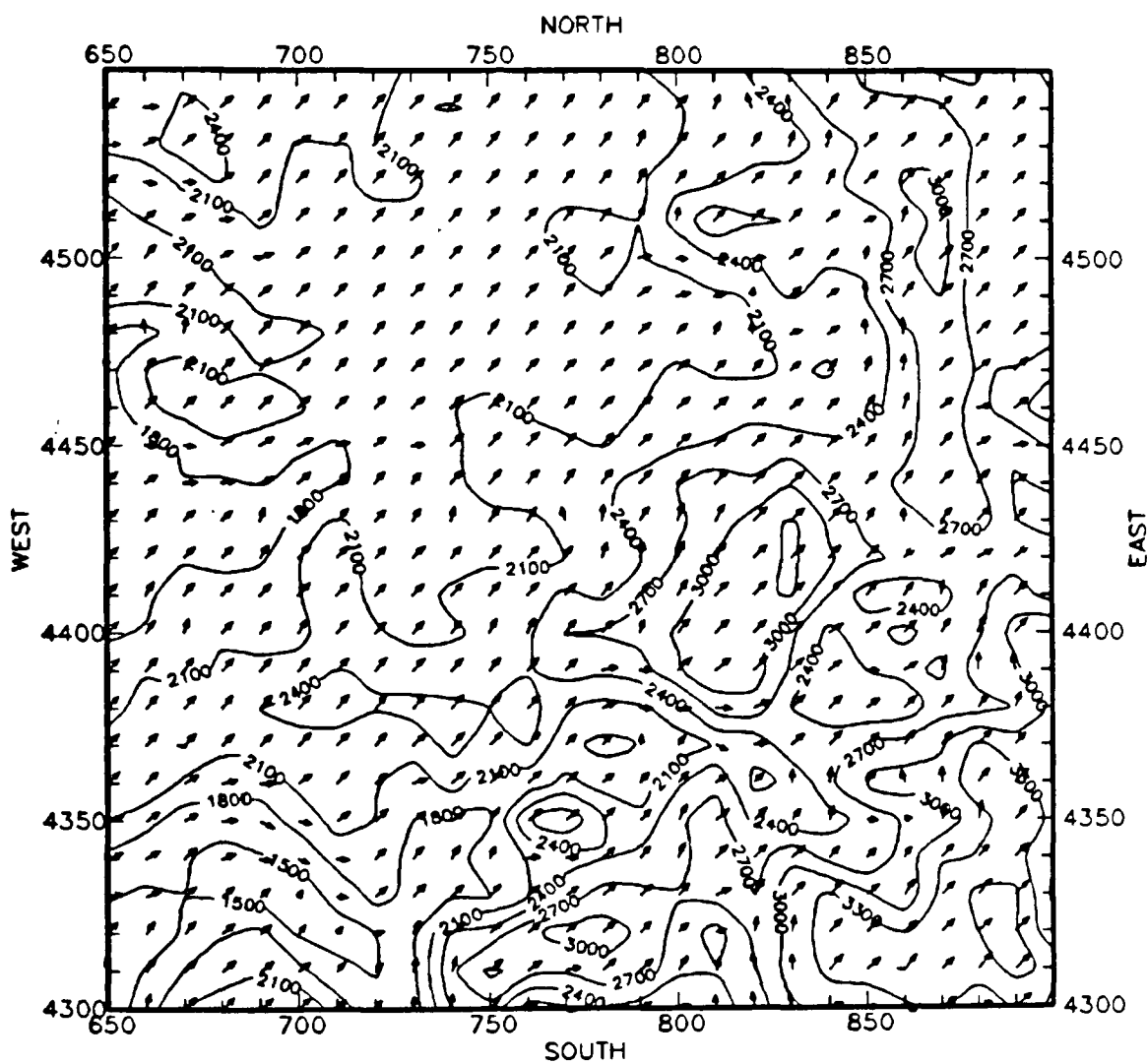
The DWM was exercised twice for each hour of the 24-hour period, once using the routine NWS data only and once with the supplemental data. In this manner the DWM can be evaluated by qualitatively comparing the wind fields generated with and without the supplemental data and performing a quantitative performance evaluation of the DWM by comparing the predicted wind speeds and wind direction from the simulation without the supplemental data with the supplemental data.

The ASCOT Brush Creek experiments were designed to study drainage winds in the Brush Creek canyon. The formation of drainage winds generally requires clear stagnant nights. If there is significant synoptic flow it will over power the drainage winds.



DWM WIND VECTORS AT LEVEL = 1  
 0 5 10 15  
 WIND SPEED (M/S)

FIGURE 4-5a. Winds generated by the Diagnostic Wind Model for simulation B2 at 50 m above ground. Scaling of plotted winds is given at lower left. Topography is contoured in meters. Horizontal grid spacing is 10 km.

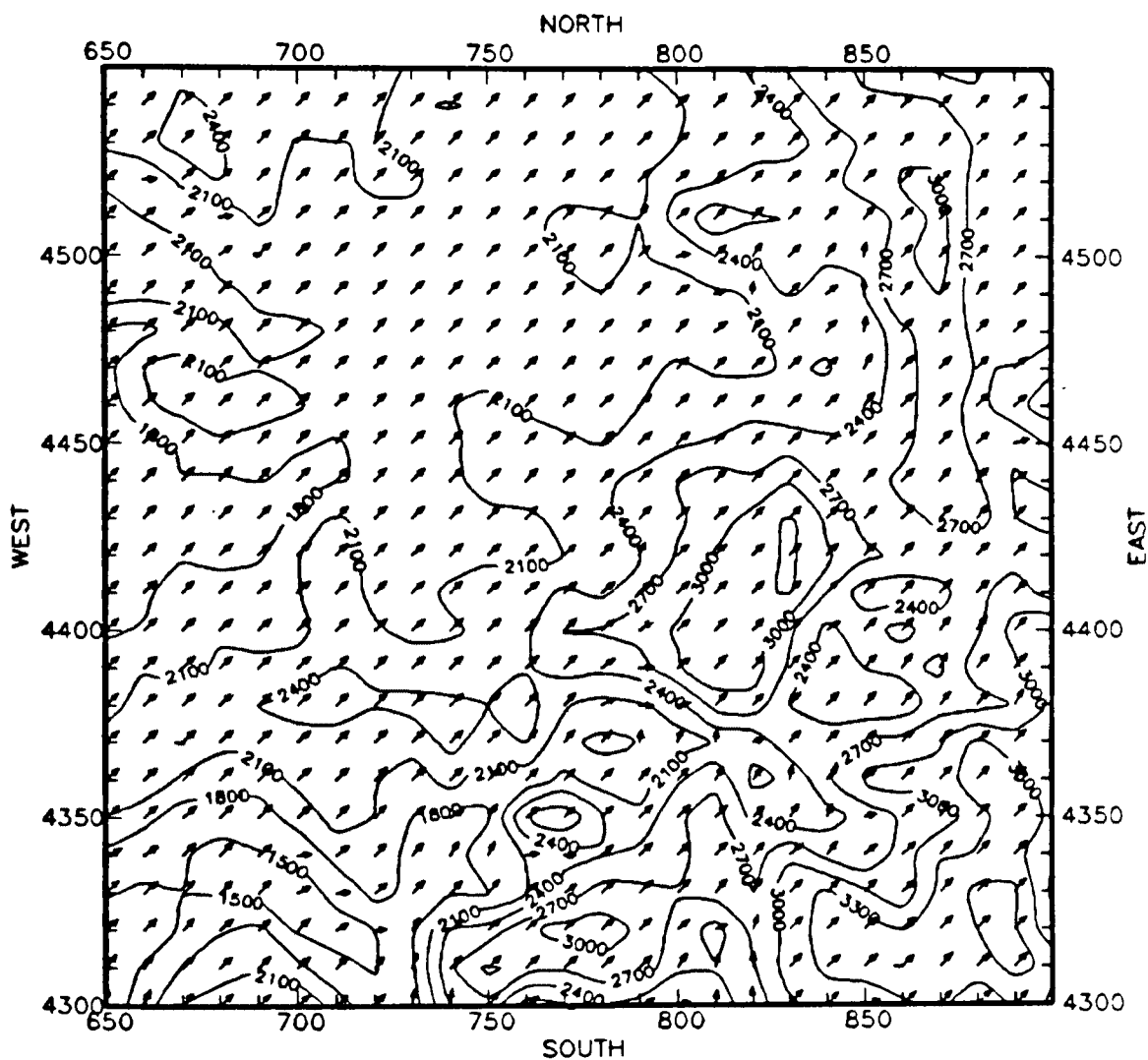


DWM WIND VECTORS AT LEVEL - 2

0 5 10 15

WIND SPEED (M/S)

FIGURE 4-5b. At 200 m.

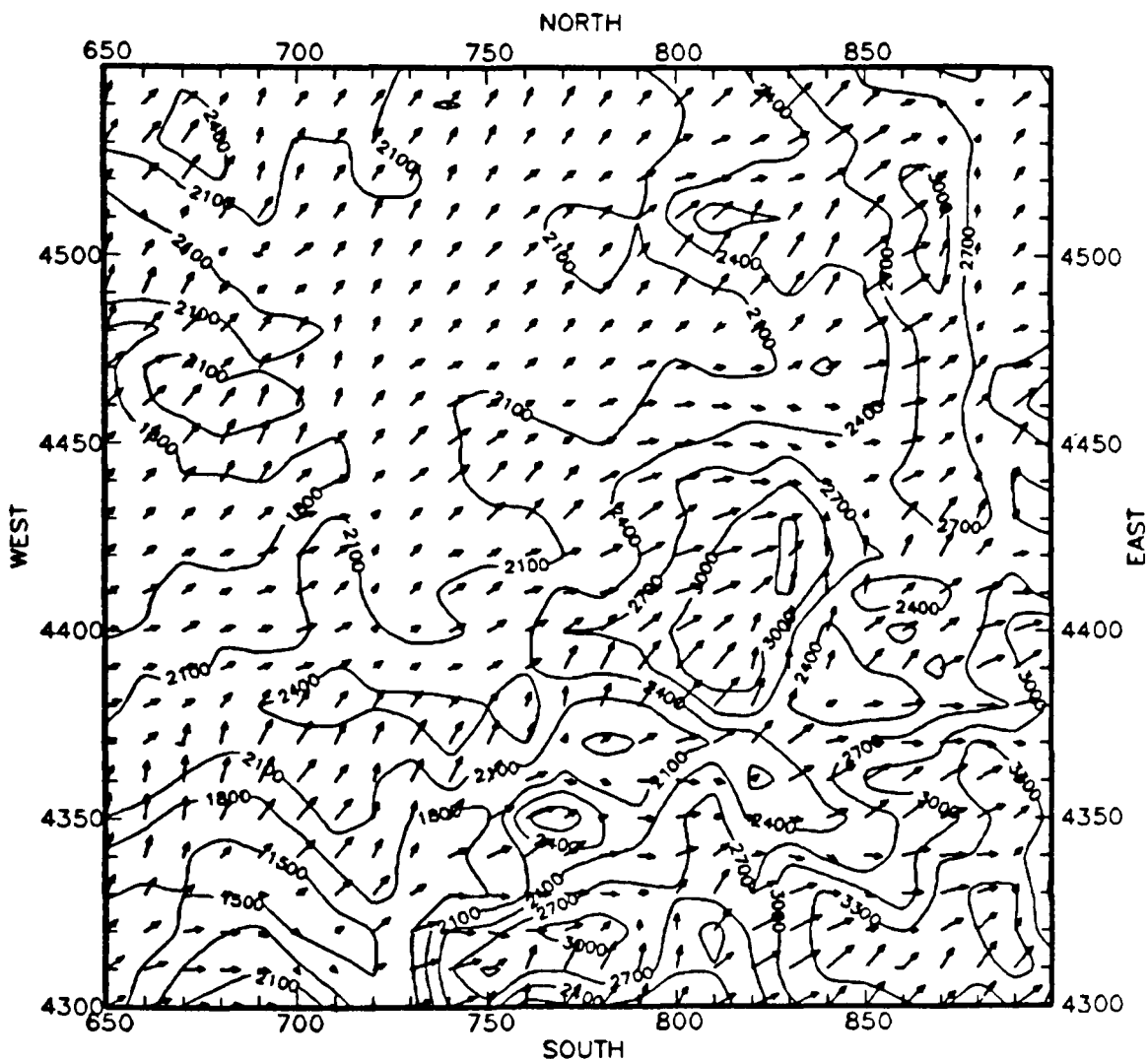


DWM WIND VECTORS AT LEVEL = 3

0 5 10 15

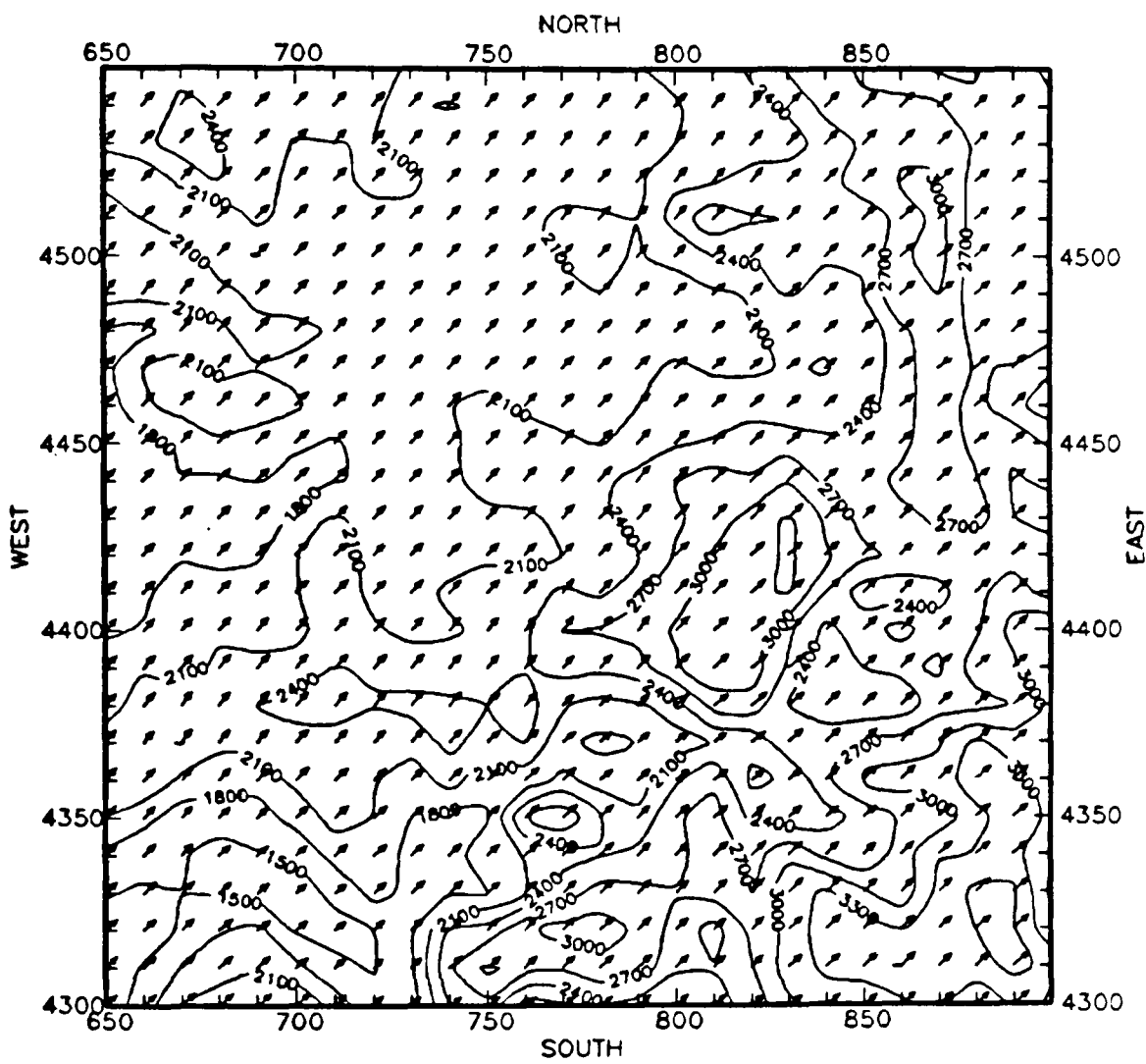
WIND SPEED (M/S)

FIGURE 4-5c. At 500 m.



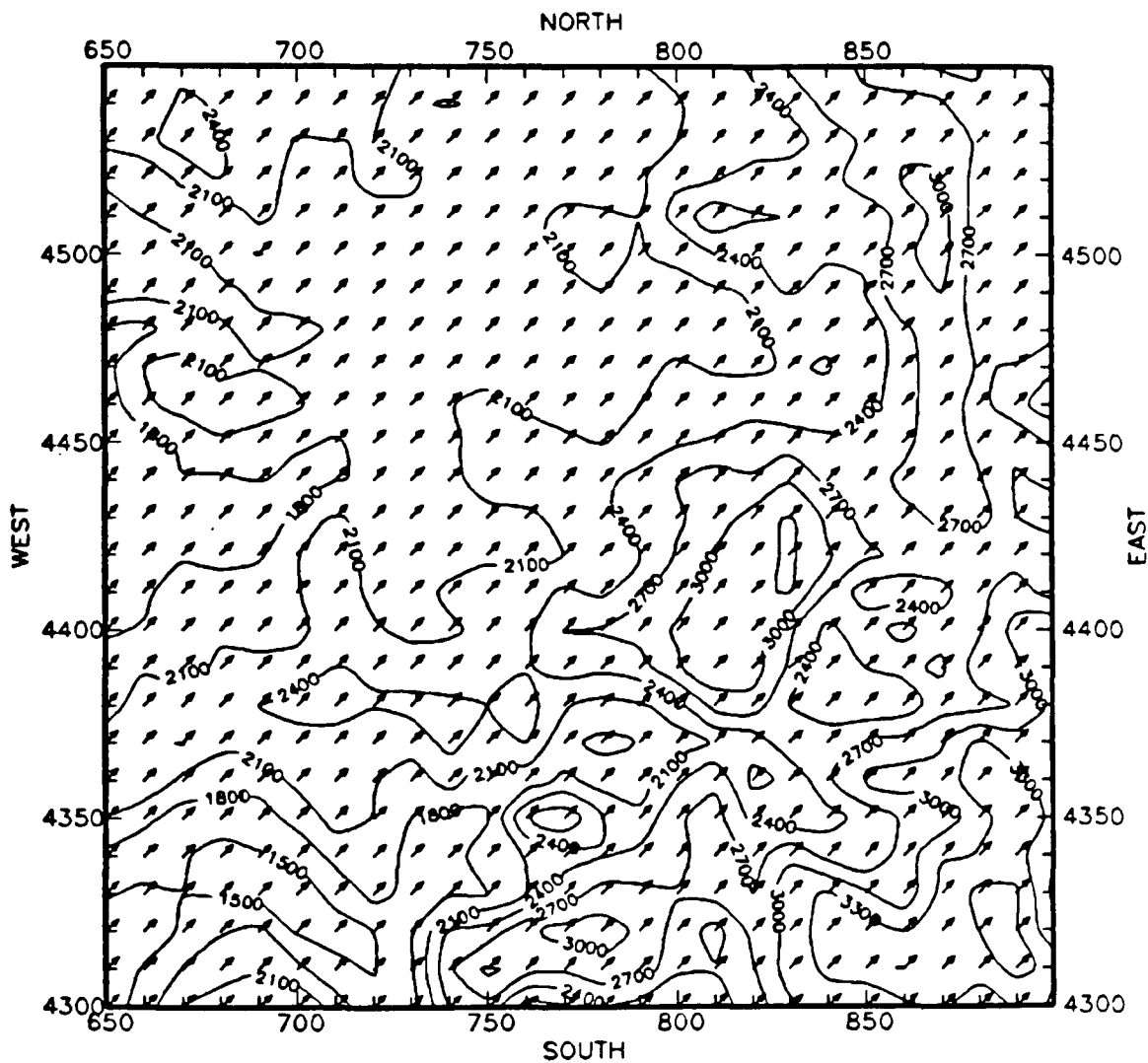
DWM WIND VECTORS AT LEVEL = 1  
 0 5 10 15  
 WIND SPEED (M/S)

FIGURE 4-6a. Winds generated by the Diagnostic Wind Model for simulation B3 at 50 m above ground. Scaling of plotted winds is given at lower left. Topography is contoured in meters. Horizontal grid spacing is 10 km.



DWM WIND VECTORS AT LEVEL = 2  
 0 5 10 15  
 WIND SPEED (M/S)

FIGURE 4-6b. At 200 m.



DWM WIND VECTORS AT LEVEL - 3

0 5 10 15

WIND SPEED (M/S)

FIGURE 4-6c. At 500 m.



#### 4.2.3.1 Qualitative Evaluation

Figure 4-7 illustrates the DWM-generated wind fields at the six vertical levels at 0500 on 18 September 1984. Figure 4-7 shows the wind fields generated by the DWM in the simulations that used all meteorological observations and the simulations that used just the routine NWS meteorological data. The routine NWS data within the mesoscale modeling domain consisted of an upper-air sounding at Grand Junction (GNDJ) and a surface site at Eagle (EAGL). The three supplemental radiosonde observation sites were located at Meeker (MKR), Rifle (RFL) and Rangely (RNG), Colorado. Additional meteorological observations outside of the mesoscale domain were used as input: Lander, Wyoming (to the north) and Denver, Colorado (to the east).

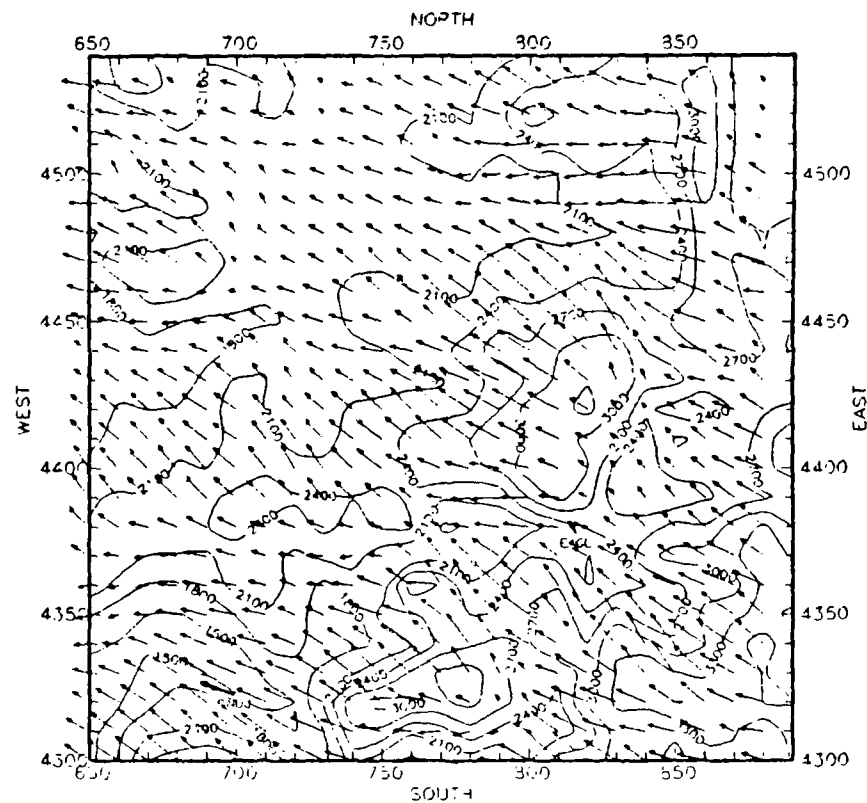
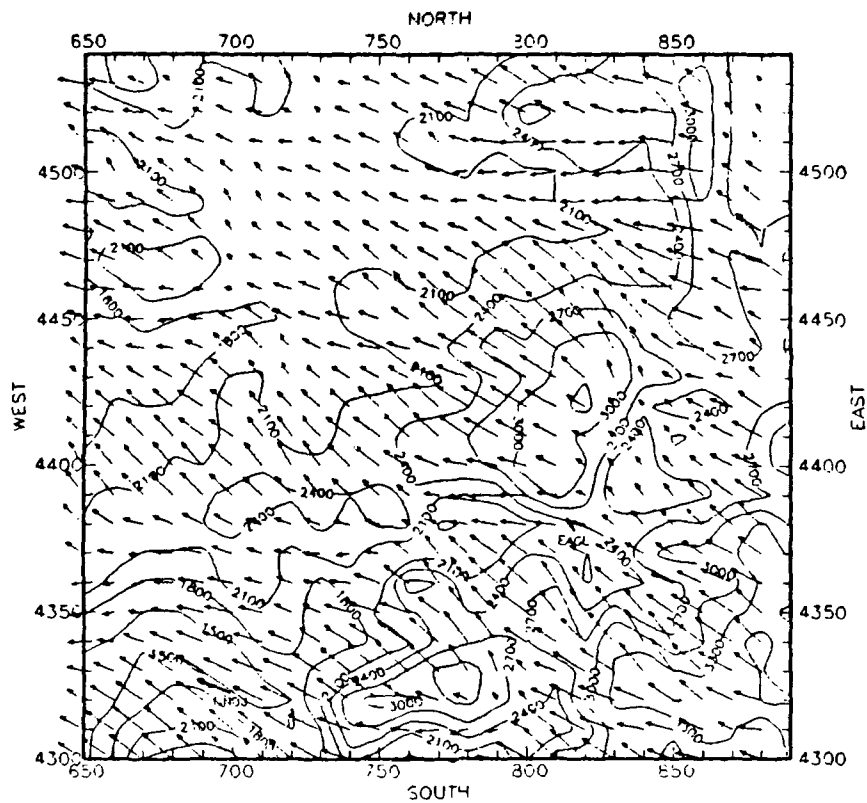
Surface wind fields generated by the DWM with and without the supplemental radiosonde observations are identical. This is because the supplemental observations did not include any observations near the surface. The surface wind fields show significant downslope flow from all of the major terrain features.

For the higher levels the effects of the supplemental data on the DWM wind fields can be seen. Of particular note is that the Rangely sounding appears to be calm from 100 to 1,500 m. The Meeker observation shows winds coming from the southeast at approximately 5 m/s at 100-300 m and then becoming calm until 1500 m. All the upper-air soundings indicate low winds from the southwest at 1500 m. Clearly the power law relationship used to extrapolate surface wind speeds to wind speeds aloft in EPA-approved models is not valid for this time period and location.

Examples of DWM-generated wind fields with and without the supplemental data at 1400 on 18 September are shown in Figure 4-8. Again the surface wind fields with and without the supplemental data are identical, only this time there is upslope flow around the terrain obstacles. For the upper levels the DWM wind fields without the supplemental data are dominated by the Grand Junction sounding, which is recording calm winds away from the surface. These calm winds are not reflected in the Rangely and Meeker supplemental observations; thus the wind fields above the surface are very different in the simulations with and without the supplemental data.

# With Supplemental Observations

# Without Supplemental Observations



DWM WIND VECTORS AT LEVEL = 1 (10M)  
 0 5 10 15  
 WIND SPEED (M/S)

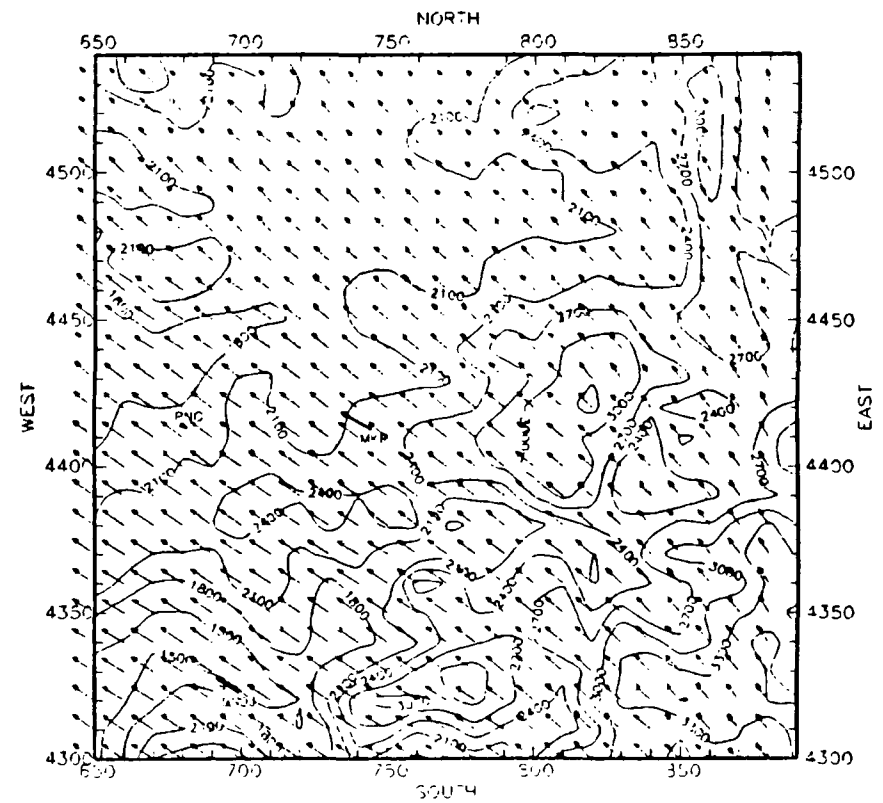
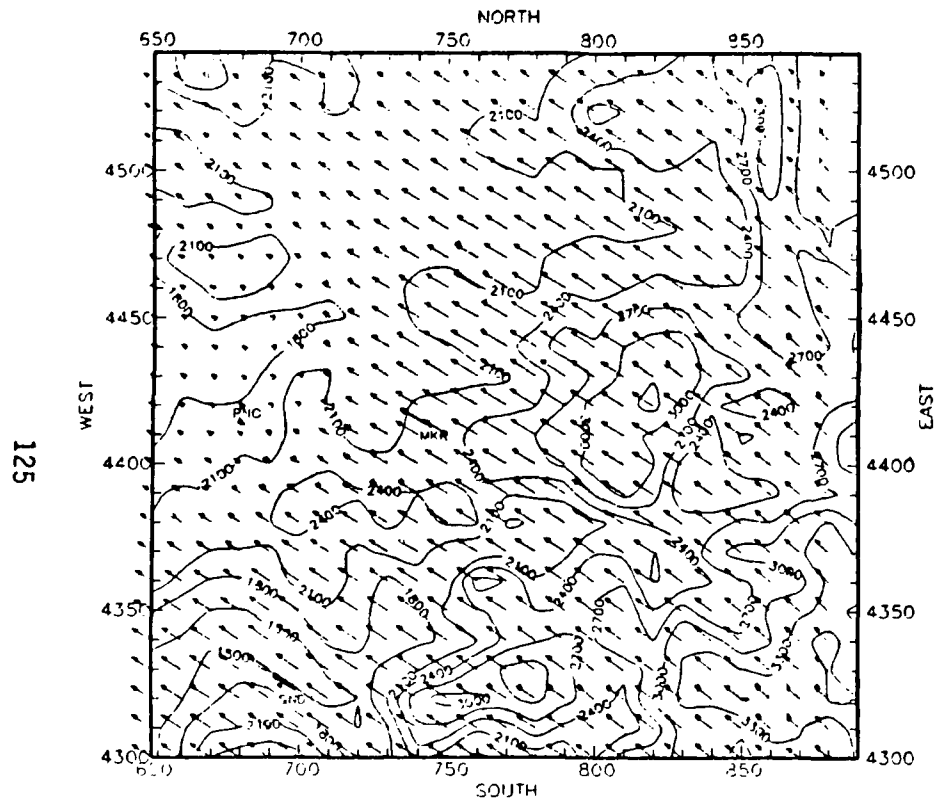
Reproduced from  
 best available copy.



FIGURE 4-7a. DWM-generated wind fields at 0500 on 18 September 1984: 10 m.

With Supplemental Observations

Without Supplemental Observations



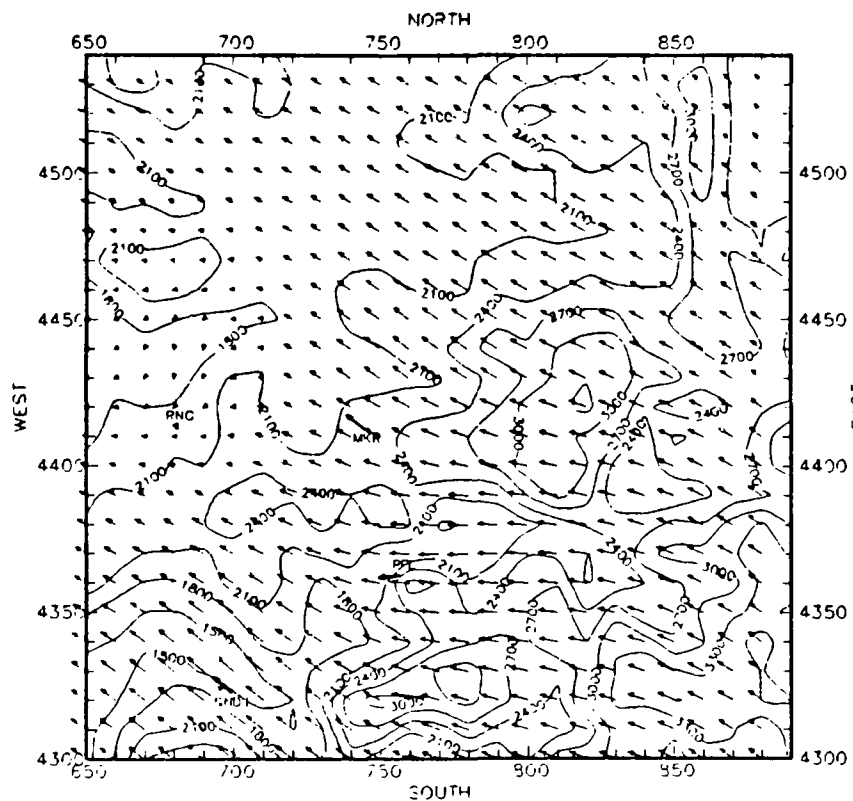
DWM WIND VECTORS AT LEVEL - 2 (100M)

0 5 10 15

WIND SPEED (M/S)

FIGURE 4-7b. DWM-generated wind fields at 0500 on 18 September 1984: 160 m.

## With Supplemental Observations



## Without Supplemental Observations

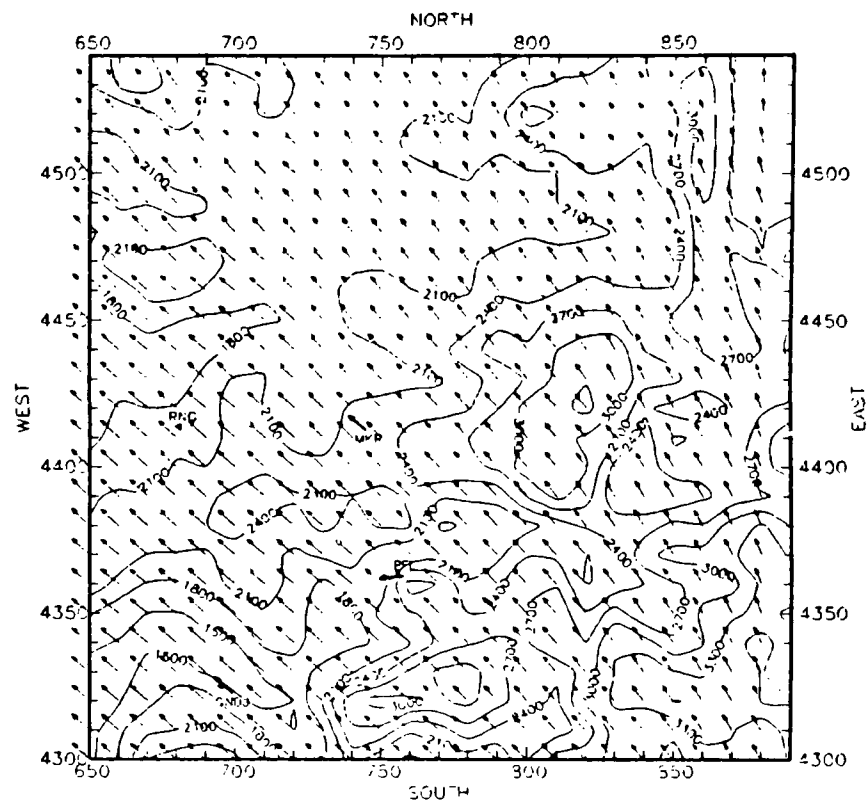
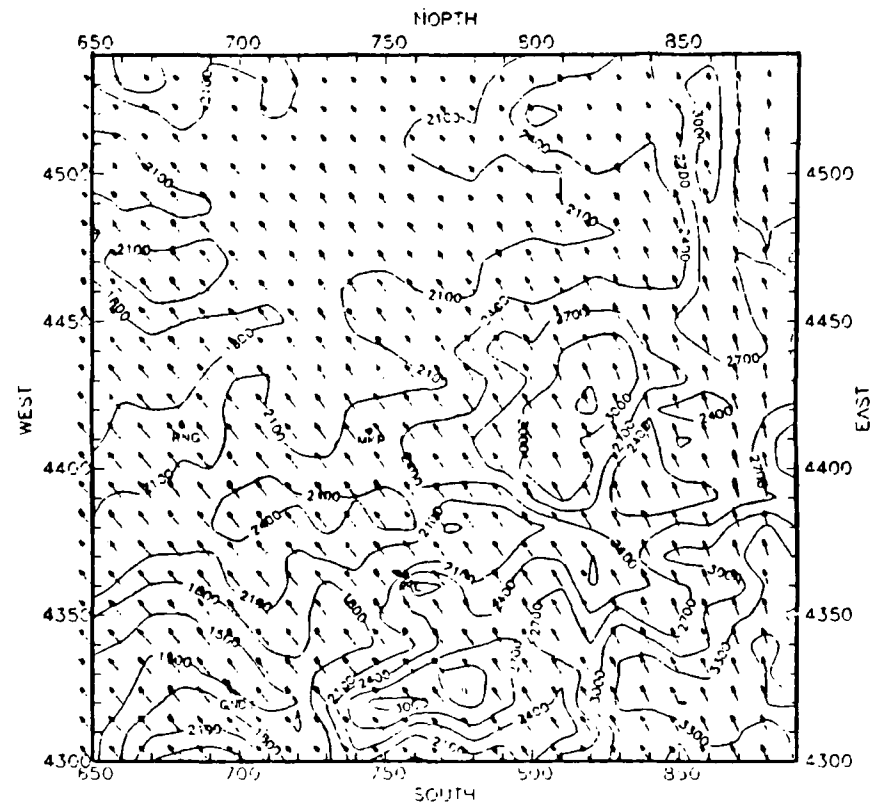
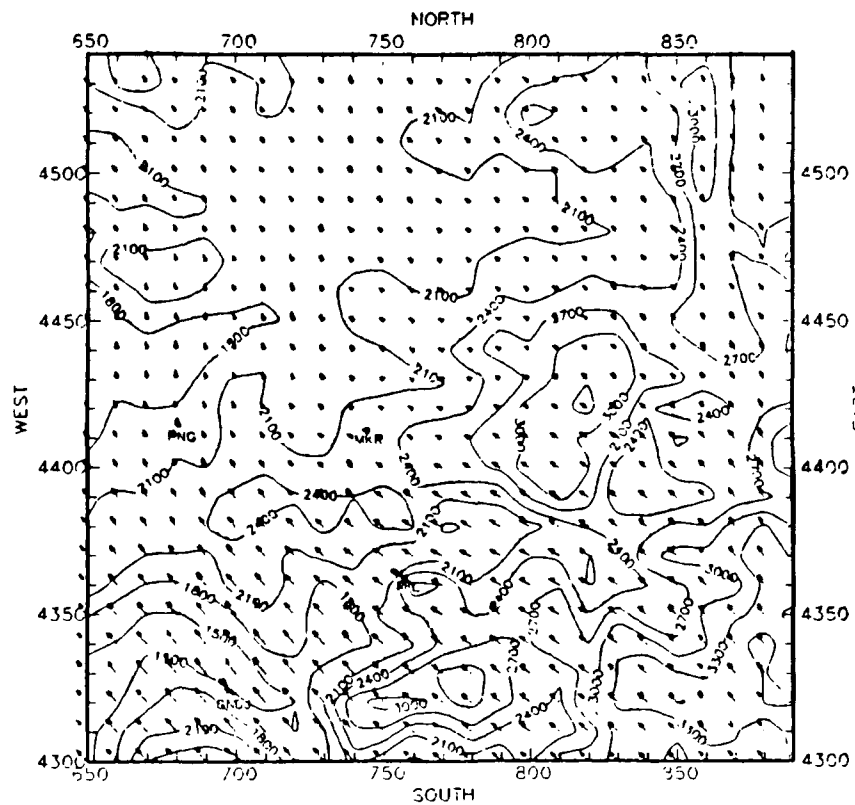


FIGURE 4-7c. DWM-generated wind fields at 0500 on 18 September 1984: 300 m.

With Supplemental Observations

Without Supplemental Observations



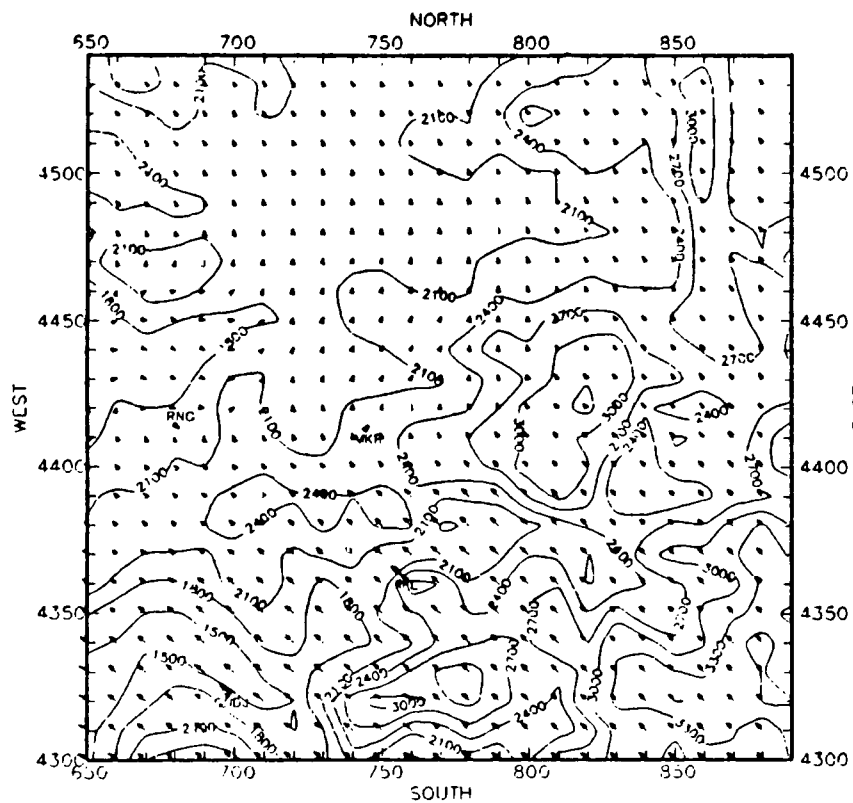
DWM WIND VECTORS AT LEVEL = 4 (600M)

0 5 10 15

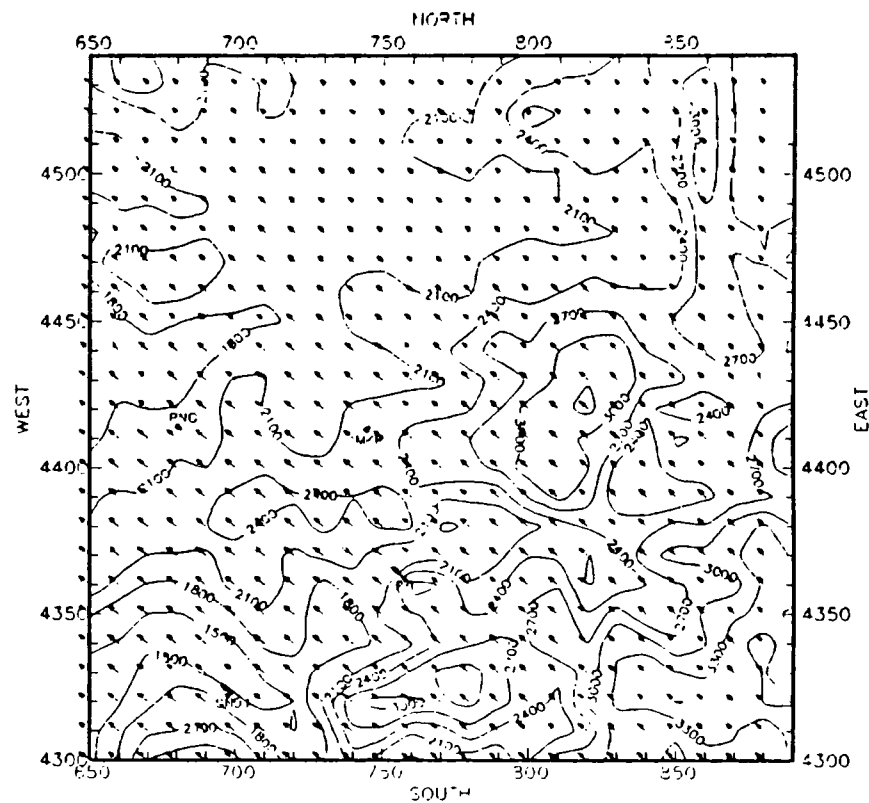
WIND SPEED (M/S)

FIGURE 4-7d. DWM-generated wind fields at 0500 on 18 September 1984: 600 m.

With Supplemental Observations



Without Supplemental Observations



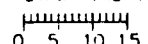
DWM WIND VECTORS AT LEVEL = 5 (1000M)  
  
 0 5 10 15  
 WIND SPEED (M/S)

FIGURE 4-7e. DWM-generated wind fields at 0500 on 18 September 1984: 1000 m.

With Supplemental Observations

Without Supplemental Observations

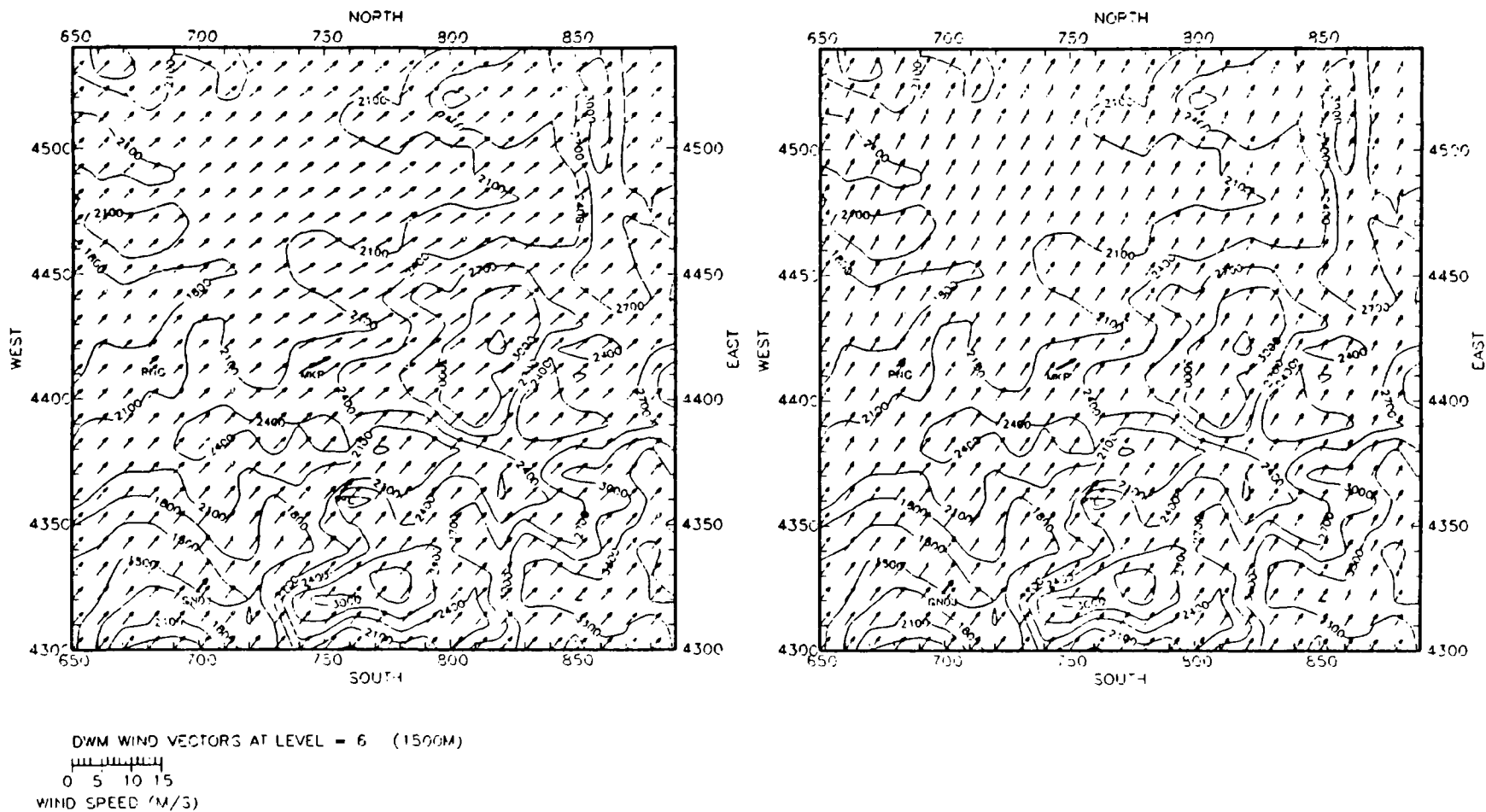


FIGURE 4-7f. DWM-generated wind fields at 0500 on 18 September 1984: 1500 m.

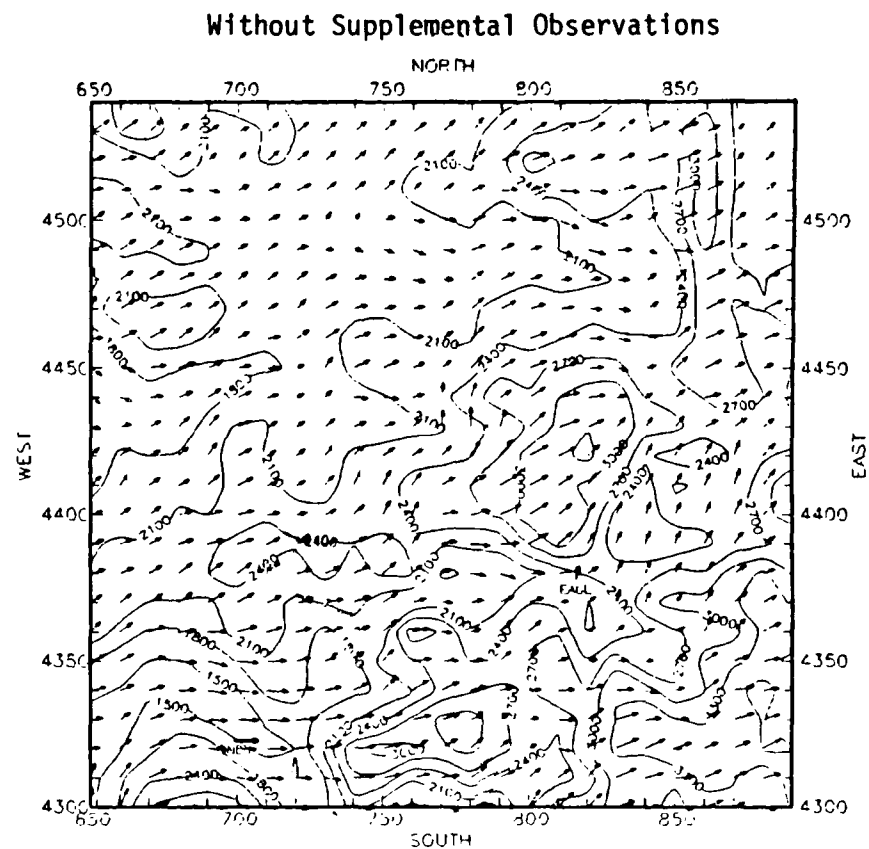
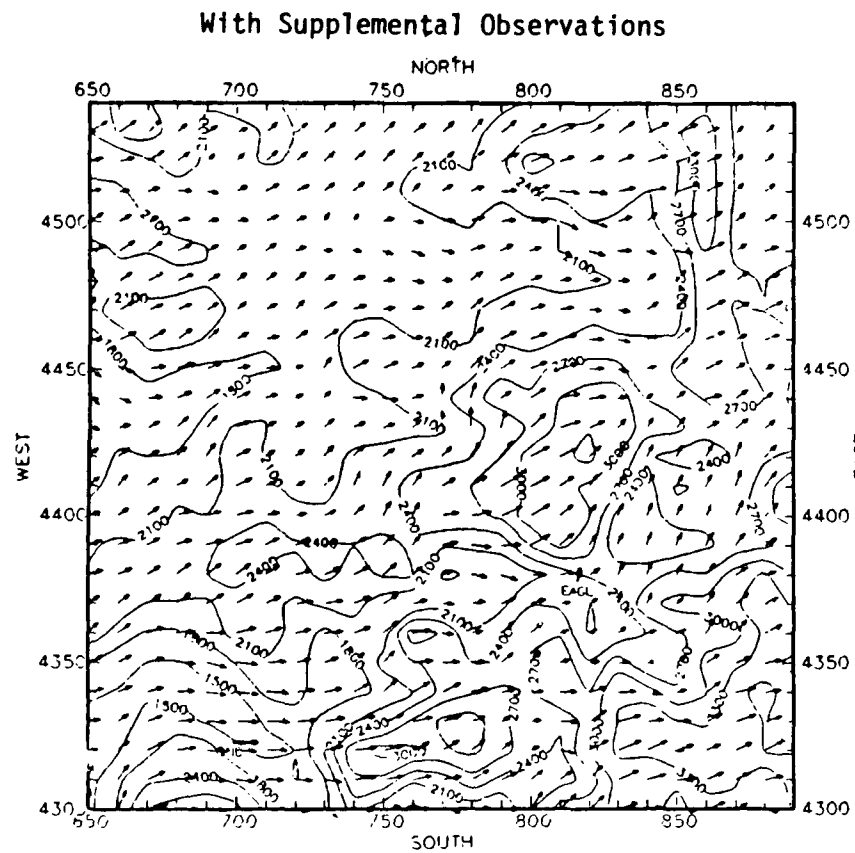
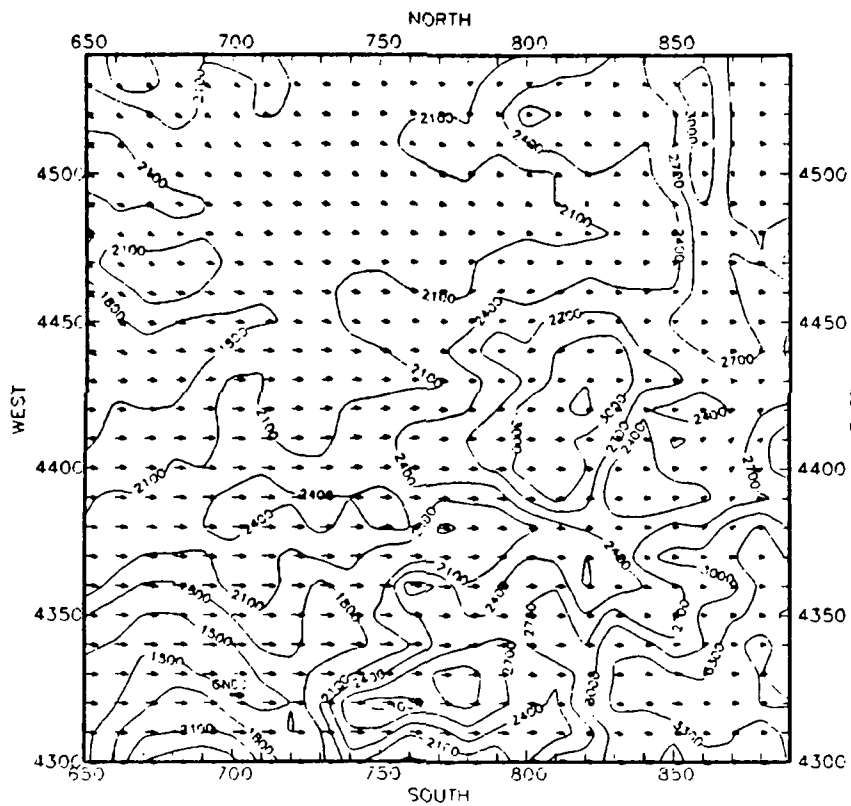


FIGURE 4-8a. DWM-generated wind fields at 1400 on 18 September 1984: 10 m.



With Supplemental Observations



DWM WIND VECTORS AT LEVEL = 2 (100M)  
 0 5 10 15  
 WIND SPEED (M/S)

Without Supplemental Observations

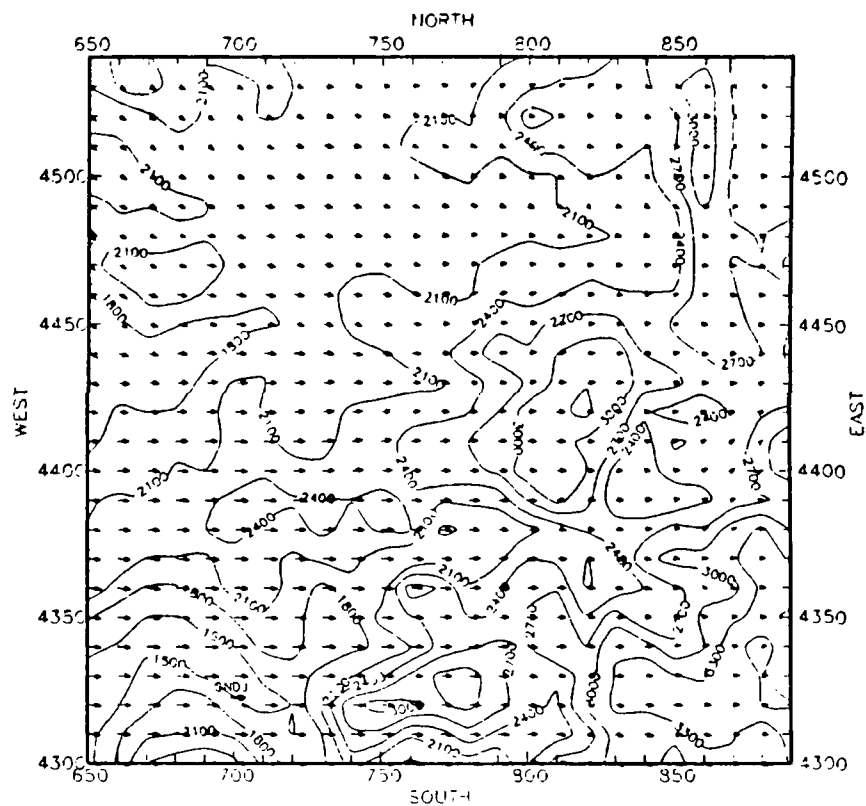
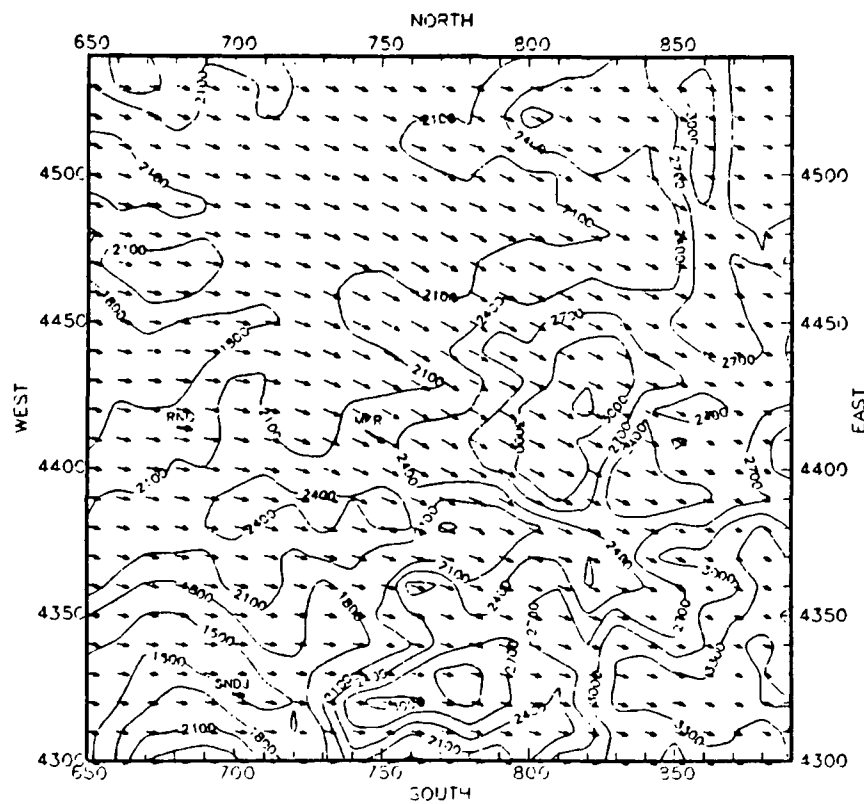
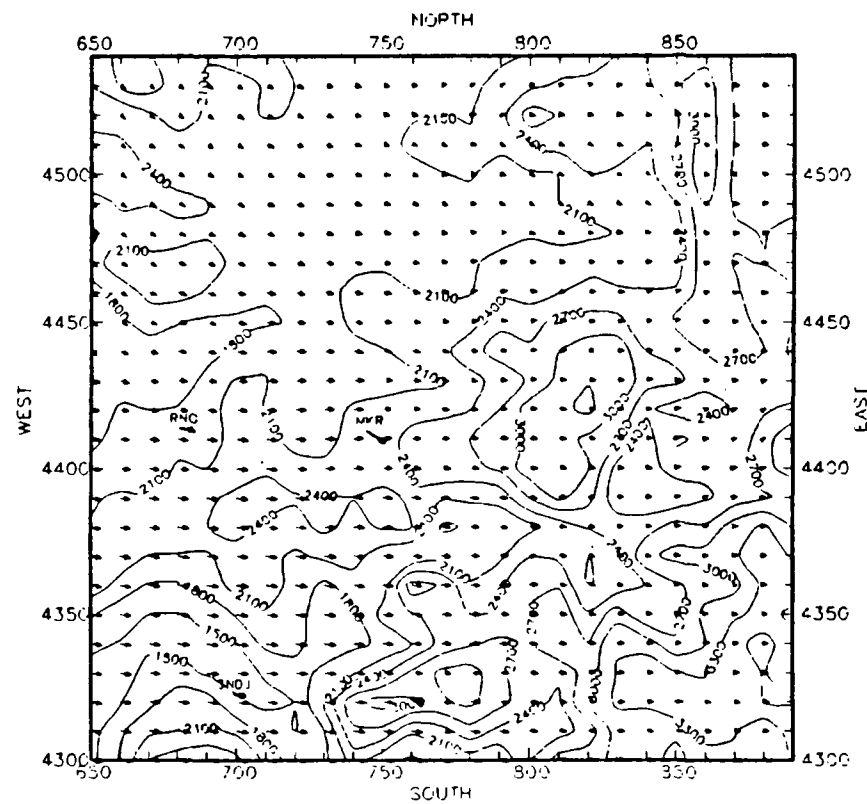


FIGURE 4-8b. DWM-generated wind fields at 1400 on 18 September 1984: 100 m.

With Supplemental Observations



Without Supplemental Observations



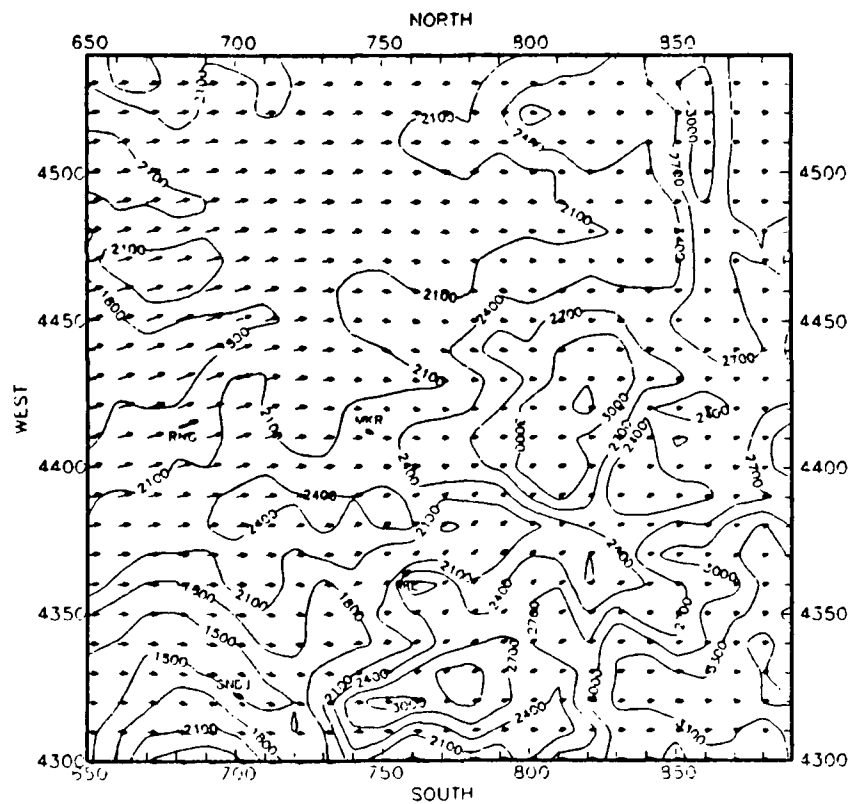
DWM WIND VECTORS AT LEVEL = 3 (300M)

0 5 10 15

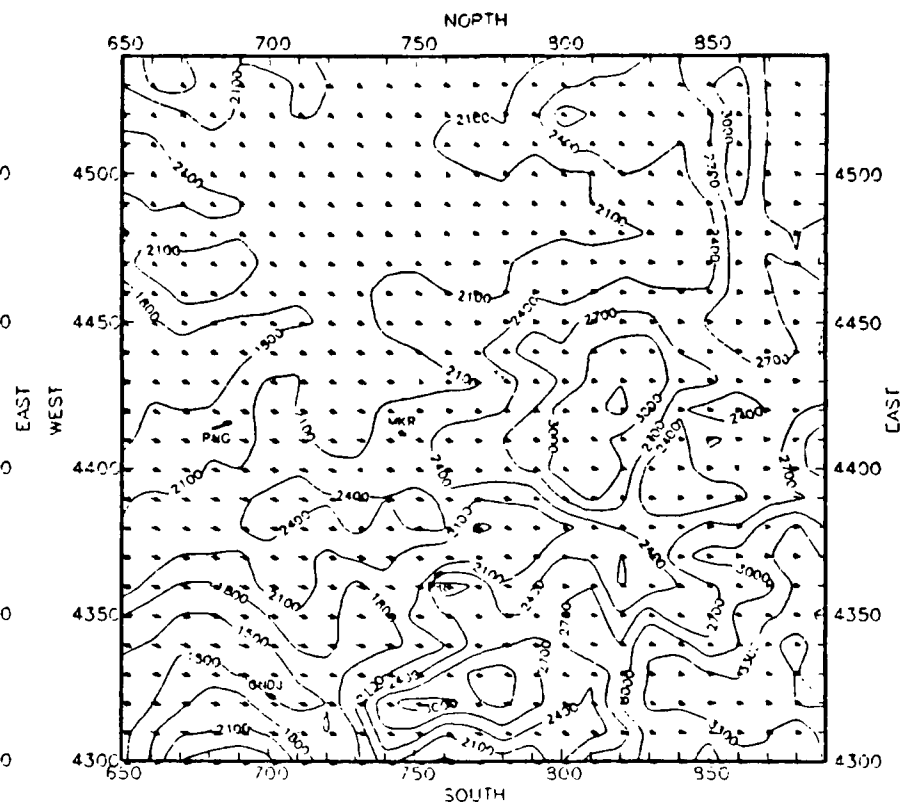
WIND SPEED (M/S)

FIGURE 4-8c. DWM-generated wind fields at 1400 on 18 September 1984: 300 m.

With Supplemental Observations



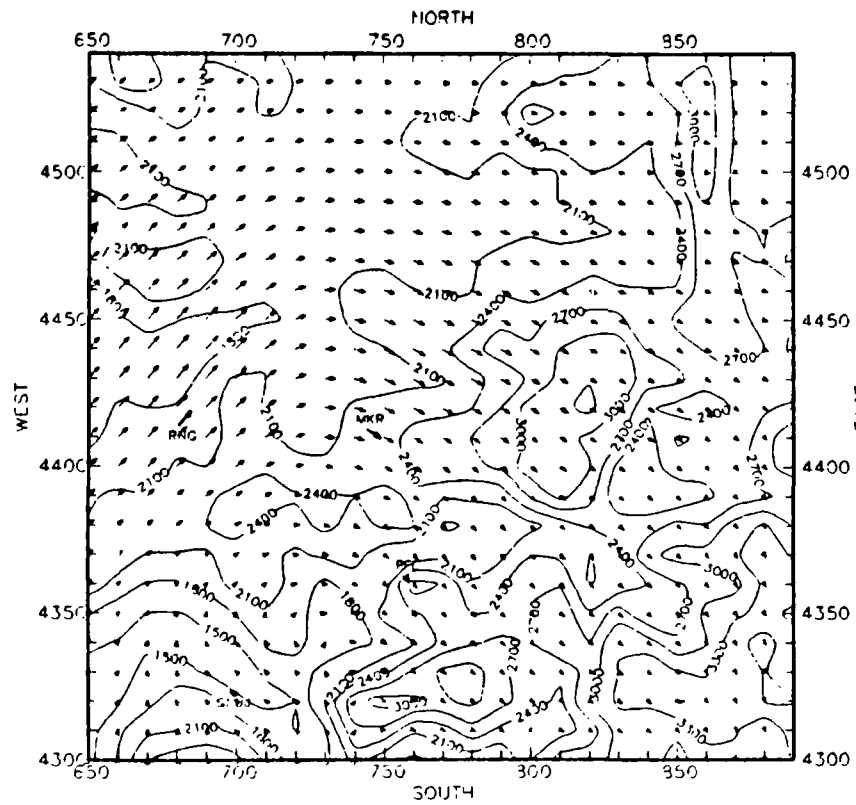
Without Supplemental Observations



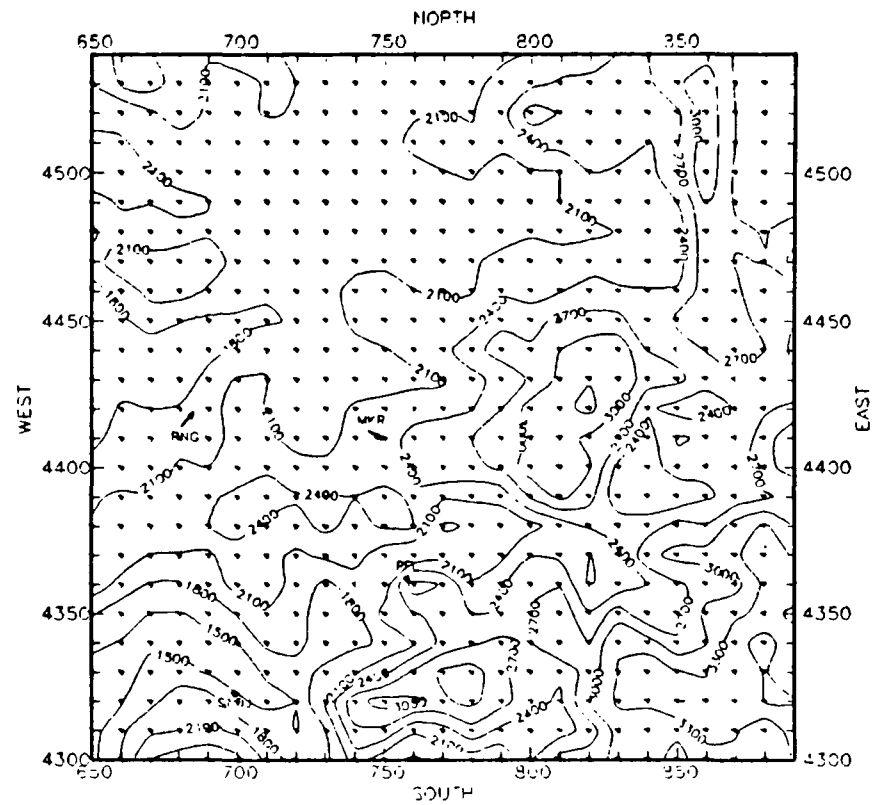
DWM WIND VECTORS AT LEVEL = 4 (600M)  
 0 5 10 15  
 WIND SPEED (M/S)

FIGURE 4-8d. DWM-generated wind fields at 1400 on 18 September 1984: 600 m.

With Supplemental Observations



Without Supplemental Observations

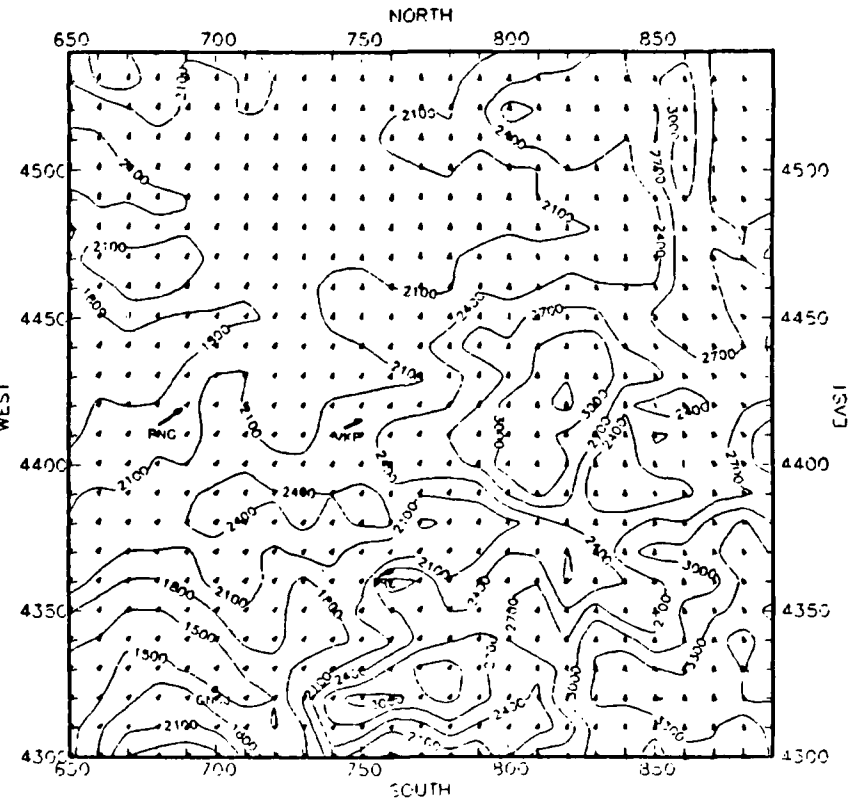
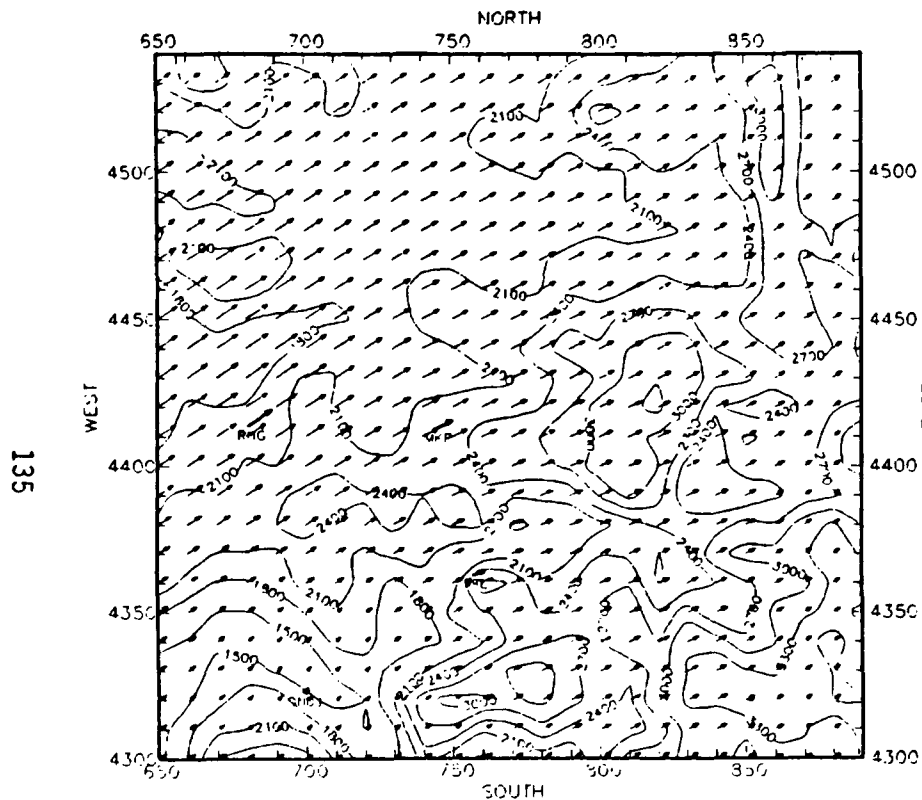


DWM WIND VECTORS AT LEVEL = 5 (1000M)  
 0 5 10 15  
 WIND SPEED (M/S)

FIGURE 4-8e. DWM-generated wind fields at 1400 on 18 September 1984: 1000 m.

# With Supplemental Observations

# Without Supplemental Observations



DWM WIND VECTORS AT LEVEL = 6 (1500M)

0 5 10 15

WIND SPEED (M/S)

FIGURE 4-8f. DWM-generated wind fields at 1400 on 18 September 1984: 1500 m.

#### 4.2.3.2 Quantitative Evaluation

A preliminary quantitative evaluation of the DWM was made by comparing the wind vectors predicted in the simulation without the supplemental data and the winds observed in the supplemental soundings. A scatter plot of the predicted versus observed wind speeds is shown in Figure 4-9. The DWM underpredicts the observed wind speed by 0.6 m/s out of an average observed wind speed of 2.1 m/s. This is because the Grand Junction sounding dominates the upper-level flows predicted by the DWM. Grand Junction is located in a valley and thus records lower wind speeds. As seen in the scatterplot, the predicted and observed wind speeds do not correlate well (correlation coefficient 0.037). The stagnant nature of the period simulated is shown by the large number (50 percent) of calm winds ( $< 1$  m/s) in the predictions and observations.

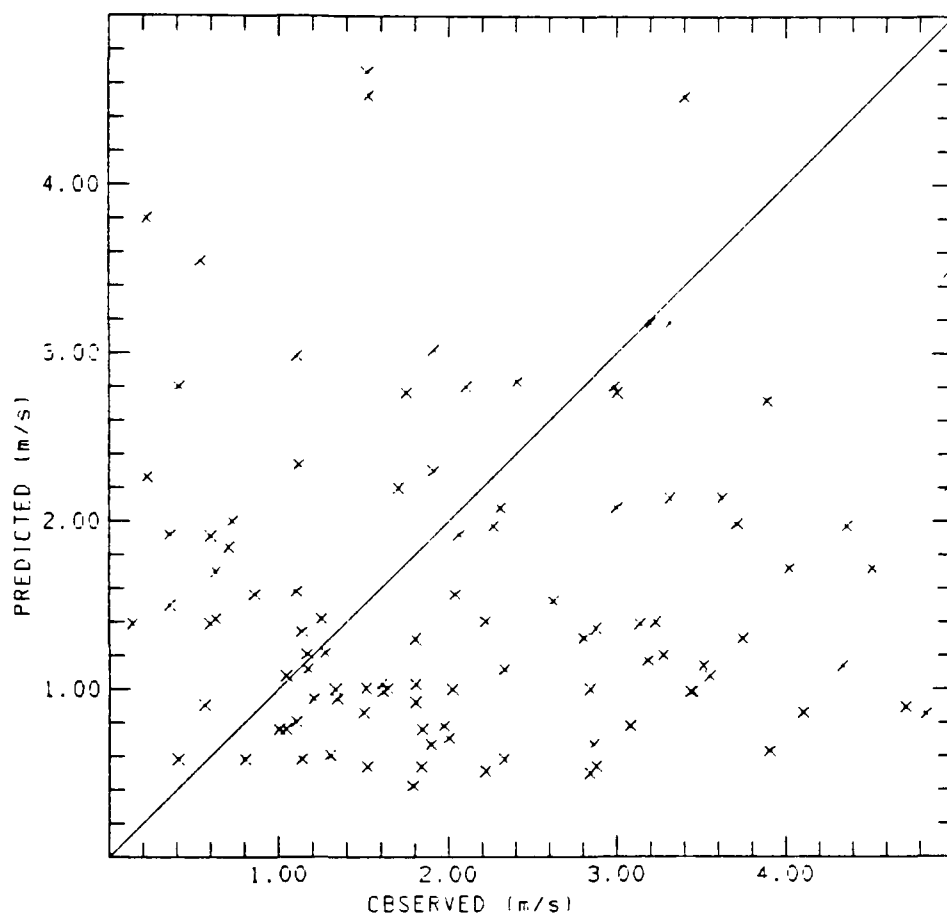
The predicted and observed wind directions are compared in Figure 4-10. Figure 4-10a shows the deviation of the predictions from the observations; Figure 4-10b is similar but the calm wind data points have been removed. As seen in Figure 4-10a, for all data, the positive and negative deviations from the observations exactly cancel each other out, resulting in a zero bias. When the calm wind conditions are removed (Figure 4-10b) there is a higher percentage of deviations near zero although there is also a net negative bias of approximately -10 degrees.

The percentage of predicted wind directions within 30 degrees of the observations is 28 percent for all data and 43 percent when the calm winds are removed. The number of predictions within 60 degrees of the observations is 51 percent for all data and 72 percent without the calm winds.

#### 4.2.3.3 Remarks

This preliminary evaluation of the DWM using observations from the Rocky Mountains is probably the most stringent test that can be designed for the model. The stagnant conditions that existed during these tests results in slope flows dominating the surface winds while local wind eddies and fluctuations dominate the observed winds aloft. The lack of good agreement between the predicted and observed wind speeds is somewhat disappointing, but the model generally did replicate the stagnant conditions, with both observed and predicted wind speeds under 4 m/s.

More encouraging was the model's ability to predict wind directions. The centering of the predicted-observed wind direction residuals on the zero line with a Gaussian-like profile indicates that deviations of the predictions from the observations are not systematic.

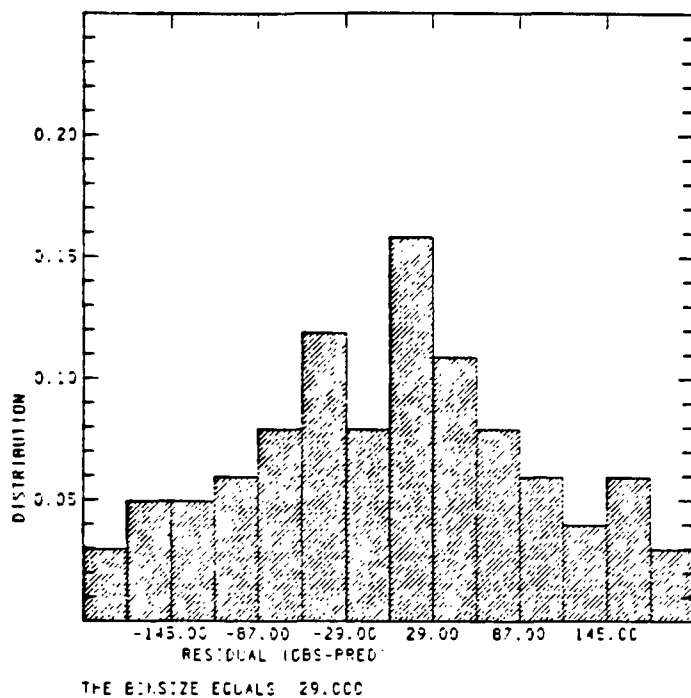


MOMENTS OF THE PROBABILITY DENSITY FUNCTION		
	OBSERVED	PREDICTED
AVERAGE	2.14554	1.58241
STANDARD DEVIATION	1.23589	0.94880
SKEWNESS	0.42819	1.25574
KURTOSIS	-0.73276	1.22461
OTHER MEASURES		
MEDIAN	1.89700	1.30400
UPPER QUANTILE	3.08100	2.00000
LOWER QUANTILE	1.14000	0.83400
MINIMUM VALUE	0.14100	0.42400
MAXIMUM VALUE	4.97400	4.66900

SKILL OF PREDICTION PARAMETERS  
 CORRELATION COEFFICIENT OF PREDICTED  
 VERSUS OBSERVED 0.032  
 THE BOUNDS OF THE CORRELATION AT THE  
 CONFIDENCE LEVEL OF 0.050 ARE  
 LOW BOUND -0.162 HIGH BOUND 0.225  
 RATIO OF OVER TO UNDER PREDICTIONS 0.451  
 PERCENT OF OVER PREDICTIONS  
 GREATER THAN 200 PERCENT OF THE  
 OBSERVED 16.505  
 PERCENT OF UNDER PREDICTIONS  
 LESS THAN 50 PERCENT OF THE  
 OBSERVED 35.922

FIGURE 4-9. Scatterplot and statistics of predicted versus observed wind speeds at the three supplemental soundings (N=103).

(a)



(b)

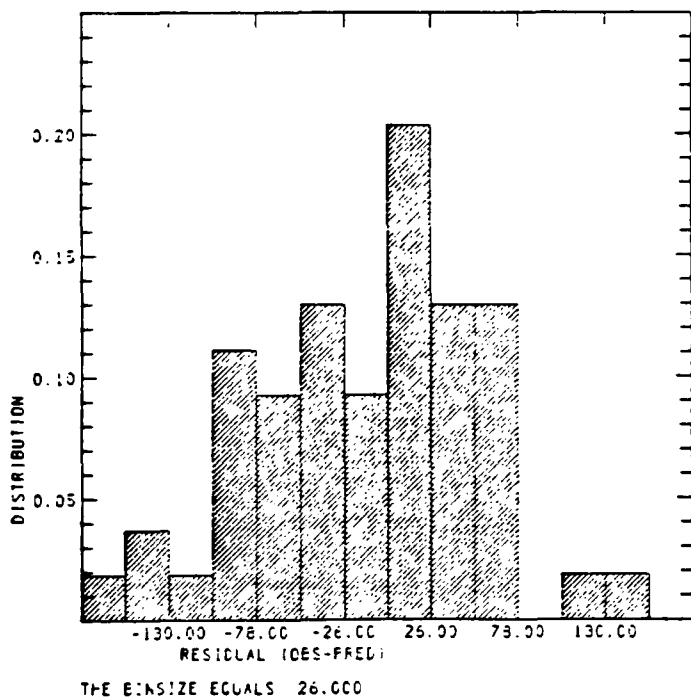


FIGURE 4-10. Histograms of deviations of predicted wind direction from observations at the three supplemental soundings: (a) all data (N = 101), (b) with calms removed (N = 5).



This evaluation further illustrates the importance of having a dense array of meteorological observations in order to reproduce observed wind fields. Even though the new DWM was designed to run with a sparse set of observations through the parameterizing of the physical processes that drive air flows in complex terrain. At any given time these parameterizations need to be tied to observations to replicate the observed conditions.

#### 4.2.4 Evaluation of the DWM in a Complex Terrain/ Coastal Environment and Within a Large Valley

The new DWM was evaluated using two different modeling regions. The first is an area along the California coast that includes complex terrain. The second region consists of part of the California Central Valley. The locations of these two regions are shown in Figure 4-11.

##### 4.2.4.1 Complex Terrain and Coastal Environment

Increased activities in oil exploration and drilling off of the coast of California near Santa Barbara has raised questions concerning the effects of these activities on air quality in the South Central Coast Air Basin (SCCAB) of California. This concern has resulted in several federal, state, and county agencies joining together to sponsor a massive meteorological and air quality measurement collection program known as the South Central Coast Cooperative Aerometric Monitoring Program (SCCCAMP). This comprehensive measurement program collected several types of meteorological and air quality data during periods of the summers in 1984 and 1985.

One of the purposes of this program was to characterize air flow patterns in the region to aid in the analysis of impacts on air quality in the SCCAB from future emission sources. The characterization of these air flow patterns is made particularly difficult because of the combined effects of the complex terrain of the Santa Ynez, San Rafael, and Santa Monica mountains and land-sea breezes generated by the Pacific Ocean. This difficulty is further compounded by the fact that most of the wind measurements are along the coast, thus there are regions with a dense array of measurements (the coastline) and regions with sparse data (inland and out to sea). Thus the DWM developed under the auspices of the Rocky Mountain Acid Deposition Model Project was identified as the most appropriate diagnostic wind model for predicting wind flow patterns in the region because of its ability to predict wind flows in areas with and without measurements in a cost effective manner.

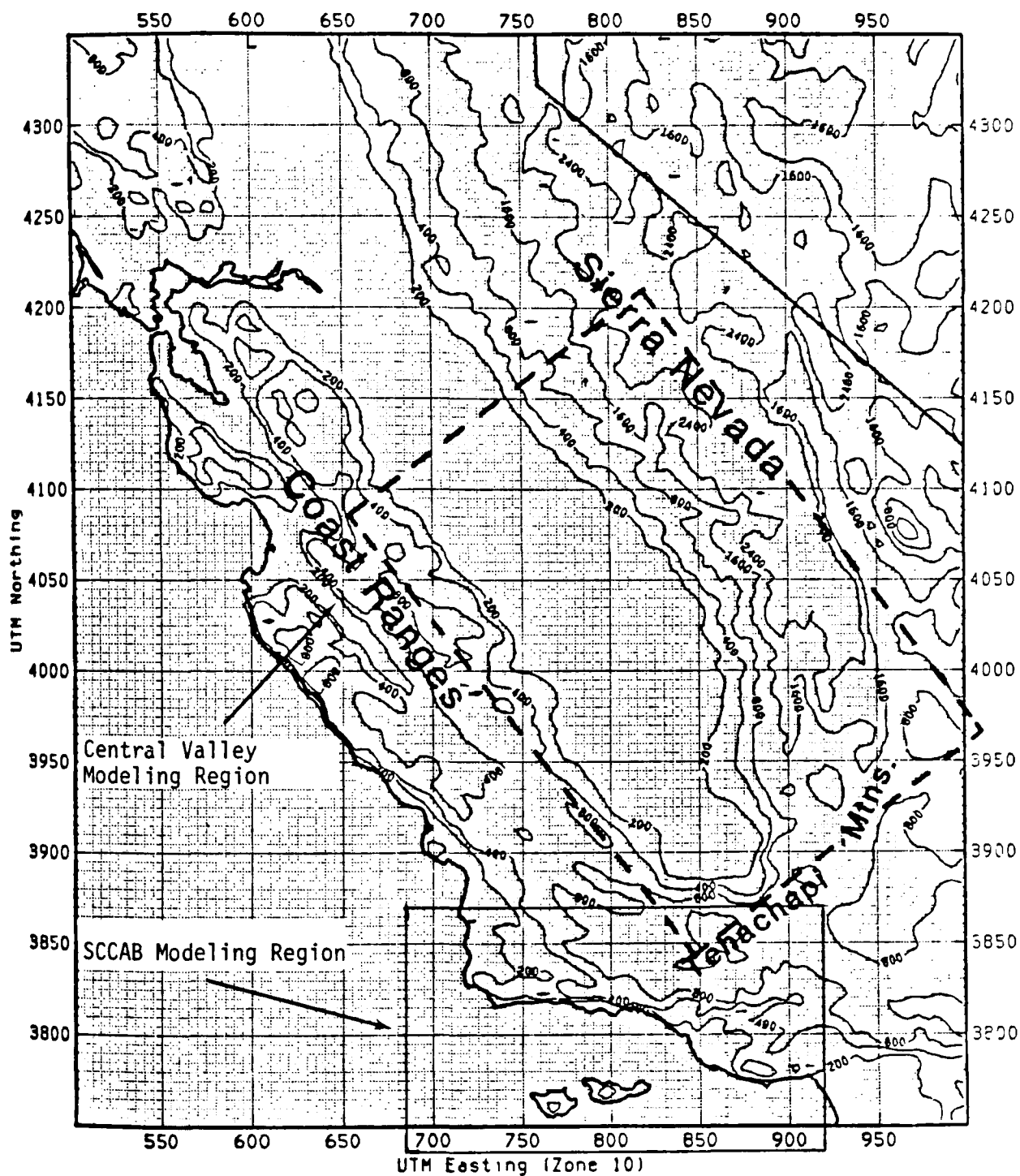


FIGURE 4-11. Locations of the SCCAB and Central Valley modeling regions.

The Minerals Management Services, the federal agency responsible for managing the oil deposits, has funded a study that uses the new DWM to characterize wind flow patterns in the region. In addition, other groups who have interests in the area, such as the Western Oil and Gas Association, have also funded efforts to use the new DWM with the SCCAMP data to predict gridded wind fields in the SCCAB. At this time, the new DWM has been used to generate hourly wind fields in the region for 11 case days from the 1985 SCCAMP study, and four case days from the 1984 SCCAMP study. For the 1985 simulations approximately 80 surface and 20 upper-air wind observation sites were used as input into the DWM. The 1984 SCCAMP data base has fewer observation sites; approximately 20 surface and five upper-air sites are available.

An example of two hours of the surface wind fields produced by the DWM and the observations used for the SCCAB region are depicted in Figure 4-12 and 4-13. Figure 4-12a shows the wind field for 0400 PDT on 23 September 1985. The simulation shows significant downslope flow, which is also evident in the observations. Also evident is the sea breeze coming from the northwest, which is deflected further south by the downslope winds coming off of the terrain features inland.

The wind fields for the SCCAB region for 1200 PDT on 23 September are shown in Figure 4-13. During the afternoon both the DWM and the observations reflect upslope winds in the complex terrain region. The sea breeze circulation around Gaviota Pass (middle left of figure) has formed the so-called Gaviota eddy. The DWM wind fields match the observations quite well, which is not surprising since they are used as input into the model.

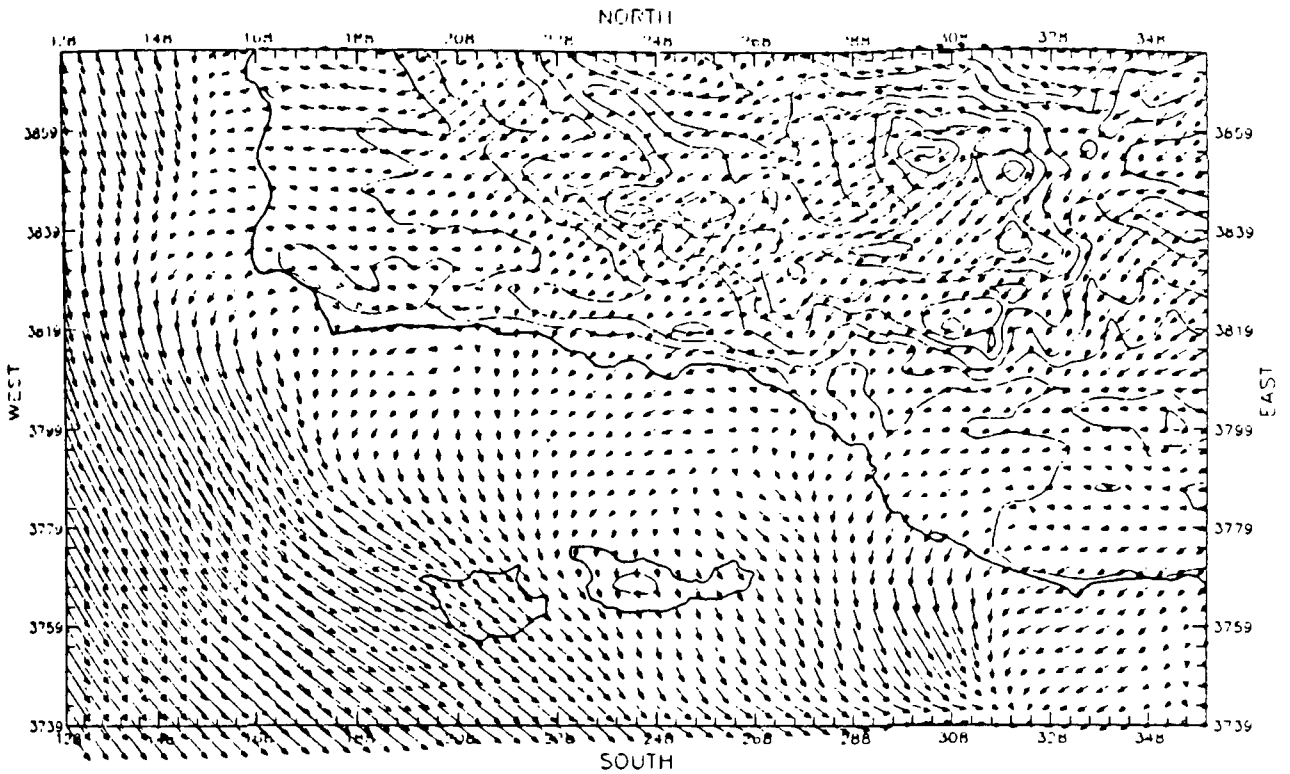
These simulations illustrate the ability of the DWM to make use of many observations in its generation of wind fields yet still produce major flow features (e.g., slope flows and terrain deflection) away from the observations. This ongoing work effort will be reported on in early 1988.

#### 4.2.4.2 Simulations in a Large Valley

In 1986 the U.S. National Park Service sponsored a scoping study to determine whether ozone concentrations produced by urban areas and oil production in the California Central Valley could be transported to national parks in the Sierra Nevada mountains (Yosemite, Sequoia, and Kings Canyon national parks). The regional oxidant model, the RTM-III (Liu, Morris, and Killus 1984), was deemed the most appropriate tool for this task.

One of the most important inputs for any regional or mesoscale air quality model is the wind fields. In the California Central Valley elevated ozone concentrations are usually associated with stagnant conditions in which

(a) DWM Wind Fields



(b) Observed Winds

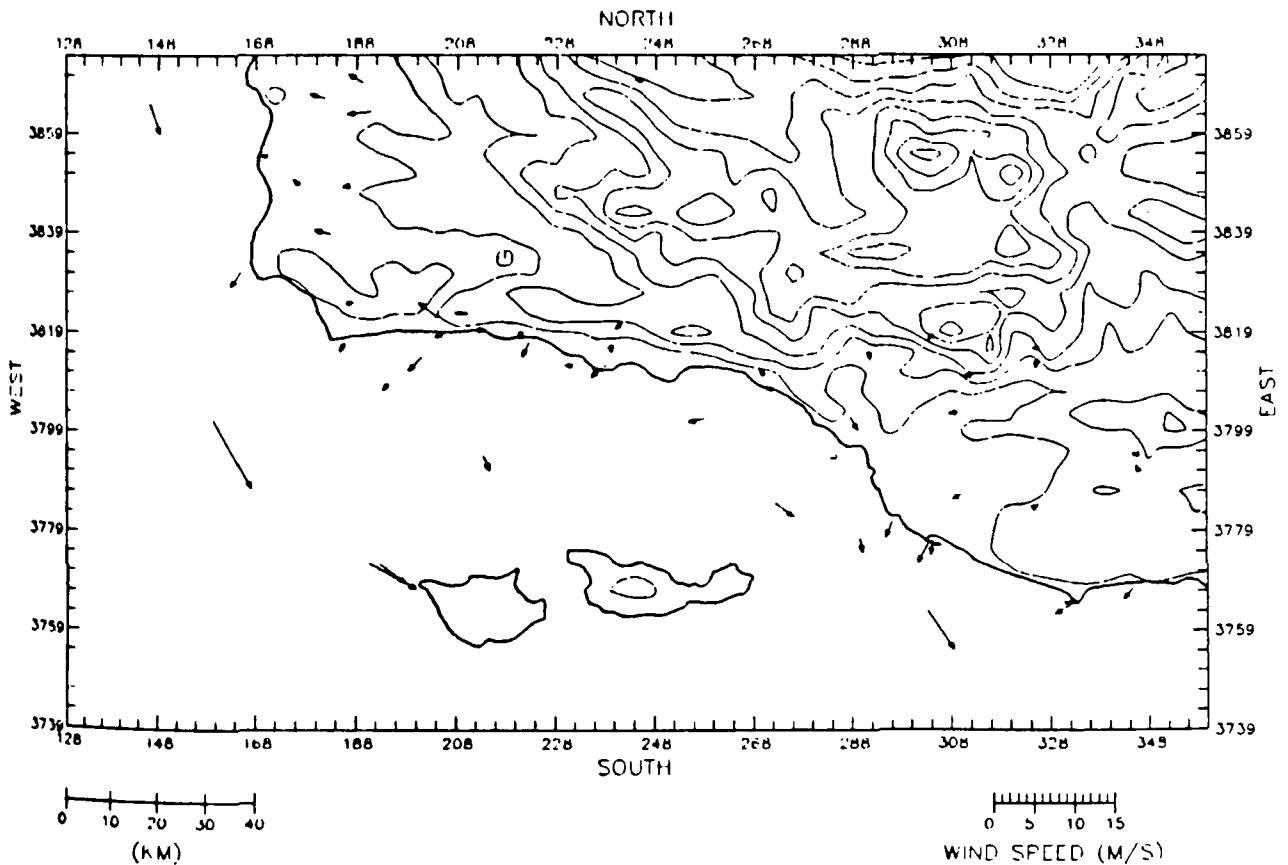
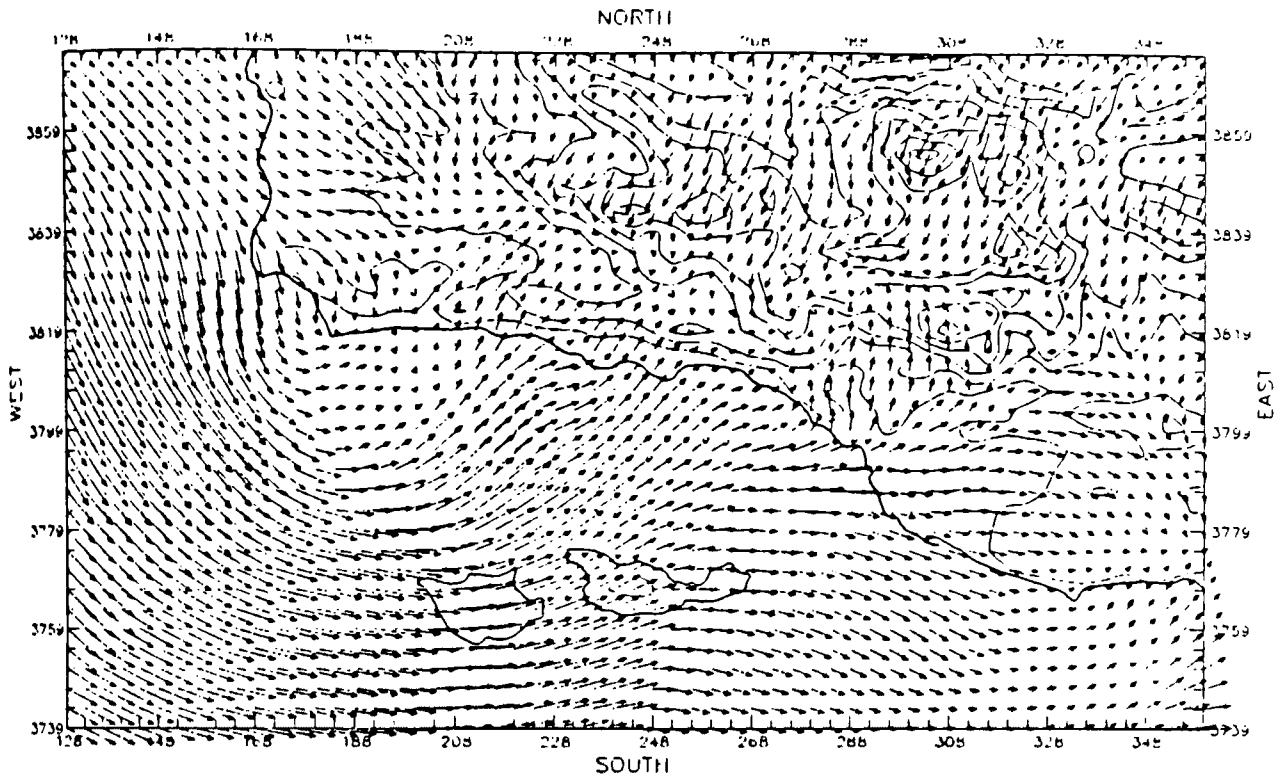


FIGURE 4-12. DWM generated and observed surface wind fields (10 m) for the SCCAB Region at 0400 PDT on 23 September 1987.

(a) DWM Wind Fields



(b) Observed Winds

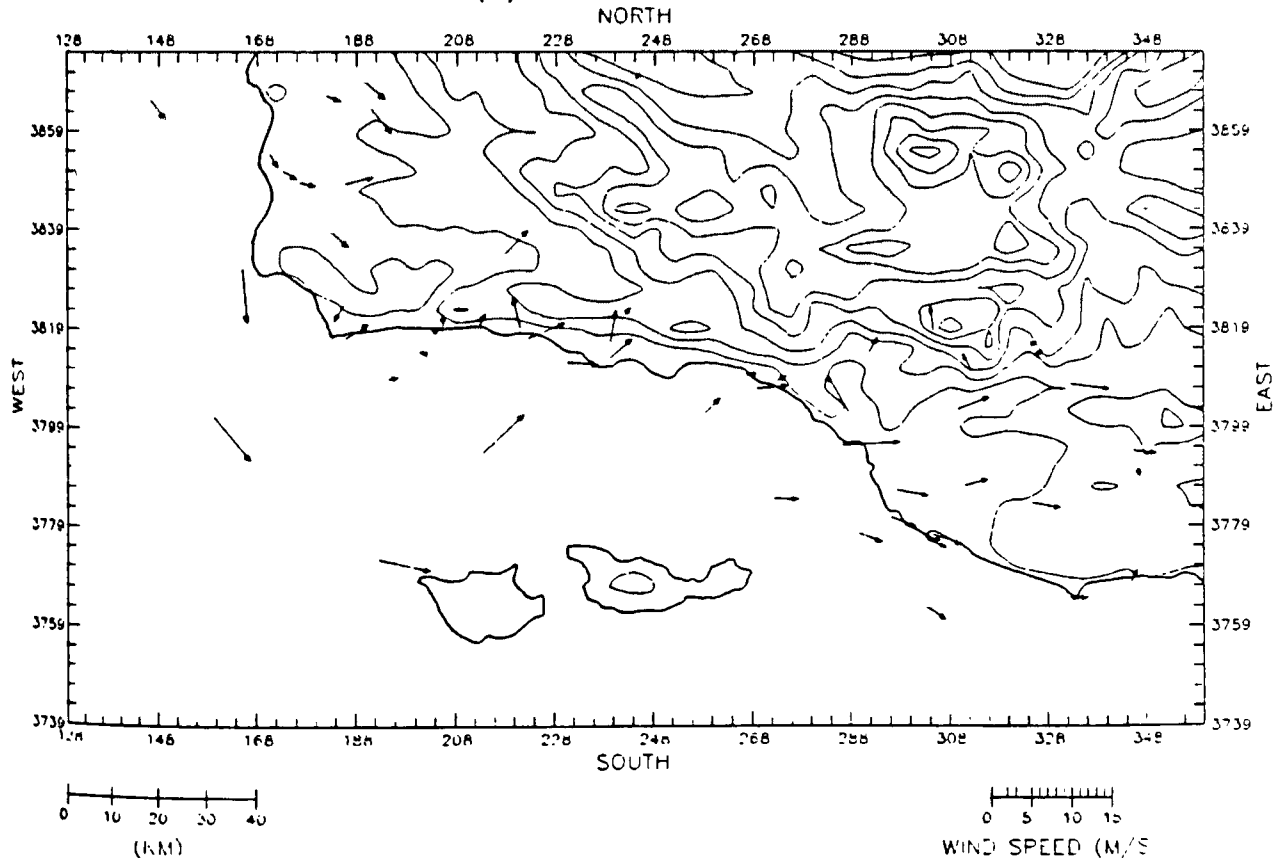


FIGURE 4-13. DWM-generated and observed surface wind fields (10 m) for the SCCAB Region at 1200 PDT on 23 September 1987.

slope flows dominant the flow regime. Thus it was initially determined that in order to simulate these complicated slope flows a three-dimensional primitive equation model was required.

A three-dimensional primitive equation mesoscale meteorological model (Pielke, 1974) was exercised for several hours of the selected oxidant episode. Although the model produced the slope flows, cost considerations precluded its use for generating three-dimensional wind fields for this study. Thus the primitive equation model was exercised in its two-dimensional form to reproduce vertical cross sections of upslope and downslope wind fields and boundary layer heights across the valley as represented in Figure 4-14.

Because of the flexibility of the formulation of the initial version of the DWM, the results of the two-dimensional primitive equation model could be input into the DWM as psuedo-observational soundings. Examples of the layer 1 and 3 wind fields generated for the California Central Valley at 0100 and 1200 are shown Figures 4-15 and 4-16. As for the Rocky Mountain and SCCAB regions, the model produced both nighttime downslope and daytime upslope winds. In addition, due to the psuedo-soundings from the primitive equation model, the model was also able to produce the return flows in the third layer (see Figures 4-15 and 4-16). Details of the application of this initial version of the DWM to the California Central Valley have been reported by Moore, Morris, and Daly (1987). The finalized version of the DWM and the RTM-III are presently being applied to an expanded region containing the California Central Valley and San Francisco Bay Area under the sponsorship of the NPS; results are to be reported in early 1988.

#### 4.3 SPECIFICATION OF OTHER METEOROLOGICAL VARIABLES

The acid deposition modeling system will require grid-point estimates of a number of meteorological variables, based on rather sparse surface and upper-air observational data. These variables include

- mixing height
- Pasquill-Gifford stability class
- friction velocity
- convective velocity
- Monin-Obukhov length
- surface temperature

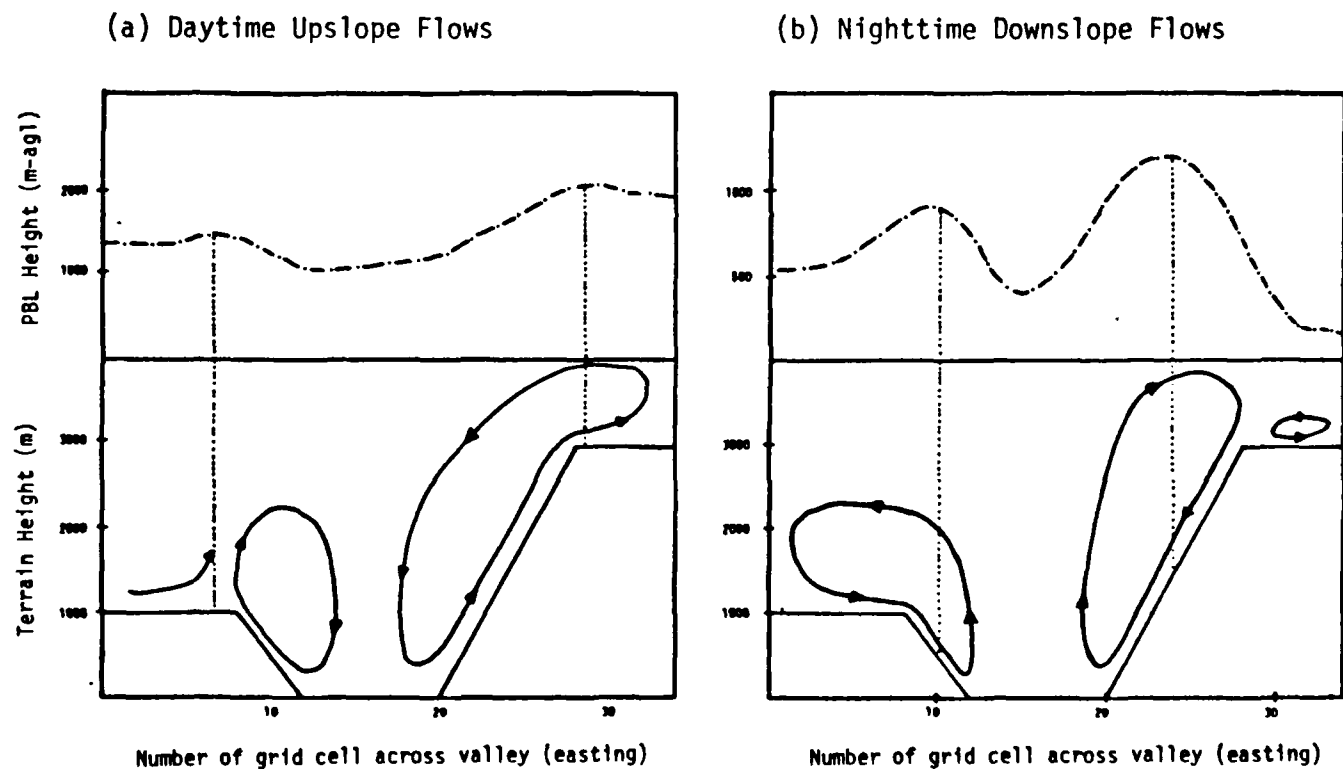


FIGURE 4-14. Depiction of wind circulation air flows and boundary heights in the California Central Valley generated by the two-dimensional primitive equation.

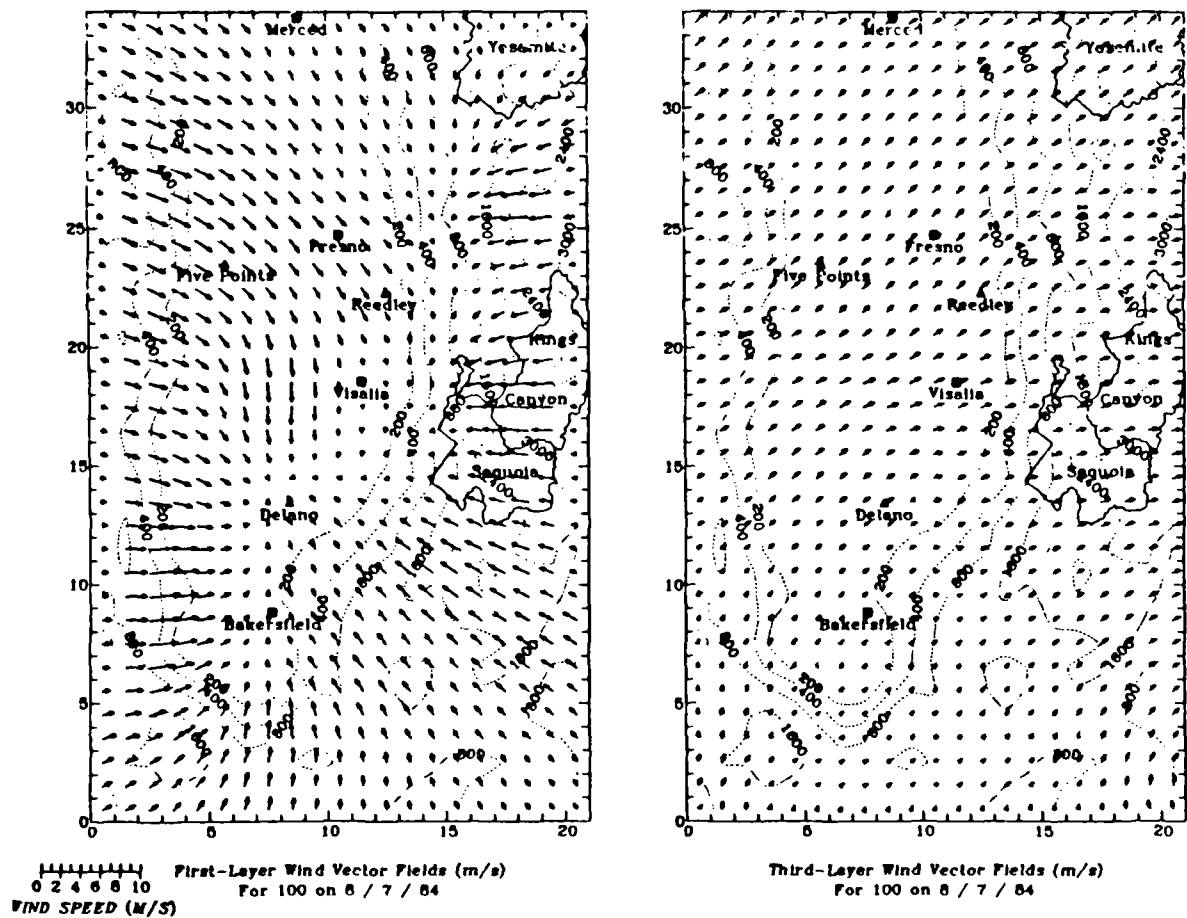


FIGURE 4-15. DWM-generated surface and upper-layer wind fields for the California Central Valley at 0400 on 7 August 1984.



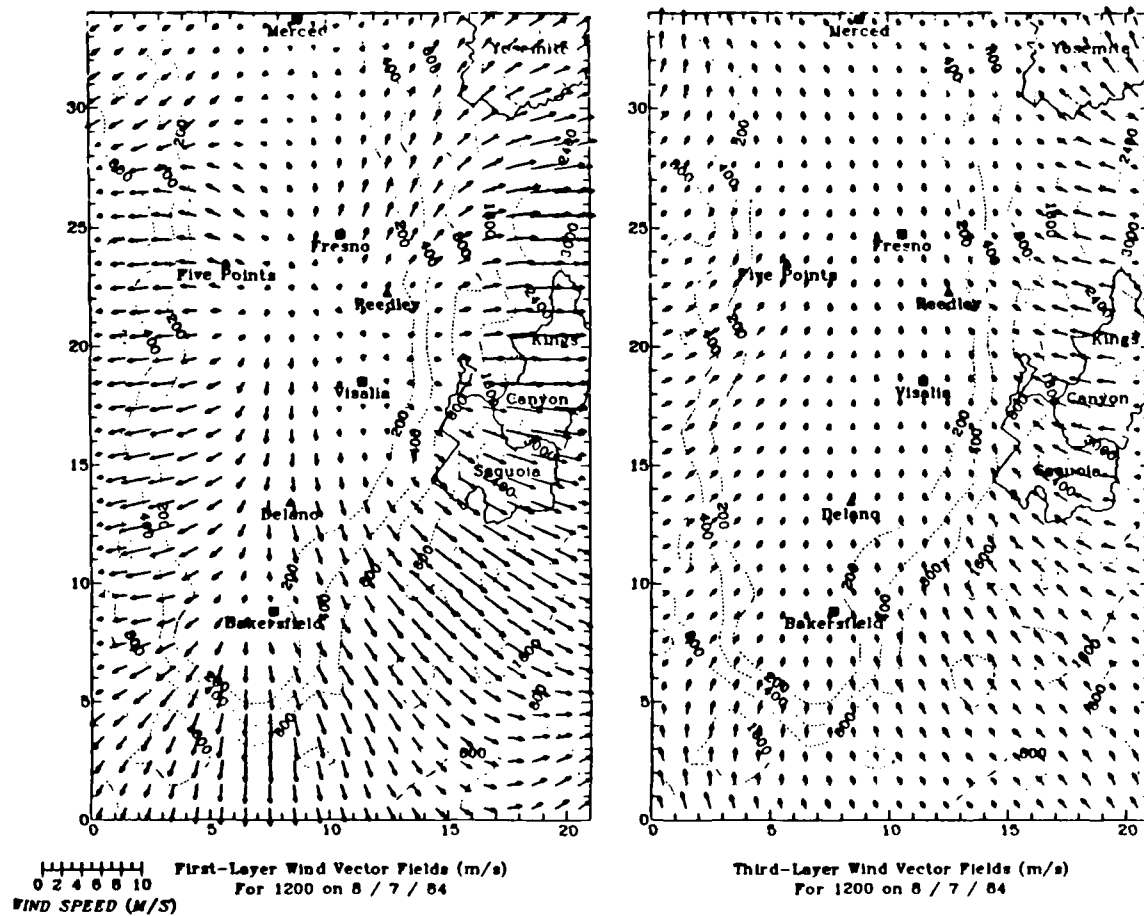


FIGURE 4-16. DWM-generated surface and upper-layer wind fields for the California Central Valley at 1200 on 7 August 1984.

surface pressure  
relative humidity  
precipitation rate

The MELSAR-MET model served as the basis for the development of the new meteorological driver for the Rocky Mountain acid deposition model. Much of the following discussion on the prescription of meteorological inputs is abstracted from the technical description of MELSAR-MET (Allwine and Whiteman, 1985).

#### 4.3.1 Mixing Heights

The gridded mixing heights are computed for each hour using surface weather observations and upper-air observations. The hourly mixing height at a grid point is the maximum of a convective mixing height or a mechanical mixing height. The convective mixing height is set equal to zero during the night. The mechanical mixing height is computed as  $53 \times 10^{-4} U_g$ , where  $U_g$  is the free stream wind speed (m/s). This formulation for the mechanical mixing height is given by Benkley and Bass (1979).

The convective mixing height is computed using a technique described by Benkley and Schulman (1979). The hourly mixing height at a weather station is estimated by determining the height of the intersection of the surface potential temperature and the morning potential temperature sounding. The technique accounts for warm or cold air advection into the region by adjusting the hourly surface potential temperature values according to an advection rate. The advection rate is determined from the difference in potential temperature between the afternoon and morning sounding at a height above the convective mixing height. The technique also makes adjustments for differences between the temperature at the surface station and the surface temperature at the radiosonde station, or makes adjustments if the minimum surface temperature occurs before the morning sounding. This is accomplished by adjusting the morning sounding to fit the minimum surface temperature observation.

Once the mixing height is computed at each weather station, the mixing height at a grid point is determined by an inverse-distance-square weighting of the station mixing heights to the grid points.

#### 4.3.2 Stability Classification

The Pasquill-Gifford-Turner (PGT) stability classes are determined for each grid cell for each hour using the approach given by Turner (1970).

Given the wind speed at the surface, the solar elevation angle, and the fractional cloud cover, the PGT stability class can be determined from the following table (from Turner, 1970):

Wind Speed at 10 m	Day			Night	
	Incoming Solar Radiation			Some	Few
	Strong	Moderate	Slight	Clouds	Clouds
<2 m/s	A	A-B	B	E	F
2-3	A-B	B	C	E	F
3-5	B	B-C	C	D	E
5-6	C	C-D	D	D	D
>6	C	D	D	D	D

#### 4.3.3 Friction Velocity

The surface friction velocity,  $u_{\star}$  (m/s), is computed for each grid cell for each hour using surface weather observations. The approach used is a modification of the approach given by Scire and co-workers (1984). The surface friction velocity for unstable conditions can be estimated by the method described by Wang and Chen (1980):

$$u_{\star} = \tilde{u}_{\star} \{1 + a \ln [1 + b Q_0 / \tilde{Q}_0]\} \quad (4-22)$$

$$\tilde{u}_{\star} = \frac{ku_m}{\ln (z_m/z_0)} \quad (4-23)$$

$$z_m = z_{ms} - 4z_0 \quad (4-24)$$

$$Q_0 = H/(\rho c_p) \quad (4-25)$$

$$H = A_0 R + H_0 \quad (4-26)$$

$$H_0 = 2.4C_0 - 25.5 \quad (4-27)$$

$$\tilde{Q}_0 = \frac{\theta \tilde{u}_*^3}{kgz_m} \quad (4-28)$$

$$a = 0.128 + 0.005 \ln(z_0/z_m), \quad z_0/z_m < 0.01$$

$$= 0.107, \quad z_0/z_m > 0.01 \quad (4-29)$$

$$b = 1.95 + 32.6 (z_0/z_m)^{0.45} \quad (4-30)$$

where

- $k$  = the von Karman constant (-0.4)
- $c_p$  = the specific heat of air at constant pressure ( $996 \text{ m}^2/\text{s}^2 \cdot \text{deg}$ )
- $u_m$  = the wind speed (m/s) measured at height  $z_{ms}$  (m)
- $z_0$  = the surface roughness (m)
- $\rho$  = the density of air ( $\text{kg}/\text{m}^3$ )
- $g$  = acceleration due to gravity ( $9.81 \text{ m}/\text{s}^2$ )
- $\theta$  = surface potential temperature (K)
- $R$  = incoming solar radiation ( $\text{W}/\text{m}^2$ )
- $A_0$  = fraction of  $R$  converted to sensible heat flux
- $C_0$  = opaque cloud cover (tenths).

During stable conditions,  $u_*$  is determined by the following method (Venkatram, 1980a):

$$u_* = \frac{C_{DN} u_m}{2} [1 + C^{0.5}] \quad (4-31)$$

$$C_{DN} = \frac{k}{\ln(z_m/z_0)} \quad (4-32)$$

$$C = 1 - \frac{4u_0^2}{C_{DN} u_m^2}, \quad C \geq 0 \quad (4-33)$$

$$u_0^2 = \frac{\gamma z_m}{k A} \quad (4-34)$$

where  $\gamma$  and  $A$  are constants with values of 4.7 and 1100, respectively, and  $C_{DN}$  is the neutral drag coefficient.

#### 4.3.4 Convective Velocity

The convective velocity scale,  $w_*$  (m/s), is computed for each grid cell for each hour using surface weather observations. The approach used is that given by Scire and co-workers (1984). During convective conditions,  $w_*$  is calculated from its definition:

$$w_* = \left( \frac{g}{T_0} Q_0 z_i \right)^{1/3} \quad (4-35)$$

where  $T_0$  is the surface air temperature (K),  $Q_0$  is from Equation 4-25, and  $z_i$  is the mixing height from Section 4.3.1. For  $Q_0$  less than zero,  $w_*$  is equal to zero.

#### 4.3.5 Monin-Obukhov Length

The Monin-Obukhov length,  $L$  (meters), is computed for each grid cell for each hour using surface weather observations. For unstable conditions it is computed from its definition:

$$L = - \frac{u_*^3 T_0}{g k Q_0} \quad (4-36)$$

whose terms have been defined earlier. During stable conditions,  $L$  is given by Venkatram (1980b) as

$$L = 1100 u_*^2 \quad (4-37)$$

#### 4.3.6 Temperature

The surface temperature,  $T_0$  (kelvins) is computed for each grid cell for each hour using surface observations and a seasonal empirical relationship between surface temperature and elevation (surface temperature lapse rate) derived from analysis of climatological data in western Colorado (PEDCO, 1981). PEDCO analyzed up to 40 years of surface temperature observations for nine stations in western Colorado. They determined the average temperature change with elevation for each month of the year. These monthly surface temperature lapse rates were plotted versus Julian day and the points connected with straight lines. The slopes and intercepts of these lines are given in Table 4-1. The hourly temperature observation at each surface station is interpolated to each grid point using an inverse-distance-squared weighting factor. The interpolated temperature from each

TABLE 4-1. Slope and intercept of temperature lapse rate correction by Julian Day.

Julian Day (d)	Slope (m)	Intercept (b)
$1 \leq d \leq 16$	-0.0152	-1.6950
$16 < d \leq 75$	-0.0607	-0.9592
$75 < d \leq 105$	0.0093	-6.2100
$105 < d \leq 136$	-0.0552	0.5619
$136 < d \leq 166$	0.0180	-9.3880
$166 < d \leq 197$	-0.0135	-4.1510
$197 < d \leq 228$	0.0116	-9.1077
$228 < d \leq 258$	0.0037	-7.2960
$258 < d \leq 289$	0.0832	-27.8223
$289 < d \leq 319$	0.0500	-18.2200
$319 < d \leq 350$	0.0261	-10.6052
$350 < d \leq 366$	-0.0152	3.8600

weather station is corrected for altitude differences between the weather station and the grid point. The corrected temperature is

$$T_G = T_S + (E_G - E_S) * LR/548.6 \quad (4-38)$$

where

$T_G$  = temperature at grid point (K)  
 $T_S$  = temperature at weather station (K)  
 $E_G$  = elevation at grid point (m MSL)  
 $E_S$  = elevation of weather station (m MSL)  
 $LR$  = correction surface temperature lapse rate ( $^{\circ}F/1000$  ft)

The lapse rate,  $LR$ , to correct surface temperature for variation in altitude is computed by

$$LR = md + b \quad (4-39)$$

where  $d$  is Julian day, and  $m$  and  $b$  are given in Table 4-1.

#### 4.3.7 Pressure

The surface pressure,  $P_0$  (mb), is computed for each grid cell for each hour using a density relationship derived by Drake, Huang, and Davis (1981) assuming dry adiabatic conditions and the gridded temperature values from Section 4.3.6.

$$P_0 = R_u T_0 \bar{\rho}(0) \left(1 - \frac{E_G}{H_a}\right)^{5/2} \quad (4-40)$$

where

$R_u$  = universal gas constant ( $2.869 \text{ m}^3 \cdot \text{mb}/(\text{kg} \cdot \text{K})$ )  
 $T_0$  = surface temperature at grid point (K)  
 $E_G$  = elevation of grid point (m MSL)  
 $\bar{\rho}(0)$  =  $353.1/\theta$ , air density at sea level ( $\text{kg}/\text{m}^3$ )  
 $H_a = c_p \theta/g$ , height of the adiabatic atmosphere (m).

In the definition for  $H_a$  and  $\bar{\rho}(0)$  above,  $\theta$  is the average potential temperature at sea level for an hour from all surface weather stations. It is obtained by first calculating the air density,  $\rho_s$ , at each surface weather station from the observed surface temperature,  $T_s$ , and pressure,  $P_s$ , at the site:

$$\rho_s = \frac{P_s}{R_u T_s} \quad (4-41)$$

then solving the following equation for  $\theta$  using Newton's method:

$$\rho_s = \bar{\rho}(0) \left(1 - \frac{E_G}{H_a}\right)^{5/2} \quad (4-42)$$

#### 4.3.8 Relative Humidity

The Lagrangian acid deposition model requires relative humidity in order to estimate water vapor concentrations used in the calculation of chemical transformation rates. The interpolation of relative humidity is an uncertain process because of its dependence on temperature. Thus the mesoscale meteorological model interpolates dew point in space and time, from which a three-dimensional distribution of relative humidity can be obtained.

The procedures used to interpolate dew point are very similar to those used for temperature. First a surface dew point field is obtained by interpolating the measurements from the surface sites using an elevation adjustment derived from an analysis of upper-air soundings from the Rocky Mountains. At each upper-air station, dew point lapse rates in the free atmosphere are calculated above and below the mixing height. These dew point lapse rates are then interpolated onto the grid using an inverse distance squared weighting procedure. The Lagrangian acid deposition model then calculates the relative humidity at any three-dimensional point in the modeling domain by first calculating the temperature,  $T$ , and dew point,  $T_D$ , at the point using the surface values and lapse rates, and then calculating the relative humidity using the following equation:

$$RH = 100 \cdot 10^{\frac{7.5 T}{237.3 + T} - \frac{7.5 T_D}{237.3 + T}} \quad (4-43)$$

#### 4.3.9 Precipitation Rate

Modeling of wet deposition requires estimates of precipitation at each grid cell of the modeling region. For the Rocky Mountain model it is expected that one-hour or 3-hour precipitation averages will be required depending on the user-defined update interval. The spatial extrapolation of precipitation at such short time scales represents a special challenge



over complex terrain such as the Rocky Mountains. Precipitation often occurs as the result of terrain-forced lifting of air masses above the point where condensation takes place. After air masses pass over such terrain obstacles, there is no moisture for precipitation on the lee side of the mountain. As a result, there is often augmented precipitation on the windward side of ridges, and rain shadows (minimums) in the lee of the ridges. Terrain height and slope are obvious factors in determining how much precipitation will fall.

Unfortunately, simple rules for spatially interpolating precipitation using terrain information do not always hold. For example, there may be substantial channeling of the paths that moist air masses may take. This channeling may be other than west-east along which most synoptic-scale storms travel over the western Rockies. Therefore such factors as north-south canyons and unresolved terrain features may act to produce precipitation variations that do not obey simple relations for precipitation estimates, such as functions of elevation and east-west terrain slope.

The goal of the present analysis was to obtain a year of short-term precipitation data at a grid resolution of approximately 5-10 km. Observed data was used as a starting point in the interpolation process. Contributions of precipitation due to terrain effects are added to precipitation estimates obtained by spatial interpolation of observed data. By making extensive use of the observations we guided the spatial interpolation process so that it did not produce spurious precipitation amounts.

Two sources of precipitation data are available--daily precipitation totals and hourly precipitation rates. In the interpolation methodology described in the following paragraphs we attempt to use all of the data to provide realistic fields of precipitation, thereby avoiding some global assumptions that leave the interpolated precipitation fields with serious departures from reality, such as the phenomena of "popping" rainfields where rainfall maximums appear simultaneously over the modeling region.

#### 4.3.9.1 Interpolation of Daily Precipitation Data

The first step in the interpolation methodology is to estimate the distance of the (i,j) grid cell from the  $k^{\text{th}}$  observation site. The following inverse distance weight is estimated for each grid cell and observation site:

$$w_{i,j}(k) = 1.0/D^3 = 1.0/[(X_{i,j} - X_k)^2 + (Y_{i,j} - Y_k)^2]^{1.5}$$

The largest two weights for each (i,j) grid cell are retained. A coefficient  $C_1$  is estimated that will make the  $w_{i,j}(k)$  over all 24-hour precipitation observation sites sum to one. This coefficient is then used to estimate new weights that sum to one, i.e.,

$$w'_{i,j}(k) = w_{i,j}(k) C_1$$

Only the highest and second largest weights are used to estimate the interpolated value at the (i,j) grid cell. The remaining portion of the concerning the underlying terrain.

The weight used to factor in the regressed value of precipitation is determined from

$$B_{i,j}(k) = 1.0 - [w'_{i,j}(\text{largest}) + w'_{i,j}(\text{2nd largest})]$$

The geographically induced portion of the precipitation,  $X_{\text{geo}}$ , is computed within the sphere of influence of each site. The sphere of influence for the  $k^{\text{th}}$  observation site is defined as all grid cells that identified the  $k^{\text{th}}$  site as having the largest weight. The interpolated precipitation estimate,  $X_{i,j}$ , is computed from the following equation:

$$X_{i,j} = X_k w_{i,j}(k) + X_l w_{i,j}(l) + X_{\text{geo}} B_{i,j}(k) \delta_{k,l}$$

where  $k$  denotes the site with the largest weight;  $l$  denotes the site with the second largest weight;  $\delta_{k,l} = 1$  if  $X_k \neq 0$ ,  $\delta_{k,l} = 0$  if  $X_k = 0$ .

The  $X_{\text{geo}}$  depends on whether the east-west slope  $S_{i,j}$  is either positive or negative. The slope is computed using the 10 km average terrain,  $H$ , in the following manner:

$$S_{i,j} = H_{i+1,j} - H_{i,j}$$

If the slope at the (i,j) cell is positive and the slope at the  $k^{\text{th}}$  observation site is also positive, the following equation is used:

$$X_{\text{geo}} = 0.01 (H_{i,j} - H_k) + X_k$$

If the slope is negative then a different set of regression equations applies. If the slope  $S_k$  is greater than zero then the following relation is used:

$$X_{\text{geo}} = X_{i,j} + 0.45 S_{i,j}$$

If the slope  $S_k$  is less than zero then the following relation is used:

$$X_{\text{geo}} = X_k + 0.45 (S_{i,j} - S_k)$$

If the slope  $S_k$  is negative, but the slope at  $S_{i,j}$  is positive, then we estimate the precipitation from ground level as follows:

$$X_{\text{geo}} = 0.01 H_{i,j}$$

These formulas can occasionally produce rainfall fields that in places are relatively discontinuous and may be somewhat spurious. To deal with these cases we first smooth the precipitation field with  $N$  passes of a simple five-point filter, i.e.,

$$\langle X_{i,j} \rangle = 0.5 X_{i,j} + 0.125 (X_{i+1,j} + X_{i-1,j} + X_{i,j+1} + X_{i,j-1})$$

The number of passes is generally less than 10 to avoid excessively smooth precipitation fields.

The interpolated rainfall using this procedure was well behaved enough so that no smoothing was required ( $N = 0$ ). In order to avoid the intrusion of precipitation into areas without rain, we take the following precautions. First, all daily precipitations of less than 0.01 inch are set equal to zero. Secondly, where the  $k^{\text{th}}$  observation site does not show any significant precipitation, interpolated precipitation values less than 0.05 inches are set equal to zero within the "dominant" sphere of influence of that station.

#### 4.3.9.2 Distribution of Rainfall Within the Day

At each of the hourly observation sites the total precipitation within each day was weighted so that the sum over all hours of the day equals 1.0. Weighted precipitation within a day was created even for days when no precipitation occurred at the site. This was done to provide weights when rain might have occurred at adjacent sites. These weights were created by linearly interpolating between days when precipitation did occur. The linear interpolation was done in such a way that the sums of these weights over the day still sum to 1.0.

The inverse distance weights for each  $(i,j)$  grid cell and  $k^{\text{th}}$  observation site were computed in the same fashion as was done for the daily data. These weights were then multiplied by the weights for calculating the distribution of the daily rainfall. The resulting product of weights had to

be such that the distributed daily total precipitation must sum to the daily observed or interpolated precipitation, i.e.,

$$X_{i,j}(k) = C_{i,j}(k) w_{i,j}(k) p_{i,j}(k)$$

where  $p_{i,j}(k)$  is the weight for the distribution of precipitation at the  $k^{\text{th}}$  site within a single day. The  $C_{i,j}(k)$  is the constant required for recovery of the observed or interpolated daily precipitation at the  $(i,j)$  grid cell. When the distributed precipitation is less than one, the precipitation is assumed to be zero.

## 5 DESIGN OF THE ACID DEPOSITION MODEL FOR THE ROCKY MOUNTAIN REGION

Our evaluation of the final four candidate acid deposition models indicates that no one of these models is the best choice for calculating source-specific acid deposition impacts in the Rocky Mountain region (Morris and Kessler, 1987). Our evaluation also indicates that the most flexible modeling approach would be the Gaussian puff model formulation. However, neither of the candidate Gaussian puff models (the MESOPUFF-II or MELSAR-POLUT) appears to be superior in all processes that lead to acid deposition. The MELSAR-POLUT model appears to describe transport and dispersion in complex terrain better than the MESOPUFF-II; however, the MELSAR-POLUT does not treat chemical transformation or scavenging. In this section we describe a new acid deposition model that uses the most scientifically sound components of the candidate models.

### 5.1 TRANSPORT

All of the candidate acid deposition models, except the CCADM, use the wind at the plume centerline to advect the puff or plume. The CCADM relies on user input for its trajectory definition. The analysis of transport as a function of height (Section 3.1) indicates that the resultant trajectory in complex terrain is very dependent on the height of the air parcel above the ground. The differences in trajectories at different heights were magnified by the stagnant conditions that existed in the evaluation tests; however, those tests did verify that defining trajectories in complex terrain is very uncertain.

Use of the wind at the plume centerline is consistent with an actual simulated air parcel trajectory at some height and with the formulation of the new Rocky Mountain Lagrangian acid deposition model. The use of a vertically vector averaged wind for advecting a puff through complex terrain may result in an impossible trajectory if sufficient wind shear exists.

In the formulation of the Rocky Mountain acid deposition model considerations are given for the future implementation of allowing vertical shearing of the Lagrangian puffs when decoupled flow conditions exist. However, for this initial version of the Rocky Mountain model, the Lagrangian puff is advected as a cohesive unit.

## 5.2 DISPERSION

Of the four candidate models, the MELSAR-POLUT parameterization of dispersion includes the most complete description of diffusion over complex terrain (see Appendix A in Morris and Kessler, 1987; or Allwine and Whiteman, 1985). Thus the MELSAR-POLUT dispersion algorithm has been implemented in the new Rocky Mountain model. The performance evaluation of this algorithm showed that it reacts as expected to changes in terrain roughness (see Section 3.2).

Since the Rocky Mountain model is intended to be used for the calculation of impacts as part of the PSD permitting process, the user should have the option of calculating dispersion in a manner similar to EPA-approved models. Thus, the MESOPUFF-II dispersion algorithms have also been implemented in the Rocky Mountain model. The MESOPUFF-II parameterization of the  $\sigma_y$  and  $\sigma_z$  curves attempts to duplicate the values suggested by Pasquill, Gifford and Turner (Turner 1970), which are used in most EPA-approved models.

## 5.3 CHEMICAL TRANSFORMATION

Of the candidate models, the CCADM contains the most comprehensive chemistry module. However, the computational requirements of CCADM and the model's need for an ambient field of background concentrations preclude its use in the Rocky Mountain acid deposition model. In the evaluations of the parameterized pseudo-first-order chemistry mechanisms used in the MESOPUFF-II and RIVAD (see Section 3.3), the RIVAD chemistry responded as expected to changes in environmental and concentration conditions. The MESOPUFF-II oxidation rates were totally insensitive to changes in temperatures, which may be important in the higher elevations of the Rocky Mountains. In addition, the MESOPUFF-II chemical mechanisms appear to be designed for the urban or polluted atmosphere of the East Coast. The RIVAD model has been applied to the western states, including the Rocky Mountains, and evaluation of the model's performance shows quite good agreement between the predicted and observed ambient concentrations.

Thus, the RIVAD chemical mechanism has been implemented in the Rocky Mountain model. In order to give the user other options for chemical transformation, the MESOPUFF-II theoretical chemical mechanism has also been implemented in the Rocky Mountain model as an option.

The modular design of the Rocky Mountain model will easily allow the insertion of new chemical mechanisms as they become available. Future mechanisms could be developed for the Rocky Mountain region by exercising

a model with a sophisticated chemical kinetic mechanism, such as the RADM or CCADM, and parameterizing the chemical reaction rates in terms of a look-up table, as is done in the RTM-IINL, or through regression equations. In addition, when the engineering version of the RADM becomes available, the chemical mechanism therein may be appropriate for the Rocky Mountain model.

#### 5.4 DRY DEPOSITION

The preferred approach for the modeling of dry deposition involves the resistance concept. The deposition velocities produced by the two candidate models that use the resistance approach, the MESOPUFF-II and the CCADM, were compared and evaluated (see Section 3.4). The deposition velocities calculated by these models were generally consistent with available measurements; notable exceptions were the deposition velocities for the aerosol species (sulfates and nitrates) calculated by the MESOPUFF-II, and the deposition velocity for  $\text{NO}_2$  over water produced by the CCADM. The CCADM calculates an areal average deposition velocity over the region occupied by the plume, while the MESOPUFF-II bases its deposition velocity on to a single land use category located at the puff's center. Thus it seems more appropriate to use the CCADM dry deposition module within the Rocky Mountain acid deposition model. The CCADM dry deposition algorithm is also the one most like the parameterization in RADM. The CCADM algorithm was extended to include dry deposition of pollutants over snow. In addition, the surface resistance of  $\text{NO}_x$  over water has been increased. This modified version of the CCADM has been implemented in the Rocky Mountain model.

#### 5.5 WET DEPOSITION

Evaluation of the wet deposition algorithms (see Section 3.5) shows that the MESOPUFF-II scavenging coefficient approach is the most flexible and consistent with the Lagrangian puff formulation of the Rocky Mountain model. The ability to easily incorporate the different scavenging characteristics of liquid versus frozen precipitation is especially important in the high elevation regions of the Rocky Mountains. Thus wet scavenging within the Rocky Mountain model is parameterized in terms of the scavenging coefficient approach. As new scavenging ratios are reported in the literature, they can be easily incorporated in the model.

#### 5.6 SUMMARY

The acid deposition/air quality module of the Rocky Mountain model incorporates the most appropriate and scientifically sound components of the

candidate acid deposition models. The model uses the Lagrangian puff model formulation and parameterizes the major processes as follows:

Transport--uses the wind vector from the new diagnostic wind model at the plume centerline height above ground.

Dispersion--uses the MELSAR-POLUT complex terrain dispersion formulas with the MESOPUFF-II parameterization of the PGT disperiosn curves also implemented as an option.

Chemical Transformation--uses the RIVAD peusdo first-order chemical reaction rate mechanism; the MESOPUFF-II theoretical rate expressions are implemented in the model as an optional mechanism.

Dry Deposition--uses the CCADM resistance approach with the cell-averaging procedure currently implemented in the RADM.

Wet Deposition--uses the scavenging coefficient approach as used in the MESOPUFF-II model.



## 6 SUMMARY AND RECOMMENDATIONS

A new hybrid mesoscale acid deposition/air quality model has been designed specifically for calculating incremental impacts of deposition of nitrogen and sulfur species and concentrations of PSD pollutants in the complex terrain region of the Rocky Mountains. The modeling system contains two principal components: a mesoscale meteorological model and an acid deposition/air quality model. The formulation of the new model combines the most technically advanced components of existing candidate mesoscale meteorological and acid deposition models that are consistent with the overall design of the modeling system. The selection of the candidate models and a preliminary evaluation was presented in a previous report (Morris and Kessler, 1987). The overall design of the modeling system was guided by the recommendations of the potential users represented by the members of the Western Acid Deposition Task Force.

A preliminary evaluation of the modeling system was conducted. The new Diagnostic Wind Model (DWM) was evaluated using a hypothetical terrain obstacle, terrain from the Rocky Mountains, a complex terrain/coastal environment with a dense observational network, and within a large valley; finally, the DWM predictions were compared with observations from the Rocky Mountains. These evaluations of the new DWM illustrated the flexibility of the DWM in simulating air flows over a variety of complex-terrain configurations in areas with and without observations.

The acid deposition/air quality component of the hybrid modeling system was evaluated by evaluating the individual modules and components that comprise the model.

Although the hybrid modeling system was constructed by using state-of-the-art components from existing models, the modeling system was designed to be flexible and easily expanded. Instead of selecting a single component for insertion into the modeling system, the model was configured with several options to treat major processes, such as transport, dispersion, and chemical transformation. In addition, as our understanding of these processes increases, the insertion of new modules into the modeling system can be easily accomplished.

The delivery of the initial version of the model is scheduled for the end of 1987. Along with the model code, a user's guide and a document describing the technical formulation of the modeling system is also scheduled for delivery. Other documents under development as part of the Rocky Mountain Model Assessment Project are a protocol for evaluating the performance of the new modeling system and a report describing the evaluation.

The performance evaluation of the new model is required in order to have confidence in the model predictions and identify any areas of the modeling system that need improvement. In particular, it must be demonstrated that the model adequately predicts source-receptor relationships of acid deposition in complex terrain. Unfortunately, there are currently no data bases for the evaluation of acid deposition source-receptor relationships. The best data bases available for evaluation source-receptor relationships consist of several tracer experiments. The model evaluation protocol will contain a review of all pertinent tracer data bases available for evaluating the new Rocky Mountain model and will select a few for the evaluation. In addition, the protocol will also recommend ways in which the new model's ability to predict acid deposition impacts can be evaluated.

## REFERENCES

- Allwine, K. J., and C. D. Whiteman. 1985. "Green River Air Quality Model Development: MELSAR--A Mesoscale Air Quality Model for Complex Terrain. Volume 1--Overview, Technical Description and User's Guide." Prepared by Pacific Northwest Laboratory, Richland, Washington, for U.S. Environmental Protection Agency (EPA 600/8-85-0176; NTIS PB 85-247211).
- Arritt, R. W., and R. A. Pielke. 1986. Interactions of nocturnal slope flows with ambient winds. Boundary-Layer Meteorol., 37:183-195.
- Atkinson, R., A. C. Lloyd, and L. Wings. 1982. An updated chemical mechanism for hydrocarbon/ $\text{NO}_x$ / $\text{SO}_x$  photooxidations suitable for inclusion in atmospheric simulation models. Atmos. Environ., 16:1341.
- Benkley, C. W., and A. Bass. 1979a. Development of Mesoscale Air Quality Simulation Models, Vol. II: User's Guide to MESOPLUME (Mesoscale Plume Segment) Model. U.S. Environmental Protection Agency, Research Triangle Park, North Carolina (EPA-600/7-80-057).
- Benkley, C. W., and A. Bass. 1979b. "Development of Mesoscale Air Quality Simulation Models, Vol. III: User's Guide to MESOPUFF (Mesoscale Puff) Model." Environmental Research and Technology, Inc., Concord, Massachusetts.
- Benkley, C. W., and L. L. Schulman. 1979. Estimating hourly mixing depths from historical meteorological data. J. Applied Meteor., 18:772-780.
- Businger, J. A. 1973. "Turbulent Transfer in the Atmospheric Surface Layer." In Workshop on Micrometeorology. American Meteorological Society, Boston, Massachusetts.
- Chang, J. S., R. A. Brost, L.S.A. Isaksen, P. Middleton, W. R. Stockwell, and C. J. Walcek. 1986. RADM, a three-dimensional Eulerian acid deposition model. Part I: Physical concepts and model formulation. Submitted to J. Geo. Res.

- Clark, T. L., and R. Gall. 1982. Three-dimensional numerical model simulations of airflow over mountainous terrain: A comparison with observations. Mon. Weather Rev., 110:766-791.
- Drake, R. L., C. H. Huang, and W. E. Davis. 1981. "Green River Ambient Model Assessment Program - Progress Report for the Regional and Mesoscale Flow Modeling Components." Pacific Northwest Laboratory, Richland, Washington (PNL-3988).
- Durran, D. R., and J. B. Klemp. 1982. The effects of moisture on trapped mountain lee waves. J. Atmos. Sci., 39:2490-2506.
- Durran, D. R., and J. B. Klemp. 1983. A compressible model for the simulation of moist mountain waves. Mon. Weather Rev., 11:2341-2361.
- EPA. 1985. Interim Procedures for Evaluating Air Quality Models: Experience with Implementation. U.S. Environmental Protection Agency, Research Triangle Park, North Carolina (EPA-450/4-85-006).
- EPA. 1986. Guideline On Air Quality Models (Revised). U.S. Environmental Protection Agency, Research Triangle Park, North Carolina (EPA-450/2-78-027R).
- Fitzjarrald, D. R. 1984. Katabatic wind in opposing flow. J. Atmos. Sci., 41:1143-1158.
- Fox, D. G. 1981. Judging air quality model performance: A summary of the AMS Workshop on dispersion model performance. Bull. Am. Meteorol. Soc., 62:599-609.
- Garland, J. A. 1977. The dry deposition of sulfur dioxide to land and water surfaces. Proc. R. Soc. Lond. A, 354:245-268.
- Gery, M. W., R. E. Morris, S. M. Greenfield, M. K. Liu, D. A. Stewart, G. Z. Whitten, and J. L. Fieber. 1987. "Development of a Comprehensive Chemistry Acid Deposition Model (CCADM)." Systems Applications, Inc., San Rafael, California (SYSAPP-87/061).
- Gifford, F. A. 1982. Horizontal diffusion in the atmosphere: A Lagrangian-dynamical Theory. Atmos. Environ., 16(3):505-512.
- Gillani, N. V., S. Kohli, and W. E. Wilson. 1981. Gas-to-particle conversion of sulfur in power plant plumes: I. Parameterization of the gas phase conversion rates for dry, moderately polluted ambient conditions. Atmos. Environ., 15:2293-2313.

- Godden, D., and F. Lurmann. 1983. "Development of the PLMSTAR Model and Its Application to Ozone Episode Conditions in the South Coast Air Basin." Environmental Research & Technology, Inc., Westlake Village, California (ERT P-A702-200).
- Goodin, W. R., G. J. McRae, and J. H. Seinfeld. 1980. An objective analysis technique for constructing three-dimensional urban scale wind fields. J. Appl. Meteorol., 19:98-108.
- Hales, J. M., and S. L. Sutter. 1973. Solubility of sulfur dioxide in water at low concentrations. Atmos. Environ., 7:997-1001.
- Hayes, S. R. 1979. Performance Measures and Standards for Air Quality Simulation Models. U.S. Environmental Protection Agency, Research Triangle Park, North Carolina (EPA-450/4-79-032).
- Heffter, J. L. 1965. Variations of horizontal diffusion parameters with time for travel periods of one hour or longer. J. Appl. Meteorol., 4:153-156.
- Henry, R. C., and G. M. Hidy. 1981. Author's reply to discussion of "Multivariate analysis of particulate sulfate and other air quality variables. Part I. Annual data from Los Angeles and New York." Atmos. Environ., 15:425-426.
- Henry, R. C., and G. M. Hidy. 1982. Multivariate analysis of particulate sulfate and other air quality variables by principal components. Part II. Salt Lake City, Utah and St. Louis, Missouri. Atmos. Environ., 16:929-943.
- Hicks, B. B. 1983. In Critical Assessment Document on Acid Deposition (Chapter VII). Atmospheric Turbulence and Diffusion Laboratory, NOAA, Oak Ridge, Tennessee (File No. 81/24).
- Hill, A. C., and E. M. Chamberlain. 1976. "Removal of Water Soluble Gases from the Atmosphere by Vegetation." Proc. Symp. on Atmosphere-Surface Exchange of Particles and Gases. ERDA Symposium Series NTIS.
- Hillyer, M. J., S. D. Reynolds, and P. M. Roth. 1979. Procedures for Evaluating the Performance of Air Quality Simulation Models. U.S. Environmental Protection Agency, Research Triangle Park, North Carolina (EPA-450/4-79-033).

- Irwin, J. S. 1979. "Estimating Plume Dispersion--A Recommended Generalized Scheme." Proceedings of Fourth Symposium on Turbulence, Diffusion, and Air Pollution, American Meteorological Society.
- Latimer, D. A., M. W. Gery, and H. Hogo. 1986. "A Theoretical Evaluation of the Role of Nighttime Nitrate Formation in the Formation of Layered Haze." Systems Applications, Inc., San Rafael, California (SYSAPP-86/012).
- Liu, M. K., R. E. Morris, and J. P. Killus. 1984. Development of a regional oxidant model and application to the northeastern United States. Atmos. Environ., 18:1145-1161.
- Liu, M. K., and M. A. Yocke. 1980. Siting of wind turbine generators in complex terrain. J. Energy, 4(1):10-16.
- MacCready, P. B., Jr., L. B. Baboolal, and P.B.S. Lissaman. 1974. "Diffusion and Turbulence Aloft Over Complex Terrain." AMS Symposium on Atmospheric Diffusion and Air Pollution, Santa Barbara, California
- Mahrt, L. 1982. Momentum balance of gravity flows. J. Atmos. Sci., 39:2701-2711.
- McMahon, T. A., and P. J. Denison. 1979. Empirical atmospheric deposition parameters--a survey. Atmos. Environ., 13:571-585.
- Moore, G. E., R. E. Morris, and C. Daly. 1987. "Application of a Regional Air Quality Model to the California San Joaquin Valley." Systems Applications, Inc., San Rafael, California (SYSAPP-87/155).
- Morris, R. E., and R. C. Kessler. 1987. "Rocky Mountain Acid Deposition Model Assessment." Systems Applications, Inc., San Rafael, California (SYSAPP-87/201, EPA-600/3-87-013; NTIS PB87-180584-AS)
- Morris, R. E., M. K. Liu, and S. D. Reynolds. 1987. "The Systems Applications, Inc. Regional Transport Model: Current Status and Future Needs." Air Pollution Control Association International Specialty Conference on the Scientific and Technical Issues Facing Post-1987 Ozone Control Strategies. Hartford, Connecticut.
- NCAR. 1985. "NCAR Eulerian Regional Acid Deposition Model." National Center for Atmospheric Research, Boulder, Colorado (Technical Note NCAR/TN-256+STR).

- NRC. 1983. Acid Deposition: Atmospheric Processes in Eastern North America. National Research Council. National Academy Press, Washington, DC.
- Owers, M. J., and A. W. Powell. 1974. Deposition velocity of sulphur dioxide on land and water surfaces using a 35S tracer method. Atmos. Environ., 8:63-67.
- PEDCO. 1981. "Colorado's Climate, Meteorology and Air Quality." PEDCO Environmental, Inc., Cincinnati, Ohio.
- Pielke, R. A. 1974. A three-dimensional numerical model of the sea breezes over southern Florida. Mon. Weather Rev., 102:115-139.
- Pielke, R. A. 1984. Mesoscale Meteorological Modeling. Academic Press.
- Pleim, J., A. Venkatram, and R. Yamartino. 1984. "ADOM/TADAP Model Development Program, Volume 4: The Dry Deposition Module." Environmental Research and Technology, Inc., Concord, Massachusetts (P-B980-520).
- Prahm, L. P., U. Torp, and R. M. Stern. 1976. Deposition and transformation rates of sulphur oxides during atmospheric transport over the Atlantic. Tellus 28:355-372.
- Prandtl, L. 1942. Führer durch die Strömungslehre. Verlag Vieweg und Sohn, Braunschweig, Germany.
- Randerson, D. 1972. Temporal changes in horizontal diffusion parameters of a single nuclear debris cloud. J. Appl. Meteorol., 11:670-673.
- Rao, K. S., and H. F. Snodgrass. 1981. A nonstationary nocturnal drainage flow model. Bound. Layer Meteorol., 20:309-320.
- Ross, D. G., and I. Smith. 1986. "Diagnostic Wind Field Modelling for Complex Terrain--Testing and Evaluation." Centre for Applied Mathematical Modelling, Chisholm Institute of Technology (CAMP Report No. 5/86).
- Roth, P. M., C. Blanchard, J. Harte, H. Michaels, and M. T. El-Ashry. 1985. The American West's Acid Rain Test. World Resources Institute (Research Report #1).
- Scire, J. S., and F. W. Lurmann. 1983. "Development of the MESOPUFF II Dispersion Model." Sixth Symposium on Turbulence and Diffusion, American Meteorological Society (paper P1.11).

- Scire, J. S., F. W. Lurmann, A. Bass, and S. R. Hanna. 1983. Development of the MESOPUFF II Dispersion Model. U. S. Environmental Protection Agency, Research Triangle Park, North Carolina.
- Scire, J. S., F. W. Lurmann, A. Bass, and S. R. Hanna. 1984. "User's Guide to the MESOPUFF II Model and Related Processor Programs." Environmental Research & Technology, Inc., Concord, Massachusetts.
- Scott, B. C. 1978. Parameterization of sulfate removal by precipitation. J. Appl. Meteorol., 17:1375.
- Sehmel, G. A. 1980. Particle and gas dry deposition: a review. Atmos. Environ., 14:983-1011.
- Sheih, C. M., M. L. Wesely, and B. B. Hicks. 1979. Estimated dry deposition velocities of sulfur over the eastern United States and surrounding regions. Atmos. Environ., 13:1361-1368.
- Smith, R. B. 1979. The influences of mountains on the atmosphere. Adv. Geophys., 21:87-230.
- Smith, F. B., and R. D. Hunt. 1978. Meteorological aspects of the transport of pollution over long distances. Atmos. Environ., 12:461-477.
- Spedding, D. J. 1969. Uptake of sulphur dioxide by barley leaves at low sulphur dioxide concentrations. Nature, 224:1229-1231.
- Turner, D. B. 1970. Workbook of Atmospheric Dispersion Estimates. U.S. Environmental Protection Agency, Research Triangle Park, North Carolina (AP-26).
- Van Aalst, R. M., H.S.M.A. Diederren, J. H. Duyzer, and G. M. Meyer. 1983. "Dry Deposition of Acid Precursors in the Netherlands." TNO, Delft, The Netherlands.
- Venkatram, A. 1980a. "Estimation of Turbulence Velocity Scales in the Stable and the Unstable Boundary Layer for Dispersion Applications." Eleventh NATO-CCSM International Technical Meeting on Air Pollution Modeling and Its Application, pp. 169-179.
- Venkatram, A. 1980b. Estimating the Monin-Obukhov length in the stable boundary layer for dispersion calculations. Boundary-Layer Meteorology, 19:481-485.



- Walcek, C. J., R. A. Brost, J. S. Chang, and M. L. Wesley. 1986. SO<sub>2</sub>, sulfate, and HNO<sub>3</sub> deposition velocities computed using regional land-use and meteorological data. Atmos. Environ., 20(5):949-964.
- Walcek, C. J., and W. R. Stockwell. 1986. The contribution of aqueous-phase radical chemistry to sulfur and H<sub>2</sub>O<sub>2</sub> chemistry in cloudy environments. Submitted for publication.
- Wang, I. T., and P. C. Chen. 1980. Estimations of heat and momentum fluxes near the ground. Proc. 2nd Joint Conference on Applications of Air Pollution Meteorology.
- Wesely, M. L., and B. B. Hicks. 1977. Some factors that affect the deposition rates of sulfur dioxide and similar gases on vegetation. J. Air Pollut. Control Assoc., 27:1110-1116.
- Whelpdale, D. M., and R. W. Shaw. 1974. Sulphur dioxide removal by turbulent transfer over grass, snow and water surfaces. Tellus, 26:195-204.
- Willmott, C. J. 1982. Some comments on the evaluation of model performance. Bull. Am. Meteorol Soc., 82:1309.

## APPENDIX

Dry deposition velocities (cm/s) predicted by the MESOPUFF-II and the CCADM for

Sulfur dioxide ( $\text{SO}_2$ )

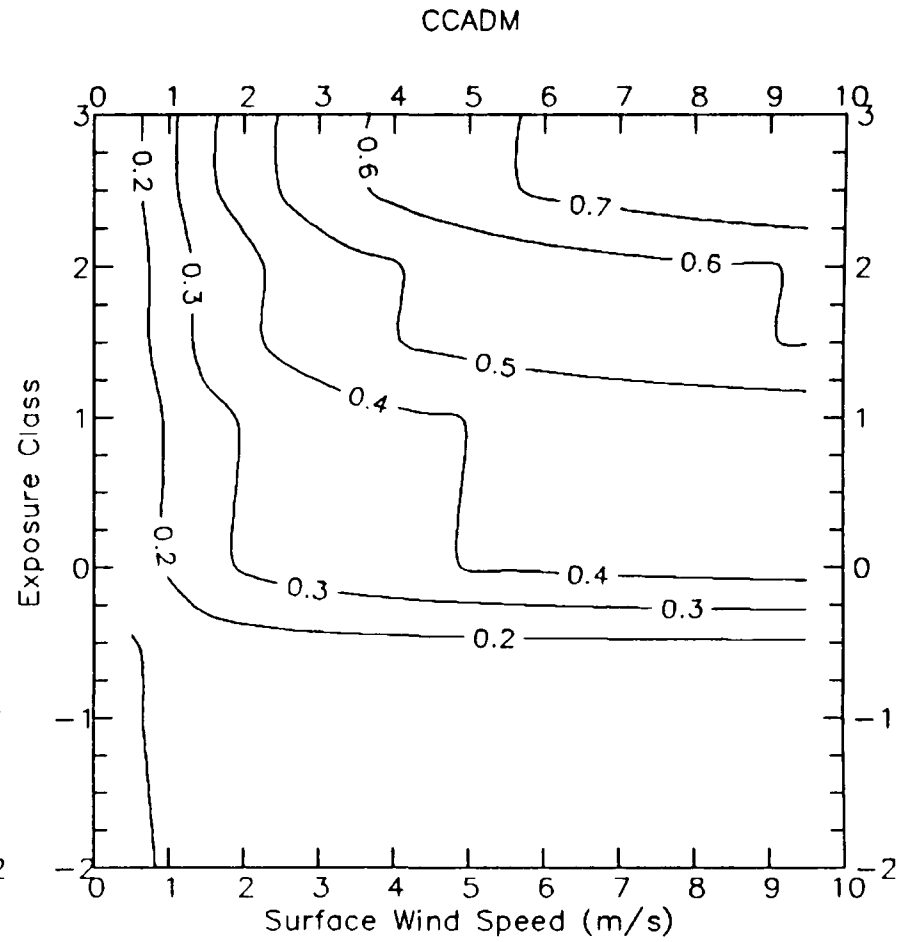
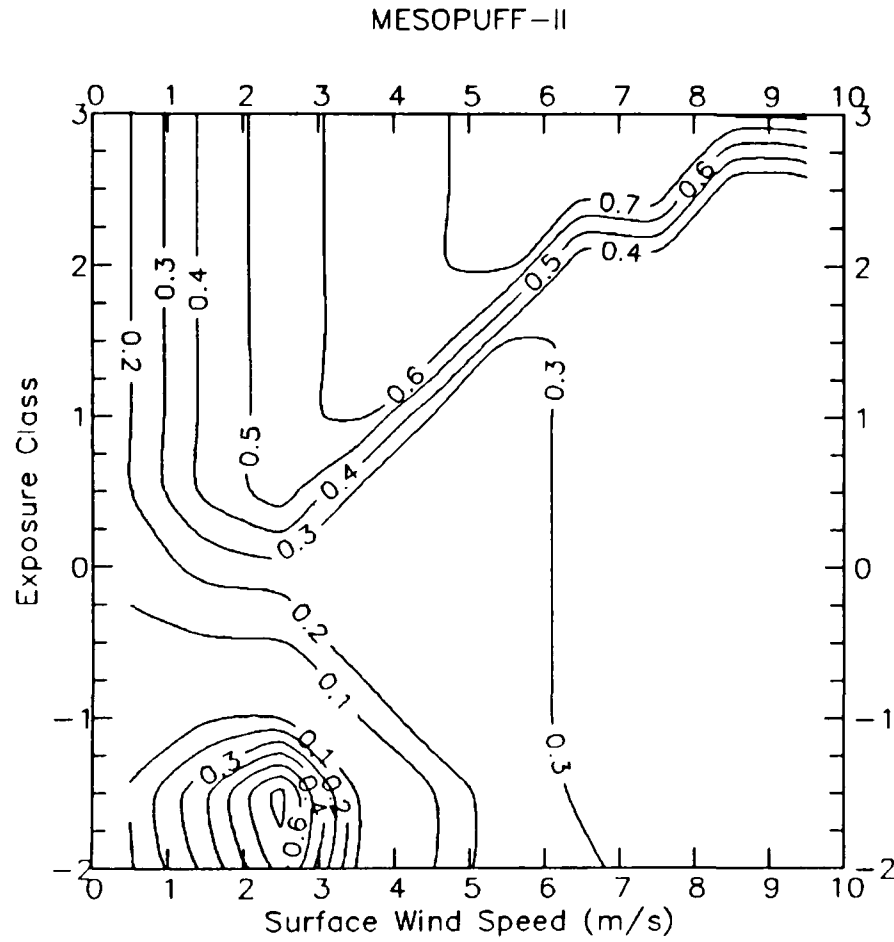
Sulfate ( $\text{SO}_4$ )

$\text{NO}_x$  ( $\text{NO}_2$ )

Nitric Acid ( $\text{HNO}_3$ )

Nitrate ( $\text{NO}_3$ )

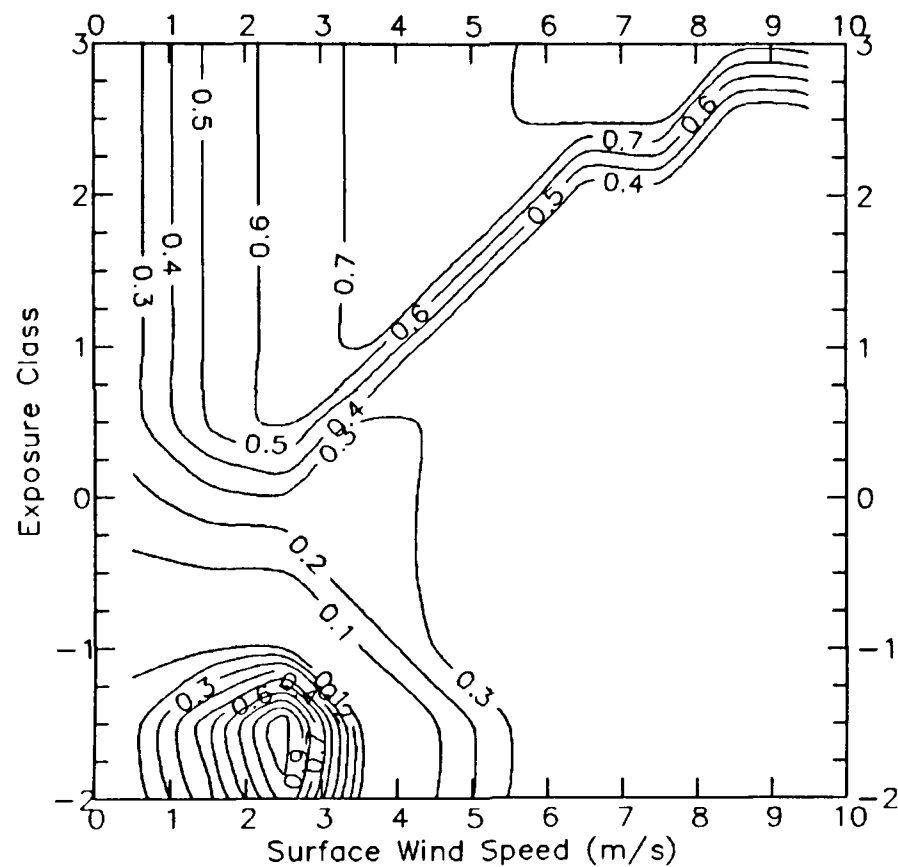
A-2



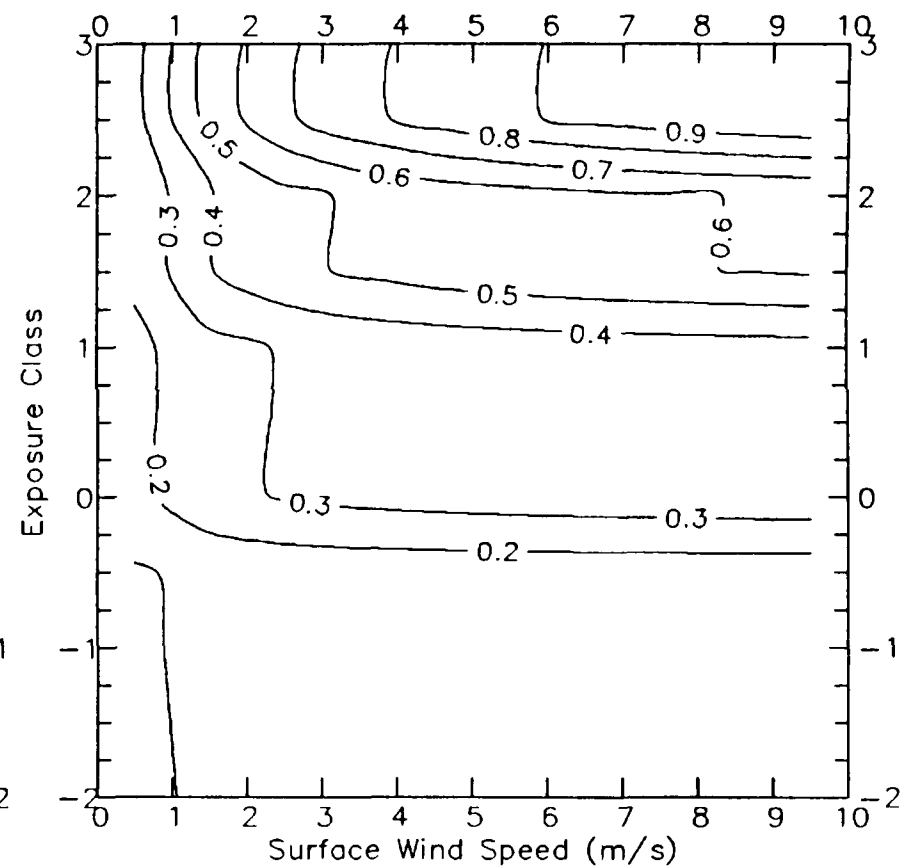
SO<sub>2</sub> Deposition Velocities (cm/s) for CROPLAND AND PASTURE Land Use Type.

A-3

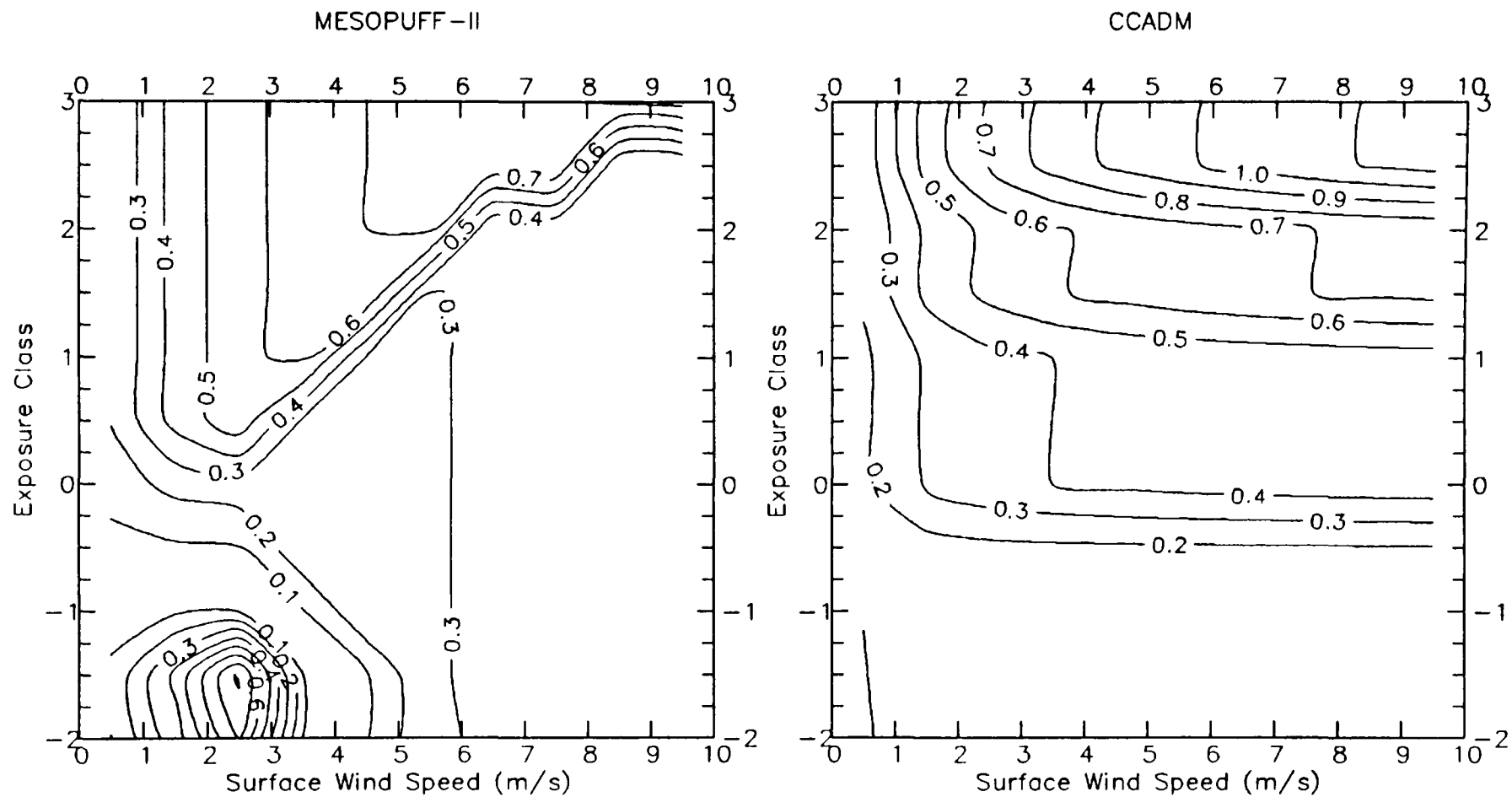
MESOPUFF-II



CCADM

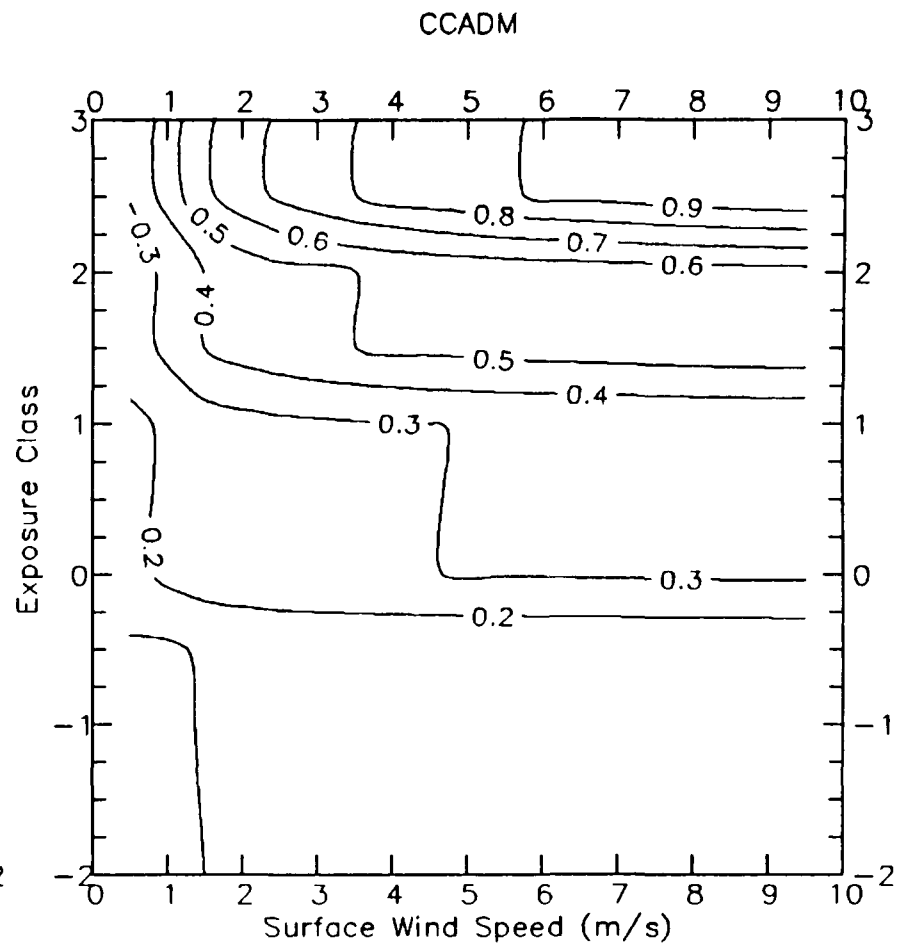
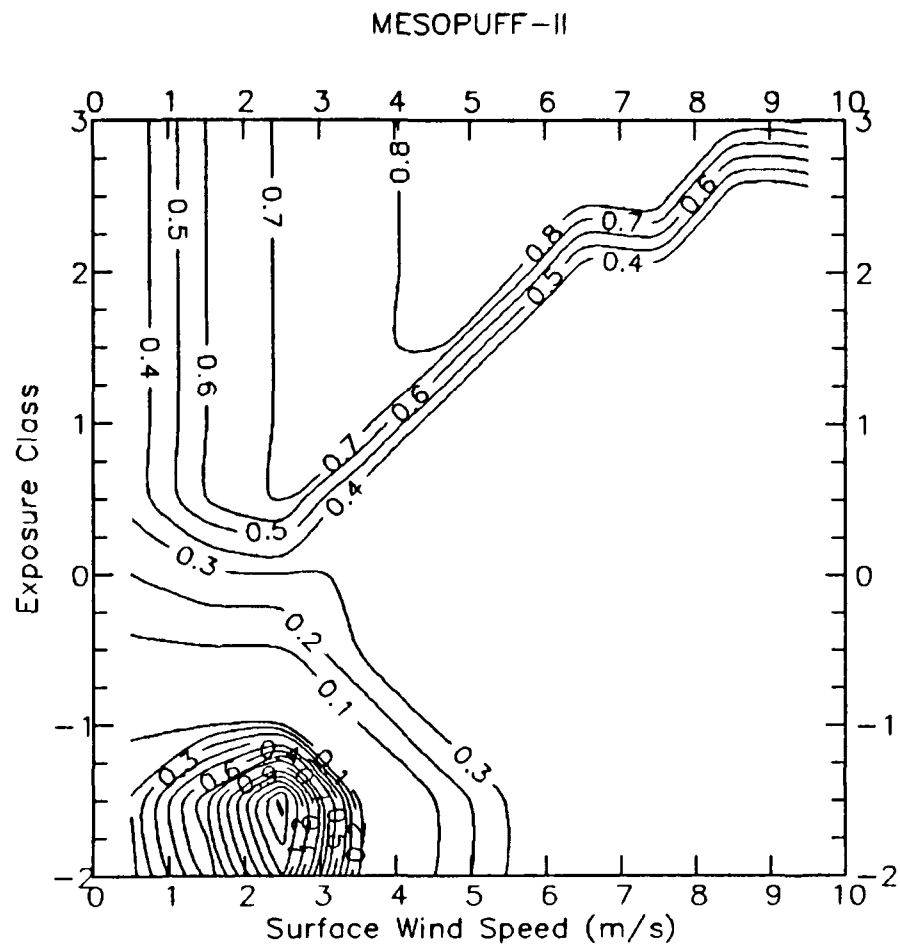


SO<sub>2</sub> Deposition Velocities (cm/s) for CROPLAND/WOODLAND/GRAZING Land Use Type.

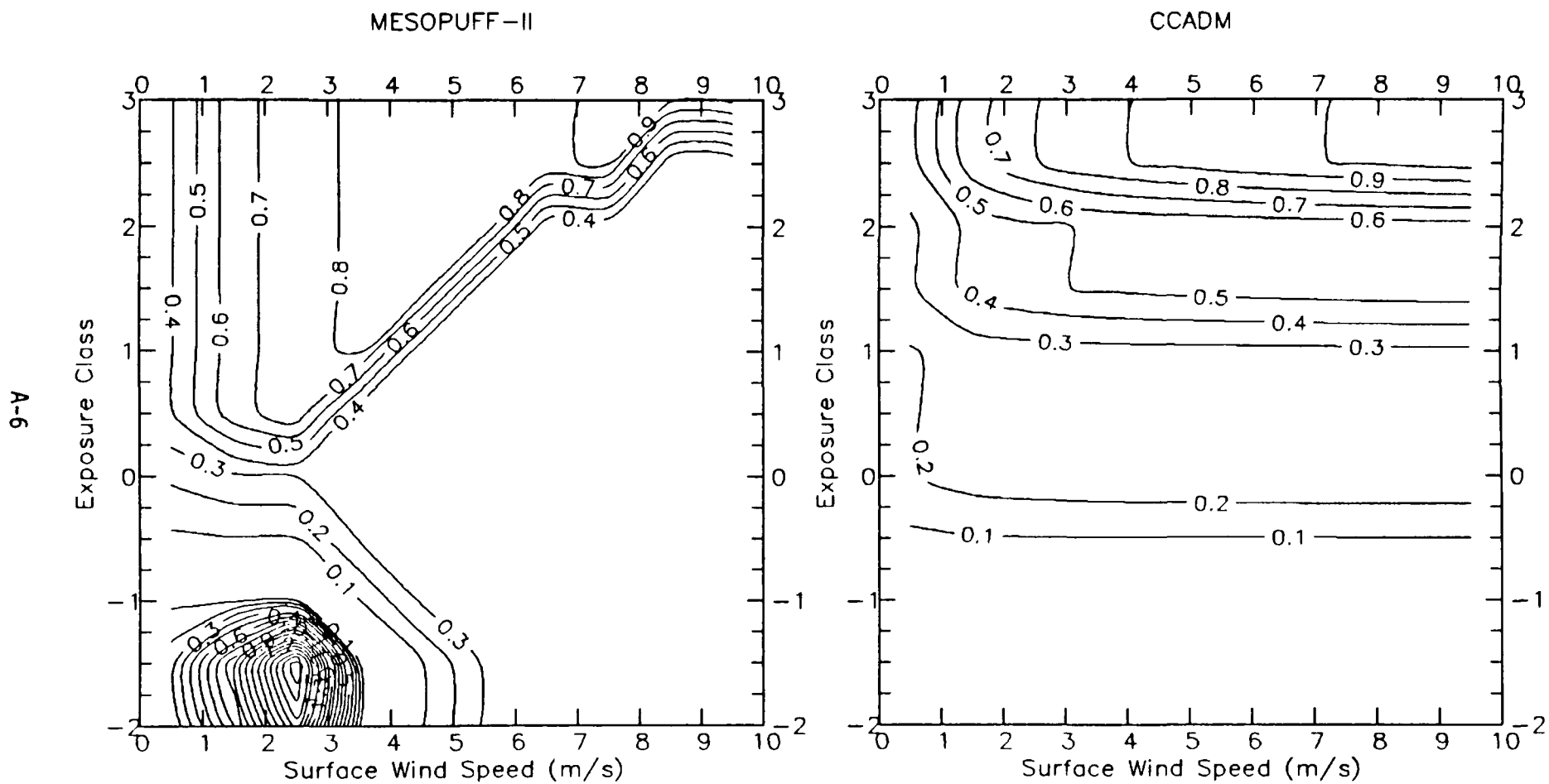


SO<sub>2</sub> Deposition Velocities (cm/s) for IRRIGATED CROPS Land Use Type.

A-5



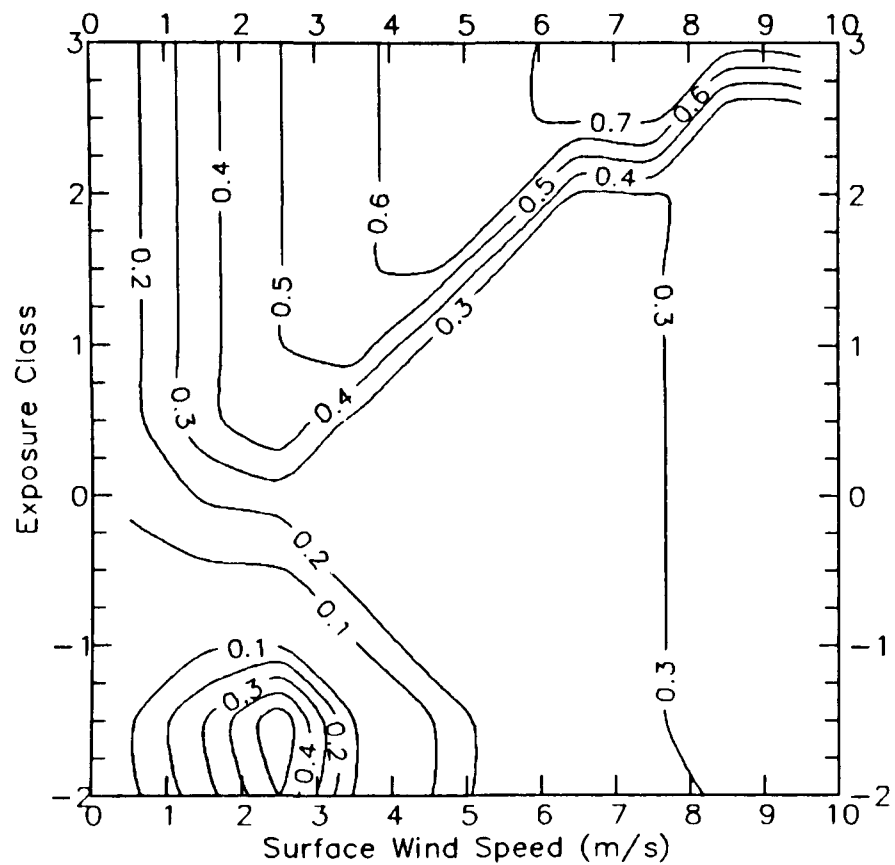
SO<sub>2</sub> Deposition Velocities (cm/s) for GRAZED FOREST/WOODLAND Land Use Type.



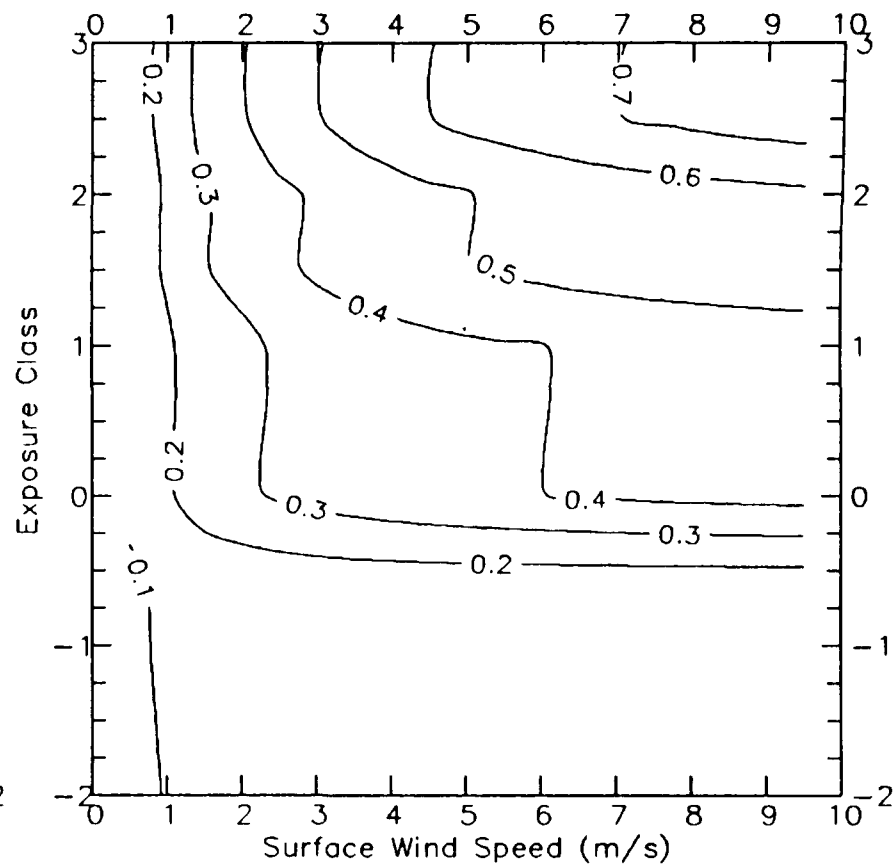
SO<sub>2</sub> Deposition Velocities (cm/s) for UNGRAZED FOREST/WOODLAND Land Use Type.

A-7

MESOPUFF-II

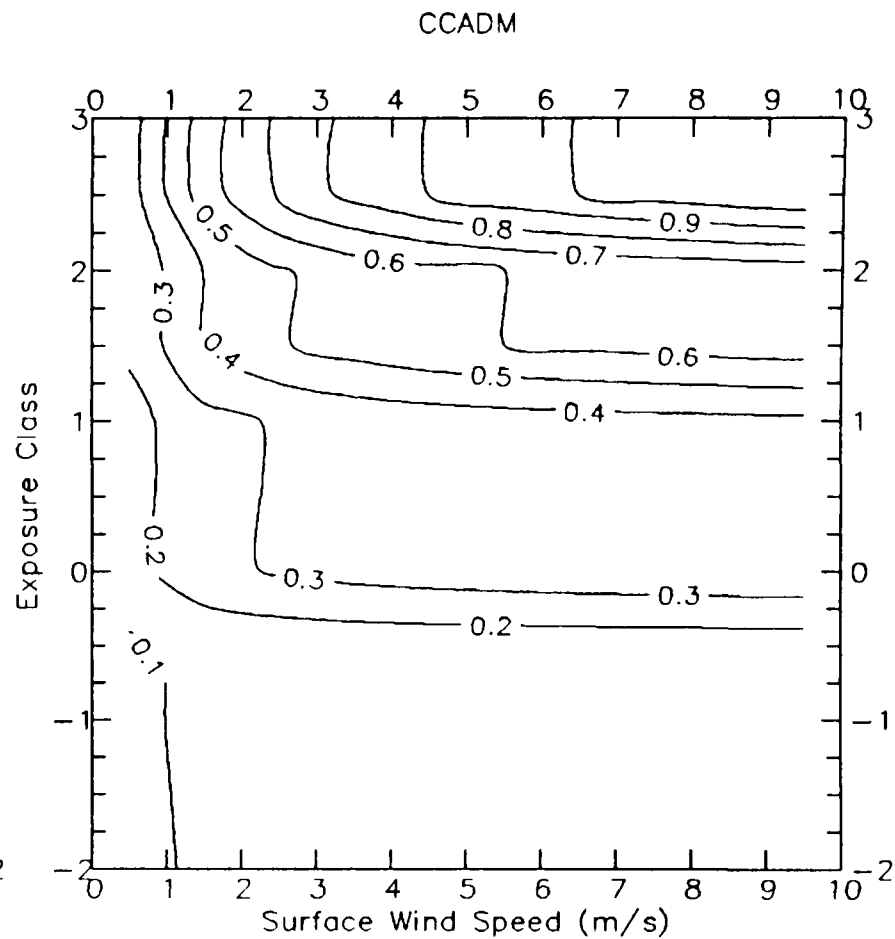
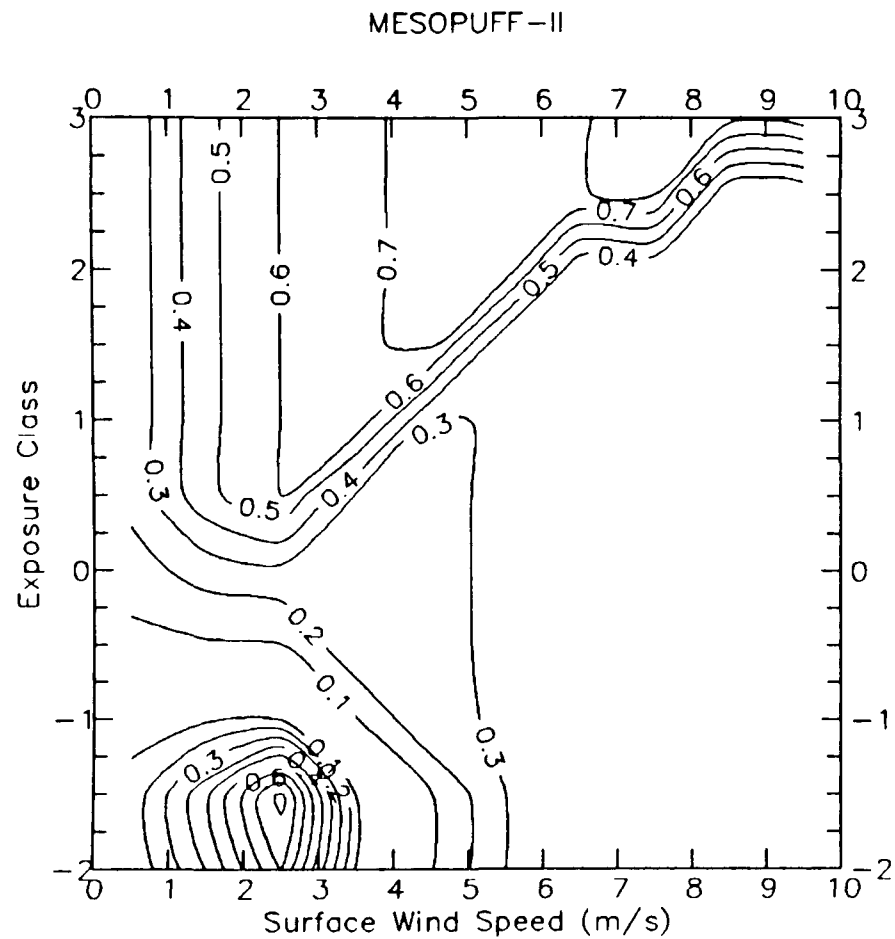


CCADM



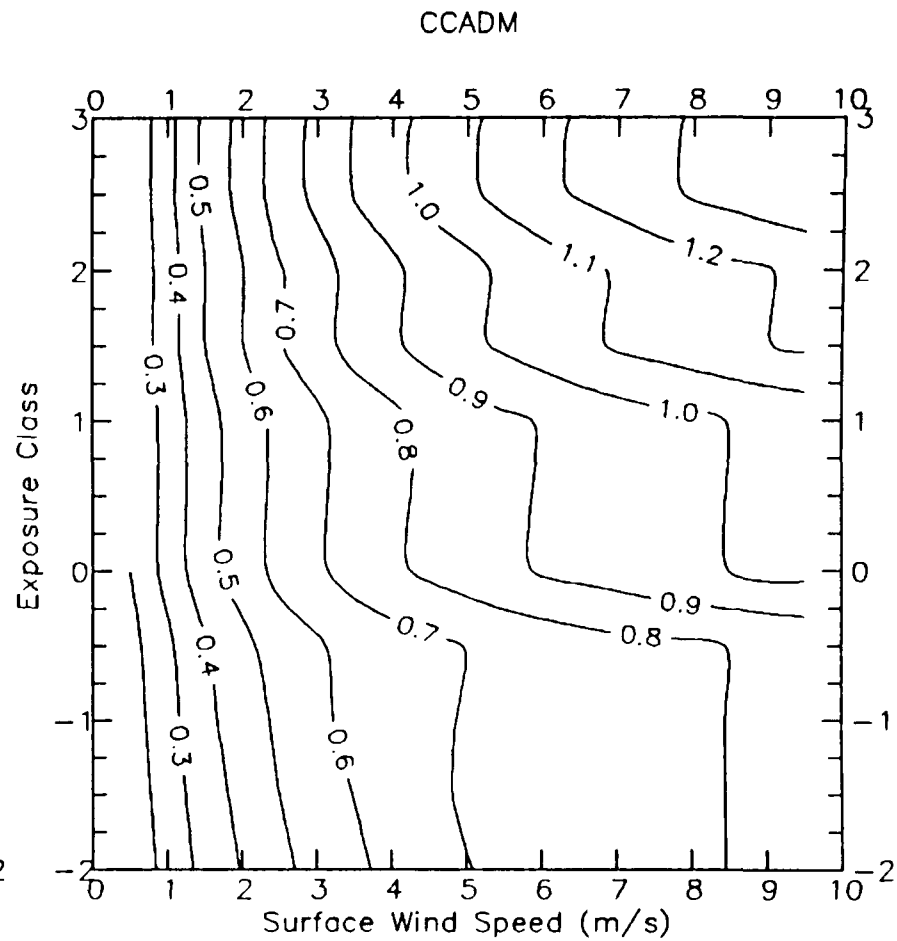
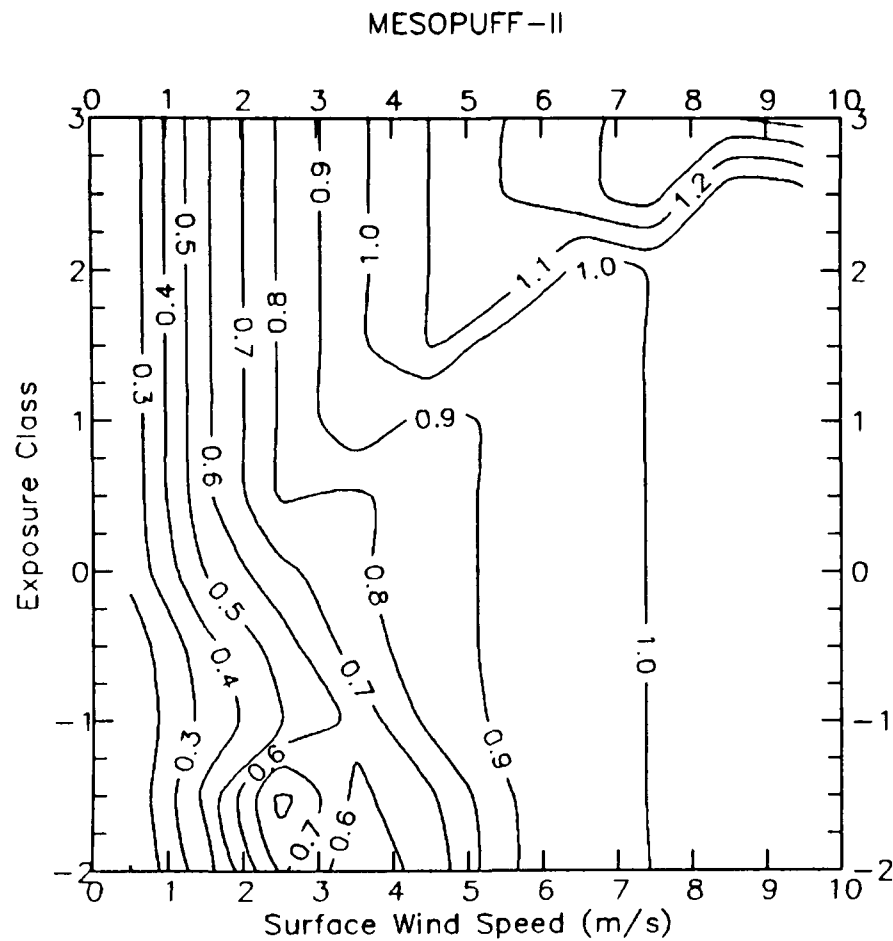
SO<sub>2</sub> Deposition Velocities (cm/s) for SEMIARID GRAZING Land Use Type.



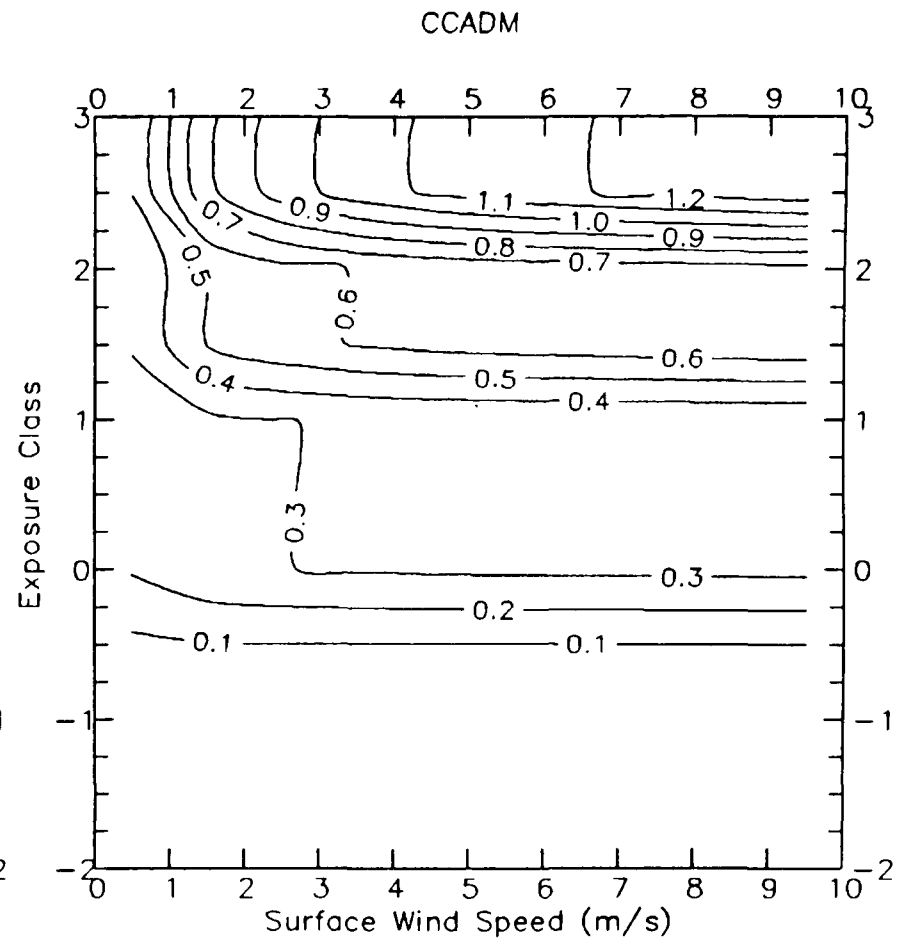
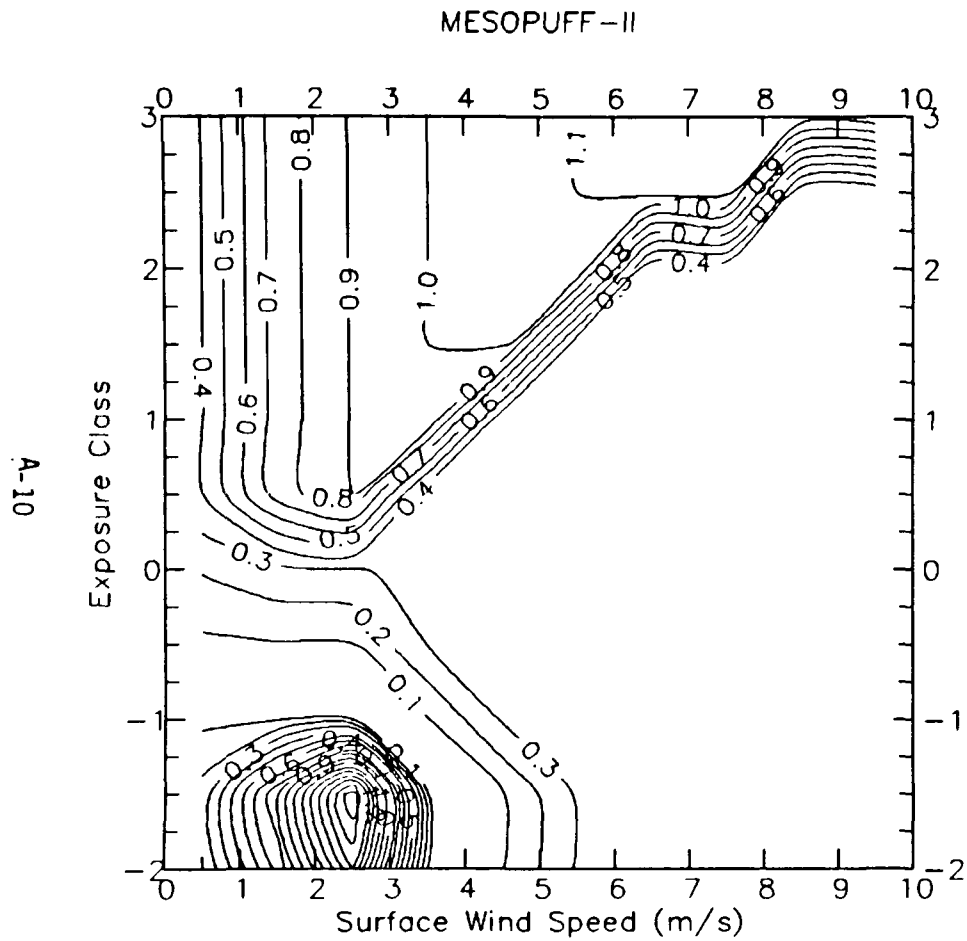


SO<sub>2</sub> Deposition Velocities (cm/s) for OPEN WOODLAND GRAZED Land Use Type.

A-9

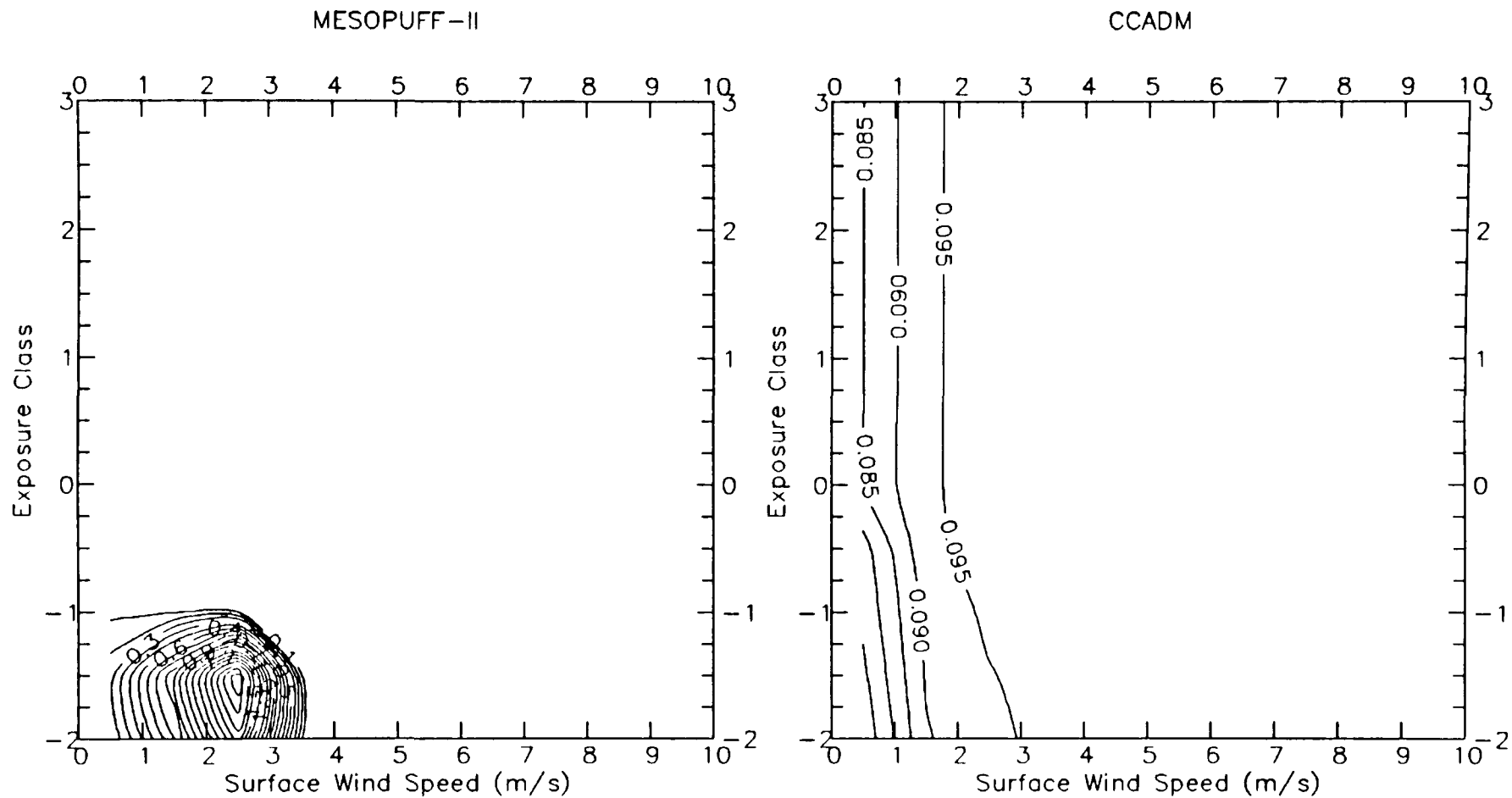


SO<sub>2</sub> Deposition Velocities (cm/s) for SWAMP Land Use Type.

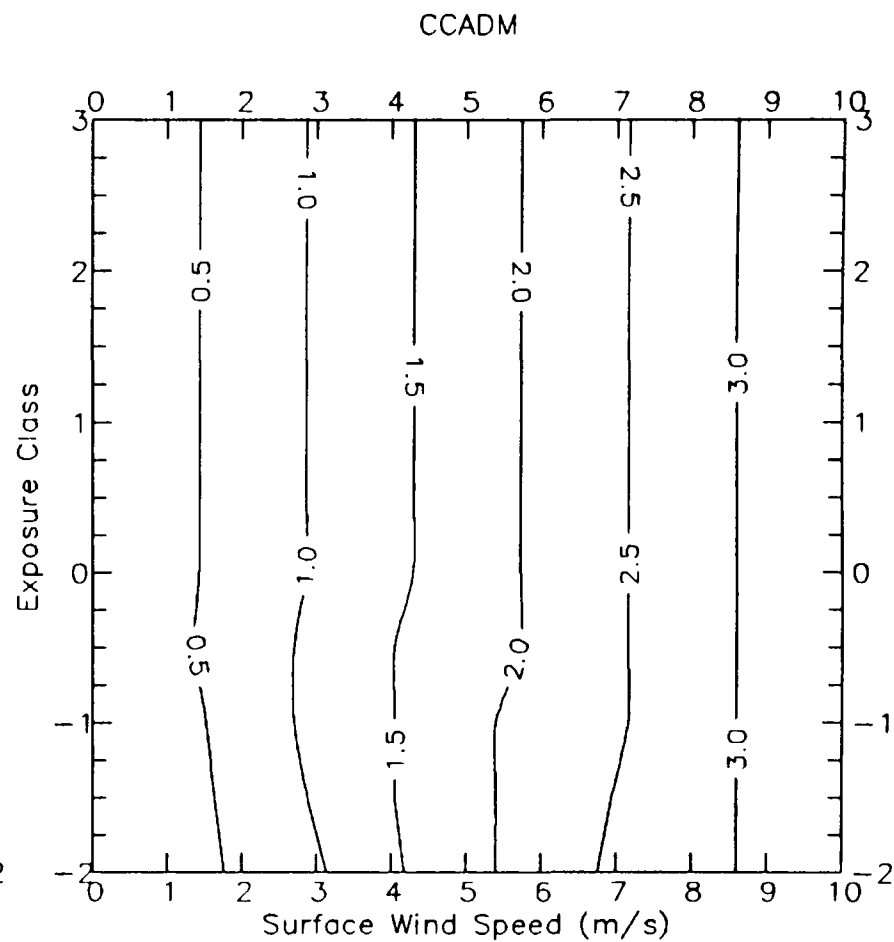
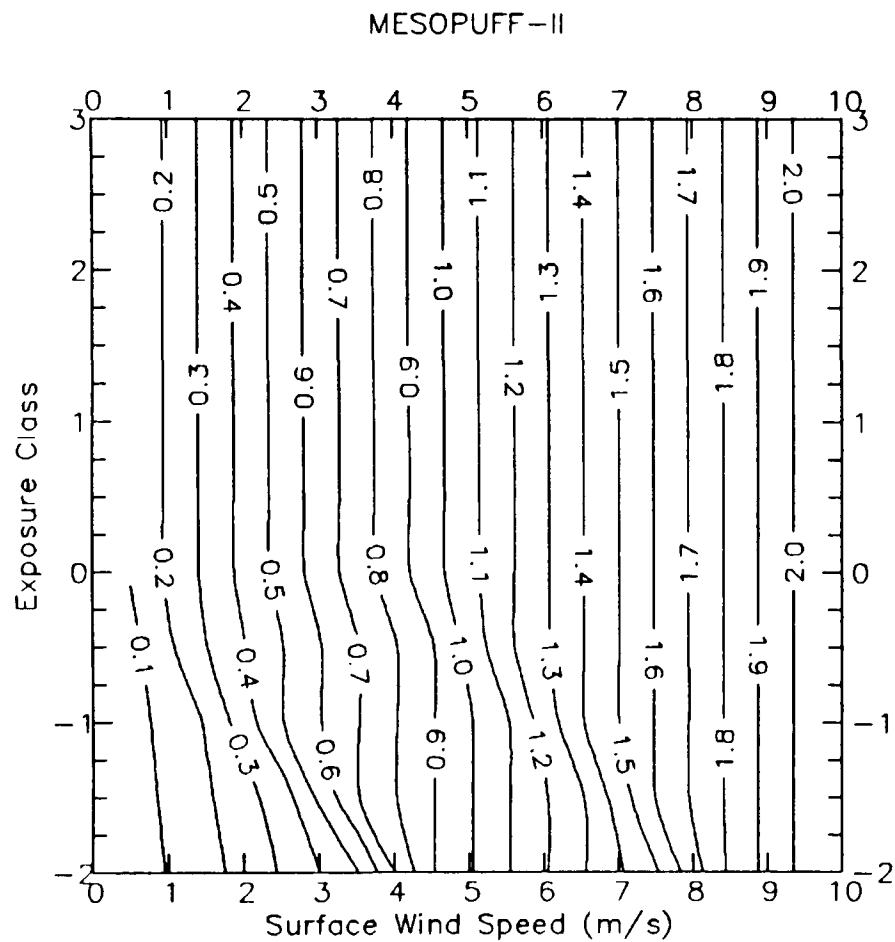


SO<sub>2</sub> Deposition Velocities (cm/s) for MARSHLAND Land Use Type.

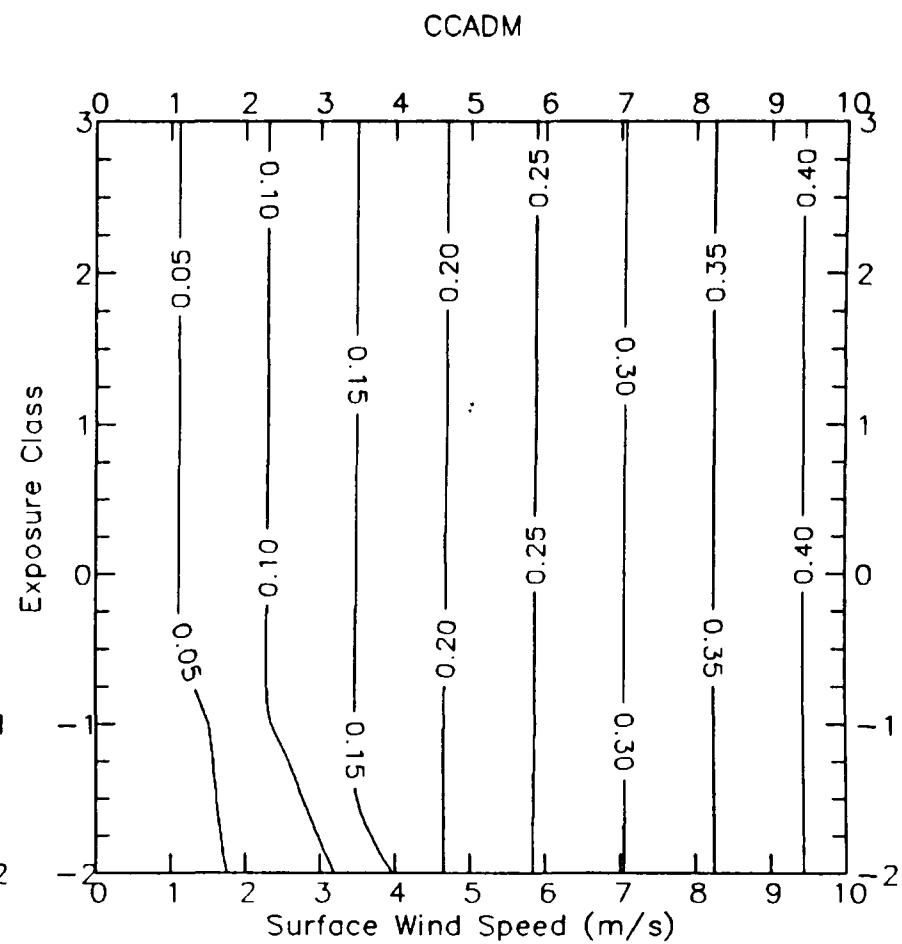
A-11



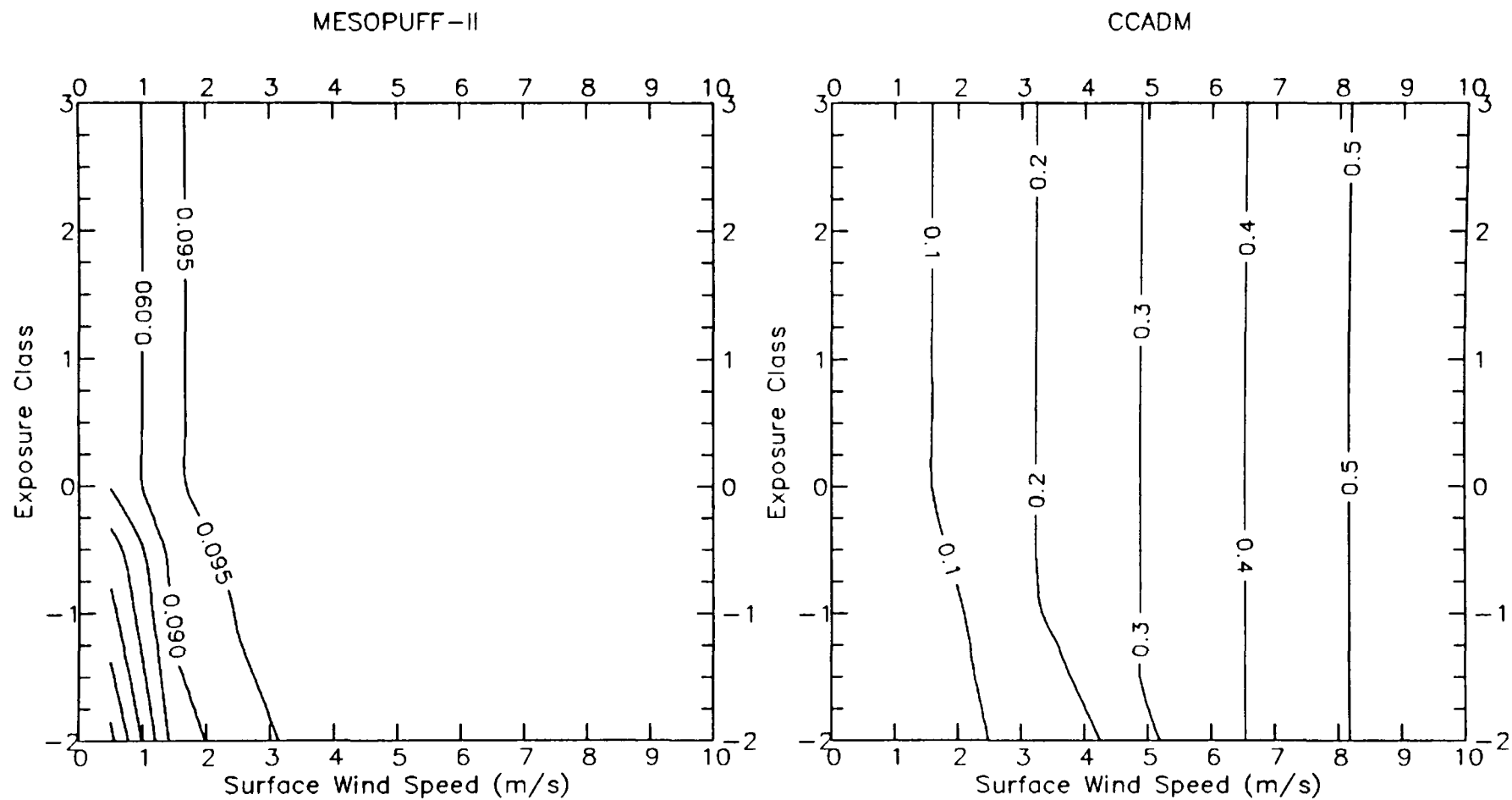
SO2 Deposition Velocities (cm/s) for METROPOLITAN CITY Land Use Type.



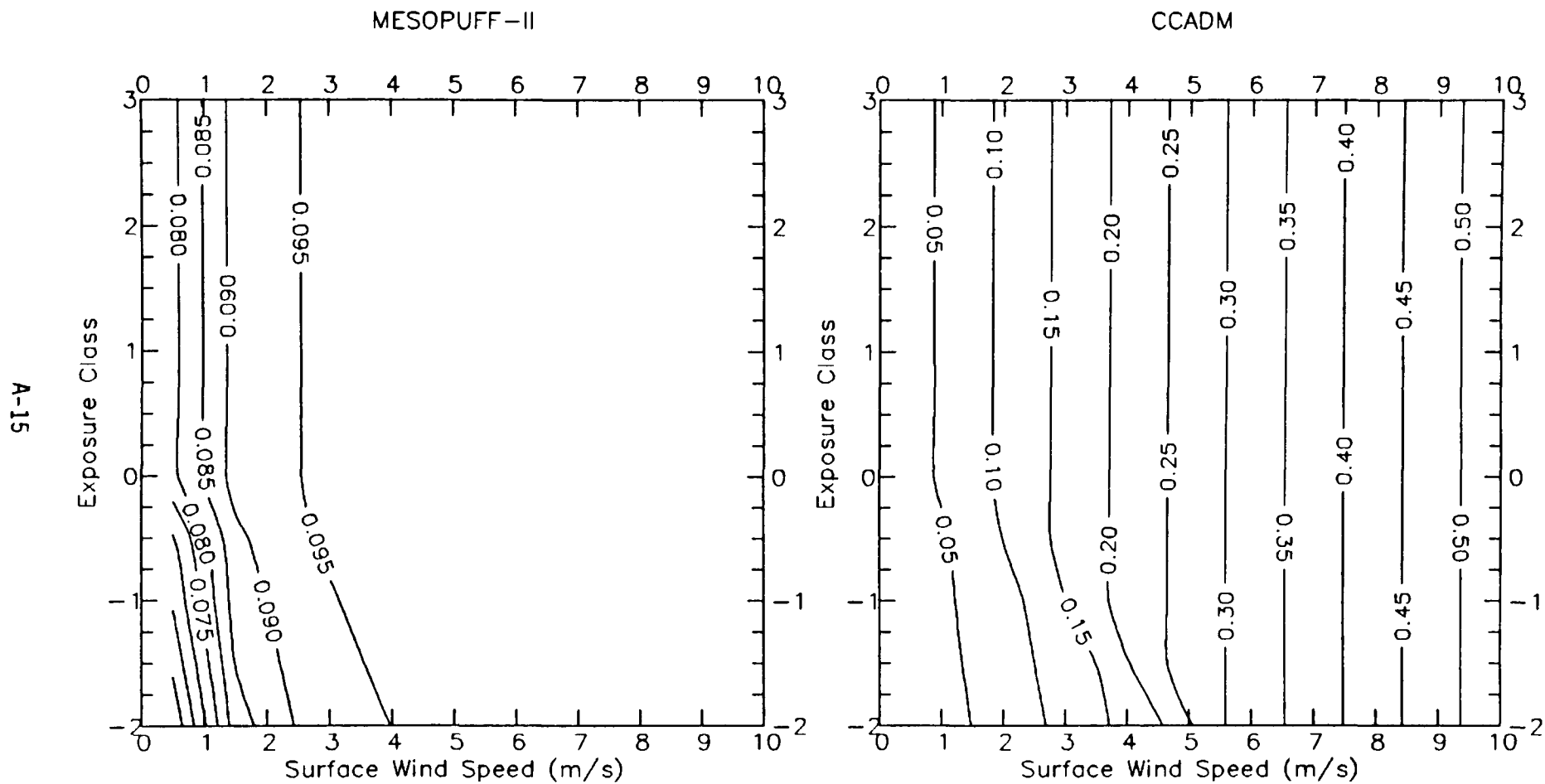
SO<sub>2</sub> Deposition Velocities (cm/s) for LAKE OR OCEAN Land Use Type.



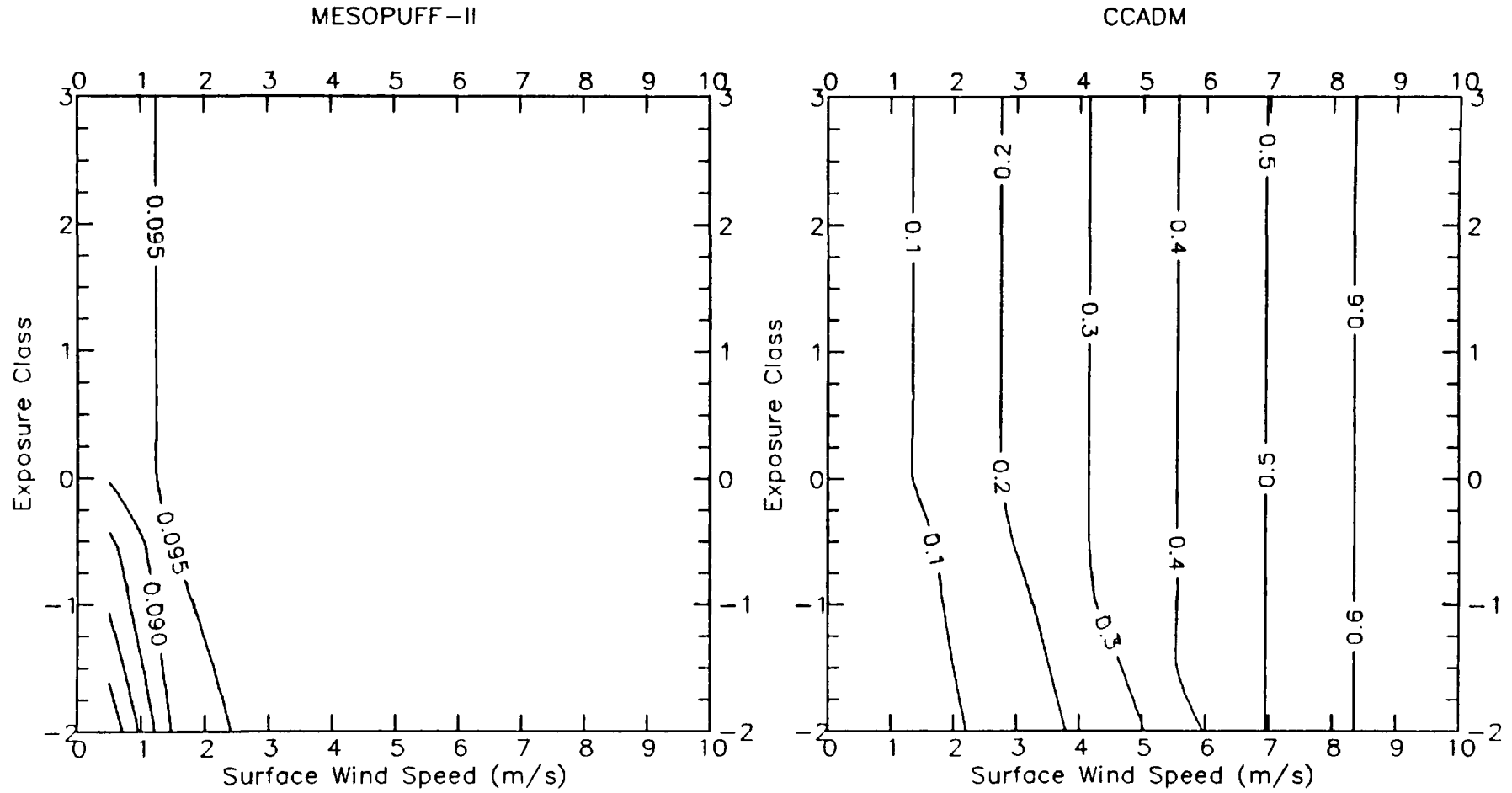
S04 Deposition Velocities (cm/s) for CROPLAND AND PASTURE Land Use Type.



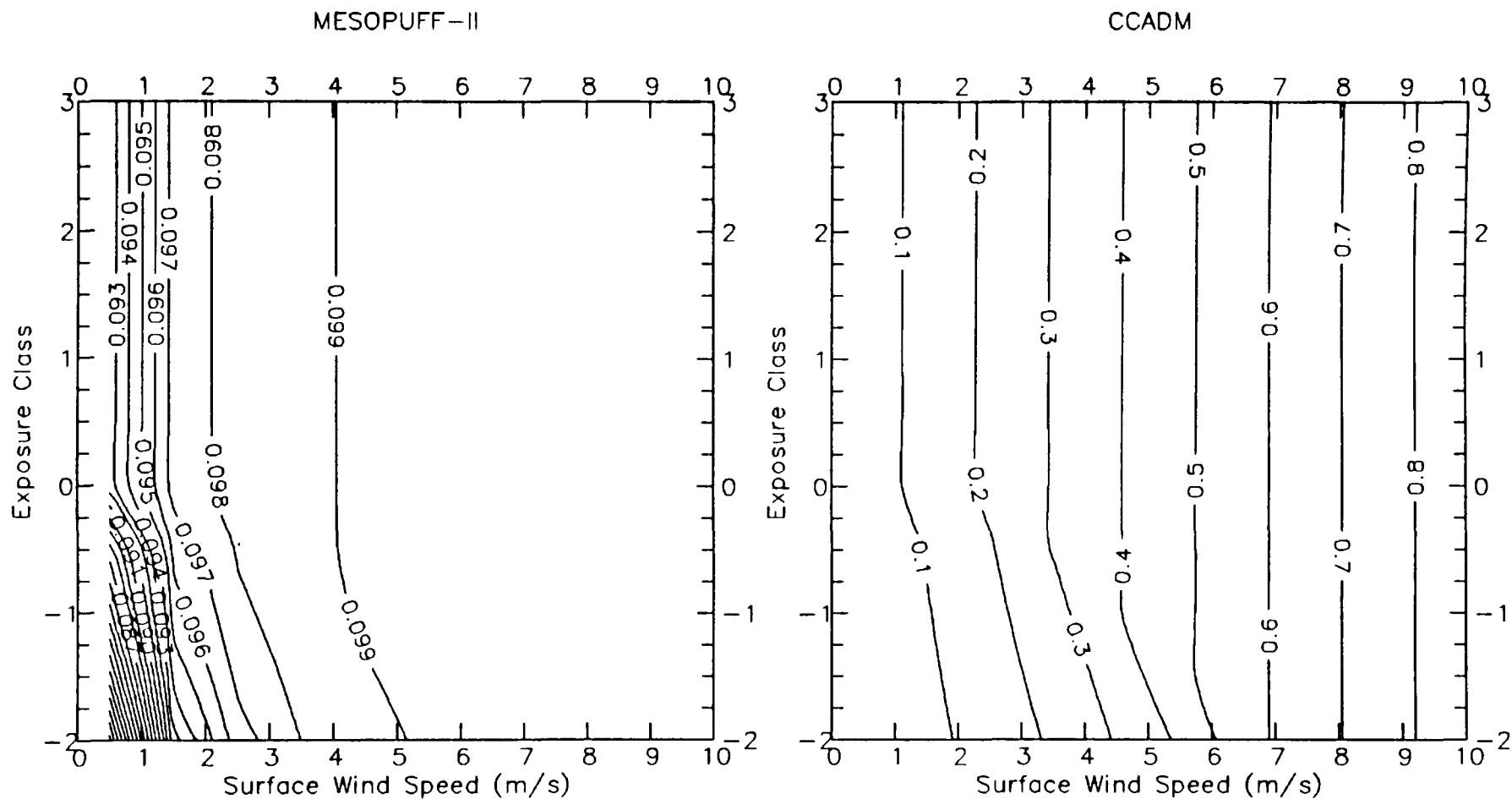
SO<sub>4</sub> Deposition Velocities (cm/s) for CROPLAND/WOODLAND/GRAZING Land Use Type.





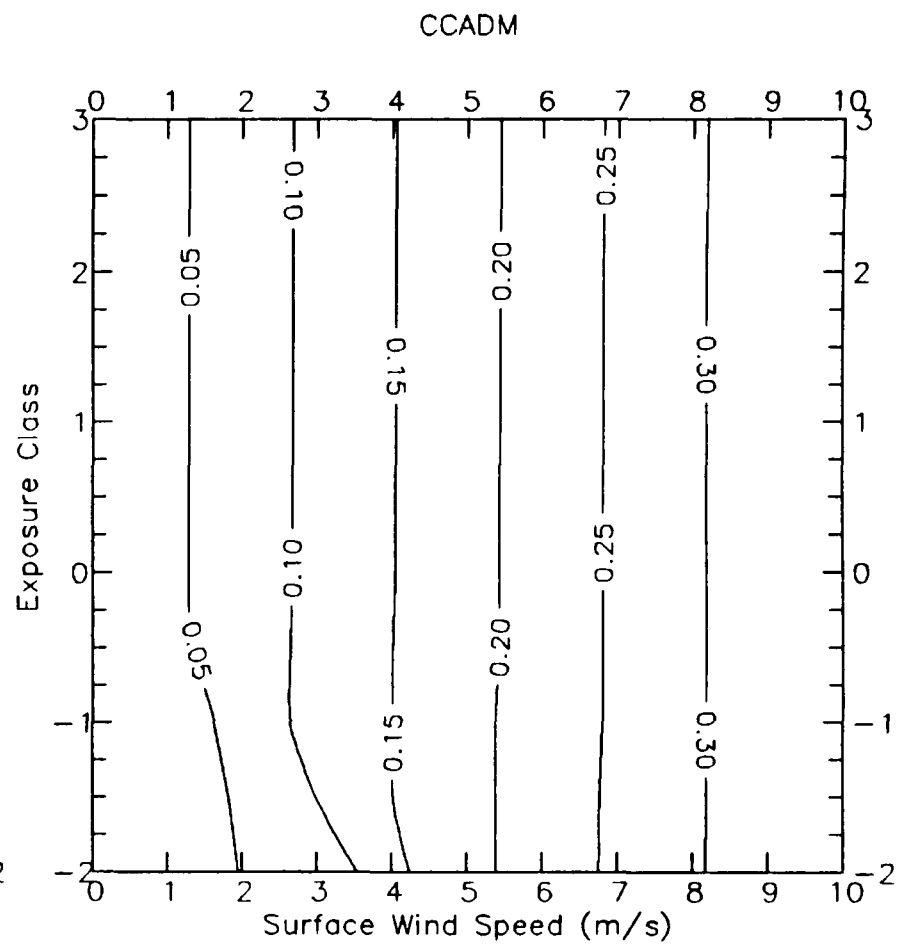
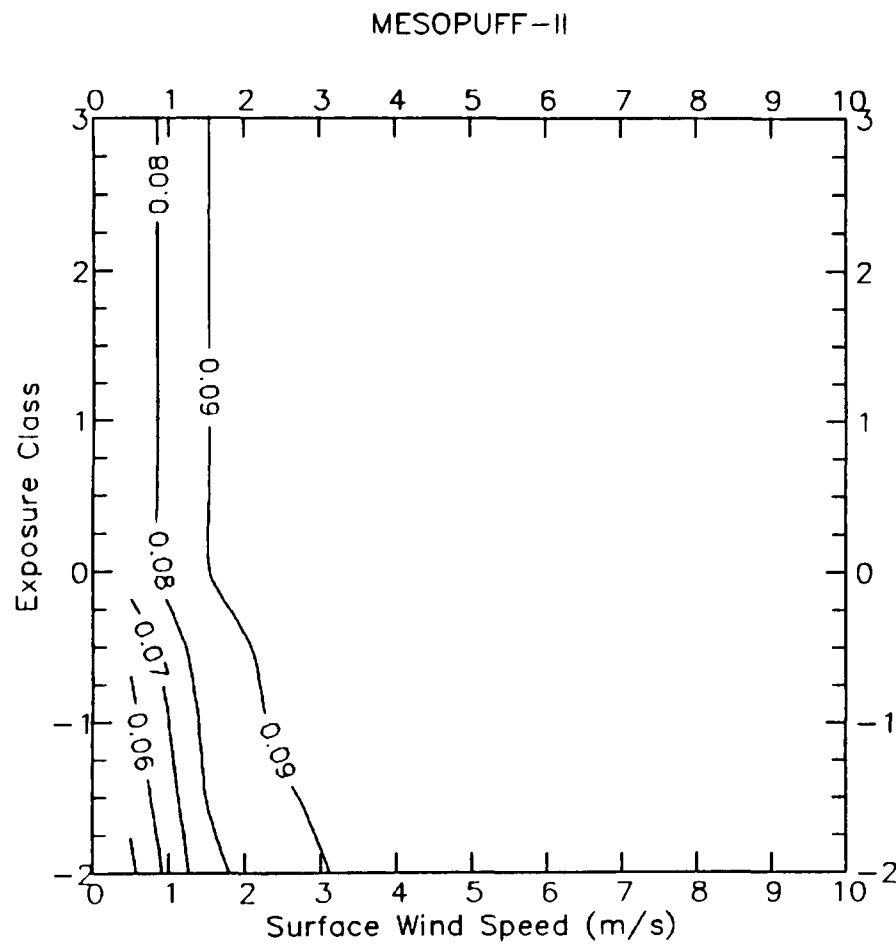


SO<sub>4</sub> Deposition Velocities (cm/s) for GRAZED FOREST/WOODLAND Land Use Type.

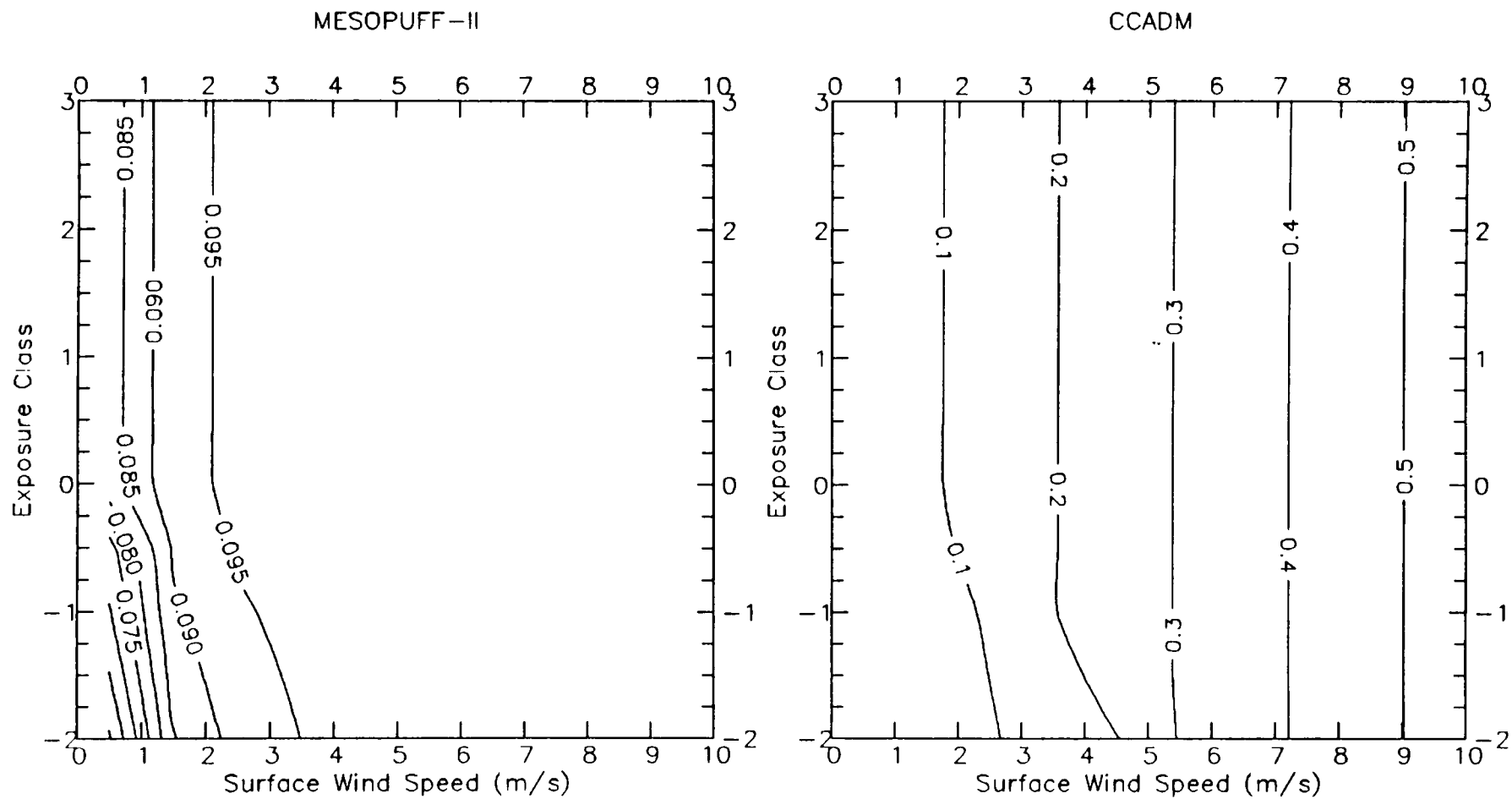


SO<sub>4</sub> Deposition Velocities (cm/s) for UNGRAZED FOREST/WOODLAND Land Use Type.

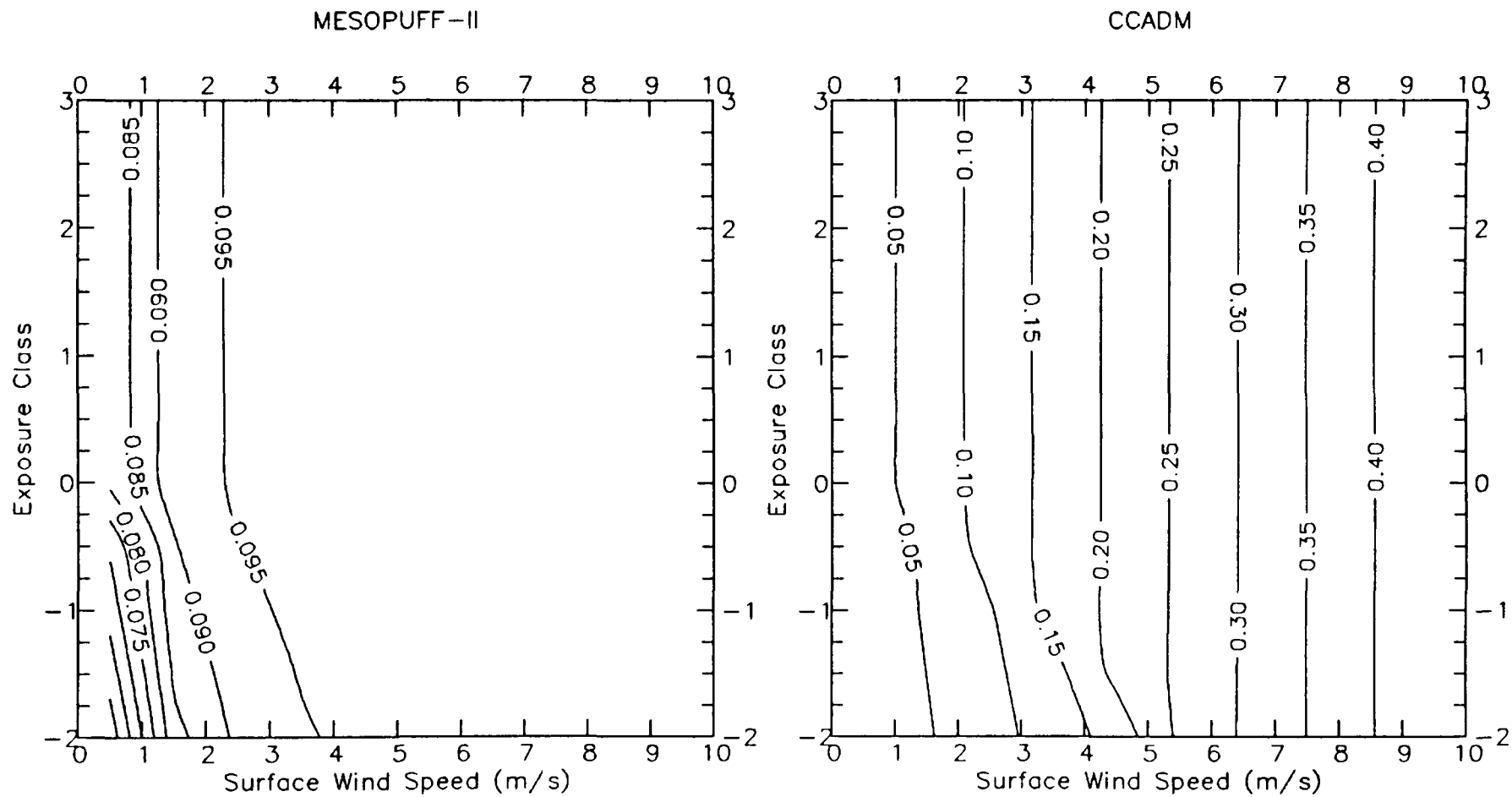
A-18



SO<sub>4</sub> Deposition Velocities (cm/s) for SEMIARID GRAZING Land Use Type.

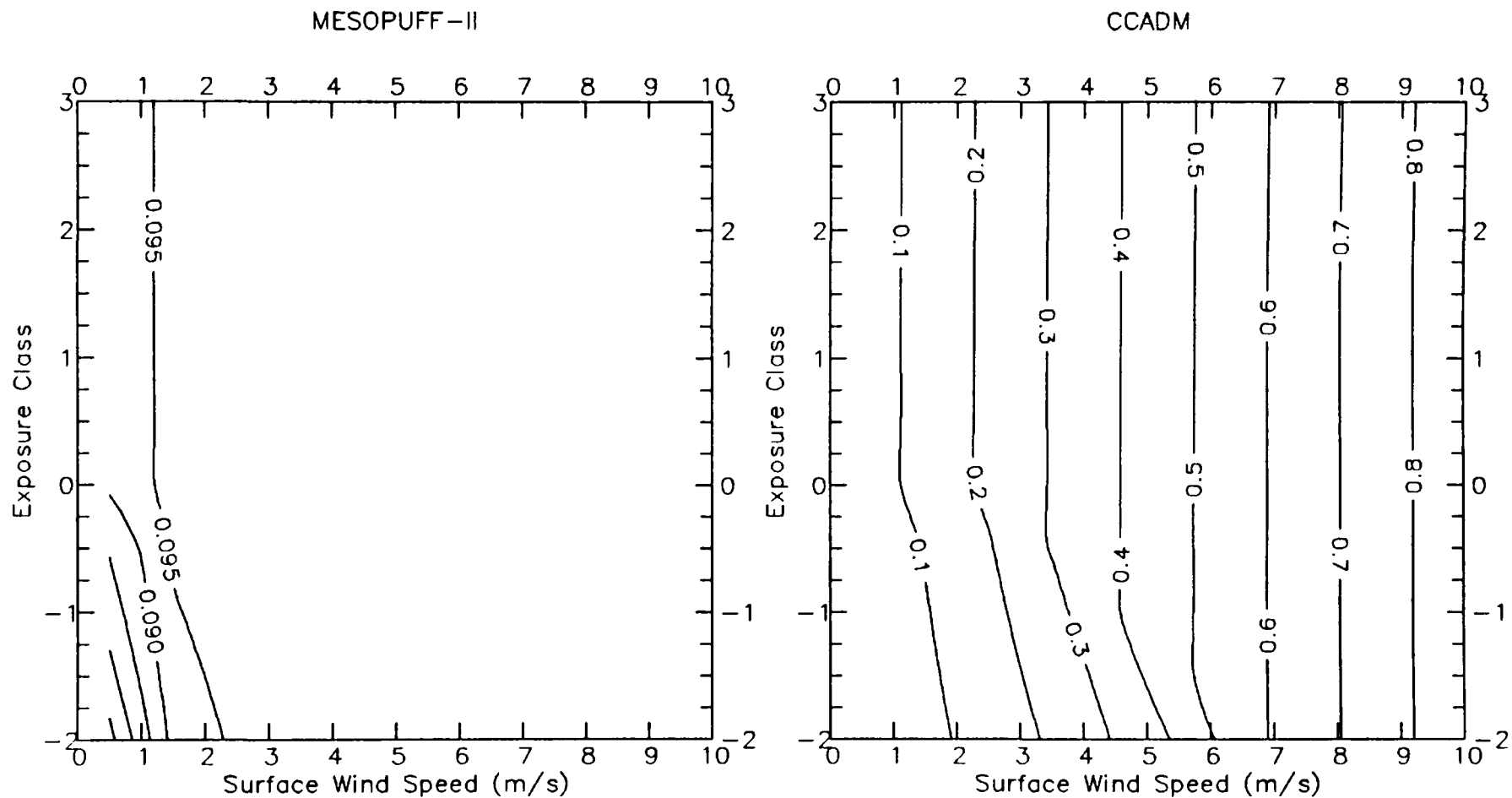


SO<sub>4</sub> Deposition Velocities (cm/s) for OPEN WOODLAND GRAZED Land Use Type.



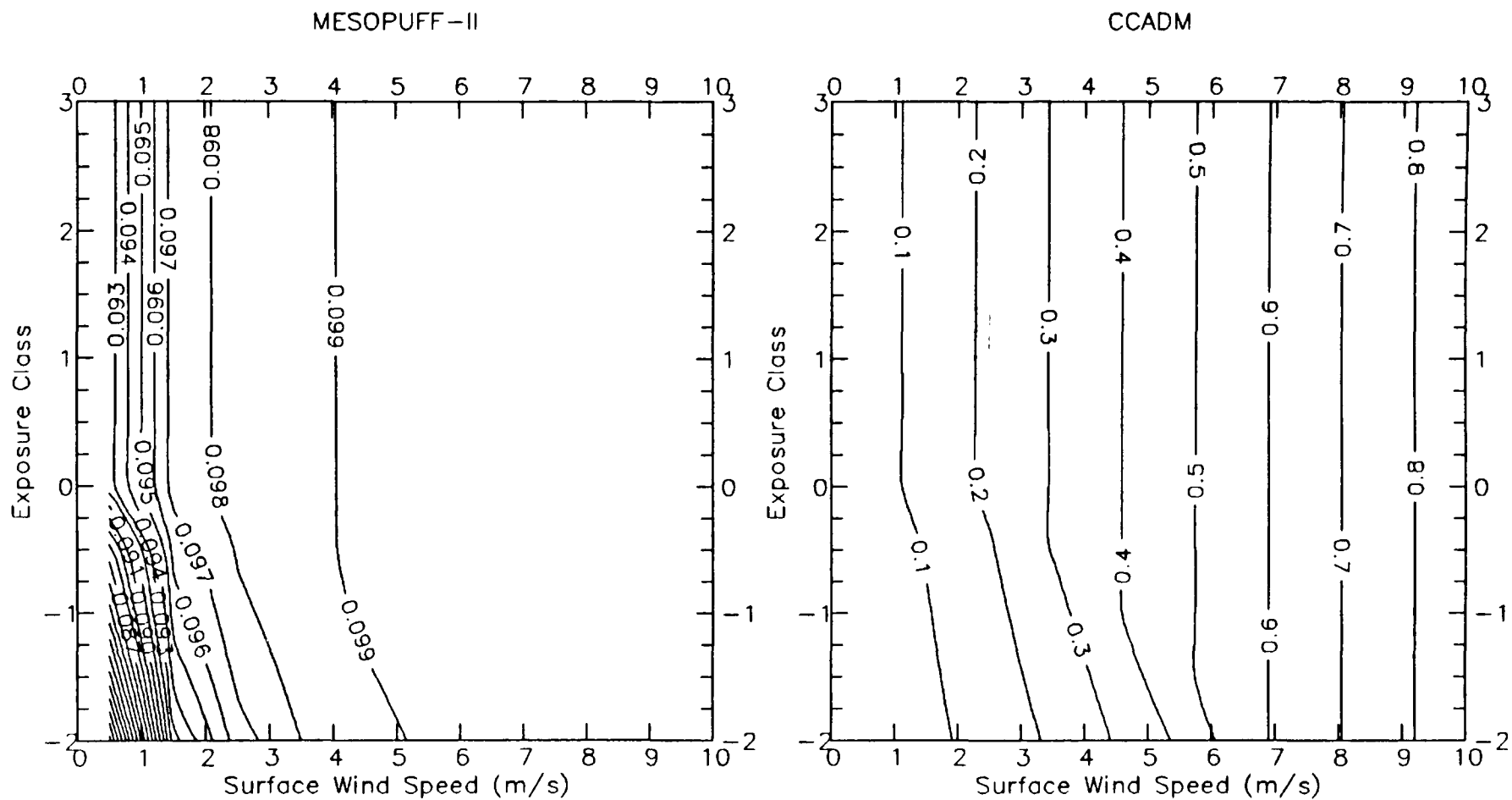
SO<sub>4</sub> Deposition Velocities (cm/s) for SWAMP Land Use Type.

A-21



SO4 Deposition Velocities (cm/s) for MARSHLAND Land Use Type.

A-22

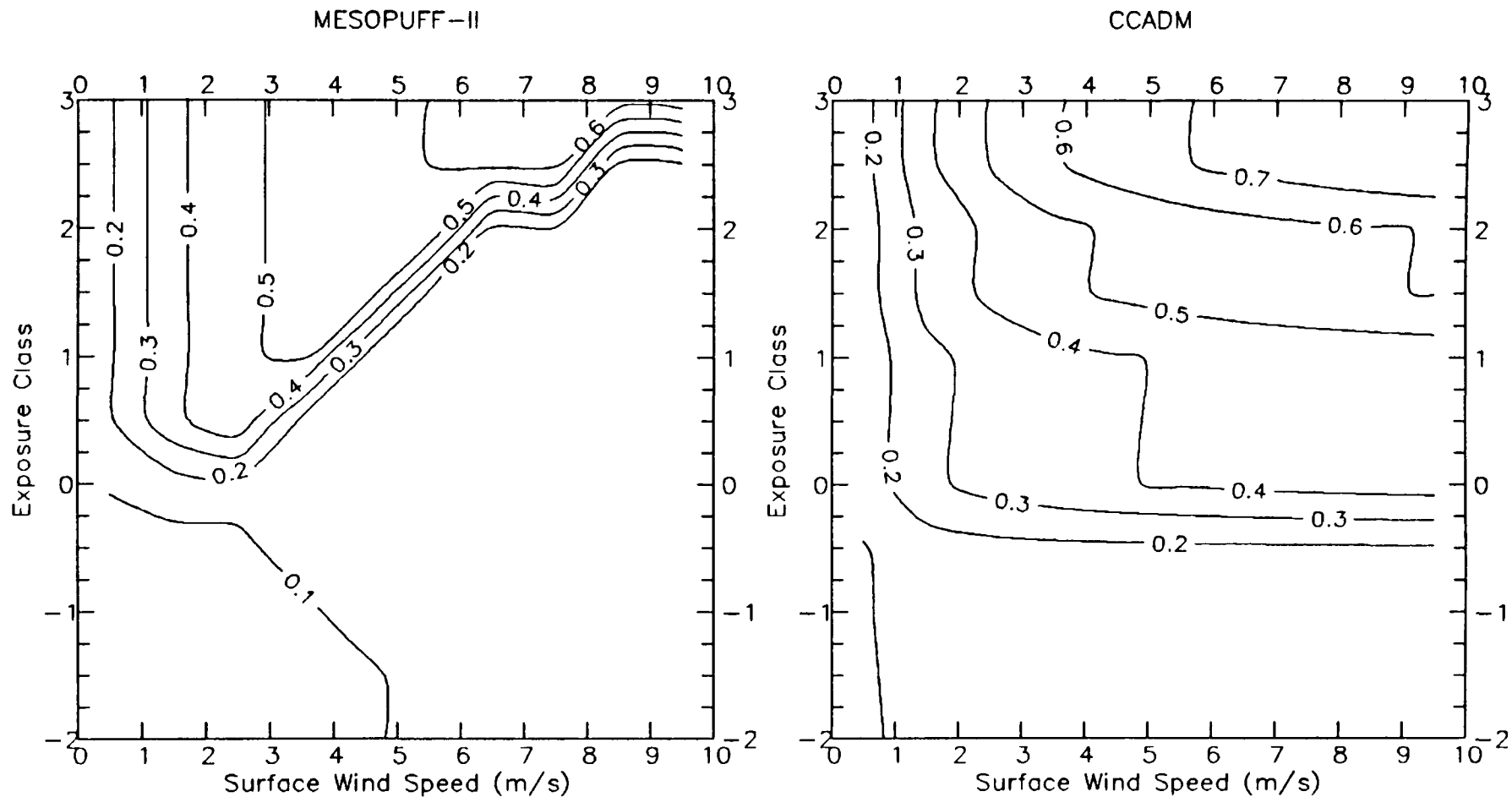


SO4 Deposition Velocities (cm/s) for METROPOLITAN CITY Land Use Type.

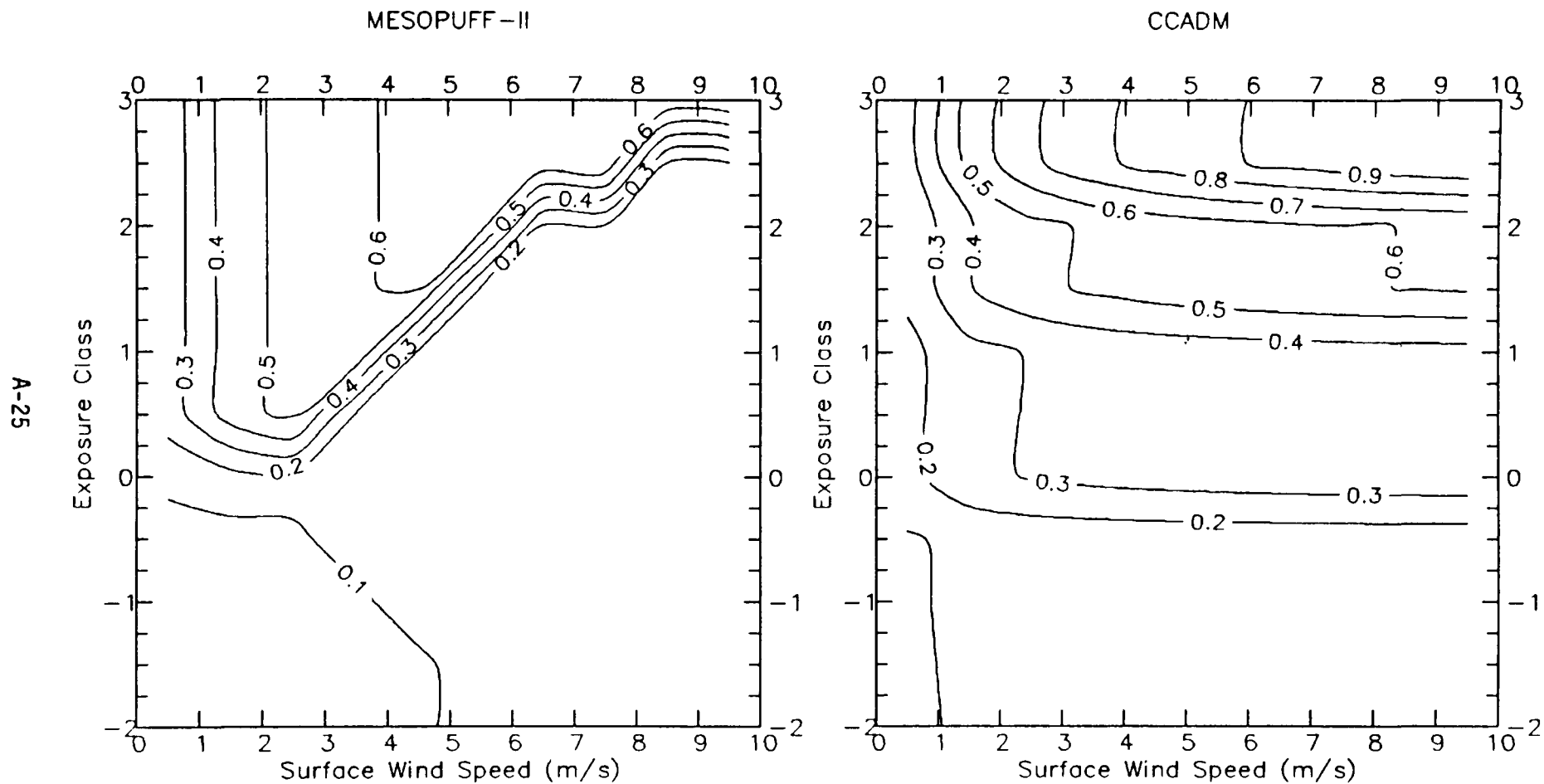
S04 Deposition Velocities (cm/s) for LAKE OR OCEAN Land Use Type.



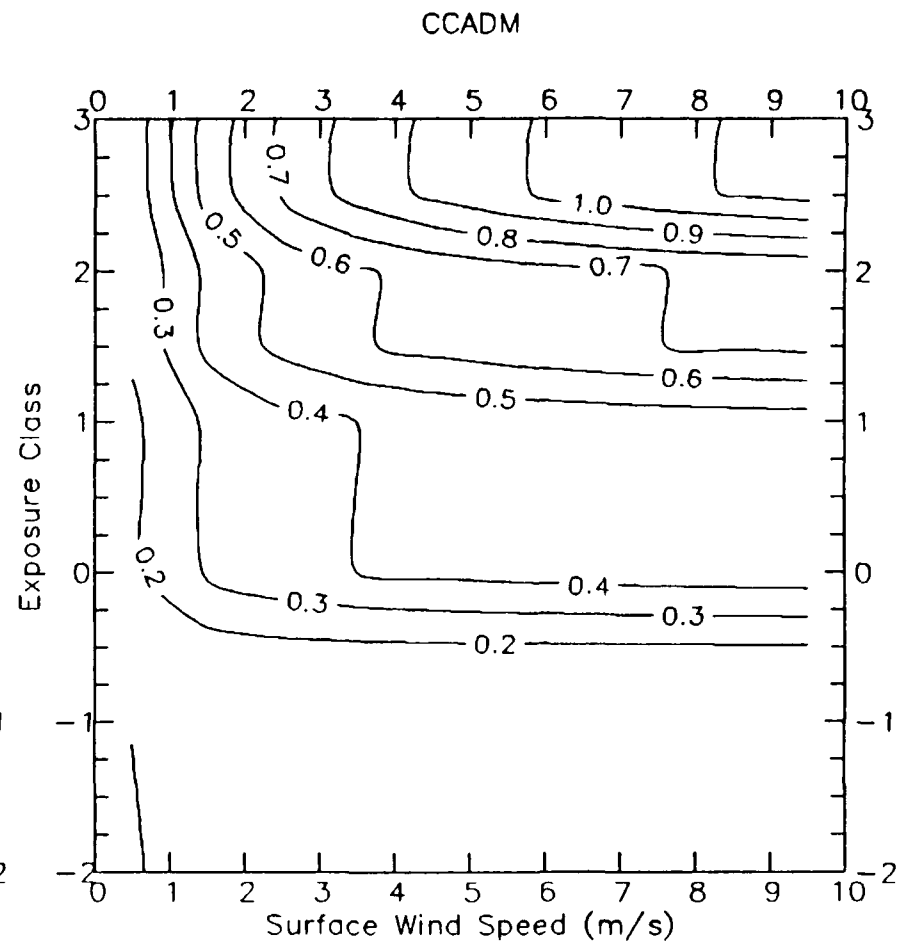
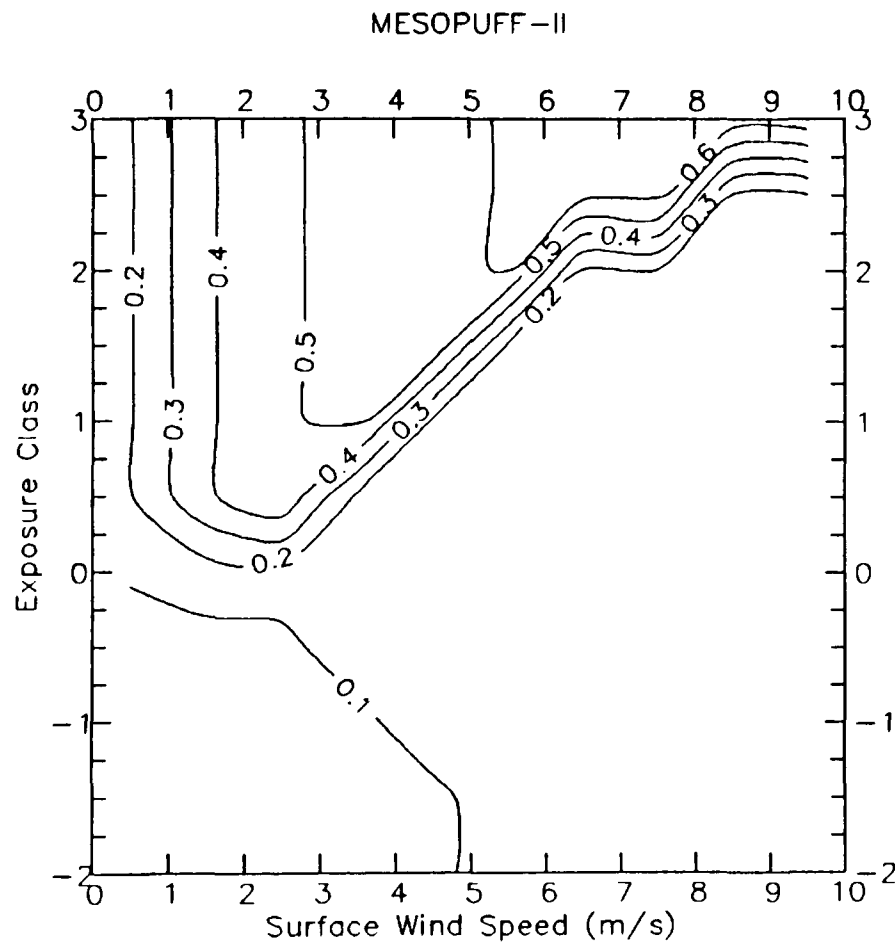
A-24



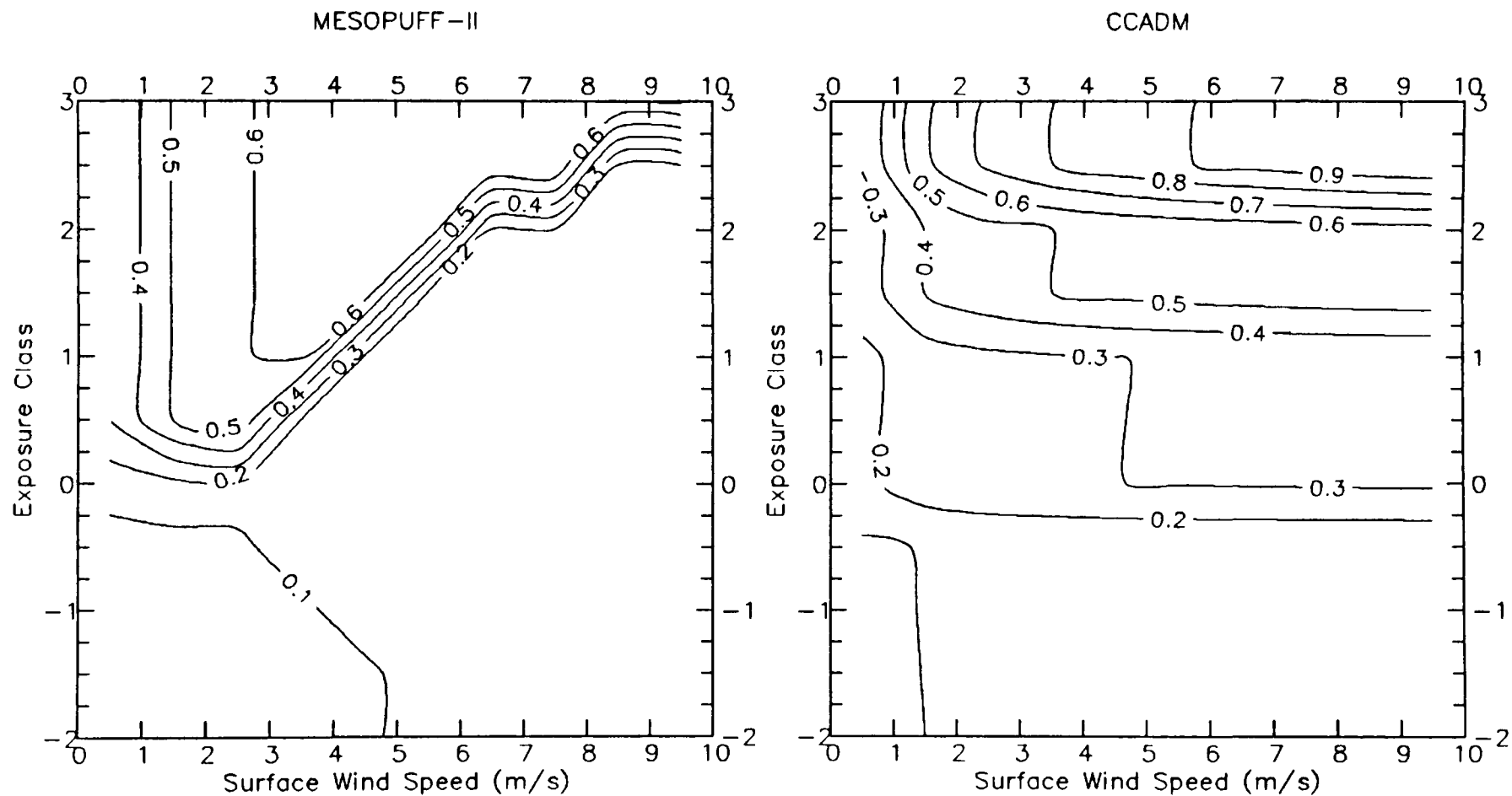
NO2 Deposition Velocities (cm/s) for CROPLAND AND PASTURE Land Use Type.



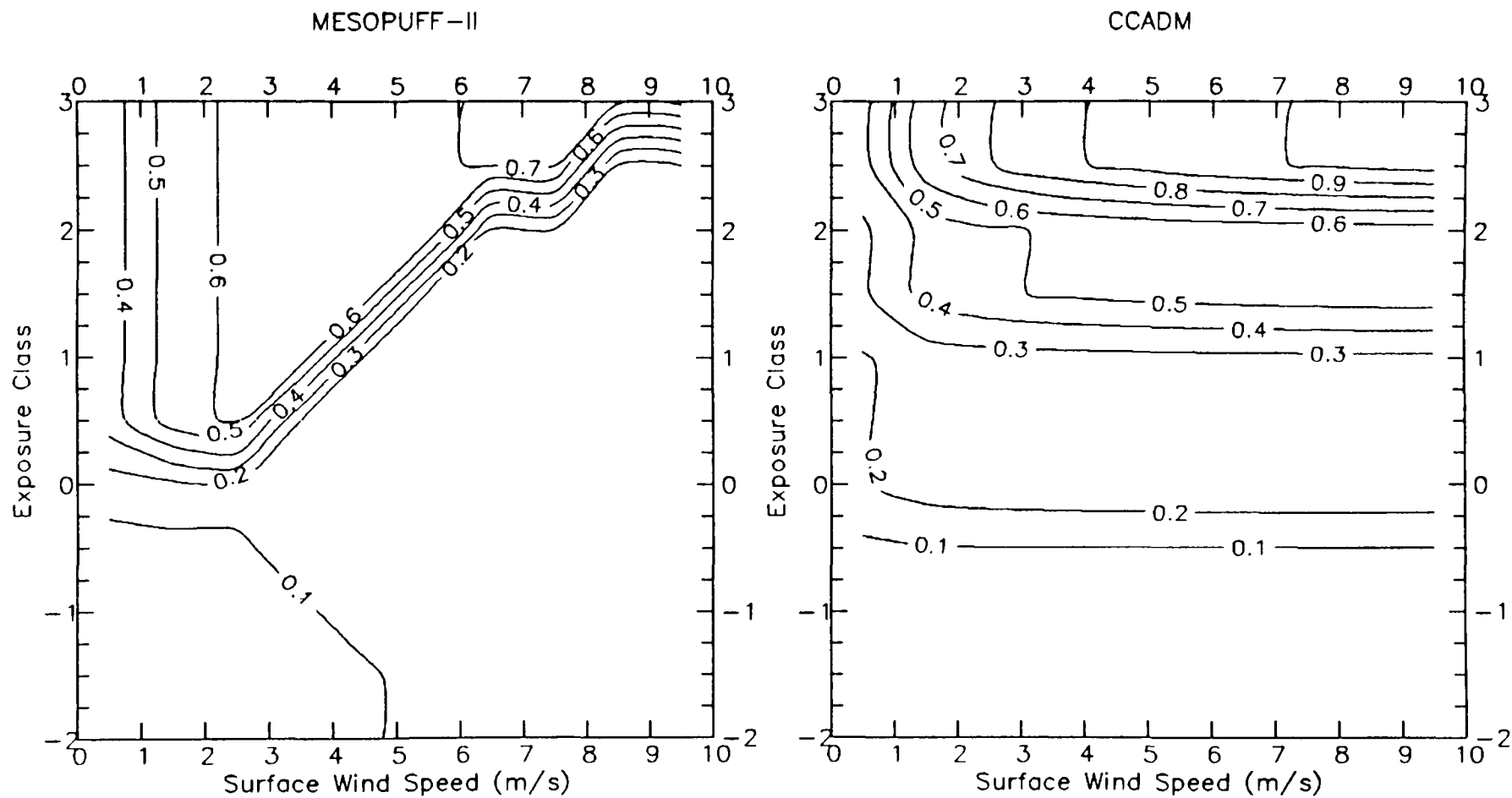
NO2 Deposition Velocities (cm/s) for CROPLAND/WOODLAND/GRAZING Land Use Type.



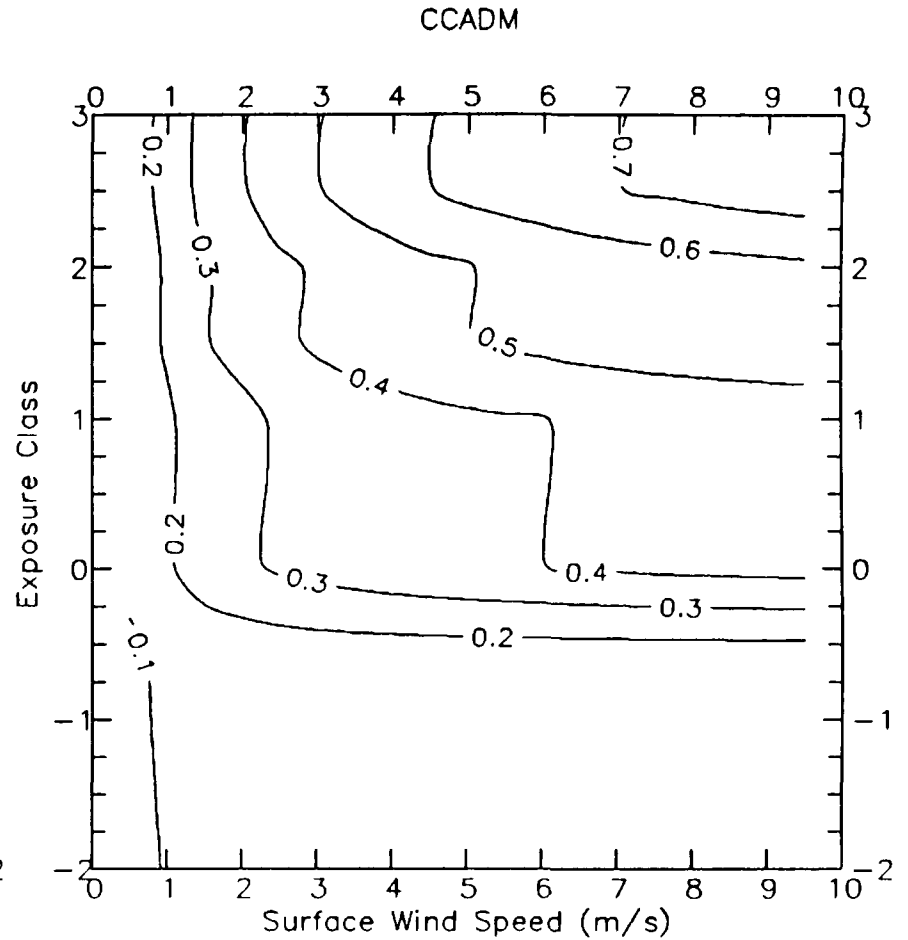
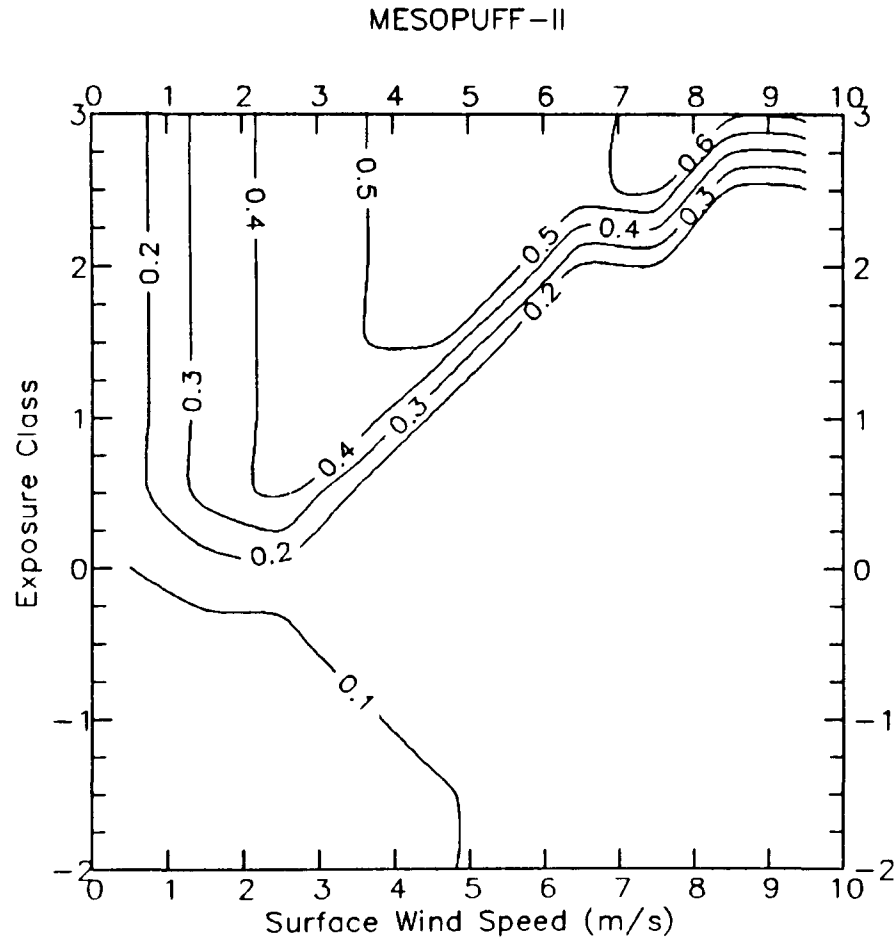
NO<sub>2</sub> Deposition Velocities (cm/s) for IRRIGATED CROPS Land Use Type.



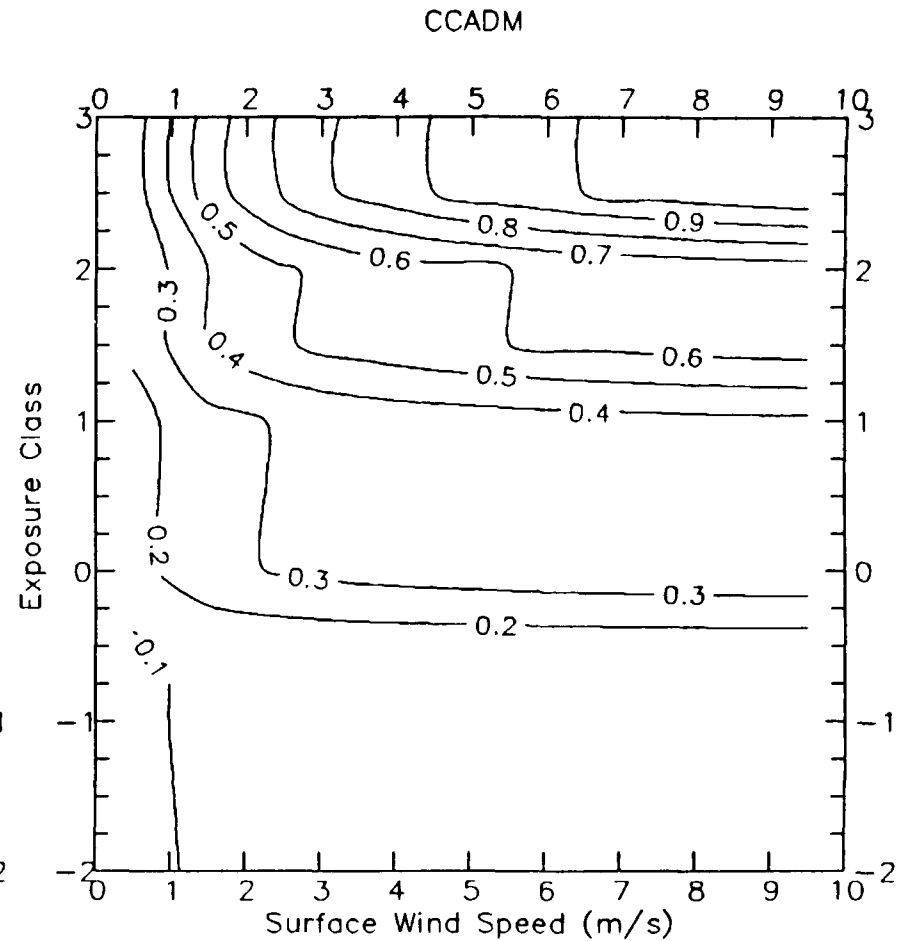
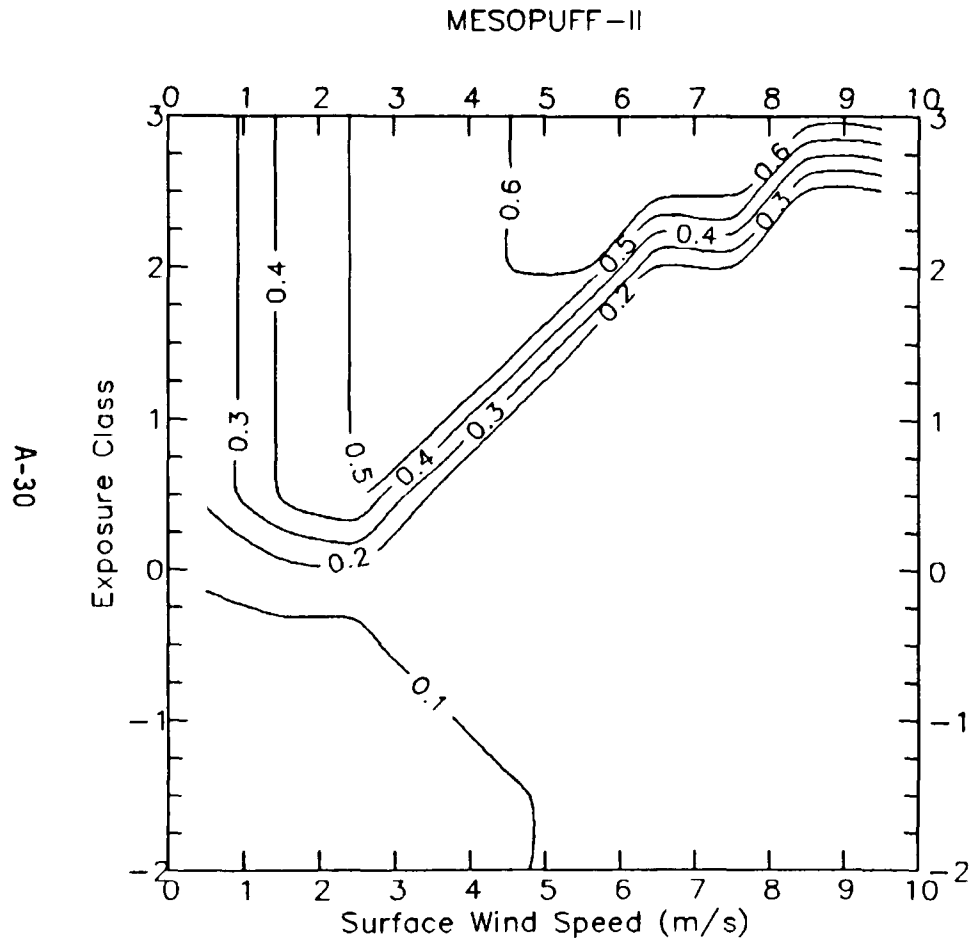
NO<sub>2</sub> Deposition Velocities (cm/s) for GRAZED FOREST/WOODLAND Land Use Type.



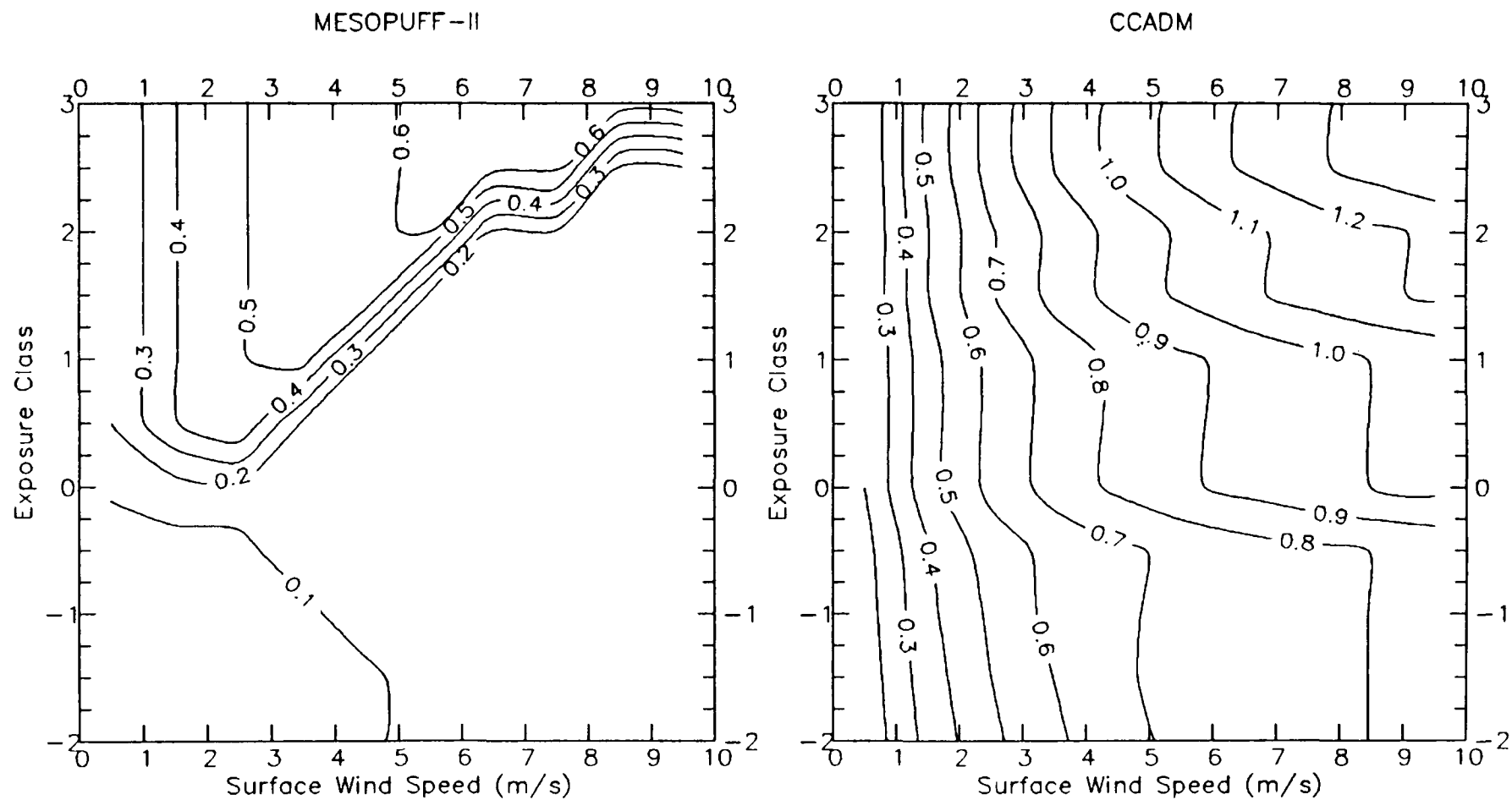
NO<sub>2</sub> Deposition Velocities (cm/s) for UNGRAZED FOREST/WOODLAND Land Use Type.



NO<sub>2</sub> Deposition Velocities (cm/s) for SEMIARID GRAZING Land Use Type.

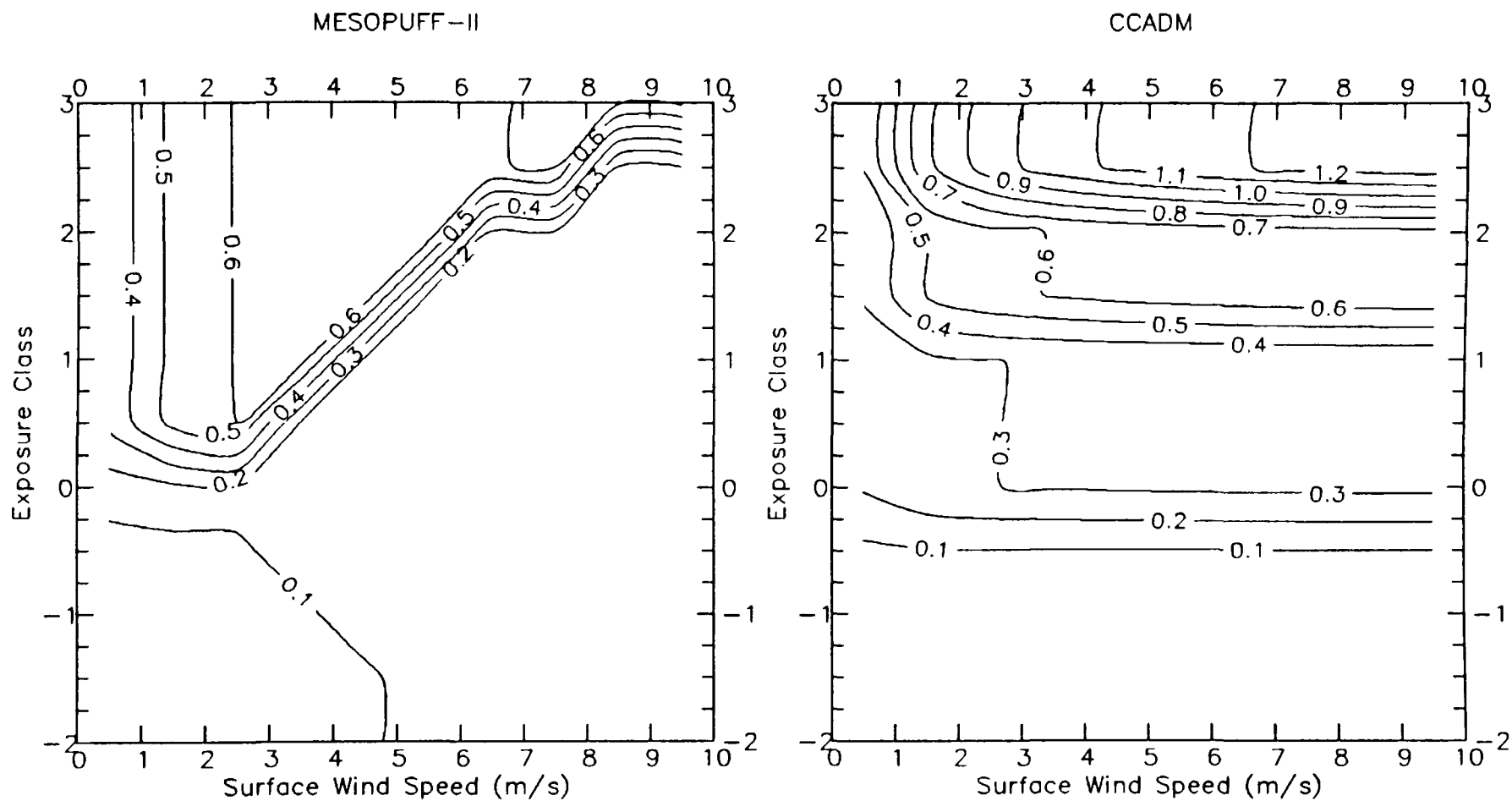


NO<sub>2</sub> Deposition Velocities (cm/s) for OPEN WOODLAND GRAZED Land Use Type.

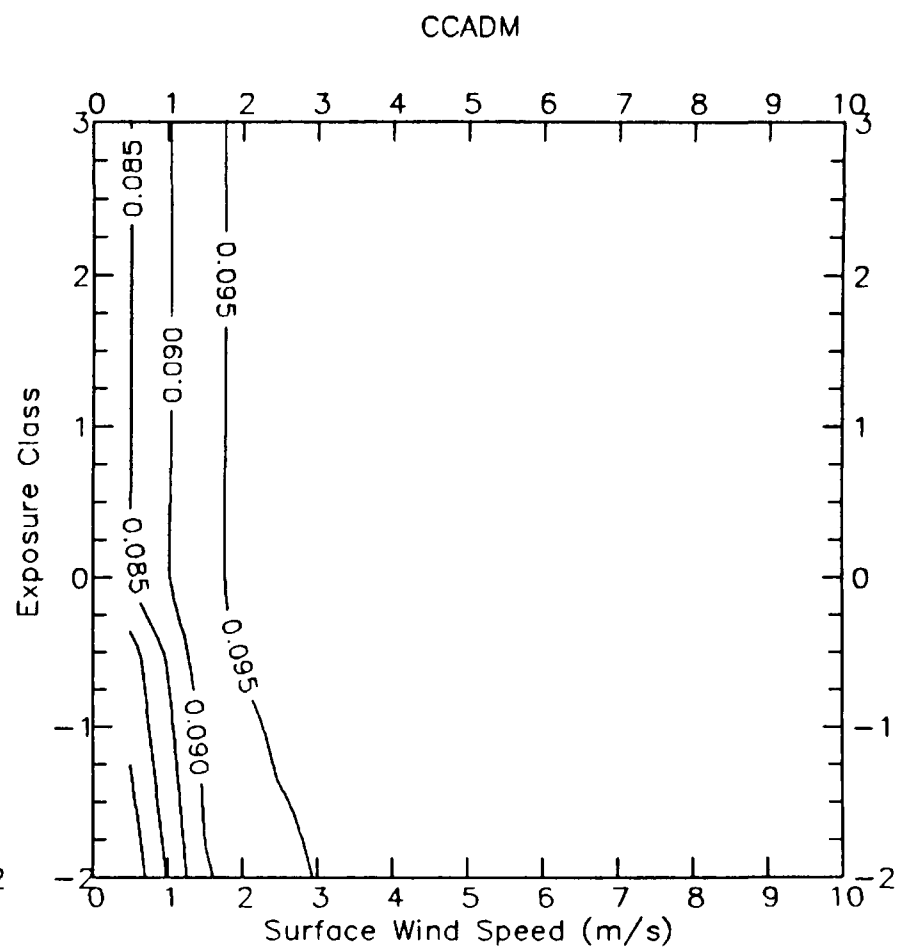
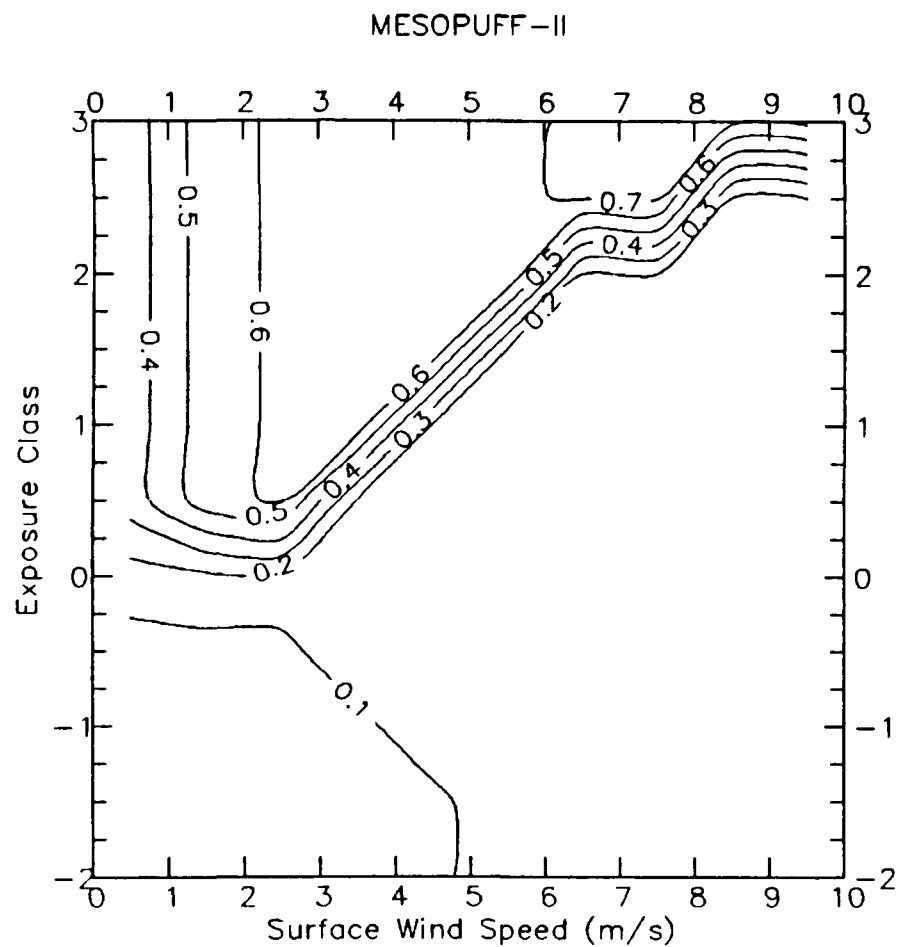


NO<sub>2</sub> Deposition Velocities (cm/s) for SWAMP Land Use Type.



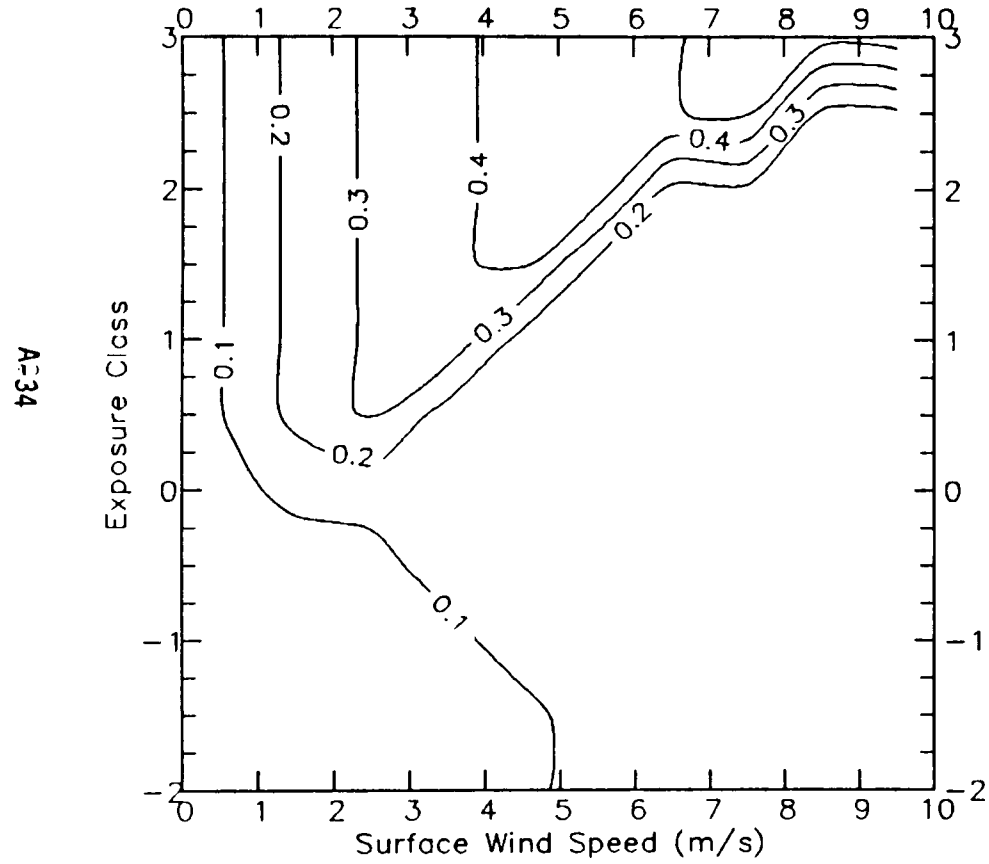
NO<sub>2</sub> Deposition Velocities (cm/s) for MARSHLAND Land Use Type.

A-33

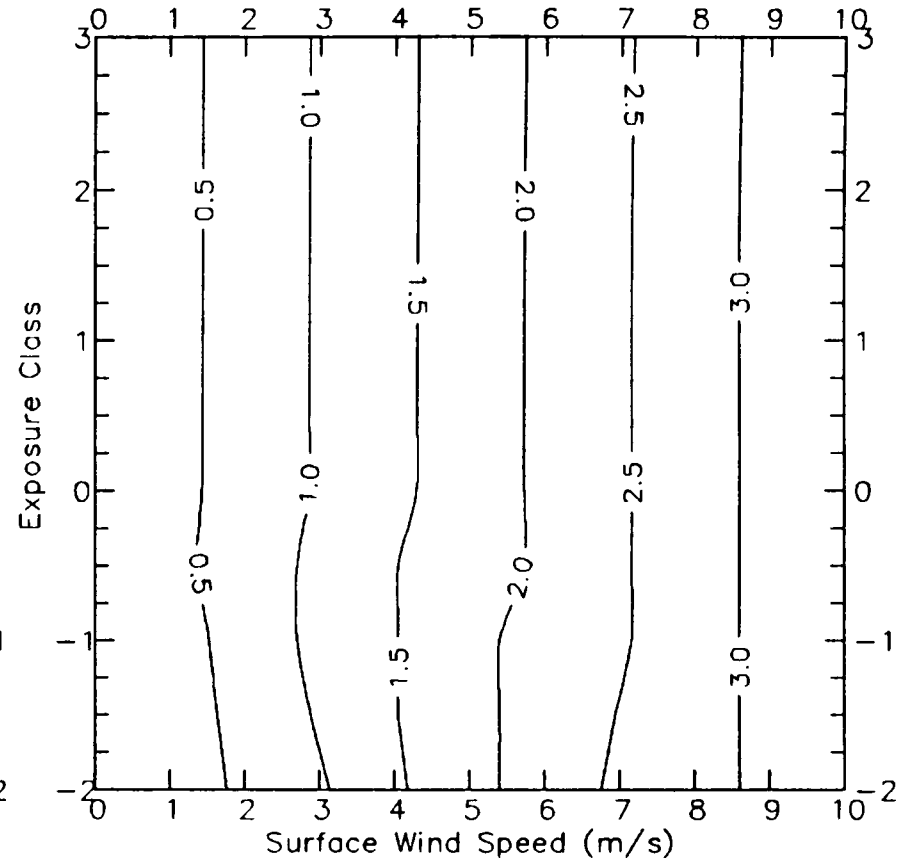


NO2 Deposition Velocities (cm/s) for METROPOLITAN CITY Land Use Type.

MESOPUFF-II

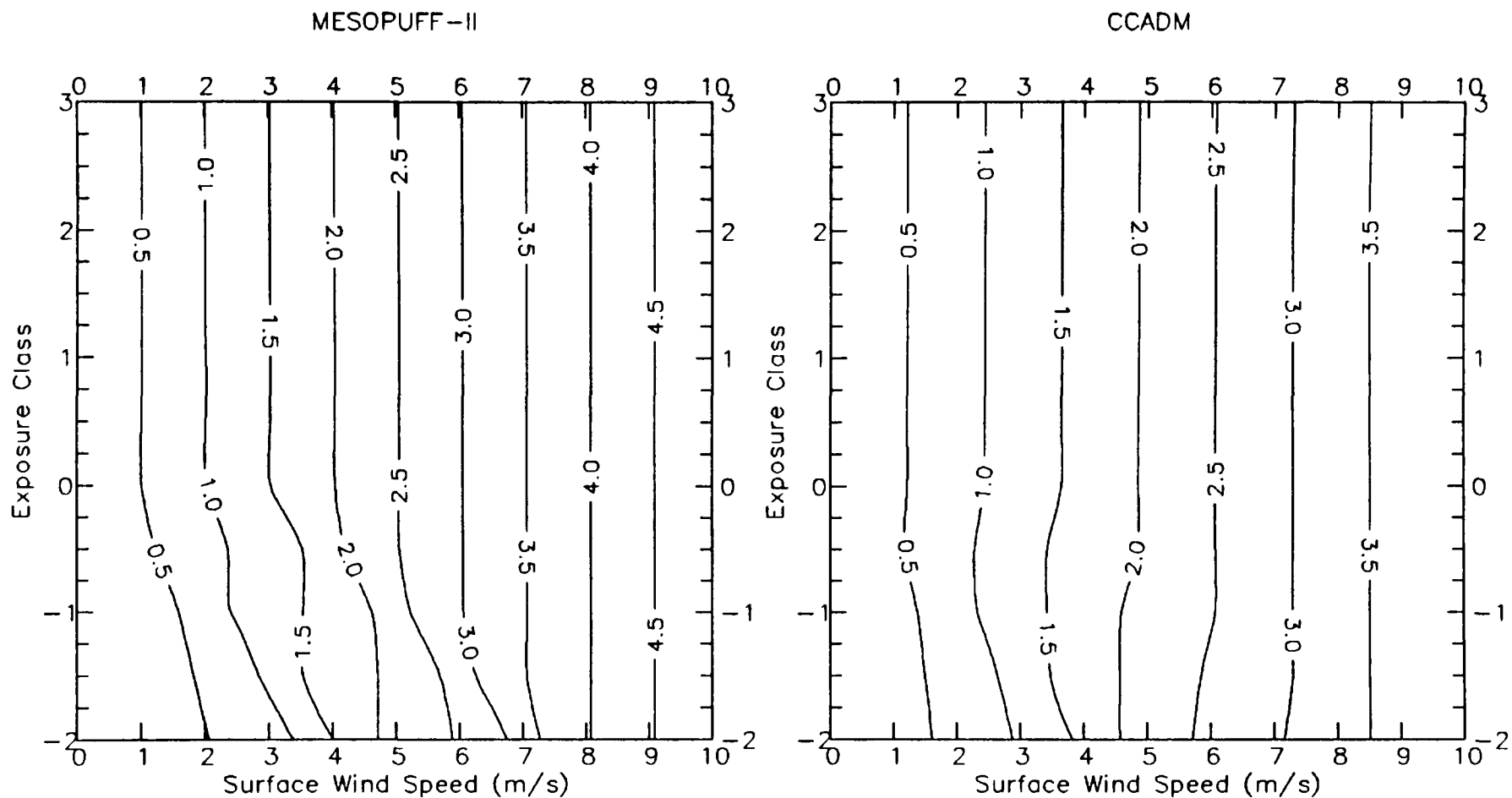


CCADM

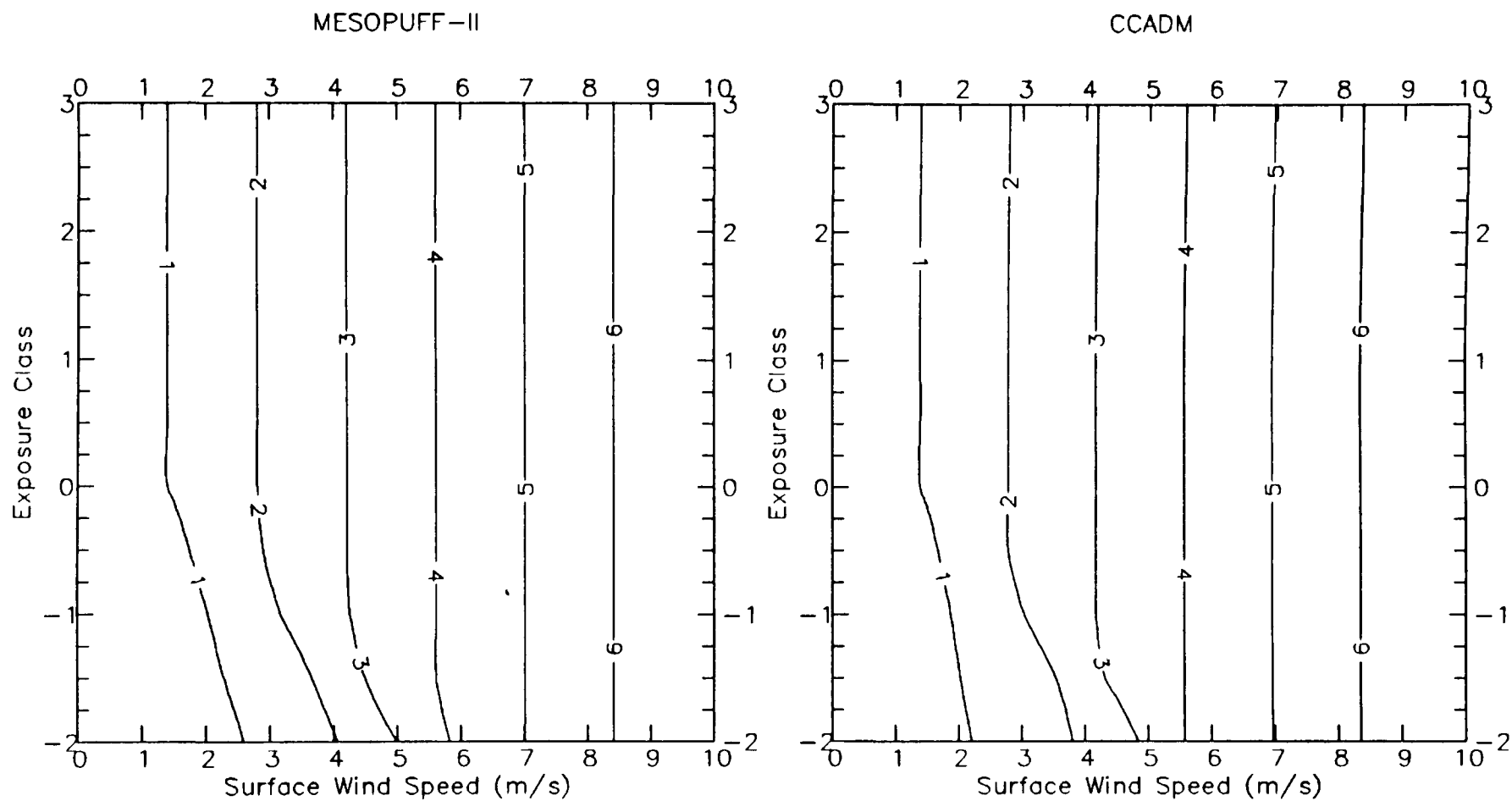


NO<sub>2</sub> Deposition Velocities (cm/s) for LAKE OR OCEAN Land Use Type.

A-35

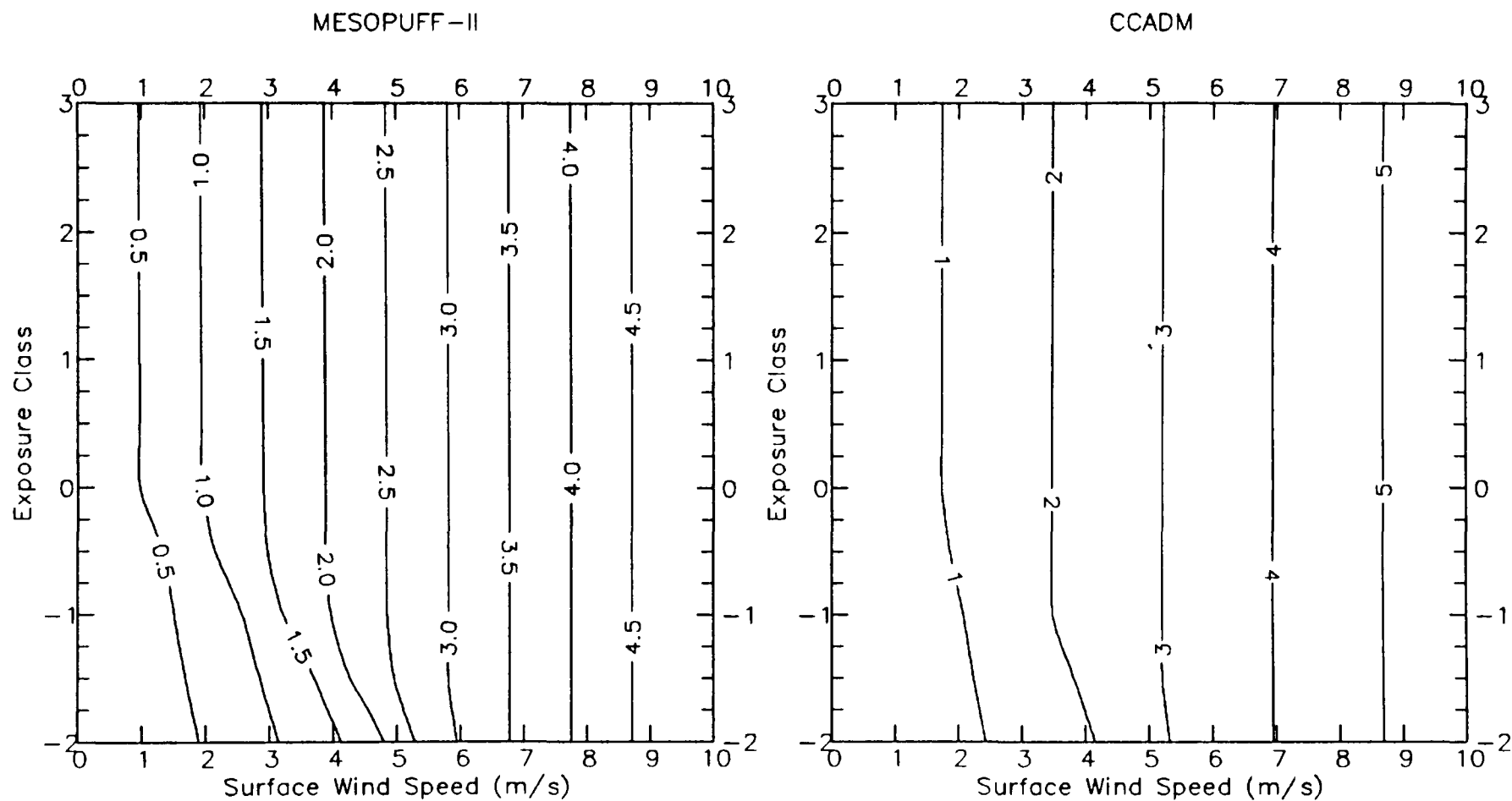


HNO<sub>3</sub> Deposition Velocities (cm/s) for CROPLAND AND PASTURE Land Use Type.

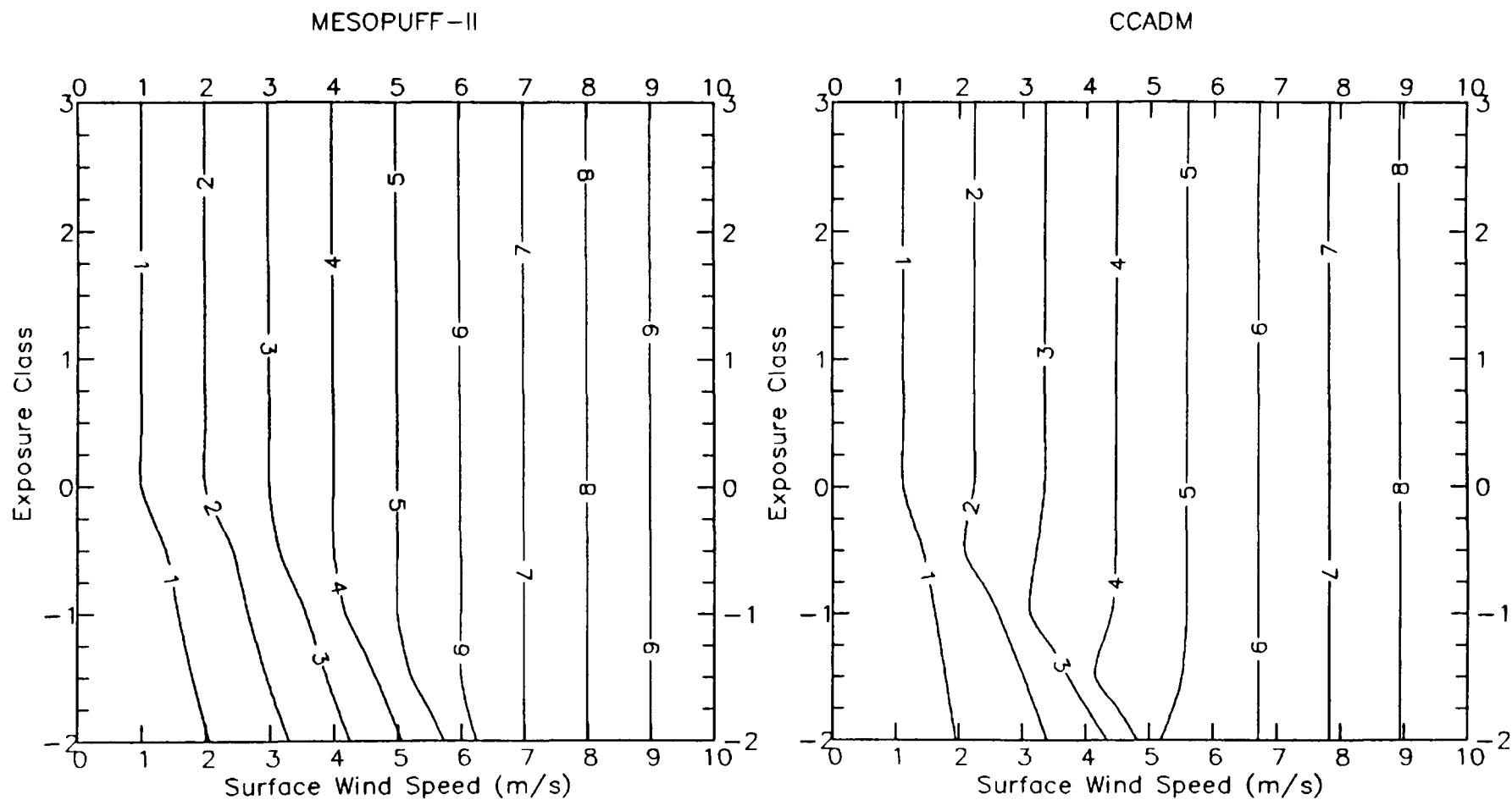


HNO<sub>3</sub> Deposition Velocities (cm/s) for CROPLAND/WOODLAND/GRAZING Land Use Type.

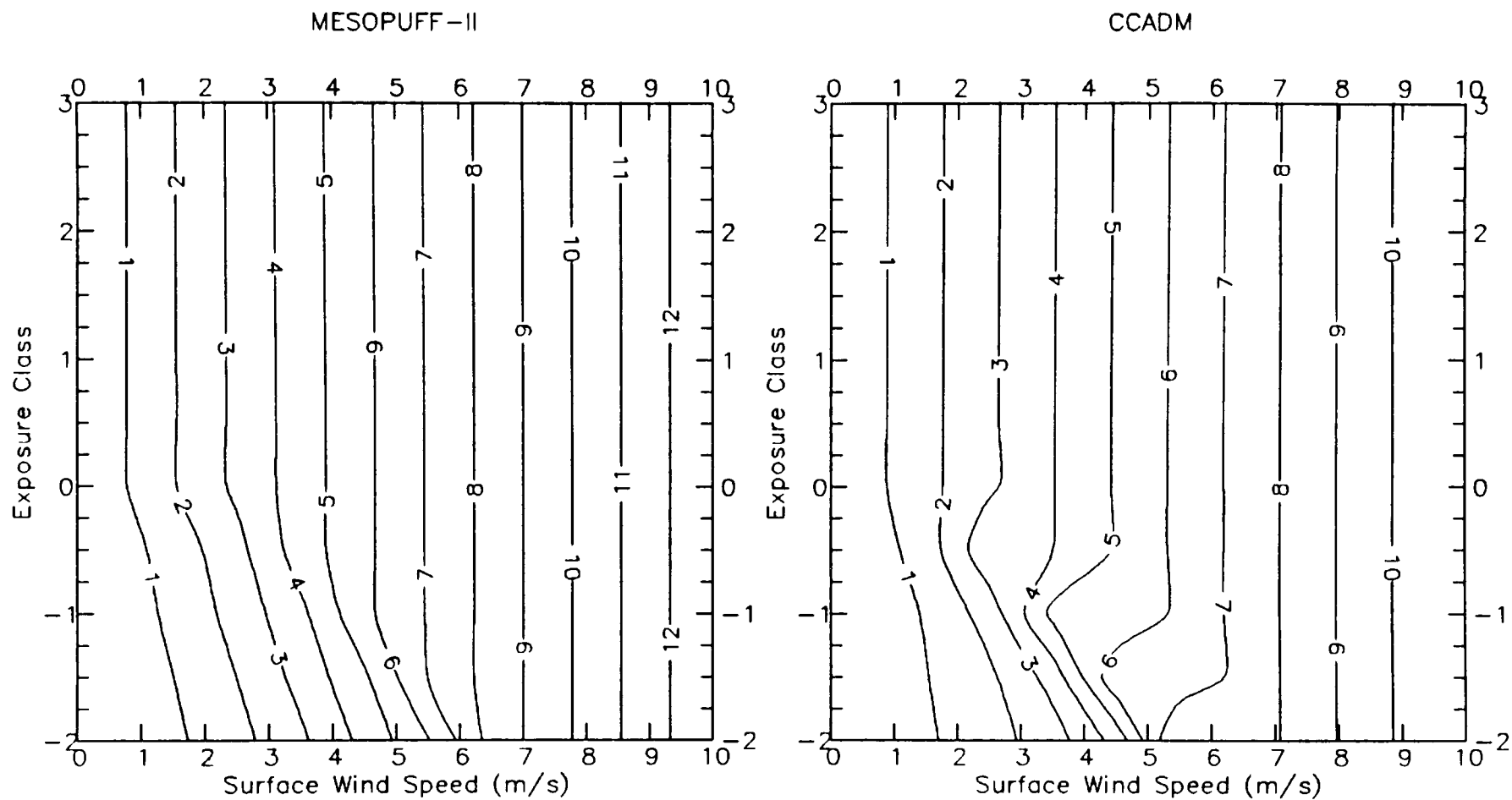
A-37



HNO<sub>3</sub> Deposition Velocities (cm/s) for IRRIGATED CROPS Land Use Type.

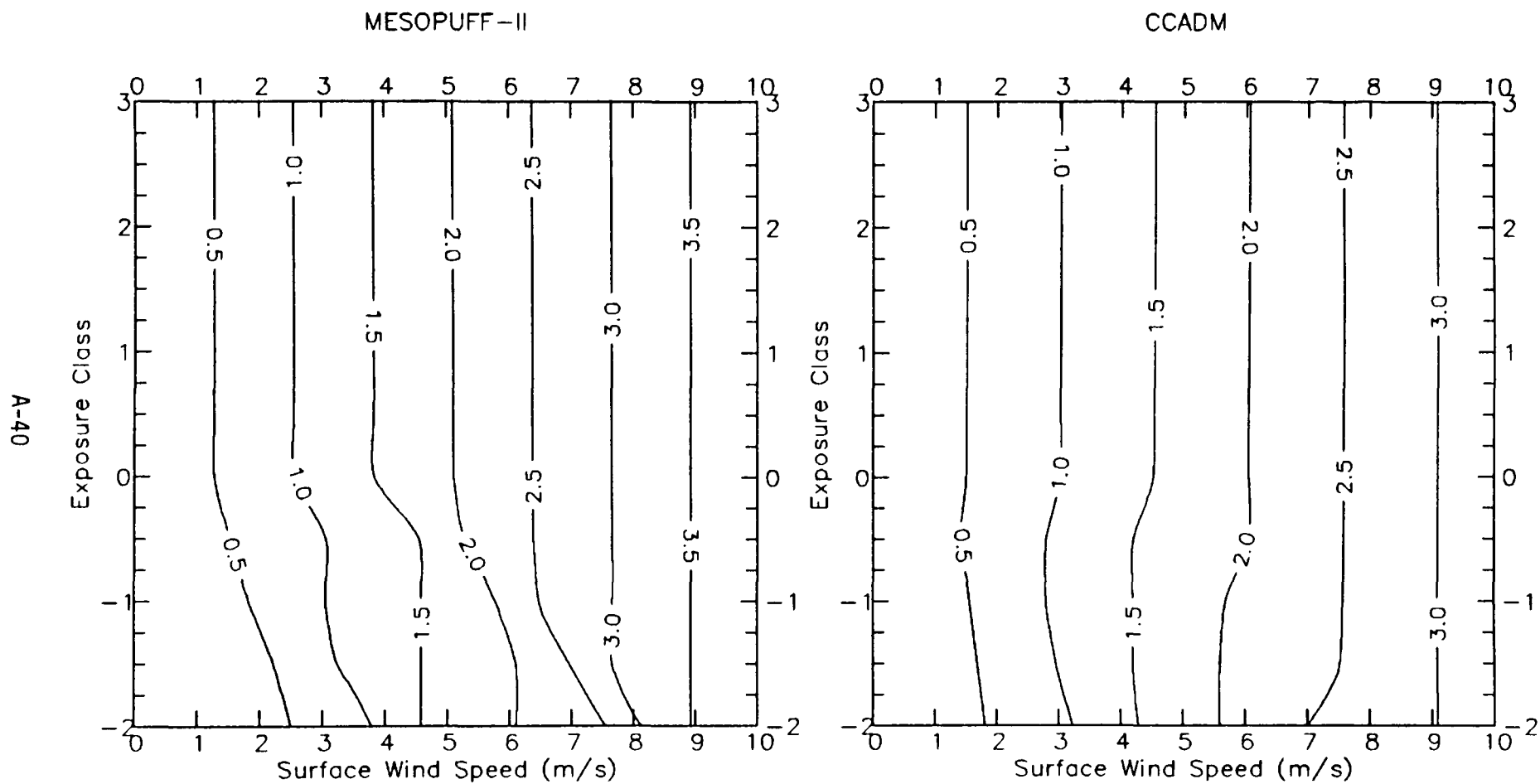


HNO<sub>3</sub> Deposition Velocities (cm/s) for GRAZED FOREST/WOODLAND Land Use Type.

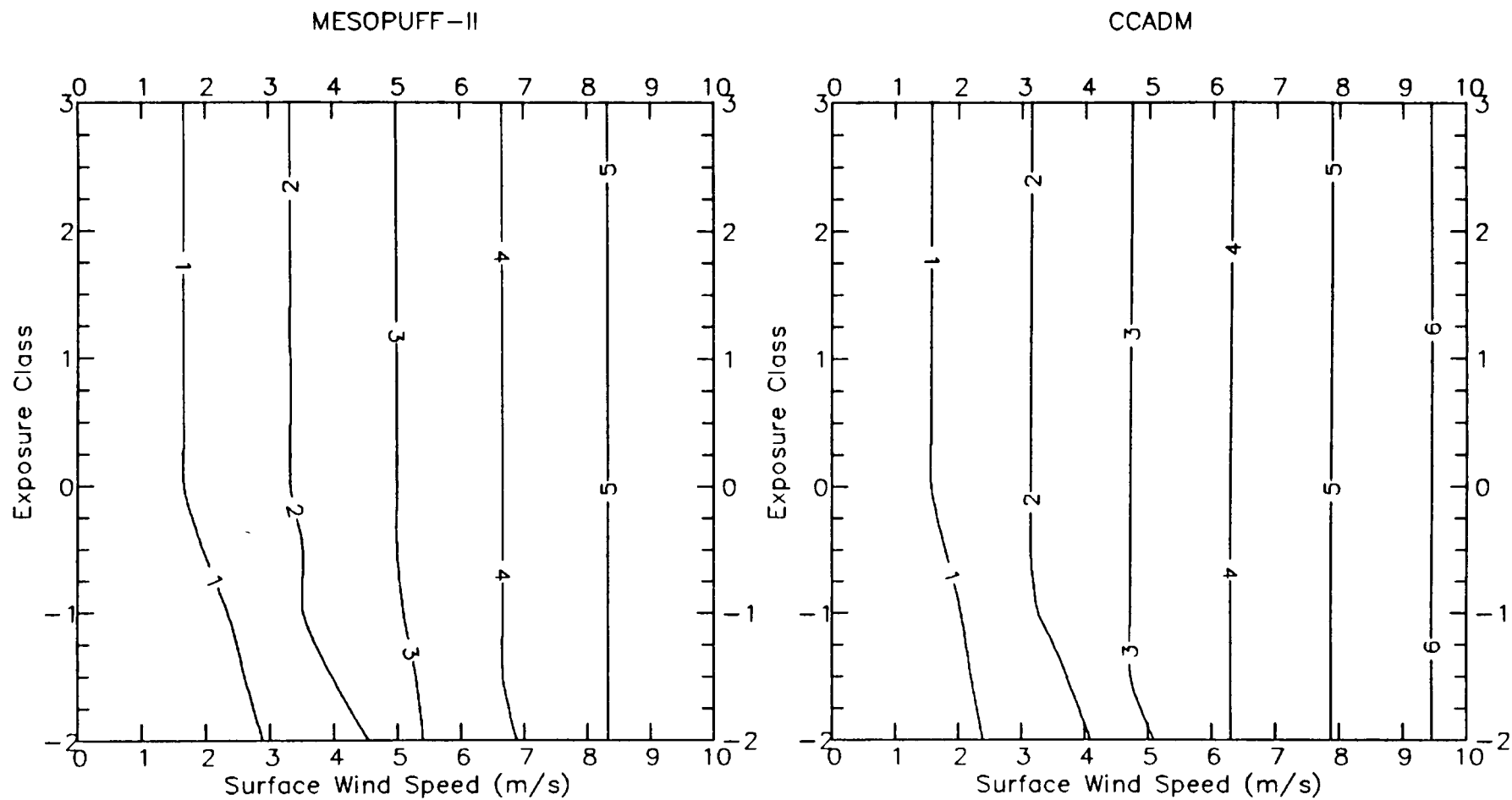


HNO<sub>3</sub> Deposition Velocities (cm/s) for UNGRAZED FOREST/WOODLAND Land Use Type.

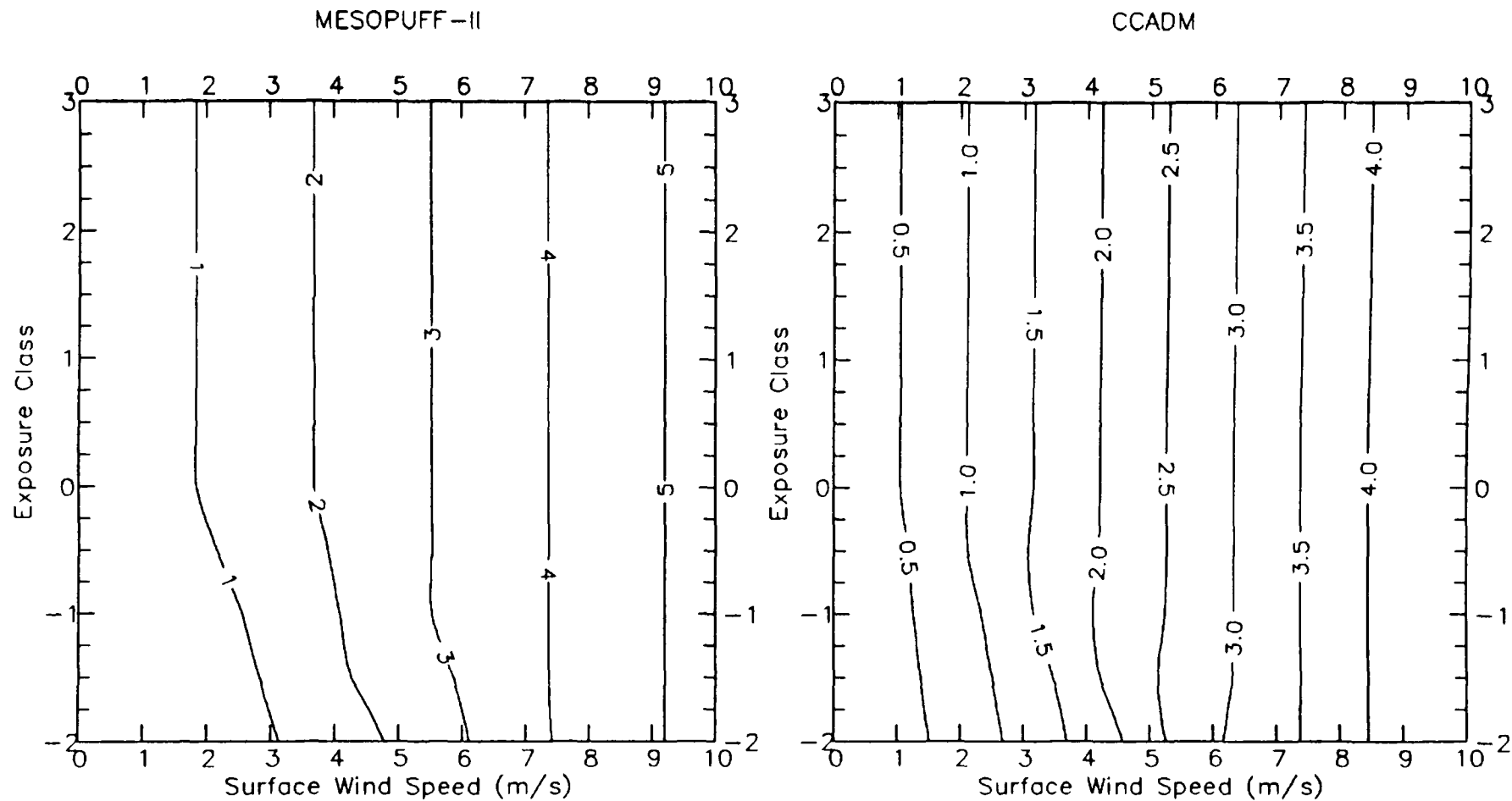




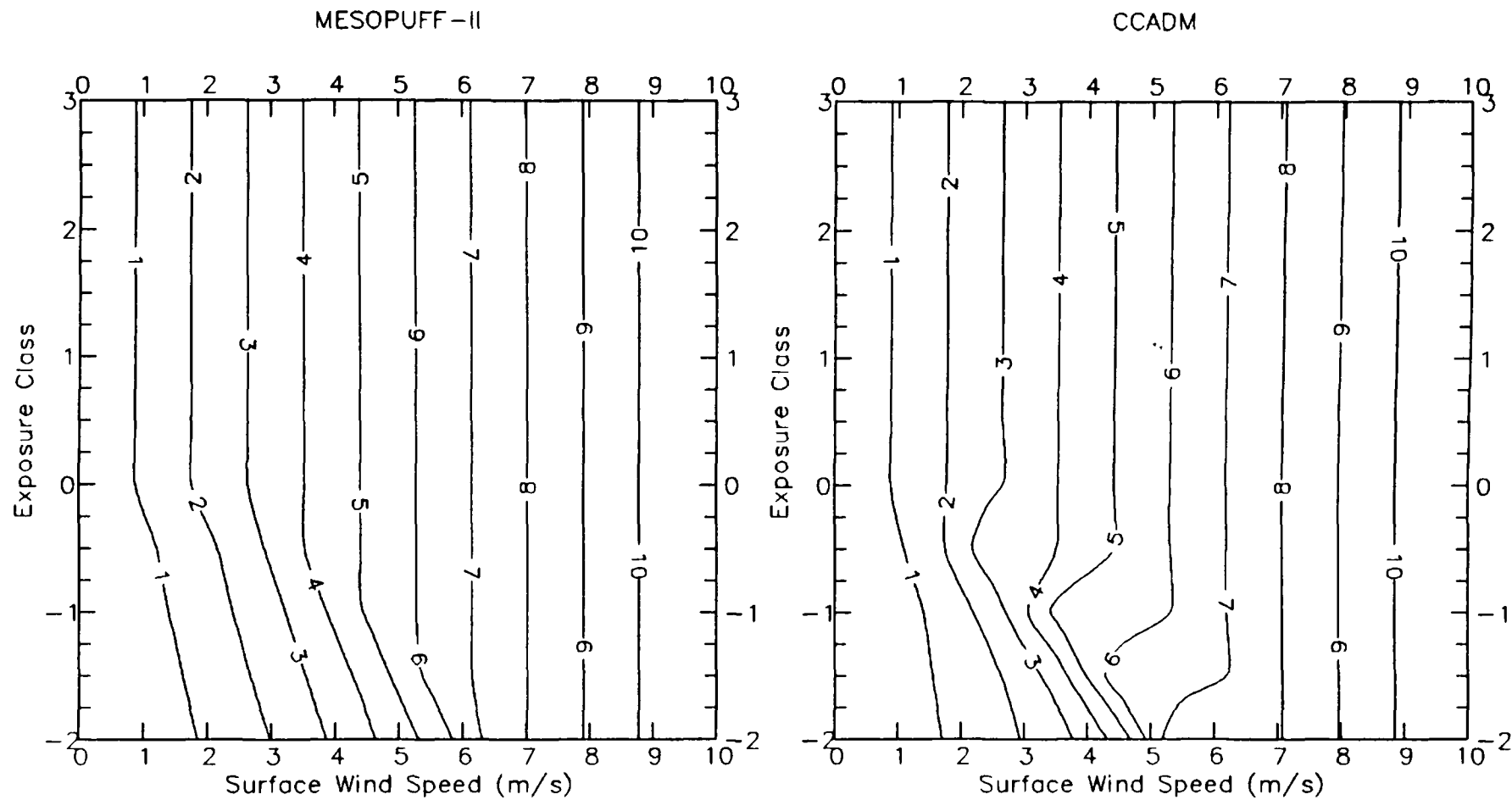
HNO<sub>3</sub> Deposition Velocities (cm/s) for SEMIARID GRAZING Land Use Type.



HNO<sub>3</sub> Deposition Velocities (cm/s) for OPEN WOODLAND GRAZED Land Use Type.

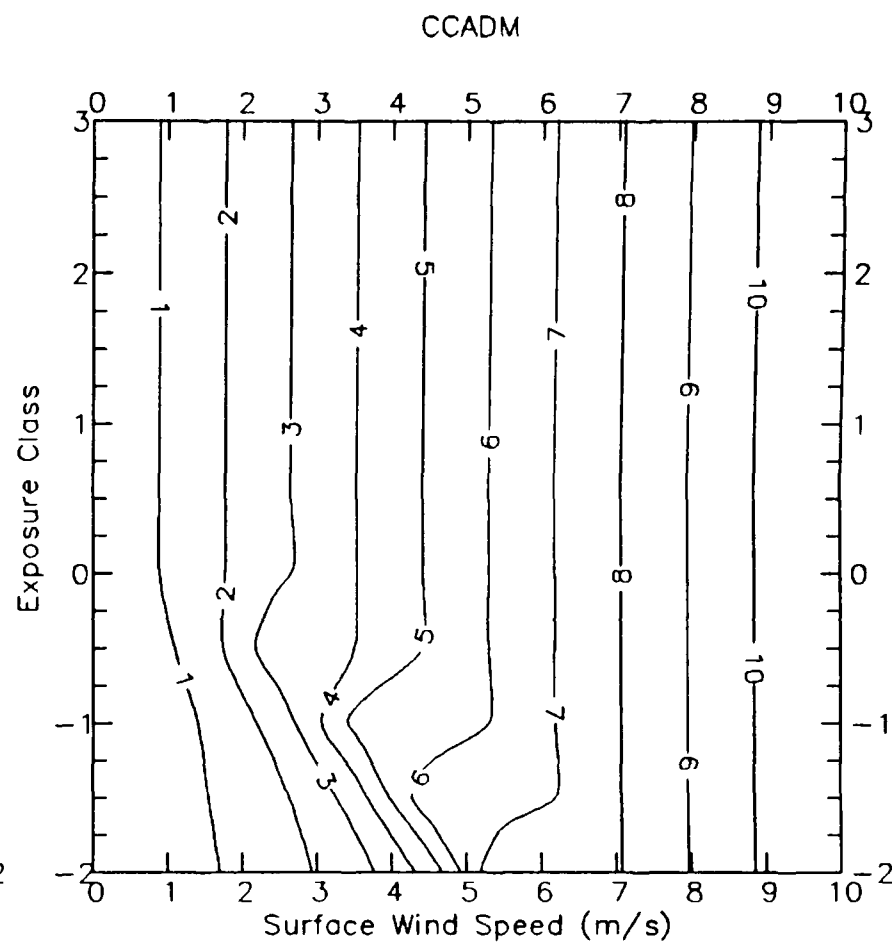
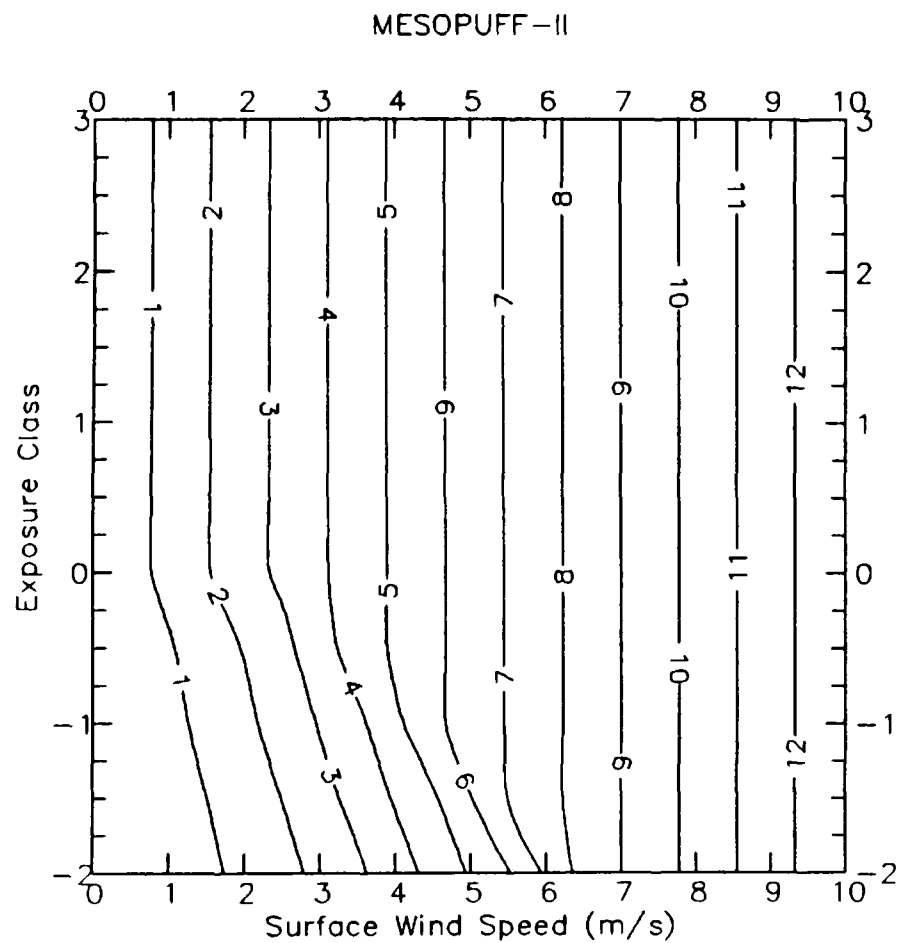


HNO<sub>3</sub> Deposition Velocities (cm/s) for SWAMP Land Use Type.

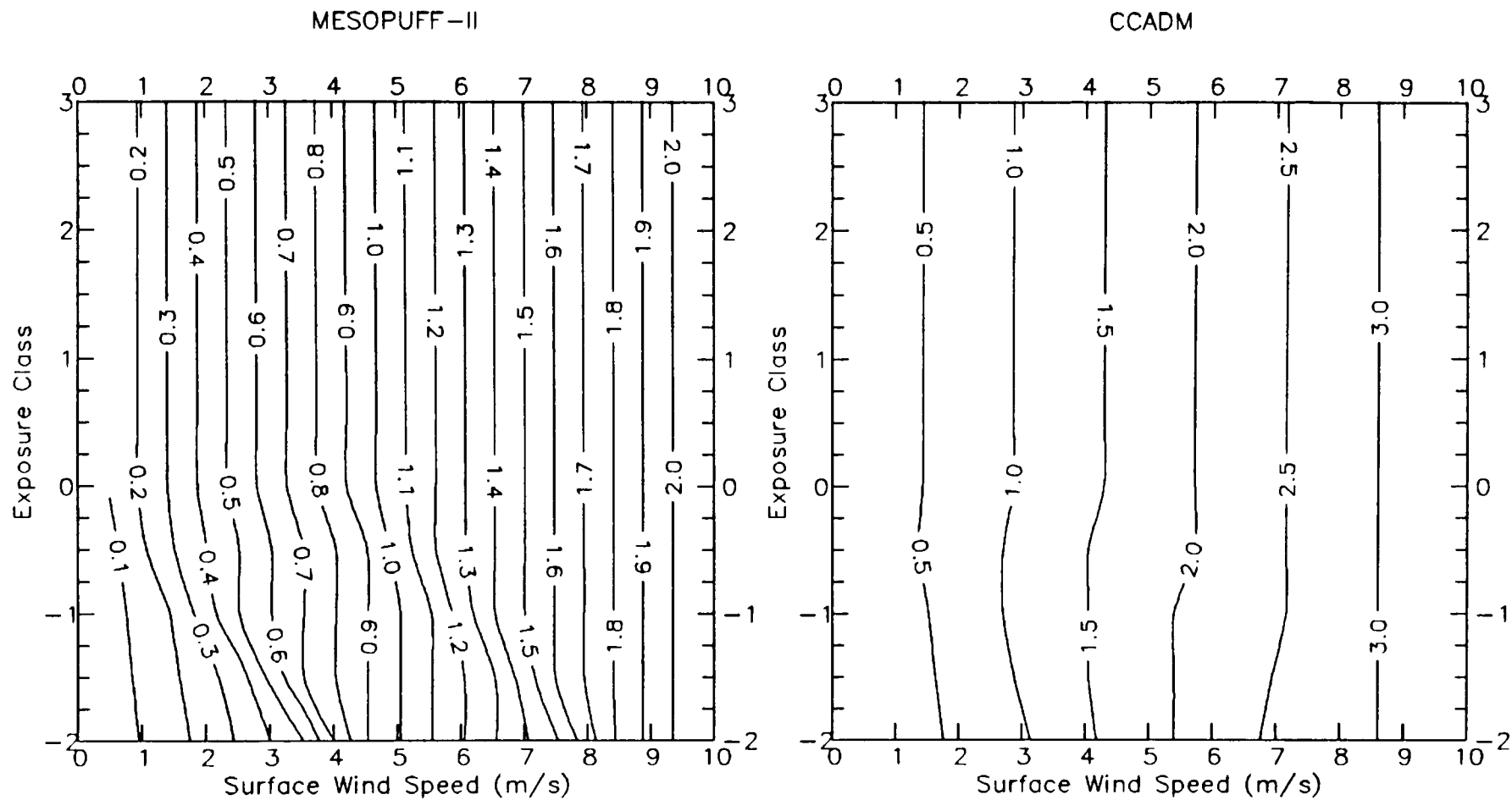


HNO<sub>3</sub> Deposition Velocities (cm/s) for MARSHLAND Land Use Type.

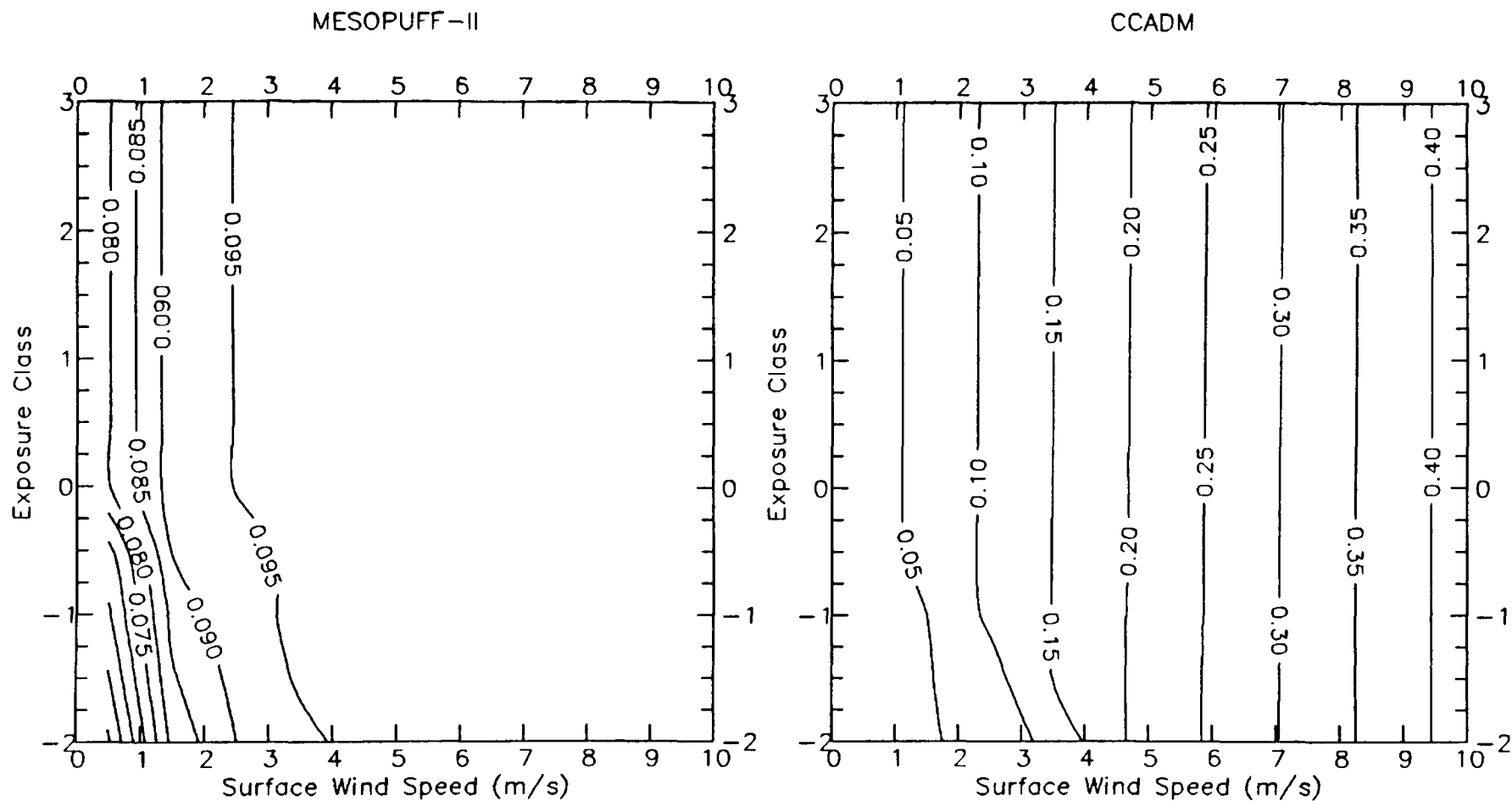
A-44



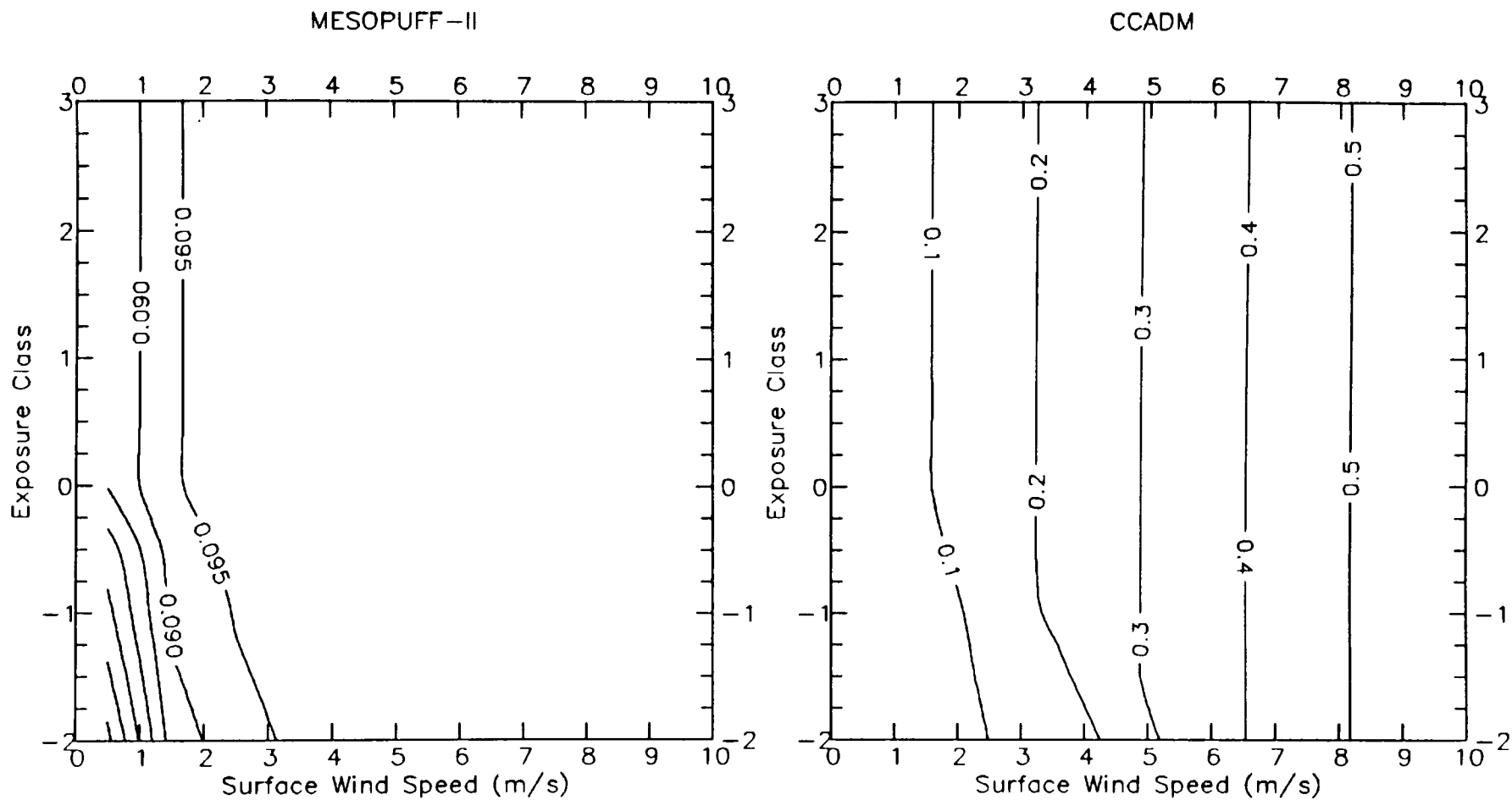
HNO<sub>3</sub> Deposition Velocities (cm/s) for METROPOLITAN CITY Land Use Type.



HNO<sub>3</sub> Deposition Velocities (cm/s) for LAKE OR OCEAN Land Use Type.

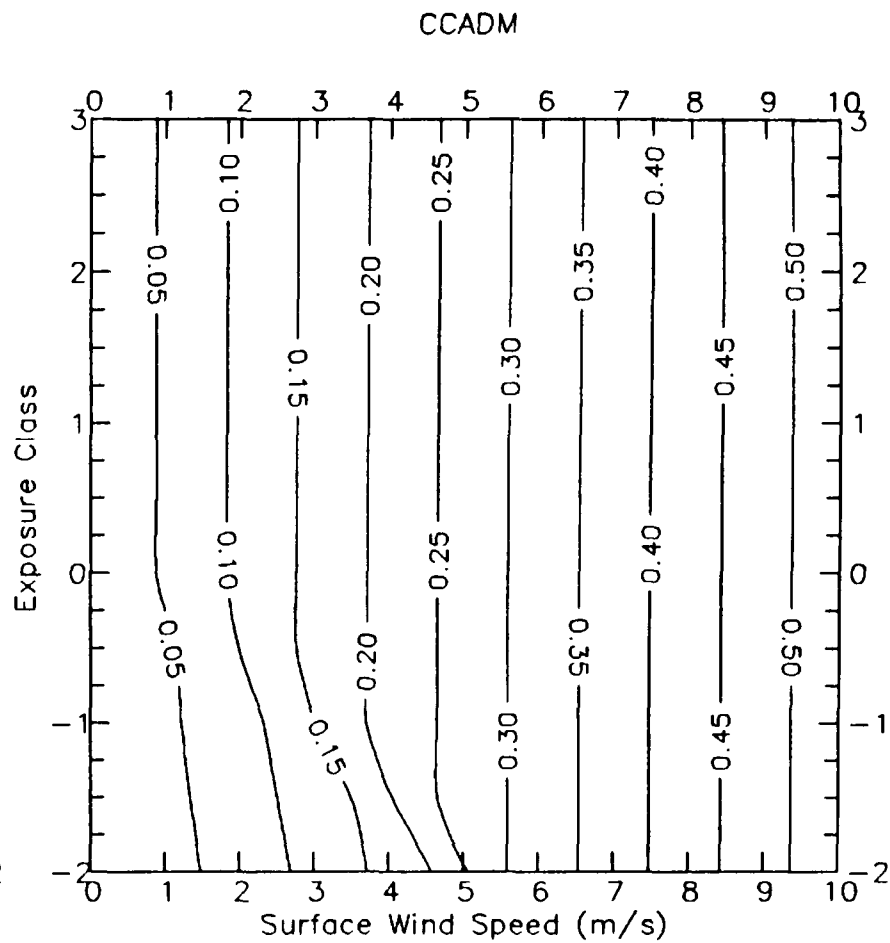
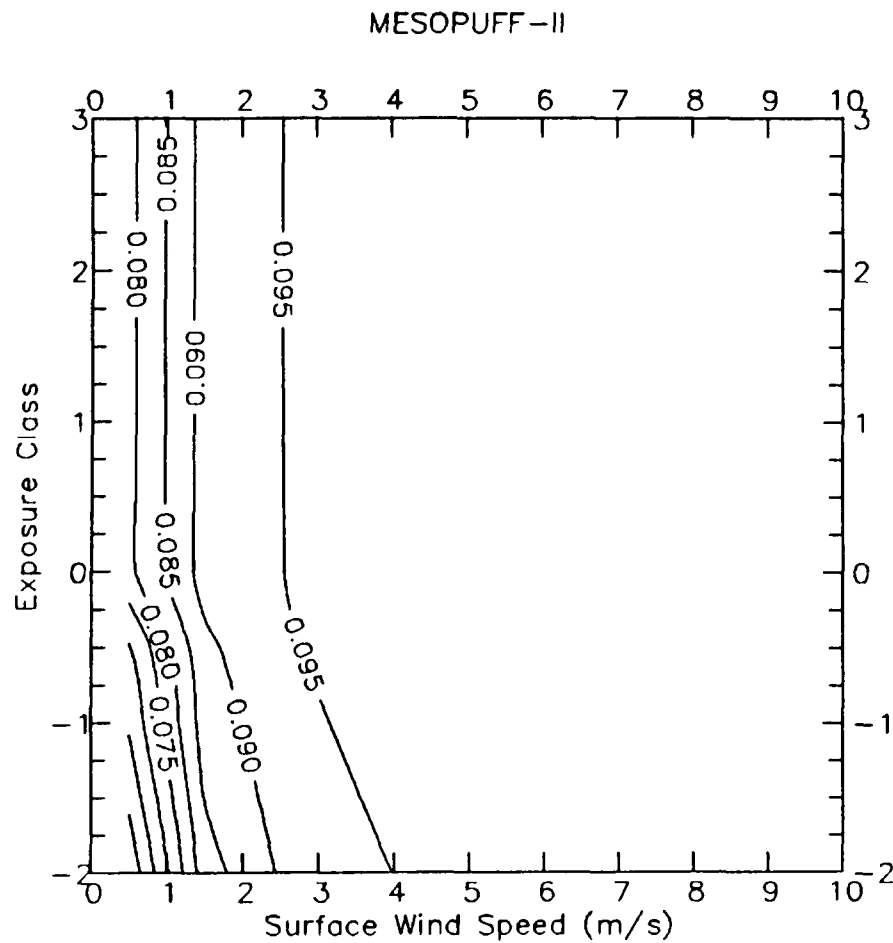


NO<sub>3</sub> Deposition Velocities (cm/s) for CROPLAND AND PASTURE Land Use Type.

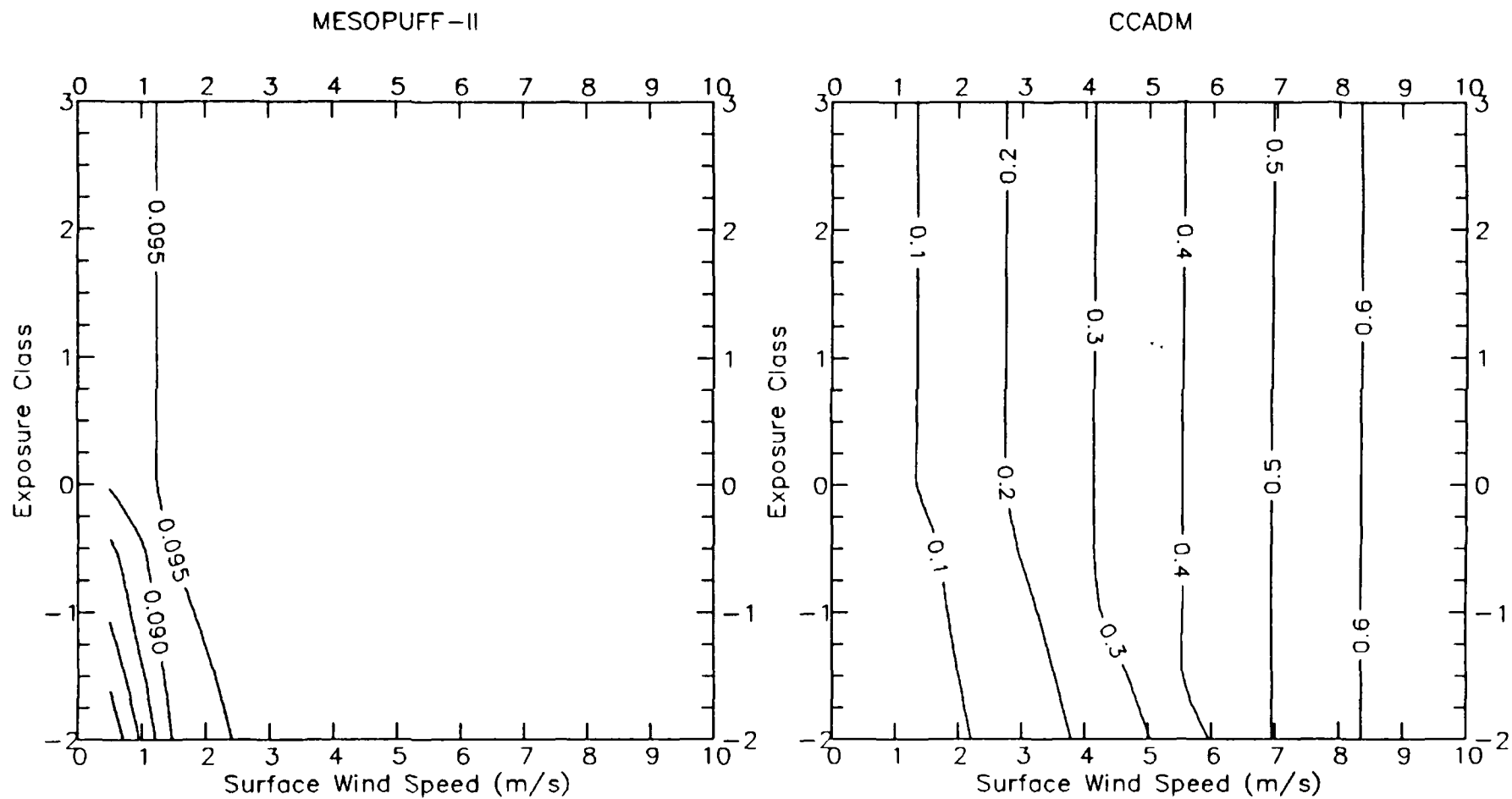


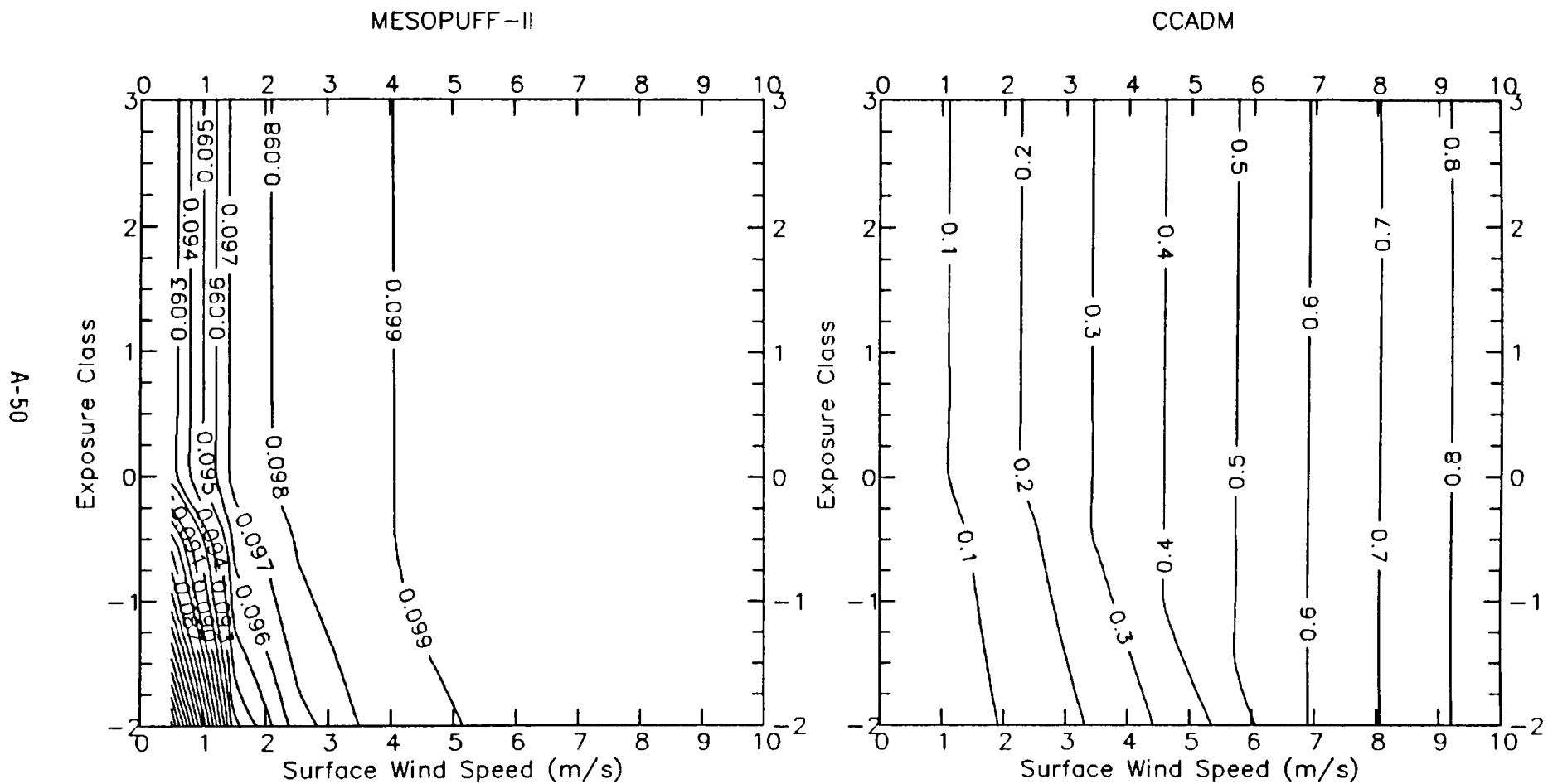
NO3 Deposition Velocities (cm/s) for CROPLAND/WOODLAND/GRAZING Land Use Type.



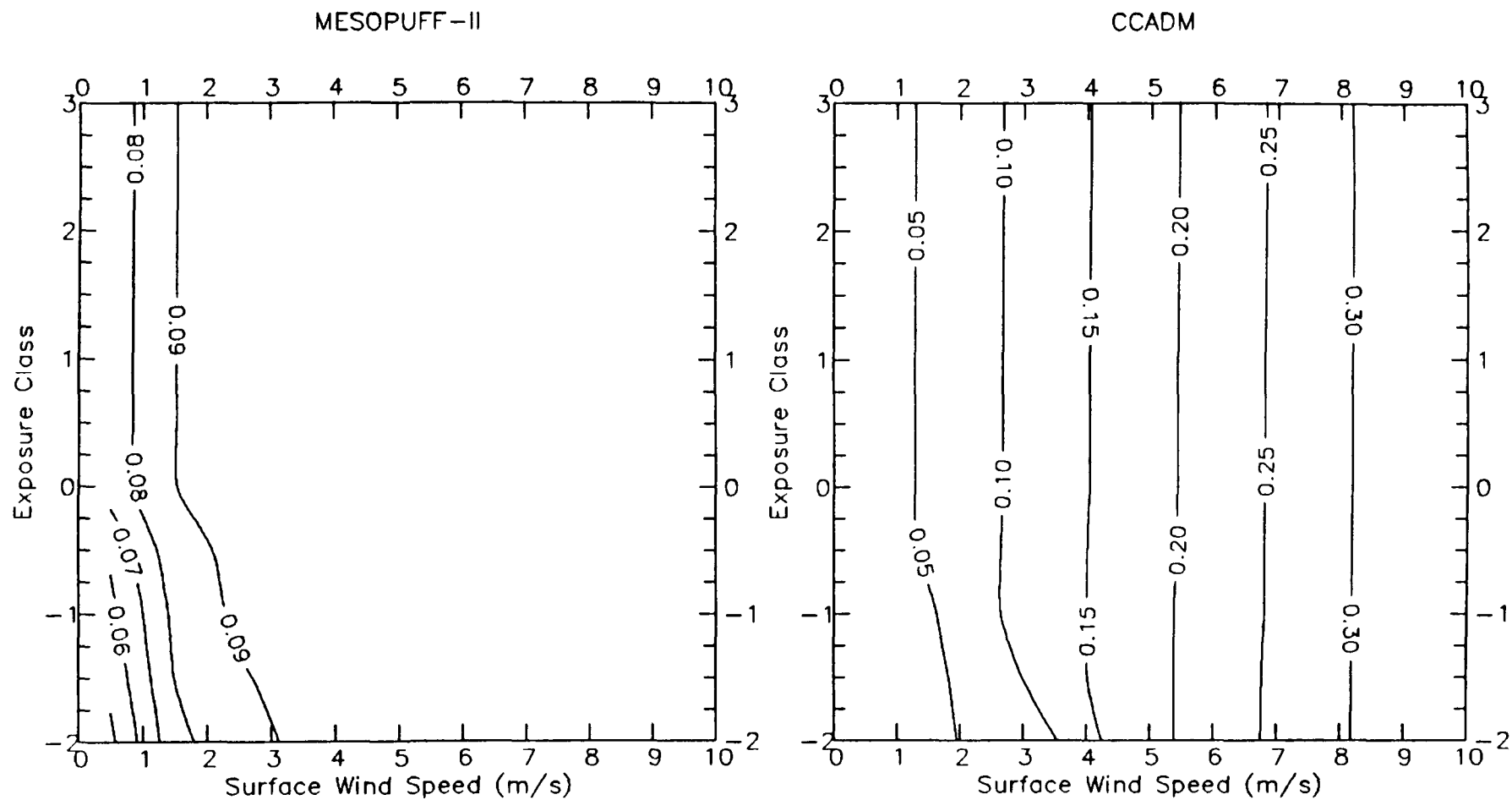


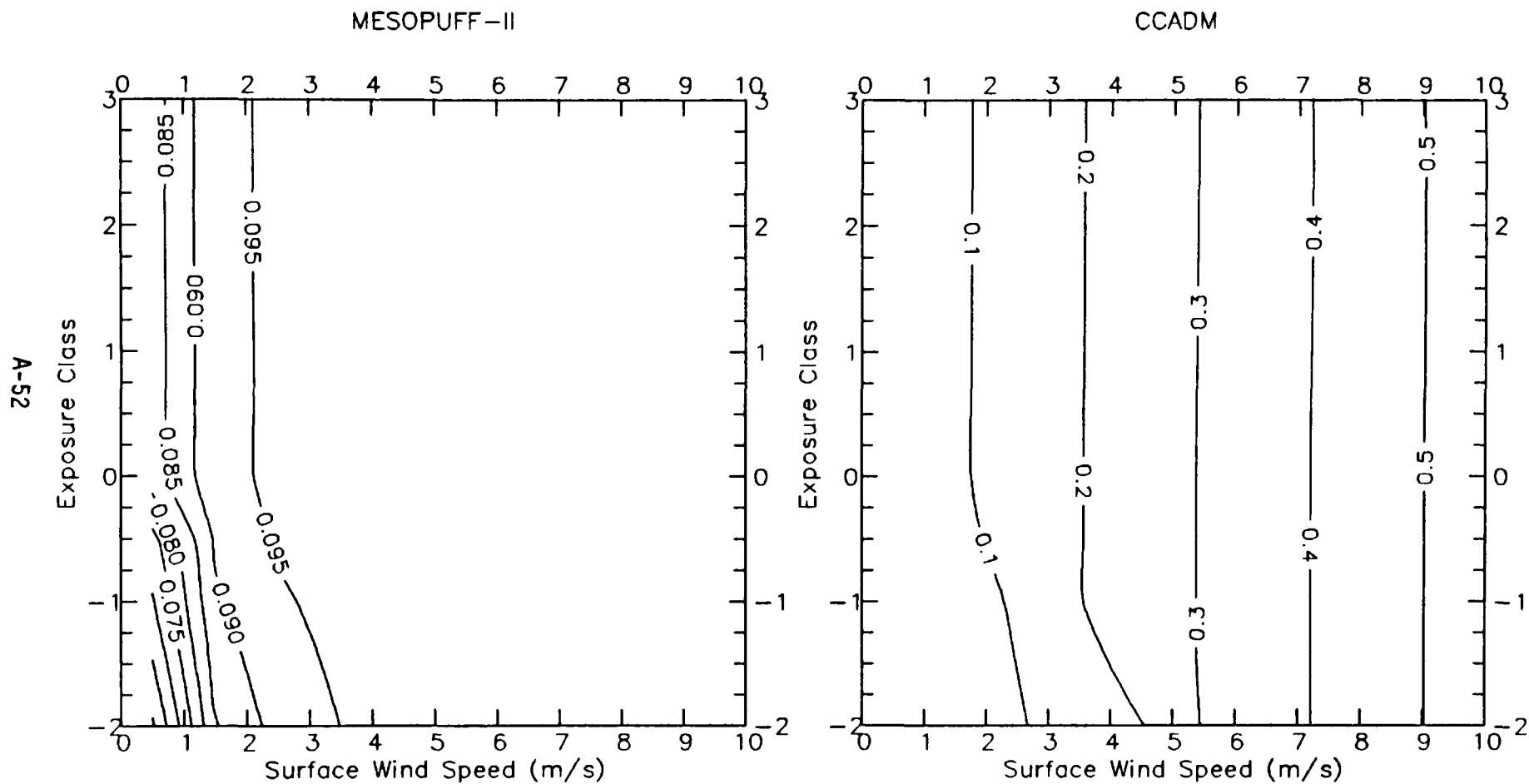
NO<sub>3</sub> Deposition Velocities (cm/s) for IRRIGATED CROPS Land Use Type.



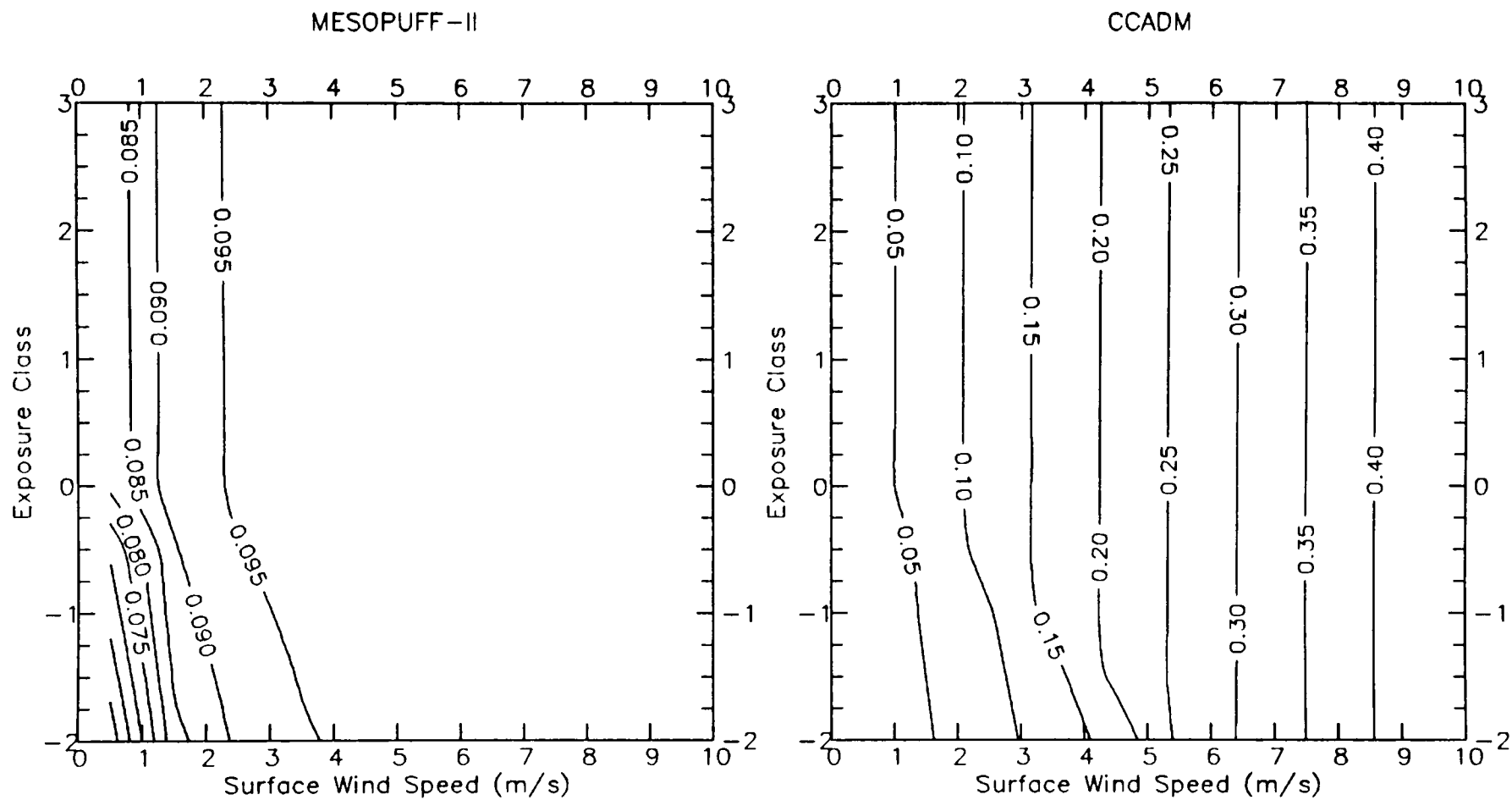


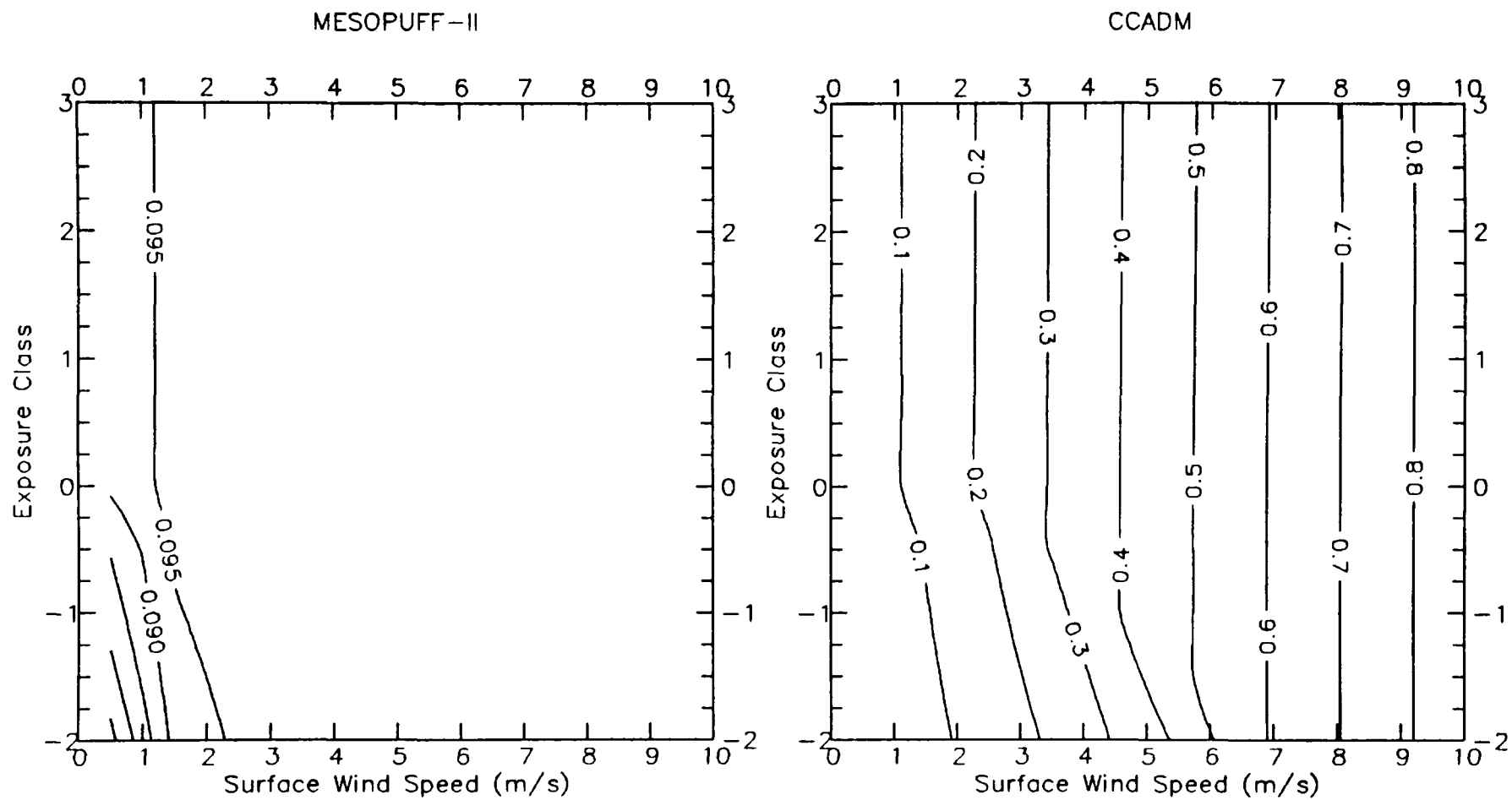
NO3 Deposition Velocities (cm/s) for UNGRAZED FOREST/WOODLAND Land Use Type.



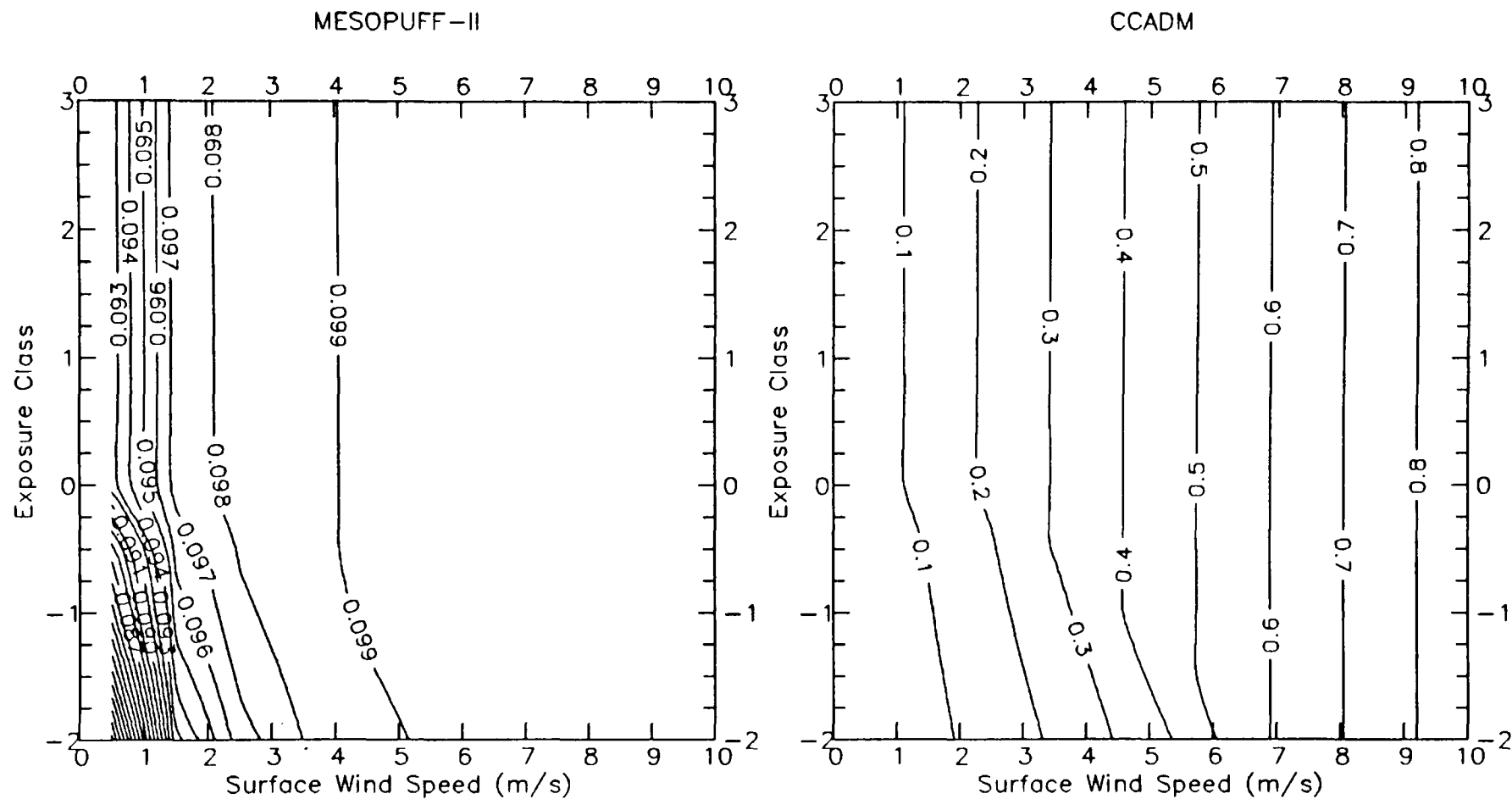


NO<sub>3</sub> Deposition Velocities (cm/s) for OPEN WOODLAND GRAZED Land Use Type.



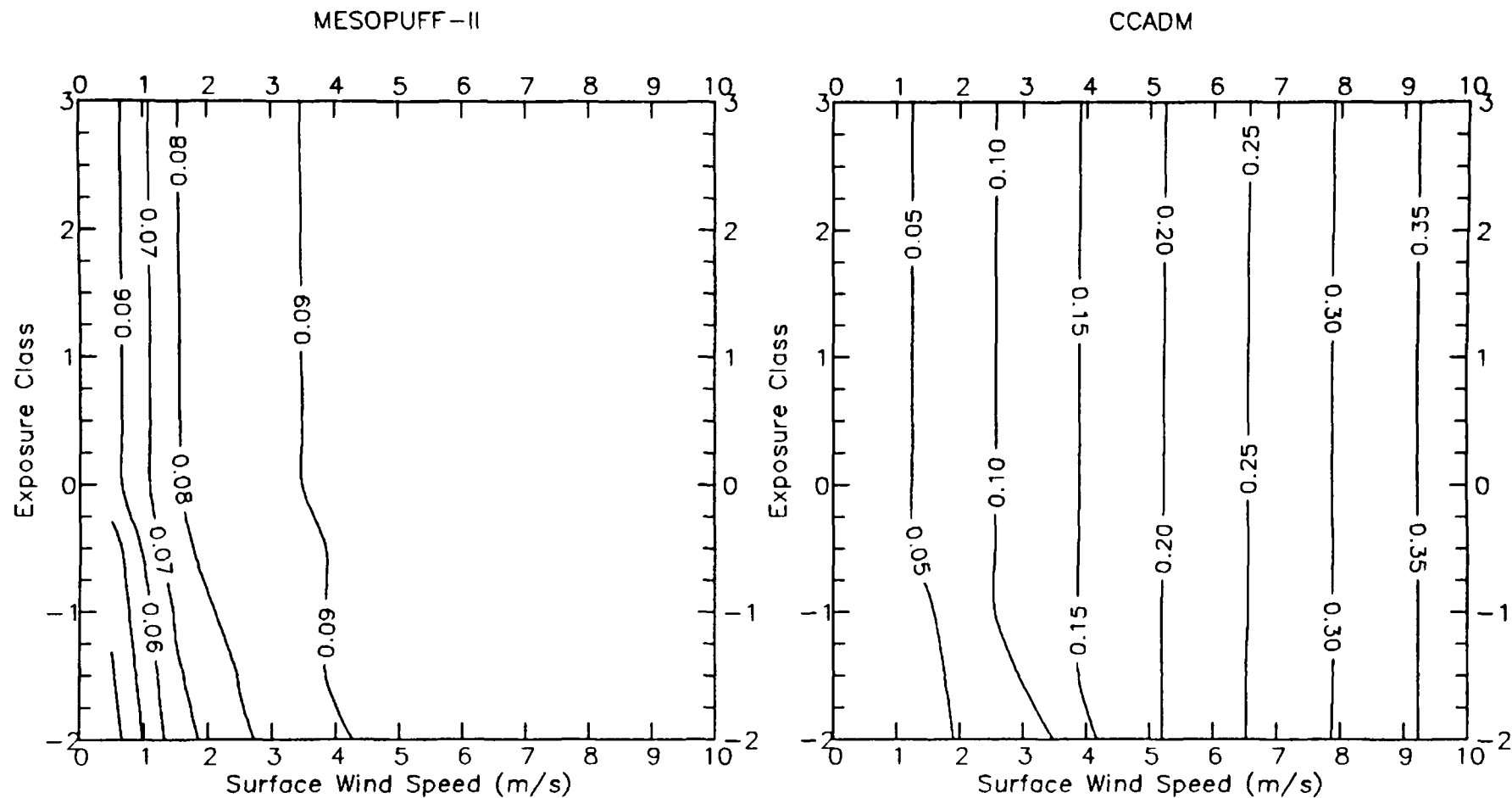


A-55



NO3 Deposition Velocities (cm/s) for METROPOLITAN CITY Land Use Type.





NO3 Deposition Velocities (cm/s) for LAKE OR OCEAN Land Use Type.